

1-1-2011

Development of an Ultra-Lightweight Buckling-Restrained Brace Using Analytical and Numerical Methods

John Andrew Tinker
Portland State University

Let us know how access to this document benefits you.

Follow this and additional works at: http://pdxscholar.library.pdx.edu/open_access_etds

Recommended Citation

Tinker, John Andrew, "Development of an Ultra-Lightweight Buckling-Restrained Brace Using Analytical and Numerical Methods" (2011). *Dissertations and Theses*. Paper 447.

[10.15760/etd.447](https://doi.org/10.15760/etd.447)

This Thesis is brought to you for free and open access. It has been accepted for inclusion in Dissertations and Theses by an authorized administrator of PDXScholar. For more information, please contact pdxscholar@pdx.edu.

Development of an Ultra-Lightweight
Buckling-Restrained Brace Using Analytical and Numerical Methods

by

John Andrew Tinker

A thesis submitted in partial fulfillment of the
requirements for the degree of

Master of Science
in
Civil and Environmental Engineering

Thesis Committee:
Peter Dusicka, Chair
Mike Gorji
Franz Rad

Portland State University
©2011

ABSTRACT

An ultra-lightweight buckling-restrained brace (ULWBRB) is developed using a highly ductile aluminum core and FRP restrainer. Utilization of lightweight materials results in a BRB that is 25% the weight of traditional mortar-filled tube varieties allowing easy installation in small to medium sized buildings requiring seismic retrofit without the need for heavy equipment. Construction utilizes commonly stocked materials able to be customized for required strength, drift, and geometry limitations.

Analytical single degree of freedom (SDOF) and Euler buckling models are compared with published equations to determine the required restrainer stiffness (RRS). SDOF models yield RRS values 200% higher than the Euler model. Applied end moments due to frame deformation are incorporated into a modified design method that gives RRS values 50% higher than Euler model without eccentricity. RRS is provided using a bundled and wrapped FRP tube configuration using a developed shear flow method considering composite action.

Uniaxial low-cycle fatigue (LCF) testing of a 6061-T6 candidate alloy provides data for a constitutive model using combined kinematic-isotropic hardening. LCF testing of round short gage coupons indicates the candidate alloy is capable of stable cycling to 2%, 3%, and 4% total strain with excellent ductility. Early fracture of specimens at 24, 18, and 11 cycles, respectively, also indicates that other candidate alloys should be examined for improved fatigue life. However, inconsistency is noted between similar tests of 6061-T6 that were able to achieve up to 76 cycles at 2.5% total strain.

ULWBRB FEA models loaded monotonically consistently give higher RRS values as compared to the analytical methods. This is due to assignment of initial imperfections, longer more realistic unbraced length, higher axial loads achieved through the post-yield region, and plastic hinging potential. Cyclic simulations of braces with the same RRS values are also able to achieve reliable and stable hysteretic behavior through 21 cycles. If a less stiff restrainer is used, cumulative energy dissipation potential is reduced considerably due to pinched hysteresis loops and strain ratcheting. Applied end moments are found to have a linear effect on the RRS that can be modeled by superposition of the buckling effect plus end moment.

TABLE OF CONTENTS

ABSTRACT	i
LIST OF TABLES	vii
LIST OF FIGURES	ix
LIST OF ABBREVIATIONS AND SYMBOLS	xv
1.0 INTRODUCTION	1
2.0 LITERATURE REVIEW	5
2.1 Introduction	5
2.2 Buckling-Restrained Braces	6
Introduction.....	6
Beginnings and Proliferation of the BRB.....	8
Specific Types of BRBs.....	10
Mortar-filled Steel Tube BRB.....	11
All-Steel BRB.....	14
Methods of Unbonding the Core and Restrainer.....	18
Building Code Provisions for BRBs in the United States.....	19
Ductility Comparison.....	20
Adjusted Brace Strength.....	21
Qualification Testing.....	21
Other Code Requirements.....	22
2.3 Use of Aluminum in Building Structures	23
Introduction.....	23

Manufacture.....	26
Applications in Seismic Force Resisting Systems.....	28
Material Level Behavior.....	29
Compression Member Tests.....	31
Building Code Provisions.....	32
2.4 Fiber Reinforced Polymers.....	33
Introduction.....	33
Applications in Civil Engineering Structures.....	34
FRP Bonded to Steel Members.....	36
FRP Unbonded to Steel Members.....	39
Galvanic Corrosion.....	43
2.5 Mathematical Modeling of BRB.....	44
Introduction.....	44
Analytical Modeling of BRB.....	44
Numerical Modeling of BRB.....	50
Hysteretic Modeling of Steel Braces.....	55
Cumulative Plastic Ductility and Deformation Capacity.....	56
3.0 MODEL BUILDING.....	58
3.1 Objective.....	58
3.2 Selection Criteria.....	58
3.3 SAC Model Building.....	60
3.4 Equivalent Lateral Force Analysis.....	63
3.5 Final Frame and Brace Geometry.....	67

4.0 BRACE CONFIGURATION	71
4.1 Objective.....	71
4.2 Core Concepts.....	71
4.3 Restrained Brace Mechanical Models.....	76
Single Degree-of-Freedom Model.....	78
Global Stability Modeled with an Euler Column.....	98
4.4 Full-scale Restrainer Design.....	103
FRP Material Properties.....	103
Composite Behavior of FRP Assemblage.....	105
Analytical Design of Restrainer Tubes.....	108
Analytical Design of Restrainer Wrap.....	115
Core Spacer Consideration.....	116
Weight Comparison between BRBs.....	118
Conclusion.....	119
5.0 BRACE SCALING	121
5.1 Objective.....	121
5.2 Core Scaling.....	121
5.3 Partial-scale Restrainer Design.....	124
6.0 COUPON TESTING	129
6.1 Objective.....	129
6.2 ASTM Test Methods.....	129
6.3 Tensile Coupon Tests.....	130
6.4 Cyclic Coupon Tests.....	133

6.5 Comparison with Other Materials.....	138
6.6 Constitutive Model.....	141
6.7 Verification of Constitutive Model.....	143
7.0 NUMERICAL MODELING.....	147
7.1 Objective.....	147
7.2 Numerical Model.....	147
Geometric Imperfections.....	148
General Model Configuration.....	150
Convergence Study.....	152
7.3 Monotonic Tests.....	156
Comparison of Analytical & Numerical Results.....	166
7.4 Cyclic Tests.....	168
Loading Protocol.....	169
Testing Parameters & Results.....	171
8.0 CONCLUSION.....	188
8.1 Overall Assessment.....	188
8.2 Recommendations for Further Research.....	192
9.0 REFERENCES.....	195
APPENDICES.....	204
Appendix A- Calculation of Bolted End Connections (Full-scale brace).....	205
Appendix B- Calculation of Bolted End Connections (Partial-scale brace).....	207
Appendix C- Calculation of Core Available Strengths (Full-scale brace).....	209
Appendix D- Calculation of Core Available Strengths (Full-scale brace).....	211

LIST OF TABLES

Table 1 – Comparison of Typical Lateral Force Resisting Systems.....	20
Table 2 – FRP Material Properties.....	34
Table 3 – Summary of Model Buildings in the Literature.....	60
Table 4 – Building Mass/Weight by Level.....	63
Table 5 – Seismic Design Criteria.....	64
Table 6 – Seismic Base Shear Calculation.....	65
Table 7 – Lateral Seismic Force Calculation.....	66
Table 8 – Full-scale Available Strength of Unrestrained Core.....	75
Table 9 – Available Plastic Moment of Reduced Section of Core.....	91
Table 10 – Summary of Pultruded GFRP Structural Shape Material Properties.....	104
Table 11 – Summary of GFRP Fabric/Resin System Material Properties.....	105
Table 12 – Available Plastic Moment of Intermediate Section of Core.....	111
Table 13 – Full-scale Required Restrainer Stiffness.....	111
Table 14 – Full-scale Wrap Shear Flow Analysis.....	115
Table 15 – Mechanical Properties of Common Plastics.....	117
Table 16 – Weight Comparison Between BRBs.....	118
Table 17 – Partial-scale Available Strength of Unrestrained Core.....	124
Table 18 – Available Plastic Moment of Intermediate Section of Core.....	125
Table 19 – Partial-scale Required Restrainer Stiffness.....	126
Table 20 – Partial-scale Wrap Shear Flow Analysis.....	127

Table 21 – Tension Test Results.....	132
Table 22 – Cyclic Test Results.....	135
Table 23 – LCF Comparison of Metallic Materials.....	139
Table 24 – Kinematic Hardening Stress-Strain Data.....	144
Table 25 – Shell Element Aspect Ratios.....	152
Table 26 – Results at 2-in Displacement (3,480 Elements).....	156
Table 27 – Monotonic Test Brace Parameters.....	157
Table 28 – Cyclic Test Displacement Protocol.....	170
Table 29 – Cyclic Test Brace Parameters.....	172
Table 30 – Cumulative P- Δ	185

LIST OF FIGURES

Figure 1 - The ultra-lightweight buckling-restrained brace	1
Figure 2 - ULWBRB development process chart	4
Figure 3 - Possible cross sectional configurations of BRB (Xie, 2005)	11
Figure 4 - BRBs at manufacturing facility in China and gusset plates on site (Brown et al., 2001)	25
Figure 5 - Modified SAC 3-story model building plan.....	61
Figure 6 - Modified SAC 3-story model building elevations	62
Figure 7 - BRBF lateral seismic forces by story, Seattle (left) and Los Angeles (right)..	67
Figure 8 - Brace seismic axial forces (P_u), Seattle (left) and Los Angeles (right).....	67
Figure 9 - BRBF and BRB geometry.....	70
Figure 10 - Full-scale Core Section Properties	74
Figure 11 - Unknown force interaction between core and restrainer.....	76
Figure 12 - Brace dimensions, unrestrained core (top) restrained core (bottom)	77
Figure 13 - Diagram of force and moment equilibrium for development of the differential equation.....	78
Figure 14 - Single degree-of-freedom mechanical model, undeflected (top) deflected (bottom).....	79
Figure 15 - Exaggerated free body diagram of column half-length.....	81
Figure 16 - Plot of core internal moment and equivalent restrainer moment versus unbraced length.....	84

Figure 17 - Plot of ratio of equivalent restrainer moment to core internal moment versus unbraced length.....	84
Figure 18 - Load-displacement curves for perfect and imperfect Euler columns.....	85
Figure 19 - Four-angle core mechanical model – pinned ends/one-way/in-plane (mode A)	87
Figure 20 - Centroidal loading of four-angle core	88
Figure 21 - Example SDOF model convergence plot with restrainer flexural stress constraint.....	89
Figure 22 - Example SDOF convergence plot without restrainer flexural stress constraint	89
Figure 23 - BRB restrainer design plot for four-angle core configuration mode A buckling.....	90
Figure 24 - Four-angle core mechanical model - fixed ends/one-way/in-plane (mode B).....	92
Figure 25 - Interaction of axial load and available moment for composite section.....	92
Figure 26 - Four-angle core axes definition (x-x, y-y are geometric axes, z-z are principal axes)	93
Figure 27 - BRB restrainer design plot for four-angle core configuration mode B buckling	94
Figure 28 - Four-angle core mechanical model - pinned ends/all-ways (mode C).....	95
Figure 29 - Hoop force diagrams for mode C buckling.....	95
Figure 30 - Transverse FRP wrap influence area for mode C buckling	96
Figure 31 - Plot of normalized required transverse wrap influence length for mode C buckling ($\phi_w = 45^\circ$).....	97

Figure 32 - Four angle mechanical model - pinned ends/out-of-plane (mode D)	98
Figure 33 - Free Body Diagram of partial Euler column with restrainer force	99
Figure 34 - Comparison of required restrainer stiffness for Euler column model to SDOF mode A model.....	102
Figure 35 - Degree of conservatism of SDOF mode A model compared to Euler column model.....	103
Figure 36 - Possible compression buckling of restrainer wrap (left) and proposed layer orientation (right).....	106
Figure 37 - Cross section of ULWBRB showing definition of shear flow variables	107
Figure 38 - In-plane moments for typical BRBF	110
Figure 39 - Full-scale Restrainer Configurations.....	113
Figure 40 - Refined brace dimensions unrestrained core (top) restrained core (bottom)	114
Figure 41 - Shear flow and required number of layers of wrap for four angles with square tube restrainer.....	116
Figure 42 - Partial-scale Core Section Properties	123
Figure 43 – Partial-scale Restrainer Configurations.....	127
Figure 44 - Shear flow and required number of layers of wrap for four angles with square tube restrainer.....	128
Figure 45 - Refined partial-scale brace dimensions.....	128
Figure 46 - ASTM E 8 coupon dimensions (all dimensions in inches).....	131
Figure 47 - Photo of tension test setup (left), tension necking of coupon (right).	132
Figure 48 - Monotonic tension test stress-strain plot.....	133
Figure 49 - Cyclic test coupon dimensions (all dimensions in inches).....	134

Figure 50 - Images of coupon C3	135
Figure 51 - Hysteresis for 2% axial strain	136
Figure 52 - Hysteresis for 3% axial strain	137
Figure 53 - Hysteresis for 4% axial strain	137
Figure 54 - Maximum cyclic stress plot	138
Figure 55 - Second half-cycle plot for 3% strain	143
Figure 56 - Coupon FEA model.....	144
Figure 57 - Coupon FEA convergence study results	145
Figure 58 - Calibration of kinematic hardening model.....	146
Figure 59 - Test brace geometry, partial-scale brace (top), full-scale brace (bottom) (all dimensions in inches).....	148
Figure 60 - Linear Buckling Analysis Results	149
Figure 61 - Full-scale test brace finite element model.....	150
Figure 62 - Rippling in between slotted connectors for local buckling study	151
Figure 63 - Location of nodal stress values	153
Figure 64 – Stress & strain convergence plots at selected nodes	154
Figure 65 - Tension & compression comparison of element formulation	155
Figure 66 - Images of buckling for inadequately restrained core	159
Figure 67 - Partial-scale load vs. displacement plot, $\Psi = 0$	161
Figure 68 - Partial-scale load vs. displacement plot, $\Psi = 0.41$	162
Figure 69 - Partial-scale load vs. displacement plot, $\Psi = 0.82$	162
Figure 70 - Full-scale load vs. displacement plot, $\Psi = 0$	163
Figure 71 - Full-scale load vs. displacement plot, $\Psi = 0.15$	164

Figure 72 - Full-scale load vs. displacement plot, $\Psi = 0.30$	164
Figure 73 - Plot of end moment ratio vs. required restrainer stiffness	165
Figure 74 - Comparison of numerical and analytical methods.....	167
Figure 75 - Extended material data plot.....	169
Figure 76 - Time vs. axial deformation plot	171
Figure 77 - Hysteresis for FS77, $\Psi = 0$	175
Figure 78 - Strain hysteresis for FS77, $\Psi = 0$	175
Figure 79 - Hysteresis for FS88, $\Psi = 0$	176
Figure 80 - Strain hysteresis for FS88, $\Psi = 0$	176
Figure 81 - Hysteresis for FS8.58.5, $\Psi = 0$	177
Figure 82 - Strain hysteresis for FS8.58.5, $\Psi = 0$	177
Figure 83 - Hysteresis for FS8.78.7, $\Psi = 0$	178
Figure 84 - Strain hysteresis for FS8.78.7, $\Psi = 0$	178
Figure 85 - Hysteresis for FS99, $\Psi = 0$	179
Figure 86 - Strain hysteresis for FS99, $\Psi = 0$	179
Figure 87 - Hysteresis for FS88, $\Psi = 0.15$ (light line is transverse disp.)	180
Figure 88 - Hysteresis for FS8.78.7, $\Psi = 0.15$ (light line is transverse disp.)	180
Figure 89 - Hysteresis for FS9.29.2, $\Psi = 0.15$ (light line is transverse disp.)	181
Figure 90 - Hysteresis for FS9.59.5, $\Psi = 0.15$ (light line is transverse disp.)	181
Figure 91 - Hysteresis for FS8.78.7, $\Psi = 0.30$ (light line is transverse disp.)	182
Figure 92 - Hysteresis for FS9.29.2, $\Psi = 0.30$ (light line is transverse disp.)	182
Figure 93 - Hysteresis for FS9.79.7, $\Psi = 0.30$ (light line is transverse disp.)	183
Figure 94 - Hysteresis for FS1010, $\Psi = 0.30$ (light line is transverse disp.)	183

Figure 95 - Compression & tension deflected shapes of inadequately restrained brace	184
Figure 96 - Linear interpolation method for cumulative P- Δ	184
Figure 97 - Comparison of cumulative P- Δ vs. restrainer stiffness	185

LIST OF ABBREVIATIONS AND SYMBOLS

A_1	cross sectional area of core at reduced section [in ²]
A_2	cross sectional area of core at intermediate section [in ²]
A_3	cross sectional area of core at full section [in ²]
A_{ti}	cross sectional area of part “i” [in ²]
b	width of core section outstand [in]
b_f	width of core tee section flange [in]
b_o	largest controlling core section outstand width [in]
b_w	width of core tee section web [in]
c	distance from composite neutral axis to the extreme fiber of restrainer [in]
C_d	seismic deflection amplification factor
C_s	seismic response coefficient
C_{vx}	vertical distribution factor for x th story
C_w	torsional warping constant [in ⁶]
D_i	inelastic seismic lateral displacement for i th story [in]
D_{ie}	elastic seismic lateral displacement for i th story [in]
e_1	load eccentricity with respect to the centroid of the composite core [in]
e_z	load eccentricity with respect to single angle’s principal axis [in]
E_c	Young’s modulus of core member [ksi]
E_{cw}	pultruded FRP flexural modulus crosswise bending [ksi]
E_p	Young’s modulus of single pultruded FRP [ksi]
E_r	Young’s modulus of restrainer assembly [ksi]

E_w	tensile modulus of fabric FRP wrap [ksi]
f_b	allowable restrainer bending stress [ksi]
F	brace transverse restraint force for SDOF mechanical model [kips]
F_a	site coefficient (acceleration)
$F_{A, B, C}$	individual core angle half-length restrainer force for modes A-C [kips]
F_{ptLW}	pultruded FRP minimum ultimate tensile stress lengthwise [ksi]
F_{ptCW}	pultruded FRP minimum ultimate tensile stress crosswise [ksi]
F_{pcLW}	pultruded FRP minimum ultimate compressive stress lengthwise [ksi]
F_{pcCW}	pultruded FRP minimum ultimate compressive stress crosswise [ksi]
F_{pbLW}	pultruded FRP minimum ultimate flexural stress lengthwise [ksi]
F_{pbCW}	pultruded FRP minimum ultimate flexural stress crosswise [ksi]
F_{wLW}	fabric FRP minimum ultimate tensile stress lengthwise [ksi]
F_{wCW}	fabric FRP minimum ultimate tensile stress crosswise [ksi]
F_v	site coefficient (velocity)
F_y	core nominal yield stress [ksi]
$F_{\phi w}$	restrainer wrap maximum allowable shear flow force [k/in]
g	gap between back to back angle legs [in]
G_p	pultruded FRP shear modulus [ksi]
$h_{i,x}$	height above base for i^{th} or x^{th} story [ft]
I_c	moment of inertia of reduced core member section [in^4]
I_r	moment of inertia of restrainer [in^4]
I_e	seismic importance factor
$I_{x,y,z}$	moment of inertia about x, y, or z axis [in^4]

J	St. Venant's torsional constant [in ⁴]
k	exponential constant
k_s	elastic spring stiffness of restrainer tubes loaded at midspan [k/in]
K	effective Euler buckling length factor
L_b	brace core end to end length [in]
L_c	brace core reduced section length [in]
L_{c2}	brace core intermediate reduced section length [in]
L_{c3}	brace core full section length [in]
L_o	brace restrainer overlap length [in]
L_r	brace restrainer full length [in]
L_{ru}	brace restrainer span length [in]
L_t	required transverse wrap influence length [in]
L_{tr}	brace transition length [in]
L_u	brace core Euler buckling length [in]
L_w	brace core work point to work point length [in]
$M(x)$	internal moment at the cut
M_{FEM}	Euler column fixed end moment [k-in]
M_{int}	Euler column internal moment [k-in]
M_p'	available plastic moment of intermediate section of core [k-in]
M_r	moment at the midspan of the restrainer [k-in]
M_{res}	equivalent restrainer resisting moment for mechanical model [k-in]
P	brace axial force [kips]
P_{cr}	Euler column critical load [kips]

P_u	strength level seismic brace force [kips]
P_y	core nominal yield strength [kips]
$q(x)$	shear flow at neutral axis of restrainer [k/in]
Q	first moment of area about the neutral axis [in^3]
$r_{x,y,z}$	radius of gyration about x, y, or z axis [in]
R	seismic response modification coefficient
S_S	0.2 second spectral response acceleration [%g]
S_1	1.0 second spectral response acceleration [%g]
S_{DS}	0.2 second design spectral acceleration [%g]
S_{D1}	1.0 second design spectral acceleration [%g]
S_r	elastic section modulus of restrainer [in^3]
$S_{x,y,z}$	elastic section modulus about x,y, or z axis [in^3]
t	thickness of core section outstand [in]
t_f	thickness of core tee section flange [in]
t_L	restrainer FRP wrap laminate thickness [in]
t_o	smallest controlling core section outstand thickness [in]
t_w	thickness of core tee section web [in]
T_a	approximate fundamental period [sec]
T_L	long period transition [sec]
$V(x)$	internal shear at the cut
V_b	seismic building base shear [kips]
$w(x)$	unknown restrainer distributed force per unit length
$w_{i,x}$	effective seismic weight for i^{th} or x^{th} story [kips]

x	length along Euler column [in]
$y(x)$	transverse displacement of buckled Euler column [in]
y_{ti}	distance from composite neutral axis to centroid of part “i” [in]
γ	ratio of L_c/L_b
δ	maximum displacement amplitude of Euler column [in]
Δ	additional transverse displacement at mid-length due to eccentricity [in]
Δ_i	initial transverse displacement at mid-length (out-of-straightness) [in]
Δ_t	total transverse displacement at mid-length [in]
ε_c	inelastic strain at core reduced section [in/in]
ε_{ce}	elastic strain at core reduced section [in/in]
η	ratio of A_1/A_2
θ	angle of brace with respect to horizontal [degrees]
ρ	seismic redundancy factor
σ_h	wrap hoop stress [ksi]
ϕ_w	angle between wrap primary fiber direction and longitudinal axis [degrees]
ϕT_{L1}	tension gross section yielding limit strength of bare core [kips]
ϕT_{L2}	tension net section fracture limit strength of bare core [kips]
ϕP_{L3}	compression global elastic buckling limit strength of bare core [kips]
ϕP_{L4}	compression torsional buckling limit strength of bare core [kips]
ϕP_{L5}	compression flexural-torsional buckling limit strength of bare core [kips]
ϕP_{L6}	compression component local buckling limit strength of bare core [kips]
Ψ	end moment ratio (M_{end}/M_p')
Ω_o	seismic system overstrength factor

1.0 INTRODUCTION

This thesis project attempts to develop an innovative ultra-lightweight buckling-restrained brace (ULWBRB) by combining three technologies that are individually at the forefront of incorporation into civil engineering structures. These are buckling-restrained braces (BRB), aluminum seismic dissipaters, and fiber reinforced polymers (FRP). The proposed ULWBRB brings the benefits of these materials together to create an efficient seismic brace that has the capability of dissipating seismic energy through cyclic plastic straining of a highly ductile aluminum core thus protecting portions of the structure designed to remain elastic. High potential for energy dissipation is realized by precluding buckling in the compression cycles creating a brace that performs symmetrically in both tension and compression. Buckling preclusion is accomplished by surrounding the core with an unbonded FRP jacket that allows the core to slide independently within. During cycling the FRP jacket remains elastic and is devoid of axial load.

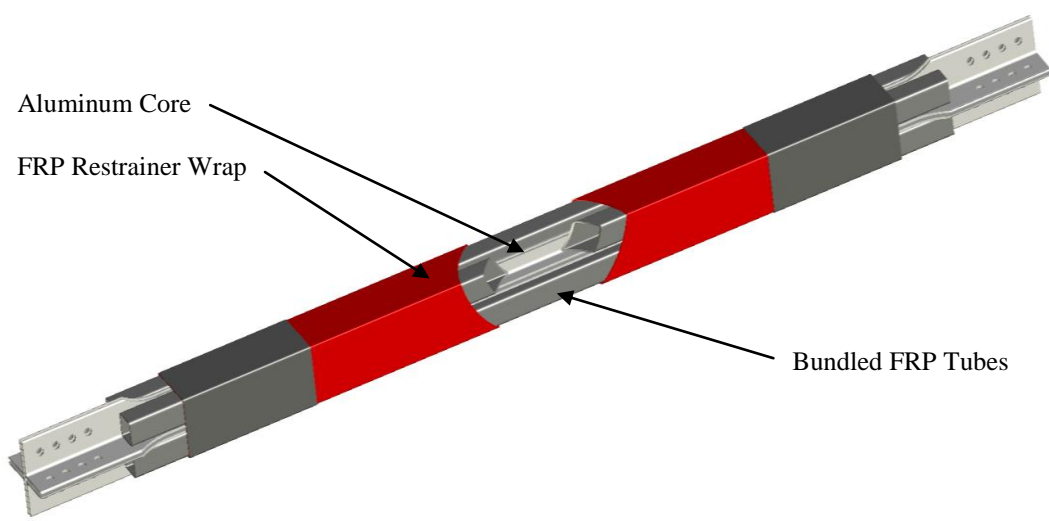


Figure 1 - The ultra-lightweight buckling-restrained brace

Lightweight BRBs constructed of all-steel components have been proposed that weigh approximately 60% of the traditional mortar-filled steel tube varieties. The ULWBRB takes the idea of lightweight to the next level by decreasing the weight of the traditional BRB system considerably. By using aluminum in place of steel and FRP in place of steel tubes and mortar, the brace is able to achieve weights as low as 25% of the mortar-filled tube. This has great benefits for constructability, and therefore feasibility, of installation of these braces in existing structures.

The ULWBRB is conceived for use in small to medium size buildings of any occupancy where seismic upgrading is desired. These structures often pose difficulties for material handling and installation of traditional BRBs due to their positioning in confined spaces with limited access for heavy lifting equipment such as cranes and forklifts. Ultra-lightweight versions have the potential to allow easy manual transport, lifting, and connection of braces to the existing structure in areas concealed by interior partitions, exterior curtain walls, or ceilings with welding and bolting work limited to preparation of the steel gusset plates. In extenuating circumstances, the FRP tubes and wrap can be placed around the core in-situ allowing the brace components to be transported to the site and installed separately.

The concept may also be applied to the stabilization of existing steel angles carrying compressive load such as increasing the buckling capacity of diagonal bracing members on existing bridge, tower, and building structures. For instance, prevention of Euler buckling in the compression brace of a chevron braced frame can increase the lateral stiffness of the frame by up to a factor of two. Manipulation of existing brace stiffness may be beneficial in correction of torsional or soft/weak story irregularities.

Execution of the development involves a thorough literature review on the three technologies proposed to be used. A suitable model building is then created that provides a context for assigning typical seismic forces and frame geometry. This model building is representative of potential seismic upgrade applications. Brace design begins with developing analytical methods from what is available in the literature on single degree-of-freedom and Euler buckling models for determining required restrainer stiffness. Then required FRP wrap strength is determined using a newly developed analytical method based on shear flow. Next, a partial-scale brace is introduced to allow future laboratory testing. Aluminum alloy coupon testing serves to establish a material constitutive model to be used in numeral modeling. This is first executed monotonically to compare with analytic results at both full and partial-scale sizes. Lastly, cyclic numerical simulation attempts to quantify energy dissipation potential. Figure 2 shows a flow chart for the process.

It is hypothesized that the analytical model will provide a quick and easy method of determining the required restrainer stiffness and wrap strength for a given axial design force and core geometry. Numerical analysis of the proposed brace will provide more accurate guidance to the amount of compressive force the brace can achieve prior to global or local buckling. This force translated into axial strain exerted over many cycles of variable amplitude will lead to a cumulative plastic ductility demand that is sufficient for large amounts of seismic energy dissipation. This is the true measure of the brace's suitability for use in seismic upgrades. The hysteresis from the numerical model should show that predictable and reliable behavior can be achieved with the ULWBRB at considerable story drift ratios.

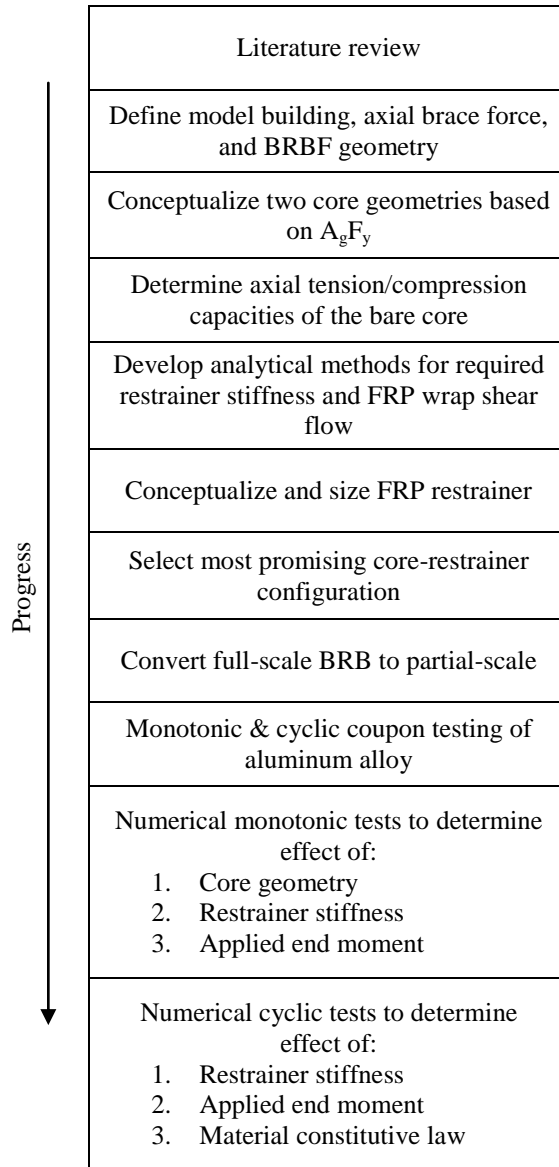


Figure 2 - ULWBRB development process chart

2.0 LITERATURE REVIEW

2.1 INTRODUCTION

Targeted exploration of the current state-of-the-art in several fields including seismic design, materials science, structural composites, and mathematical modeling are necessary for development of the ULWBRB. Research into the aforementioned fields delves into reports on cutting-edge technologies such as lightweight buckling-restrained braces, superplastic aluminum alloys, fiber reinforced polymer strengthening of steel structures, and treatment of multi-component brace analytical and numerical models. The state of knowledge in these research frontiers continues to develop at a fast pace. Evidence of this can be seen in the very recent publication of many of the citations listed within. The background presented within this review serves as a base for expansion of the ideas presented by other researchers that leads to a functional assemblage of these technologies.

The more distant history of each topic is judged equally as important as the most recent research as many of the original concepts presented at the outset of a new development embedded in more complex treatments of it. Thus, an effort to provide a comprehensive literature review is made. However, given the constraints present in this forum for expansion on previous research ideas and results, the reader is urged to perform their own critical review of these citations as they see fit.

For the purpose of arranging these fields for the ensuing discussion, four research subtopics have been identified. They include buckling restrained braces (BRBs), use of

aluminum in civil engineering structures, use of fiber reinforced polymers (FRP) in civil engineering structures, and mathematical modeling of BRBs. The research pertaining to these subtopics are presented separately. Although, there are many points of intersection between them as they are usually not employed as discrete technologies. This will hopefully become clear.

2.2 BUCKLING-RESTRAINED BRACES

Introduction

Research into using metallic yielding devices as part of the primary structural system of buildings to dissipate seismic energy was originally reported in 1975 (Skinner, Kelly, & Heine, 1975). Introduction of steel members with a known yield point and reliable plastic plateau to work as axial, shear, bending, or torsion-type hysteretic dampers was the original concept. Separation of the extreme lateral load resisting system from the main gravity load resisting system reduced the demand significantly on the majority of the primary structural members. The idea of ductile members performing beyond their elastic limit repeatedly in cyclic loading eventually led to many of the seismic energy dissipating systems in practical use today. For instance, the axial yielding mechanism specifically can be found in commonly used systems like the concentrically braced frame (CBF) and the high-performance buckling-restrained braced frame (BRBF) which is simply a recent refinement of the former.

The most important characteristic of BRBFs is they have more ductility than traditional CBF systems because brace global and local buckling in compression is precluded at design level forces. Typical CBF systems neglect the contribution of braces

acting in compression due to buckling instability in calculation of lateral load strength and stiffness. In these frames, buckling of the compression member is typically allowed through weak axis bending of enlarged gusset plates. Because of this unchecked buckling of the compression brace in CBFs, energy dissipation is limited to axial yielding in tension only. The BRBF's superiority is made possible by de-coupling axial strength from buckling resistance by providing transverse restraint to the brace thus allowing the brace to yield equally in tension and compression. One of the more common methods for precluding brace buckling is to install a robust steel restraining tube around the more slender axially loaded core element. This tube is in some instances filled with mortar in order to serve as an incompressible medium between the two. Axial load transfer between the core element and the restrainer can be carefully omitted from the system by using a debonding layer between the steel and mortar.

Using an analogy, the BRB component can be thought of as the structural "fuse" that is part of a vertical braced frame system. Ideally, this "fuse" element serves as the sacrificial member during severe seismic loading protecting the remainder of the structure. For a well-designed BRB, the cyclic force-displacement hysteresis exhibits clear elastic performance followed by yielding on tension cycles as well as compression cycles. This symmetric yielding mechanism allows the dissipation of copious amounts of seismic energy by conversion of kinematic energy into strain energy as the core material deforms repeatedly into the plastic range. Predictable energy dissipation potential and relatively compact size make the use of BRBs ideal in buildings constructed in zones of moderate to high seismicity. Also worth noting is the BRB's stiff elastic response for load ranges below those expected in a significant seismic event allowing the system to

perform well under the influence of wind or minor seismic lateral loading. Reasonable elastic lateral drift ratios can easily be achieved.

Beginnings and Proliferation of the BRB

The original concept for a buckling-restrained brace came in the form of “Shear Wall with Braces” almost 40 years ago (Yoshino & Karino, 1971). This concept consisted of a yielding flat steel plate sandwiched between concrete wall panels providing buckling restraint. Unbonding materials between the walls and the steel brace were provided to allow it to move independently. Building on this idea, the first workable concept of conventional steel braces encased in mortar-filled steel tubes was developed by Kimura et al. (1976). The first experiments on this concept achieved some stable hysteretic cycles but subsequently failed due to transverse deformation of the mortar thus allowing local buckling of the core element outstands within the restraining tube. No unbonding material between the yielding core and the surrounding mortar was provided so approximately 10-15% of the longitudinal strains of the core were transferred to the restraining tube. A slight divergence for the restraining member concept used a cast-in-place reinforced concrete encasement of the core without the steel tube jacket (Mochizuki, Murata, Andou, & Takahashi, 1980). The surrounding concrete was prevented from adhering to the steel core with a shock absorbing material. The concrete section cracked under repetitive loading thus allowing core member global buckling. This report was the first to use the vocabulary “unbonded brace” which was later developed as a trade name for the original proprietary BRB by Nippon Steel Corporation, Japan through subsequent research by Watanabe et al. (1988), Wada et al. (1989), and Watanabe and Nakamura (1992). As its name describes, one of the break-through

developments in the typical mortar-filled steel tube concept was the unbonding of the core element from the surrounding mortar.

By the time the development of the “unbonded brace” was reaching the point of practical application, its potential for predictable and stable hysteretic behavior was witnessed in numerous laboratory simulations. It subsequently was employed in several different types of structures in Japan as early as the late 1980s and proliferated to hundreds of applications by the 1990s. The mortar-filled steel tube concept eventually made it to the United States in 1999 when the first U.S. tests were conducted at the University of California, Berkeley as qualification for installation in two new buildings that were constructed at the Berkeley campus and at University of California, Davis (Black, Makris, & Aiken, 2004). Adoption of BRB technology has made some inroads into seismically active areas of Europe as well, but it remains a practical technology primarily in Asia, Canada, and the United States. However, interest in the system in other seismically active areas is high. For example, variations of the mortar-filled tube concept are currently being explored in Italy as a way to provide damping to existing reinforced concrete structures originally designed without rigorous seismic building codes (Castellano, Balducci, & Antonucci, 2008).

Since BRBFs had essentially the same configuration on the system level as the widely adopted CBF, practical employment in buildings was relatively swift. For many years CBF systems have been incorporated into buildings ranging from one-story, large-plan warehouses to high-rise office towers and all other types of structures in between. The location of CBFs, and likewise BRBFs, typically occur on the main grid lines of the structural frame. It is common practice to conceal brace elements in an interior or

exterior wall due to their interference with occupied space in between the columns. Many times the braced frames are located at interior stair and elevator openings at a building's core. The braces may also be exposed at the perimeter of the structure as in cases where the structural frame is not in-plane with the building envelope. This is becoming more common as expression of the building's structure is increasingly being seen by architects as an appropriate aesthetic treatment of the building facade.

Another method of employing the BRB in building structures is as a non-linear damper installed in tandem with another lateral force resisting system. The addition of a damper serves to reduce the seismic force demand on the main lateral force resisting system during periods of high excitation. Japan has seen the most widespread use of damping systems working in tandem with moment frames (Takeuchi, Ida, Yamada, & Suzuki, 2008). This application has its own competition including fluid viscous (dashpot), visco-elastic, and friction dampers. BRB dampers fall under yet another metallic-yielding category. While popular in other countries, this method has seen limited use in the United States.

Specific Types of BRBs

One of the most compelling research prospects for BRB technology is variations on the well-established mortar-filled tube concept. These are presented by various researchers with differing motivations. A comprehensive, although brief, discussion of these developmental reports is warranted in order to provide a context for the ULWBRB. Furthermore, literature reports of concepts stemming from the original successful mortar-filled tube concept provide an introduction to the many pathways available for providing high-quality BRB performance. Reports on these concepts introduce vocabulary such as

mortar-filled, all-steel, low-tech, detachable, lightweight, and partially-restrained. Clearly, there are many.

Mortar-filled Steel Tube BRB

The original mortar-filled steel tube concept is undoubtedly one of the most successful in practical applications today. This concept itself has many variations developed typically as proprietary products by manufacturers in countries as diverse as Japan, Taiwan, China, the United States, and Canada. The type of steel core and the restraining jacket are the main variants. Rectangular bar, WF section, cruciform, round pipe, and WT sections have been either developed or proposed. Figure 3 shows some of these proposed core sections ((a) through (c) are mortar-filled tubes, (d) is a bolted precast concrete restraint, and (e) through (l) are all-steel configurations).

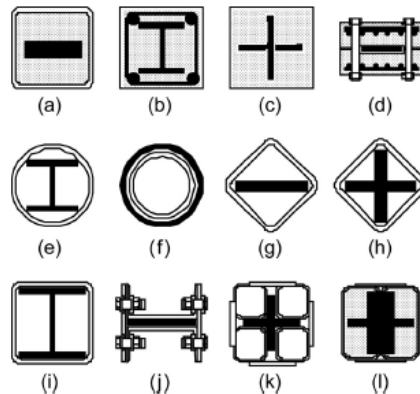


Figure 3 - Possible cross sectional configurations of BRB (Xie, 2005)

Research by Black et al. (2004) was certainly one of the most comprehensive of its time on mortar-filled steel tube BRBs. This article reports on component level experiments conducted in 1999 and 2000 on full-scale specimens subjected to loading protocols agreed on by the building designers and state authorities to be representative of seismic demand. Specifically, one brace specimen was subjected to large-deformation,

low-cycle fatigue tests with brace strains corresponding to 1% story drift. This test was able to achieve 31 cycles without failure. The other specimen also proved stable after being subjected to two simulated design basis and upper bound earthquake displacement history tests that reached maximum strain amplitudes of 1.11% and 1.38%. Both of these braces had a cruciform type core surrounded by a high compressive strength mortar matrix which controlled local buckling of the cruciform outstands. The authors discuss cumulative plastic ductility (CPD) demand as a practical way to measure the amount of cyclic inelastic deformation experienced by the BRB beyond the yield deformation. The formulation for this measure is discussed later in the mathematical modeling section. For the purpose of developing an ULWBRB, it should be mentioned that the weight of the braces was as high as 150 pounds per linear foot for a 10 inch by 10 inch restraining tube.

Component level experimental programs comprise most of the reports on mortar-filled steel tube BRBs as can be expected due to the lesser cost of individual brace tests. Nevertheless, the literature contains limited reports on near full-scale system level tests. These are reported for one-bay, four-story chevron type BRBFs subjected to earthquake simulations where the primary purpose was to determine the adequacy of beam-column-brace gusset plate connections (Fahnestock, Ricles, & Sause, 2007). Depending on the brace end connections, secondary in-plane bending moments were reported to have developed in the braces at large story deformations which have the potential to effect axial behavior. The paper demonstrates the ability of BRBF systems to sustain high CPD demand if beam to column connections, gusset plates, and brace to gusset connections are properly detailed.

Recognizing that previous researchers have reported mixed results on the effect of

in-plane bending moments on BRBs at high story deformations, further experiments with varied end connections were reported (Tremblay, Bolduc, Neville, & DeVall, 2006). The magnitude of this moment depends on the interaction of the brace core and confining material (restrainer) and cannot be easily determined. Experimental results on six full-scale mortar-filled tube specimens with hourglass shaped flat steel plate cores showed that in-plane flexural stresses in the BRB can be predicted by simple frame analyses assuming that the BRB is elastic and rigidly connected at the ends to the gusset plate. This flexural demand did not appear to affect the axial performance of the braces. This report reinforces the notion that treatment of the brace ends as either pinned or fixed (or anywhere in between) needs to be assessed during mathematical modeling.

Full-scale, two-story reinforced concrete frames were constructed on a shake table to test buckling-restrained axial dampers (Castellano, Balducci, & Antonucci, 2008). The strength and stiffness of these dampers were scaled by using an aluminum core to provide a low enough yielding force for the constraints of the tested subassembly frame. Unfortunately, the authors provided little discussion of the BRB details relating to this steel restrained system with an aluminum core.

Another variation of the mortar-filled steel tube was described as a “low-tech dissipative buckling-restrained brace” (Palazzo, Lopez-Almansa, Cahis, & Crisafulli, 2009). This concept is quite elegant and is proposed to be employed with simplicity, low cost, easy production, and basic materials primarily in developing countries with large numbers of previously constructed buildings requiring seismic retrofit. This system consists of a round steel bar core element surrounded by a mortar-filled round steel pipe casing. This brace concept achieved stable hysteretic behavior during testing with one of

the most critical failure modes being local buckling of the unrestrained core ends due to insufficient rigidity of welded on trapezoidal stiffener plates. Also, the rotation capacity of the pinned core member end connections was reported to be critical to the dissipation capacity of the unbuckled core. This statement correlates with analysis of in-plane bending moments reported by Fahnestock et al. but disagrees with Tremblay et al.

All-Steel BRB

There are many reports pertaining to the elimination of the complexity and expense during fabrication and erection of mortar-filled steel tube BRBs. The substantial weight of these BRBs has been mentioned, but also the requirement of pouring and curing the concrete or mortar contributes greatly to the fabrication costs. Lightweight all-steel systems attempt to reduce these drawbacks through omission of the mortar altogether. However, a lightweight all-steel system may still weigh as much as 75 pounds per linear foot.

Tests of both mortar-filled and all-steel variations of BRBs in direct comparison were first reported by Tremblay et al. (2006). This report was already introduced in the previous section, but important in the current discussion is the four specimens that were all-steel BRBs comprised of an hourglass-shaped flat plate steel core element sandwiched between hollow structural section (HSS) restrainers. The restrainers were in contact with the weak axis side of the core and bolted together. Guide plates and shim plates located between the HSS members served to further confine the core element from buckling. All four of these BRB test specimens were compared to results of a baseline unrestrained brace subjected to similar loading protocols. Problems occurred with the all-steel specimens, specifically with local buckling (rippling) at the core plate hourglass

transition zone. This was attributed to too large of an initial gap between the core and the guide plate that was adjusted using filler shims as well as too large of bolt spacing along the longitudinal axis of the restrainer. Local buckling led to high longitudinal friction forces at the peaks of the core's buckled shape and the tests were terminated prior to failure. Core local buckling was concentrated at the ends of the reduced core during compression cycles. Conversely, plasticity in tension was concentrated at the mid-length of the reduced core section. Since these plasticity zones did not coincide, the buckled shape remained after stretching. Providing unbonding material between the core and restrainer was recommended as well as a highly rigid restraining tube and close bolt spacing in order to develop uniform strain demand in the core member. As reported in other literature as well, the authors recommended utilizing a sufficiently long reduced section (hourglass center) to keep inelastic strain demand low enough such that low-cycle fatigue fracture does not occur during a severe earthquake.

Another concept for a “detachable” all-steel BRB was proposed that was constructed of a non-prismatic stiffened flat bar core and a bolted two-piece omega-shaped restrainer with interior steel stiffeners (D'Aniello, Della Corte, & Mazzolani, 2008) (D'Aniello, Della Corte, & Mazzolani, 2009). The development of this BRB was motivated by the feature that it could be inspected after each seismic event, and, if necessary, the core element could be replaced with a new unyielded section. One of the drawbacks to a metallic yielding energy dissipater is the damage that occurs to the core through repeated excursions into the plastic range. The cyclic yielding subsequently causes work hardening in the steel which may cause potential for low-cycle fatigue fracture upon resisting a second seismic event. Furthermore, the plastic working of the

brace core may not allow the building to self-right to its original position after the earthquake. Removal of this permanent inelastic deformation by replacement of the yielded core is another benefit of this detachable system although it was not specifically introduced by the authors. This brace had a thin profile in the frame's out-of-plane direction to conceal it within exterior wall masonry infill. Inner clearance between the yielding core and the restraining sleeve was kept to 0.039 inches per side to allow for Poisson expansion that could lead to frictional forces thus axially coupling the core and restrainer. Failure mechanisms in the cyclic testing program were unrestrained core end buckling due to stiffener to core weld failure, improper core-restrainer clearance leading to frictional forces, and higher mode core buckling (rippling) leading to plastic deformation of the restrainer. Global stability typically remained intact up to failure at core strains representative of 3% story drift as measured on system level tests of a full-scale reinforced concrete building.

A variation on the concept of an all-steel, detachable BRB applied to real full-scale reinforced concrete buildings was explored by the same researchers. All-steel BRBs made of rectangular flat steel bars restrained by rectangular hollow structural sections (HSS) on each side fully welded together (Type I), or bolted together (Type II), were proposed as an advanced retrofitting technique (Mazzolani, Della Corte, & Faggiano, 2004). The BRBs were comparatively tested along with other advanced methods including base isolation, carbon fiber reinforced polymer (CFRP) column wraps, steel eccentric braces (EBF), shape memory alloy braces, and dissipative metallic shear panels. The results of this testing program were subsequently reported (Mazzolani, Della Corte, & D'Aniello, 2009). Similar to past research, the tests of welded all-steel BRBs

reported failure by local buckling of the unrestrained core element near the brace ends. This design did not employ welded plate stiffeners as seen in Tremblay et al (2006). The restraining tube walls also experienced localized plastic flexural failure due to forces imposed by the buckled core member. The failure of the Type I specimen was attributed to the non-tapered (not hourglass shaped) core member that exhibited buckling at the transition from side bar restraint. If properly detailed, the core could have forced inelastic strain and potential buckling to the mid-length of the brace away from the vulnerable free end of the restraining tube. Overall ductility of the welded Type I brace was limited to displacements of 1.9% story drift.

The local buckling problem at the restrainer ends was remedied in the Type II bolted configuration by detailing the core with a three tier taper and additional parallel welded side support bars. The Type II BRB test specimen failed in higher mode buckling (rippling) of the core with stable hysteretic response up to 5.6% story drift for all but one of the braces where local buckling of the core outside of the restrainer occurred. Local buckling of the core member outside the restrainer was attributed to gusset plate deformation accumulated in prior tests leading to out-of-plane brace geometric eccentricity as well as the flexible end restraints of the brace. These together produced a higher effective length (KL) and superimposed torsional effects. It was evident that the more common rippling failure mode could be attributed to the inadequate stiffness of the bolted restrainer, too large a bolt spacing, and inadequate fabrication tolerances leading to localized eccentricities.

Other lightweight, all-steel BRBs have been proposed for use as high-performance dampers. For example, a component level test for BRBs to be installed in

bridge structures is reported (Usami, Ge, & Kasai, 2008). This system was constructed of a prismatic steel plate brace member and a steel restraining member constructed of a pair of stiffened T-shaped steel plates connected by bolts at equal spacing. The interesting advancement in this proposal was an unbonded 1 mm thick butyl rubber tape wrapped around the core plate to prevent frictional forces between the core and restrainer. After achieving mostly successful results, the authors called for further research into developing this idea further by introducing aluminum alloy and shape memory alloys.

Methods of Unbonding the Core and Restrainer

An important characteristic for all BRBs is the prevention of friction between the yielding core element and the restrainer thus allowing axial independence. Correctly chosen unbonding material has the capability of preventing the buildup of peak stress from frictional binding that can lead to unevenly distributed yielding. This uneven yielding can lead to low-cycle fatigue and premature local buckling. Transfer of axial force into the restrainer can also lead to decreased flexural stiffness available for global buckling prevention as the restrainer's axial plus bending stress exceeds the elastic limit. In addition, transverse volume change of the core element during elastic (Poisson expansion) and inelastic axial strain can lead to binding of the core element if inadequate gaps are provided on all sides of the core. The methods used by previous researchers to provide these gaps are now presented.

The first debonding experiments were pull-out tests of eleven steel bar specimens embedded in concrete (Wakabayashi, Nakamura, Katagihara, Yogoyama, & Morisono, 1973). A parametric study where epoxy resin, silicon resin, and vinyl tapes were applied to the bar specimens showed the effectiveness of these methods. Other researchers have

attempted to provide a uniform gap around the core element with the application of a brushed-on silicon coating or wrapping the core section with vinyl-mastic tape, styrol foam, two layers of 0.15-0.20 mm thick polyethylene film sheet, 1.5 mm thick butyl rubber sheets, or 2 mm thick silicone rubber sheets, amongst other techniques (Xie, 2005). In the low-tech BRB reported by Palazzo et al. (2009), the core was coated with Teflon, lubricated with grease, and finally wrapped with rubber sheets. The experimental program reported by Tremblay et al. (2006) used 3 mm thick Dow Ethafoam 222 on the edges of the core plate for Poisson expansion and wrapped this assembly in four layers of 0.2 mm polyethylene film to break the bond to the mortar. In the all-steel (Type II) BRBs by the same researchers, thin steel plate shims were used to regulate the core to restrainer gap. It is consistently reported that the amount of gap provided, if excessive, may lead to increased chance of rippling as potential geometric eccentricity is increased. This discussion will be presented in further detail in the mathematical modeling section.

Building Code Provisions for BRBs in the United States

As practical use of the BRB has grown in the United States since the early 2000s, building code provisions have followed. The implementation of a BRBF system in a building requires understanding of how its use is regulated by localities who have adopted the *International Building Code* (International Code Council, 2009). This model building code adopts both the *AISC Seismic Provisions* (American Institute of Steel Construction, 2005b), hereafter referred to as the *Provisions*, and the *ASCE Minimum Design Loads for Buildings and Other Structures* (American Society of Civil Engineers, 2005) which govern the design of these structural steel seismic systems. At this time, the design provisions for the BRBF, and therefore BRB, are minimal with mostly

prescriptive requirements relating to the appropriate over-strength of BRB connections to the frame and the frame itself. Over-strength serves to prevent failure of components not expected to exceed their elastic limit such as beams, columns, gusset plates, and bolted or welded connections. After claiming unavailability of sufficient test data from structural engineers on BRBF systems, the *Provisions* are primarily based on qualification testing until the body of such data increases. At that time the need for additional testing is expected to diminish.

Ductility Comparison

Along the ductility spectrum of different seismic lateral force resisting systems, the BRB falls on the end along with the most ductile. The building code measures the ductility of different types of lateral force resisting systems with the Response Modification Coefficient (R) with more ductile systems being assigned a higher number.

Table 1 Comparison of Typical Lateral Force Resisting Systems		
System	Response Modification Coefficient (R)	Deflection Amplification Factor (C_d)
Ordinary Moment Frames (OMF)	3.5	3
Intermediate Moment Frames (IMF)	4.5	4
Special Concentrically Braced Frames (SCBF)	6	5
Eccentrically Braced Frames (EBF)	7	4
Special Plate Shear Walls (SPSW)	7	6
Buckling-Restrained Braced Frames (BRBF)	7	5 1/2
Special Moment Frames (SMF)	8	5 1/2

These numbers represent a direct ratio of elastic to inelastic design spectra and range from 1.0 to 8.0. Table 1 shows some typical steel framed systems and how they relate to that of the BRBF (American Society of Civil Engineers, 2005). It can be seen that BRBF

is only surpassed by SMF in the amount of load reduction achieved by the system undergoing inelasticity.

Adjusted Brace Strength

The value of over-strength required for designing frame members and brace connections is given as “adjusted brace strength” in the *Provisions* which is calculated as follows.

First, the brace design axial strength ($P_{y_{sc}}$) is calculated by multiplying the specified minimum yield stress of the core element ($F_{y_{sc}}$) by the net area of the steel core (A_{sc}) as shown in Equation 1 for Load and Resistance Factor Design (LRFD). Then accounting for compression buckling restraint (β), the material expected yield stress (R_y), and strain hardening (ω), Equation 2 is given for compression. The buckling restraint term is omitted for tension as shown in Equation 3. Both of these equations are multiplied by 1.1 when working in LRFD. As given in the commentary of the *Provisions*, this additional multiplier accounts for the possibility of braces being subjected to deformations exceeding 200% of the design story drift ratio. Given the rudimentary nature of the design requirements for the BRB itself, much of the emphasis has been given to qualification testing of the BRBF as the basis for acceptance. A more comprehensive discussion of the code requirements follows.

$$P_{y_{sc}} = F_{y_{sc}}A_{sc} \quad (1)$$

$$P_u = 1.1\beta\omega R_y P_{y_{sc}} \quad (2)$$

$$P_u = 1.1\omega R_y P_{y_{sc}} \quad (3)$$

Qualification Testing

Brace qualification testing falls under the requirements of the *Provision's* Appendix T “Qualifying Cyclic Tests of Buckling-Restrained Braces.” The entirety of

these requirements are too numerous to list here, but those of loading sequence are particularly important to the discussion at hand. The *Provisions* require that loading applied to the test subassembly produce specific axial deformations in the BRB's steel core thus making the test displacement controlled. The loading sequence consists of two cycles at the deformation corresponding to $\Delta_b = \Delta_{by}$, two cycles at the deformation corresponding to $\Delta_b = 0.5 \Delta_{bm}$, two cycles at the deformation corresponding to $\Delta_b = 1\Delta_{bm}$, two cycles at the deformation corresponding to $\Delta_b = 1.5 \Delta_{bm}$, two cycles at the deformation corresponding to $\Delta_b = 2.0 \Delta_{bm}$, with additional complete cycles of loading at the deformation corresponding to $\Delta_b = 1.5 \Delta_{bm}$ as required for the brace test specimen to achieve a cumulative inelastic axial deformation of at least 200 times the yield deformation. Where Δ_b is the total brace axial deformation, Δ_{bm} is the brace axial deformation corresponding to the design story drift, and Δ_{by} is the brace axial deformation at first significant yield of the test specimen. This loading sequence is only intended to be a minimum for qualification, as is the basis for most building codes. The engineer of record may further specify loading protocols based on specific earthquake time histories. Numerous examples of special loading protocols are reported in the literature.

Other Code Requirements

Besides the items discussed above, the *Provisions* offer the following additional requirements. As described previously, the buckling restraint system shall limit local and overall buckling of the steel core for deformations corresponding to two times the design story drift. This is required to be demonstrated through subassembly testing that is either already established and documented, as is the case with many proprietary systems, or through tests conducted specifically for the project. The BRB steel core has been

designated as a “protected zone” that must satisfy requirements pertaining to limitations of discontinuities created by fabrication or erection operations including drilling, welding, notching, or similar in order to maintain reliable ductility without crack propagation leading to fracture. Likewise, splices in the steel core are not permitted.

2.3 USE OF ALUMINUM IN BUILDING STRUCTURES

Introduction

Aluminum as an industrial material has been available for almost a century with roots leading back to the beginnings of the industrial revolution at the end of the 1800s. The chemical element itself was first isolated in 1807 by Sir Humphrey Davis although only in small quantities not useful in material constructs. It turns out that massive production of aluminum requires large amounts of electrical energy in the form of an electrolytic process that was first patented in 1866 by Paul Louis Touissant Heroult of France (Mazzolani, 1985). Following this ingenious development, aluminum’s use in the industrial United States began in earnest during World War I. Different alloys found their way into the aeronautical, ground transportation, subway cars and automobiles, and the shipping and container industries. Its high strength, light weight, and corrosion resistant properties were a boon to many diverse industrial sectors. The use of aluminum alloy in building or bridge structures has seen increasing attention in recent years but still remains largely unexplored.

Building structures largely excluded the implementation of such a lightweight building material until perhaps the last 40 years where the material has found its way into many secondary structural components such as curtain walls, exterior canopies and

awnings, floor bar grating, planks and checker-plate, as well as numerous interior miscellaneous metals such as trim, kick plates and stairs. Its adoption in these instances is again due to its light weight, corrosion resistance, high strength, and undoubtedly its aesthetics. In the primary structural elements of large structures the benefits of aluminum have unfortunately been seen as less important. Typically, the main structural elements are erected with the use of large cranes and erectors familiar with handling heavy materials. Conversely, interior applications are usually installed after the building envelope is enclosed making easy manual handling a priority. There are obviously instances where lightweight building materials are advantageous for the primary system as well.

Lightweight building materials are desired in applications where the majority of the gravity load on the structure is due to the members themselves as in tubular freestanding space structures (Zhu & Young, 2006). Lightweight aluminum two-story building frames were proposed for residential buildings in highly seismic regions of Greece (Spyrakos & Ermopoulos, 2005). These systems allowed installation similar to wood framing where a team of workers was able to hand-lift members into place one at a time without the need for heavy equipment. This ease of erection certainly has many benefits for highly developed and confined urban settings. Another possible use is where confined spaces within existing buildings severely constrain forklift or crane access for material handling. Naturally, this brings the discussion to that of existing building retrofit. It is very common to retrofit existing structures with braces or other seismic load resisting systems many years after their initial construction in order to gain building code compliance for life-safety. Again, this can be seen in countless examples, but one worth

mentioning is the retrofit of the Wallace F. Bennett Federal Building in Salt Lake City, Utah where 344 buckling-restrained braces were installed in an eight-story reinforced concrete structure originally built in the early 1960s (Brown, Aiken, & Jafarzadeh, 2001). This installation required heavy lifting equipment for the massive mortar-filled tube BRBs shown in Figure 4. This large BRB system shows one end of the spectrum, but what about the other end where small compact BRBs are installed in smaller two to three-story structures where complete reconstruction of the exterior envelope is not desired? This question leads to the exploration of ultra-lightweight ideas for BRBs. To a limited extent, the development of lightweight aluminum alloys for use in seismic energy dissipation systems can be found in the literature.



Figure 4 - BRBs at manufacturing facility in China and gusset plates on site (Brown et al., 2001)

However, the state-of-the-art remains below the level required for practical implementation of such technologies. A comprehensive discussion of these reports follows as a necessary departure point for the understanding of aluminum's potential in future seismic force dissipating systems.

Manufacture

Aluminum as a building material has many differences from more commonly used steel. Like steel, aluminum is available in many shapes and sizes including I-sections, angles, T-sections, channels, and plates. A method for manufacturing unique to aluminum is extrusion. The extrusion process is accomplished by forcing heated material through a die which can result in many more shapes than the steel hot rolling process including bulb angles and tees, cruciform sections, seamless tubing, and virtually anything else that does not require hydraulic press force above the plant's equipment capacity. (e.g. window mullion sections with integrated stiffeners, grooves, and highly complex profiles are very common.) One of the largest benefits to creating shapes with extrusion is the designer has the ability to put the material exactly where it is most effective without expensive welding as is common in built-up steel sections. These extruded shapes are typically straightened by traction after the extrusion process and before tempering. It is possible to create extrusions up to 30 inches in section but cost constraints dictate that a reasonable section size will fit within a 15 inch diameter circle (Aluminum Association, 2000).

Aluminum alloys are available in many different chemical formulations all possessing specific properties that can be optimized for a given use. The ASTM designations for these formulations are called series. The most commonly used aluminum alloys in civil engineering structures are 5000 series for sheet or plates and 6000 series for extrusions. Chemical compositions are Aluminum-Magnesium (Al-Mg) for 5000 series and Aluminum-Silicon-Magnesium (Al-Si-Mg) for 6000 series. The specific type of alloy is selected for its strength, availability, ductility, corrosion

resistance, and ability to be used in either bolted and welded applications as the design dictates (Mazzolani, 1985).

The 2000, 6000, and 7000 series alloys are known as heat-treatable alloys and can be strengthened with several different types of heat treatments as denoted by “T” tempers, while 1000, 3000, 4000, and 5000 series cannot. These alloys are work-hardenable, so they are typically strengthened by various degrees of cold working as denoted by “H” tempers which essentially means strain-hardened. The fracture toughness of many of the high-performance, high-strength alloys used in aerospace has been evaluated (Aluminum Association, 2000). However, the non-aerospace alloys are typically too ductile to be evaluated by linear elastic, plane strain fracture mechanics methods. It is generally understood that ductility is easily achieved for these wrought products used in buildings and bridges.

Similar to steel, the aluminum manufacturing processes can lead to undesirable residual stress in portions of member cross sections. This attribute is discussed by a few researchers in the literature. Residual stresses are typically less in extruded shapes as compared to hot rolled shapes because of uniformity of distribution of the temperature through the cross section during processing (Mazzolani, 1985). This is especially the case in cold worked steel sections such as HSS where they may approach 25-70% of the yield strength of the material (Shaat & Fam, 2007).

The consequence of the presence of these stresses typically result in a reduction of the flexural rigidity of slender columns and consequently in a lower buckling strength as discussed in a report by Shaat and Fam (2007). Even though the residual stresses are in equilibrium across a member section, the regions with higher residual stress may reach

the yield stress before other regions. This can cause a reduction in the effective moment of inertia as the member behaves partially plastic. In their experiments on compressively loaded short steel columns, a distinct yield point was not observed as the section underwent gradual yielding beginning at the regions with the highest residual compressive stress.

Applications in Seismic Force Resisting Systems

Aluminum plate shear panels as seismic dissipaters have been proposed (Rai, 2002). Results are presented for inelastic cyclic buckling tests of aluminum alloy 3003-O shear panels as observed in tests of medium scale (1:4) I-beam specimens that were comprised of welded together plates and subsequently annealed to relieve residual welding stresses prior to testing. All specimens were cycled quasi-statically to failure. The shear yielding mechanism of the panel was very ductile and had significant energy dissipation potential if inelastic web buckling was prevented by the addition of stiffeners. Without these stiffeners web buckling caused severe pinching of the hysteresis loops. Similar tests and analytic modeling of pure aluminum shear panels used as an energy dissipating device utilized the material's low yield point and high ductility (Brando, De Matteis, & Mazzolani, 2009).

An analytical study of aluminum shear links that could be strategically installed in various structural systems, specifically at the beam to brace vertex connection of chevron type concentrically braced frames and at mid-span of special truss moment frames, was reported (Rai & Wallace, 2000). In this concept, I-section links of low yield strength material served as a sacrificial fuse for dissipating seismic energy and thus preserving the steel elastic members from damage. Yielding of the I-section web in shear was the

dissipation mechanism. Localized damage would allow easy link replacement after a significant seismic event.

The concept of high-strain-rate superplastic Zn-Al alloy dampers was also reported (Kushibe, Makii, Chiang, Tanaka, Kohzu, & Higashi, 2005). The authors called this a “maintenance-free seismic damper” because the alloy had a very low work hardening rate which allowed the yielding element to undergo repeated seismic events before replacement was necessary. This high-performance material was applied in three different systems. These systems were a shear panel system, rod bending system, and a plate bending system for use in traditional Japanese houses. Problems were reported with unstable local deformation causing localized fracture because of the low hardening properties of the alloy. This being an intrinsic property of superplastic materials because strain is not evenly distributed by the self-correcting nature of work hardening forcing strain to move to regions of lesser strain.

Material Level Behavior

Aluminum’s material level response to low-cycle fatigue (LCF) loading is important to a discussion on its use in the seismic energy dissipating system. Although testing of aluminum in this way has not been the focus of many studies, a few notable examples are reported in the literature. For instance, uniaxial tensile coupon tests were reported by Hopperstad et al. (1995). In this study, cylindrical reduced section specimens of AA6060-T4 and T6 alloy were cycled to failure in order to identify material parameters to be used in constitutive models (i.e. finite element structural analysis). Monotonic stress-strain curves and hystereses were used to develop a mathematical cyclic plasticity model that included non-linear kinematic and isotropic hardening to

create the bi-asymptotic shape. The model was shown to have good correlation with experimental data. Specifically, the T4 temper exhibited cyclic hardening at a high rate the first several cycles (exponential phase) and then a slower, moderated constant phase while the T6 temper exhibited cyclic softening at a low rate throughout the test. The cyclic hardening process was reported to be relatively slow as compared to kinematic hardening and thus had a negligible influence on hysteresis loops.

LCF studies were performed on extruded 6063 round bars (Ma, Chen, Tian, Che, & Liaw, 2009). These studies examined the difference between as-extruded, solution treated, and solution plus aging treatment to determine their effect on fatigue life and cyclic hardening or softening. Coupons were subjected to fully-reversed total axial strain amplitudes of +/- 0.3 – 1.0% at a loading rate of 0.5 Hz. The as-extruded and solution treated alloys exhibited cyclic hardening during the whole loading sequence while the one subjected to solution plus aging exhibited initial cyclic hardening followed by a stable cyclic stress response. The coupons subjected to +/- 1.0% strain reached approximately 110 cycles prior to failure for all three tempers.

The influence of temperature and strain amplitude were also examined on round rods of 7075-T6 alloy (Li & Marchand, 1989). Little was claimed to be known about this alloy's behavior in LCF even though much testing has been reported on high cycle fatigue and stress corrosion cracking. The coupons were subjected to constant total strain amplitudes of +/- 0.4 – 1.2% under temperatures ranging from 20 - 260° C with a constant strain rate of 0.2% per second. Results showed that the alloy experiences little cyclic hardening and was able to achieve approximately 100 cycles at the 1.2% strain amplitude before failure when tested at 20° C.

Aluminum alloy AA7030 coupon specimens cut from extruded cylindrical rods were tested in low-cycle push-pull fatigue to determine the effect of heat treatment on fracture behavior and cyclic deformation (Hornqvist & Karlsson, 2008). Tests were conducted at 0.1% per second strain rate. The material was tested in two different states, naturally aged (NA) and peak aged (PA). (Peak aged correlates to ASTM designation T6) It was reported that the NA temper showed rapid initial hardening during the first 5% of fatigue life followed by slow continuous hardening until the onset of crack induced softening and failure within the last 10-30% of fatigue life. The plastic strain amplitude was found to decrease continuously during cyclic loading as the material hardened. The PA temper showed a rapid initial hardening, although to a lesser extent than the NA temper, followed by a long period of softening, about 70-80% of fatigue life, until failure. At a given plastic strain amplitude the NA temper was found to outlast the PA temper.

Similarly, age hardened 6082-T6 and 6060-T6 alloy low-cycle fatigue tests were conducted by Borrego (2004). Prediction of fatigue life on round and tube coupon specimens subjected to a given stress-time history was reported. Cyclic softening for axial strain amplitudes lower than 0.82% and cyclic hardening for higher amplitudes for alloy 6082-T6, and stable cyclic behavior for alloy 6060-T6 are shown through experimental results. The transition fatigue life was found to be approximately 744 and 1030 cycles for 6082-T6 and 6060-T6, respectively.

Compression Member Tests

Experimental tests on 6063-T6 and 6061-T6 aluminum alloy compression members in the form of extruded square and rectangular hollow section columns was reported (Zhu & Young, 2006). This report presents an interesting discussion on

measured geometric imperfections of the specimens that proves useful in the subject of mathematical modeling of BRBs. Overall geometric imperfections about the major and minor axis for the square specimens, and minor axis only for the rectangular specimens were measured on all 27 columns prior to testing. Mid-length maximum values ranged from $L/1,608$ to $L/3,107$. Local geometric imperfections were measured on just five of the specimens by section cutting samples from the full-length piece. The maximum imperfections measured at the mid-length of each of the section faces ranged from 0.0027 to 0.019 inches depending on tube size. The remainder of the report concentrates on comparing test values to those achieved by design strength equations as calculated by the *Aluminum Design Manual* (Aluminum Association, 2000) and comparable international codes.

Building Code Provisions

As just mentioned, in the United States the governing specification for the design of aluminum structures is the *Aluminum Design Manual*. Design specifications are provided in dual format allowable stress design (ASD) and load and resistance factor design (LRFD) formulation. The LRFD factors of safety are essentially identical to the older ASD method as the LRFD method was calibrated to be equivalent through probabilistic analyses. At this time, neither of the design specifications include provisions for seismic design. The LRFD method is intended for use only in building structures while the ASD method is able to be used in the design of building, bridge, or other structures with a higher factor of safety.

The design equations provided for tension and compression design of aluminum sections follow the principal of conventional elastic structural analysis. Ultimate limit

states for commonly encountered structural members and elements include yield, fracture, plastification, buckling, and crippling. Similar to steel, the required stress of aluminum axial tension members must meet available stress provisions for both limit states including yield strength of the gross section and ultimate (fracture) strength of the net section. Compression in columns is significantly more complicated. Limit states consist of global buckling, local buckling, compression yielding, and torsional buckling. The global buckling limit state for members in the elastic range is simply the Euler column formula for slender columns and the compressive yield strength for stout columns. For doubly or singly symmetric columns subject to torsional or torsional-flexural buckling, the same Euler column formula is used with a modified KL/r ratio. Local plate element (section component) buckling limit states are dependent on slenderness parameters for different section profiles. Section component slenderness limits as well as the presence of stiffeners modify the governing equations. Local element buckling is based on post-buckling strength rather than buckling strength as shown in tests performed on stub-columns with cruciform cross sections (Aluminum Association, 2000).

2.4 FIBER REINFORCED POLYMERS

Introduction

The third topic to be discussed is the use of fiber reinforced polymers in civil engineering structures. FRP can be generally described as fibrous polymers bonded together with an epoxy resin matrix resulting in a super lightweight anisotropic composite that can have very high strength and modulus of elasticity. (The composite is essentially

a brittle material so any discussion of stiffness will pertain only to Young's modulus.) The polymer component is typically constructed of either glass (GFRP) or carbon (CFRP) fibers. The fibers may be procured as either flexible woven sheets, rigid plates, or as pultruded laminated sections with many available strength and modulus values. At this point it is useful to present a summary of typical FRP fabric material properties given by a typical manufacturer as shown in Table 2. Values for typical steel and aluminum material designations used in buildings are provided for comparison. It can be seen that FRP is superior to low-strength metallic materials in both strength and stiffness.

Table 2 FRP Material Properties (Courtesy of the Sika Corporation)			
Material	Tensile Strength (ksi)	Tensile Modulus (ksi)	Flexural Modulus (ksi)
CFRP (SikaWrap Hex230C)	500	33,400	-
GRFP (SikaWrap Hex 430G)	330	10,500	-
Epoxy Resin (SikaDur 300)	8.0	250	500
Steel (ASTM A992)	65	29,000	-
Aluminum (6061-T6 Extrusions)	38	10,100	-

Applications in Civil Engineering Structures

The use of FRP in civil engineering structures can be divided into two groups. The more developed and widespread use of this technology is in the application of bonded FRP to reinforced concrete members which is not applicable to development of ULWBRB. The other group is application to structural steel members which can be further subdivided into bonded and unbonded applications to the steel substrate that it is

serving to reinforce. An informative summary report has been prepared on steel strengthening with bonded FRP by Zhao and Zhang (2007). As related to the development of the ULWBRB, an understanding of the unbonded group serves to be the most useful.

There are numerous reports of using FRP to strengthen concrete beams and slabs, strengthen and confine concrete columns, and enhance concrete member and joint ductility by wrapping them with several layers of bonded GFRP or CFRP. This technology was developed primarily in the 1970s as a means to preserve functionality of deteriorated bridge and building structures or in seismic retrofit. It has quickly matured to the point of easy implementation in practice through the use of product manufacturer's literature and design guides such as ACI 440.2 R-08 (American Concrete Institute, 2008) that was first published in 2002. This document serves as the industry and practice standard for use of FRP in strengthening concrete structures. No similar document exists for FRP strengthening of steel structures which further highlights the infancy of this technology. Specific informative building code provisions are likewise non-existent.

The use of FRP technology in strengthening existing steel structures is the subject of many recent research papers even though its practical application has been limited. The authors of these papers highlight the benefits of this concept over traditional steel strengthening techniques as follows: decreased dead load on existing members, no need to field shape steel member profiles to match existing members, no field welding and associated fatigue notching, reduced susceptibility to corrosion, and reduced need for expensive shoring systems. Typically, FRP is used in bonded flexural tension applications. Reports on steel compression member strengthening applications are at this

time rare. However, since preclusion of compression buckling is the intended use of the FRP in the ULWBRB the few that are available will be discussed.

FRP Bonded to Steel Members

Bonded unidirectional CFRP sheets wrapped around special truss moment frame (STMF) double channel chord members have enhanced plastic hinge behavior during cyclic loading to 7.6% drift (Ekiz, El-Tawil, Parra-Montesinos, & Goel, 2004). Large scale element tests compared different wrapping parameters to an unwrapped control specimen. Hysteresis results of the wrapped specimens improved over unwrapped. This was attributed to an extended yielding area at the plastic hinge region due to control of local element buckling of the double channel flanges and flexural buckling of the channels. The authors suggested the method be used to improve the behavior of new structures or upgrade existing structures in regions of high seismic risk.

CFRP strips bonded longitudinally to either the mid-depth or the compressive web regions of an I-section steel flexural member to delay local compression buckling of the web have been successful (Sayed-Ahmed, 2006). This application of CFRP served to increase web stability enough to allow the member to reach its full yield or full plastic moment capacity for non-compact and compact sections, respectively. Parametric investigation of strip placement showed mixed results on the effectiveness of this concept.

Longitudinally oriented, rectangular GFRP strips bonded to the compression flange of steel I-section flexural members in an effort to enhance flange outstand stability by delaying the onset of local buckling are also reported (Accord & Earls, 2006). The intended application for this technique was to enhance ductility at the plastic hinge region

adjacent to connections in a moment frame. The research was conducted through the use of numerical finite element models and is reported to have forced the beam into a global mode of buckling, otherwise known as lateral-torsional buckling. Experimental verification of the numerical results was recommended.

Researchers have used these stability concepts on pure compression members instead of merely compression elements of flexural members. An experimental program in which GFRP and CFRP strips were bonded to the web of WT sections loaded axially in compression improved member stability (Harries, Peck, & Abraham, 2009). This paper contains results for elastic (global) buckling of slender WT members and inelastic (local) buckling of short WT members subjected to reversed cyclic loading.

Experimental results showed a negligible effect of FRP strengthening on elastic global buckling of long members. Conversely, a significant effect on inelastic (local) web buckling was attributed to significantly increasing the element outstand's radius of gyration over the unstiffened case. The overall increase of the radius of gyration on the entire WT section, as in the case of global buckling, was relatively insignificant as compared with the local case. The typical failure mode was FRP unbonding followed by inelastic (local) web buckling after an unreported number of compression cycles. Increasing in energy dissipation by withstanding a greater number of cycles before failure was mentioned as a future research focus.

Another compression member application is bonding high-modulus CFRP pultruded plates longitudinally to hollow structural section (HSS) test columns and then wrapping the entire assembly in bonded transversely oriented CFRP sheets. This concept has been investigated as a method for delaying local buckling of the tube walls for short

columns and global flexural buckling of long slender columns when loaded concentrically in compression. The researchers first examined this concept through experiments with limited success. Strength achieved at short column local buckling and long column global buckling was improved over the plain columns by a maximum of 18 and 23%, respectively (Shaat & Fam, 2006). In a follow-up paper, elaborate non-linear analytical and numerical models based on the concepts of equilibrium and strain compatibility correlated well with experimental results (Shaat & Fam, 2007). These models considered initial column out-of-straightness, residual stresses, material and geometric non-linearities, slenderness and CFRP reinforcement ratio. Finally, the authors reduced these models down to a simplified design-oriented analytical model based on a modified radius of gyration through a transformed section analysis effectively converting CFRP flexural contribution to that of steel (Shaat & Fam, 2009). They reported that the effectiveness of their CFRP strengthening system increased substantially with higher column slenderness ratios. CFRP failure was due to unbonding and subsequent crushing at the mid-length flexural compression side either prior to, simultaneously, or after global buckling for slenderness (KL/r) ratios 46, 70, and 93, respectively. Very similar tests on concrete filled HSS were reported by Tao et al. (2007) that failed by outward tube wall buckling mechanisms causing CFRP rupture.

The last application of bonded FRP to be discussed relates most directly to the concept of BRBs. This is called the partially-buckling-restrained brace (PBRB) (Abraham, 2006). This concept employs GFRP or CFRP strips bonded to the web of six WT-specimens and subjected to cyclic compressive loading until failure with the aim of achieving stable hysteretic behavior. The PBRB was proposed to be used in seismic

applications as a metallic yielding energy dissipater where the performance, and additional expense, of a full BRB is not warranted. The concept achieved minimal success due to the effect of initial loading eccentricity and the failure mode of lateral-torsional buckling and subsequent FRP debonding that was reached prior to the compression yield point.

FRP Unbonded to Steel Members

A topic more closely related to the ULWBRB is the use of unbonded FRP in strengthening steel members. Reports of research, and certainly practical, applications of this method are rare. One of the original concepts of an unbonded FRP wrapped brace was reported by Dusicka & Wiley (2008). Their original concept was targeted for use in in-situ retrofitting of existing steel bridge structures containing steel angle braces that required enhanced transverse stiffness. The concept consisted of fitting an 8 foot long, 2 by 2 by $\frac{1}{4}$ inch steel angle with a 4 by 4 by $\frac{1}{4}$ inch pultruded FRP tube and wrapping the assembly in GFRP fabric. The fabric was allowed to bond to the FRP tube but not the steel angle by applying a $\frac{1}{32}$ inch thick silicone sheet around the angle thus creating axial independence between the FRP restrainer and core. Compression experiments resulted in early plastic hinge formation near the end of the FRP restrainer. Splaying angle legs caused the wrap to tear at the end of the FRP tube. Exacerbation of the plastic hinge behavior was attributed to the pinned end boundary conditions not explicitly representative of a true brace gusset connection. Before plastic hinging, an unsustained compressive force equal to 35% of the tensile strength was reached. Although these limited experiments did not reach the stable hysteretic behavior required for a BRB, further refinement of the idea leading to a useable BRB was reported to have potential.

Another very similar program for developing FRP restrained braces was reported and has reached a much higher state of development than that by Dusicka and Wiley. This concept utilizes transverse and longitudinal CFRP wrap around either mortar or solid PVC blocks that were taped to a steel brace member (Ekiz & El-Tawil, 2008). This concept aimed to allow the steel core to undergo inelastic hysteretic behavior before global or local buckling modes were developed. The authors intended relatively easy construction by low-skilled workers utilizing small and lightweight materials especially in retrofit applications. Rehabilitation of steel brace members in-situ to achieve BRB behavior was specifically mentioned as a practical application potentially in deficient bridge structures, hardening for security purposes, and of course, seismic upgrading.

In this parametric experimental and numerical study, 22 small-scale 12 inch long by 2 inch wide rectangular dual-grade ASTM A36/A572-Grade 50 steel bar specimens were tested under monotonic compressive loading. Rectangular bar was chosen to limit the potential failure mode to that of global buckling. Both prismatic and hourglass shaped bars were tested. Fixed-fixed end conditions gave a standard slenderness (KL/r) ratio of 83. For this program, the success evaluation was made by defining yield prior to buckling (YPB) or buckling prior to yield (BPY). Many of the bars reached strains above yield strain, or YPB, with the highest maximum load to yield load ratio (P/P_y) of 1.53 for the mortar block specimen. Failure was by fracture of longitudinal FRP layers, fracture of transverse FRP layers near the end, local buckling of FRP layers on the flexural compression side, or higher (second) mode buckling of the steel bar inside of the restraining system followed by crushing of the core material and bulging of the FRP.

Their parametric investigation gave the following generalizations for improved

performance: the mortar core specimens reached a higher compressive strain than the PVC specimens, the steel core with a reduced (hourglass shaped) section exhibited better inelastic performance than the prismatic core, specimens with unbounded steel to FRP interface performed better than those that were bonded since bonded specimens appeared to trigger overall buckling, CFRP that was bonded to the mortar or PVC blocks behaved more predictably given that the separate unbonded thin layers were prone to buckling, an increase in the thickness of the core blocks performed better than thin blocks due to an increased radius of gyration, and lastly, a greater number of longitudinal layers of CFRP (1 to 5 layers were tested) incrementally increased the maximum axial compressive load. Furthermore, tapering the steel cores at mid-length reduced the potential for transverse fiber failure at the specimen ends.

This concept was further developed by seven full-scale reversed cyclic axial loading tests on 134 inch long, 2 ½ by 2 ½ by 3/16 inch dual-grade ASTM A36/A572-Grade 50 steel angle brace specimens of either single or double angle configuration (El-Tawil & Ekiz, 2009). The angles were wrapped with both longitudinal and transverse CFRP sheets after taping mortar blocks to them.

Both pinned and semi-fixed boundary conditions were tested although the effect of attempting to restrain the end condition was reported to be minimal. Main parameters that were varied in this experimental only program were: fixed or semi-fixed end connections, number of longitudinal CFRP layers, thickness of mortar core blocks, use of extra stitch plates between the legs of back to back double angles, bond between steel and CFRP, and bond between the core blocks and steel member. Displacement demands of the test frame corresponded to story drifts ranging from 0.3 to 4%, or axial strains of 0.15

to 2.7%. Although repeated excursion into the inelastic range was unsuccessful beyond two to three cycles, cumulative energy dissipation over bare angles was reported to be increased 80% for the single angle and 10-270% for the double angle. Note that the small 10% increase was the specimen where local buckling occurred between stitch plates as mentioned below.

Failure modes for the bare angle control specimen were local buckling of the angle legs at the mid-length followed by global buckling of the entire brace prior to compression yielding, as expected. CFRP strengthened specimens exhibited a number of different failure modes including punching of the transverse layers of CFRP wrap at the member ends due to inadequate gap between the angles and the CFRP, local buckling of back to back angle legs inside of the restrainer in between the uniformly spaced stitch plates, crushing of mortar blocks due to local buckling of steel, and separation and buckling of longitudinal CFRP layers on the flexural compression side after the mortar blocks were damaged.

This paper noted a number of generalizations for improved performance based on these experimental results including adding another layer of transverse CFRP near the member ends to help prevent tearing caused by core member buckling, addition of frequent stitch plates between back to back angle legs of double angles to prevent local buckling, unbonding the steel from CFRP layers to help prevent axial loading and subsequent buckling of the thin section, and extending mortar blocks beyond the ends of steel angles to prevent the stretching angle from punching or tearing CFRP on the axial tension cycle. Larger block cross-sectional dimensions had an effect although limited test data could not verify this assertion. The compressive strength of the core blocks was

also noted as an area for improvement given the crushing caused by steel local buckling.

Galvanic Corrosion

It is prudent to briefly mention that there is a considerable amount of research on the potential for galvanic corrosion of metallic elements due to the presence of CFRP (Schnerch, Dawood, Rizkalla, Sumner, & Stanford, 2006). Carbon is a very noble cathodic material that can drive the corrosion of many materials galvanically coupled to it. Steel and aluminum have similar positions in the galvanic series and will behave anodically in carbon's presence. One technique reported to prevent this reaction is to introduce a non-conductive layer between the base metal and carbon. Past methods that have been used in practice, or by various researchers, have been epoxy films or insertion of a GFRP sheet between the two materials. However, insertion of glass fiber sheets within a carbon fiber system is reported to have caused blistering of the composite by development of strong osmotic pressure in exterior applications (Schnerch, Dawood, Rizkalla, Sumner, & Stanford, 2006). Elimination of the necessary bridge of electrolytic solution between the anode and cathode by applying a coating of water resistant sealant to the exterior of the assembly is another reported technique. Long term durability of this method is in question (Sloan & Talbot, 1992). Essentially the durability of any of these methods depends on factors such as: exposure to moisture or deicing salts, humidity levels, freeze-thaw cycles, and sun exposure. Generally, the interior application of these methods is more feasible than exterior ones such as highway bridges.

2.5 MATHEMATICAL MODELING OF BRB

Introduction

Mathematical modeling of BRBs is presented by most researchers as a means to develop reasonable test specimens to be used in either developmental or practical applications. As previously mentioned, the *Provisions* contain no empirically based equations for preliminary design of the BRB restraining element or the entire BRB assembly acting as a system. Designers thus far have used previous qualification test data (on usually patented products), experience, crude analytical modeling, and in some cases numerical modeling to specify BRBs in practical situations. Usually the project specification is performance-based where only the dimensional, material yield point, and brace forces are specified by the engineer of record. The remainder is typically left up to the BRB supplier as they are the experts on their own specific products.

This provides a good departure point for the summarization of these mathematical methods. Specifically, analytical and numerical modeling of BRB, hysteretic models of steel braces, and an introduction to the concepts of cumulative plastic ductility (CPD) demand and cumulative deformation capacity as a means for quantifying BRB performance are presented comprehensively.

Analytical Modeling of BRB

Design of buckling-restrained braces involves primarily an examination of the potential for instabilities in the compression regime and for this researchers have typically subdivided the subject of analytical modeling of BRB into three distinct buckling modes. These are global flexural buckling of the entire brace (mainly the restrainer), local buckling of core element outstands, and plastic torsional buckling of the

unrestrained core ends.

One of the earliest relationships used in the determination of adequate restrainer strength was made with empirical test data by Kimura et al. (1976) and has been used by other researchers to gauge the required restraining force (D'Aniello, Della Corte, & Mazzolani, 2008). This relationship is shown in Equation 4 and provides a minimum ratio of Euler's limit of the restraining member (N_E^B) to yield strength of the brace core (N_y) of 1.9. Tests by Kimura et al. showed that if this minimum ratio was satisfied global buckling would be resisted.

$$\frac{N_E^B}{N_y} > 1.9 \quad (4)$$

For global flexural buckling of the entire brace, the classical method of stability analysis, or Euler's theory, can be applied to the outer tube of mortar-filled BRBs.

Equation 5 shows that this failure mode can be expressed in terms of critical buckling stress (σ_{cr}) where K is the effective length factor, L is the core member length, A_i is the cross-sectional area of the core, and E_o and I_o are the Young's modulus and moment of inertia of the restraining member, respectively (Black, Makris, & Aiken, 2004).

$$\sigma_{cr} = \frac{P_{cr}}{A_i} = \frac{P_e}{A_i} \approx \frac{\pi^2 E_o I_o}{A_i (KL)^2} \quad (5)$$

This relationship was converted to critical buckling load N_{cr} for elastic buckling of a composite brace comprised of a steel bar encased by a reinforced concrete member as shown in the summary report by Xie (2005). This analysis assumed that the deformations of the encasing concrete and the brace were the same. This assumption was based on the application of an equal and opposite force imposed by the restrainer for any brace buckling force acting on it. Essentially the buckling capacity was taken as the sum

of the contributions of the two separate parts as shown in Equation 6 where n is the buckling mode ($n=1$ for global buckling), L is the core member length, and $E_s I_s$ and $E_c I_c$ are the flexural stiffness of the steel and concrete, respectively.

$$N_{cr} = \frac{n^2 \pi^2}{L^2} (E_s I_s + E_c I_c) \quad (6)$$

Further developing the global buckling analysis to that of mortar-filled steel tubes, and assuming the concentrated restraining force is imposed at the mid-length of the core, the required stiffness and strength as a pair for the encasing member was derived. Initial core out-of-straightness was taken as a sinusoidal curve. Equation 7 was recreated by Xie (2005) and shown below. Where N_E^B is the Euler buckling load, N_y is the core member yield force, E_B is the modulus of elasticity of the steel tube restraint, σ_{ky} is the yield stress of the steel tube, L_b is the length of the steel tube restraint, D is the depth of steel tube, and a is the initial imperfection at the mid-length of the brace.

$$\frac{N_E^B}{N_y} = 1 + \frac{\frac{\pi^2 E_B}{2 \sigma_{ky}} \left(\frac{a}{L_b} \right)}{\frac{L_b}{D}} \quad (7)$$

Second order formulations that account for initial geometric imperfections, non-linear behavior of the core, and interaction between the core and the mortar were reported (Palazzo, Lopez-Almansa, Cahis, & Crisafulli, 2009). These are modified equations from those reported by Black et al. (2004) that were described to be more conservative. In Equation 8, M_1 gives the required moment for designing the casing for the first buckling mode where P is the brace axial compressive force, P_E is the Euler load for the casing, e_1 is the sum of the initial gap between the core and the surrounding mortar plus the initial eccentricity of the core, L is the core member length, and E_{ca} and I_{ca} are the Young's

modulus and moment of inertia of the casing, respectively.

$$M_1 = E_{ca} I_{ca} e_1 \left(\frac{\pi}{l_1} \right)^2 \frac{\frac{P}{P_E}}{1 - \frac{P}{P_E}} = \frac{P e_1}{1 - \frac{P}{P_E}} \quad (8)$$

$$\text{Where for pinned ends } (K = 1) \quad P_E = \frac{\pi^2 E_{ca} I_{ca}}{L^2} \quad (9)$$

The required moment capacity of the stiffening, or restraining, member was similarly derived by El-Tawil and Ekiz (2009). They use the following governing differential equation shown in Equation 10 for a steel bar stiffened with a supplementary restraining member. The differential equation was set equal to zero to preserve moment equilibrium at any point along the length of the member. This differential equation was then solved assuming that the steel core had no flexural stiffness after reaching the yield load, the ends of the steel core member were free to rotate, and the initial deflection along the steel member was a sine curve. The resulting minimum moment capacity of the stiffening member to preserve global stability (M_{cap}) is shown in Equation 11 where D is the effective stiffness of the stiffening member, L is the length of the stiffened member, v is the deflection at any point along the stiffened member, v_o is the initial deflection, and N_y is the axial yielding load.

$$D \frac{d^2 v}{dx^2} + (v + v_o^2) N_y = 0 \quad (10)$$

$$M_{cap} > M = \frac{N_y}{1 - \frac{N_y L^2}{\pi^2 D}} \quad (11)$$

Higher mode or local buckling of the core can also be expressed as a critical stress (σ_{cr}) as given in Equation 12 for a mortar-filled tube by Black et al. (2004). This critical

stress can be calculated by either an energy method or by direct integration. Where β is the distributed spring constant representing the stiffness per unit length of the encasing mortar, E_t is the tangent elongation modulus, and I_i and A_i are the moment of inertia and area of the inner core, respectively.

$$\sigma_{cr} = \frac{P_{cr}}{A_i} = \frac{2\sqrt{\beta E_t I_i}}{A_i} \quad (12)$$

Recent research has examined the possibility of local buckling of the core element where mortar cover is thin, i.e. where rectangular plate cores are used in mortar-filled tubes where only ½ inch or less of mortar exists between the core and the inner wall of the restraining tube (Takeuchi, Hajjar, Matsui, Nishimoto, & Aiken, 2010). This problem is exacerbated by the addition of gap material on the narrow end of the core plate to allow for Poisson expansion. This failure mode was modeled as a core plate restrained by an elasto-plastic spring support in the strong axis direction where the spring coefficient (β_r) was given by Equation 13 where E_{tr} and I_r are the tangent modulus and moment of inertia of the restrainer wall, respectively, and B_r is the width of the tube restrainer wall. Modeling considered the tube wall as a short fixed-fixed beam with a span equal to the tube wall width and a depth equal to the tube wall thickness.

$$\beta_r = \frac{192E_{tr}I_r}{B_r^3} \quad (13)$$

The force required to achieve local buckling of the core plate (P_{crl}) was then given in Equation 14 where E_{tc} and I_c are the tangent modulus and moment of inertia of the core plate, respectively. This formulation is similar to that presented by Black et al. (2004) except it is in terms of force not stress.

$$P_{crl} = 2\sqrt{\beta_r E_{tc} I_c} \quad (14)$$

Above equations accounted for spring forces in the elastic range only. After yielding of the tube wall occurred, E_{tc} and β_r were reduced with subsequent cyclic loading. Local buckling failure occurred when P_{crl} become smaller than the core plate yield force.

Takeuchi et al. also reported the length of the local buckling wave (l_p) for a core plate in the strong axis and the perpendicular force components (P_r) working on the restrainer wall at the peak of the buckling wave as shown in Equations 15 and 16, respectively.

Where B_c is the width of the core plate, σ_{cy} is the core plate yield stress, s is the clearance between the core plate and the restrainer, ν_p is the plastic Poisson's ratio, ε_t is the maximum tensile strain of the core plate, α is the hardening ratio of strength after yielding, and t_c is the thickness of the core plate.

$$l_p = i_c \bar{\lambda} = \frac{\pi B_c}{2} \sqrt{\frac{E_{tc}}{3\sigma_{cy}}} \quad (15)$$

$$P_r = \frac{2s + \nu_p \varepsilon_t B_c}{l_p} P_{cy} = \frac{2s + \nu_p \varepsilon_t B_c}{l_p} B_c t_c \alpha \sigma_{cy} \quad (16)$$

Other researchers have considered local buckling of the core that does not involve buckling of the restrainer (Palazzo, Lopez-Almansa, Cahis, & Crisafulli, 2009). The core was proposed to behave as if embedded in an elastic medium. For small lateral displacements the medium was assigned a stiffness representative of the rubber gap material surrounding the core which was basically insignificant. For larger lateral displacements, the stiffness of the medium was that of the surrounding mortar.

Lastly, is the failure mode of torsional buckling of the unrestrained core ends. To prevent this undesirable buckling mode, this region of the core element is typically

stiffened with welded on plates or in the case of cruciform sections, with integral element outstands. Plastic buckling of a cruciform section was reported to have been studied extensively (Black, Makris, & Aiken, 2004). Methods for arriving at a critical buckling stress (σ_{cr}) formula were described as formulated by other researchers. These methods include an elastic buckling stress as given by Timoshenko and Gere (1961) amongst others. Finally, they cited a recent study that considers plastic torsional buckling through small-strain theory. An incremental plasticity approach was described to be more conservative than the total deformation theory. Critical buckling stress (σ_{cr}) is given in Equation 17 where E_t is tangent elongation modulus of the core, σ_y is the yield stress of the steel core, b is the width, t is the thickness, and l is the length of each of the four flanges of the cruciform section.

$$\sigma_{cr} = \frac{E_t}{3} \left[\frac{\pi^2 b^2}{3 l^2} + 1 + 3 \frac{\sigma_y}{E_t} \right] \frac{t^2}{b^2} \quad (17)$$

Numerical Modeling of BRB

Many instances of numerical modeling of buckling-restrained braces have recently been reported in the literature. The most common manifestation of these has been in the form of non-linear finite element analysis (FEA). Since the development of this method in the 1960's, it has proven to be an effective and numerically efficient way of simulating behavior of structural members. FEAs are best described as approximate simulations that are based on numerical techniques that discretize the entire member into a finite number of individual elements connected by nodal points, boundary lines, or surfaces. The model's initial geometry can be based on gathered experimental measurements in order to identify imperfections of typical members such as out-of-

straightness or cross-section variance. Model material properties are likewise taken from experimental data in order to better simulate phenomena such as inelasticity, strain or cyclic hardening, residual stress distribution, inhomogeneous distribution of material properties, anisotropy, and the Bauschinger effect. The presence of imperfections in materials such as those described above, either geometric or material, have been termed the “Industrial Bar” as if relating back to real world conditions (Mazzolani, 1985). This is certainly a more comprehensive and accurate method of simulating behavior than classical methods termed as the “Ideal Bar” where imperfections are ignored. Finally, it is important to note that it is usually considered good practice to correlate results from these mathematical simulations with experimental test results. Without this proof the model’s accuracy remains in question.

One of the largest differences between the FEAs found in the literature is the type of elements that were used to construct the BRB representation. Brace members modeled with fully integrated four-node isoparametric shell elements were reported for full-scale steel angle specimens (Park, Iwai, Kameda, & Nonaka, 1996). This study is not directly related to BRBs, but it gives important insight to how very low cycle failure processes can be modeled in asymmetric compression members. Fixed loading block boundary conditions at the end of the angle experimental specimens were simulated with the use of rigid shell elements in the model. The mesh fineness was increased at the mid-length of the unrestrained angle member where stress concentrations and local buckling were expected to occur. Convergence of the model was determined by monotonic displacement results for four different mesh gradations of 154, 230, 306, and 466 elements. Non-linear materiality was simulated as bilinear-elastoplastic with kinematic

hardening. Good correlation between the experimental results and numerical model were reported for load-displacement and overall deformed shape including local buckling deformation.

When looking at the local buckling stability of the compression flange of a flexural beam, Accord and Earls (2006) also used four-node shell elements to model an I-shaped steel beam that was fitted with GFRP strips bonded to the flange. The two GFRP strips were modeled as eight-node continuum elements and the flexible adhesive between the two was also modeled as continuum elements. The element mesh was linearly graded along the length of the cantilever beam in order to limit the total number of nodes for computational efficiency. A denser element gradation was provided at the fixed support end where local buckling was expected to occur. In order to promote the lowest energy, and therefore dominate, first-mode of buckling, initial geometric imperfections were modeled into the beam flange and scaled to $L/1000$. This was taken from the maximum out-of-straightness limit for compression members per the *AISC Code of Standard Practice* (American Institute of Steel Construction, 2005a). Material non-linearity was simulated with a piecewise linear stress-strain relationship. The bonding adhesive was inputted as an isotropic elastic material with a modulus one-fourth that of the GFRP material. Since no experimental tests were conducted, the authors recommended future verification of model results.

Finite element modeling of CFRP strips fitted to the web of I-shaped flexural members was also used to control the onset of local web buckling (Sayed-Ahmed, 2006). Five eight-node, six degree of freedom shell elements were used across the thickness of the beam web. One element was for the web with one each side for both the epoxy

adhesive and the CFRP strip.

A flat bar steel core sandwiched between two concrete filled channels that were bolted together was numerically modeled (Chou & Chen, 2009). A parametric study of 22 models was compared with experimental data. The steel core, restraining member, concrete infill, and bolts were modeled with eight-node solid elements (C3D8R). An initial imperfection was introduced into the core member by scaling the first buckling mode. The parametric study found that if the restraining member was designed with $P_e/P_y > 2.0$, $L_b/L_w < 2.0$ and a tensile demand to capacity ratio of the bolt < 1.5 , the BRB would be able to achieve maximum compressive loads of $1.4 - 1.5 P_y$ where P_e is the Euler buckling load of the restrainer, P_y is the yield load of the core, L_b is the bolt spacing, and L_w is the local buckling wavelength.

Both shell and solid elements were used to model buckling-restrained steel bars where the buckling restraint consisted of CFRP wrapped mortar blocks surrounding the steel core (Ekiz & El-Tawil, 2008). Both the steel bar core and mortar core elements were fully integrated eight-node brick elements. The steel member had four elements through its depth and the mortar blocks had two elements. The CFRP wrap was modeled using fully integrated, layered unidirectional shell elements. When the mortar core elements and the steel core were allowed to slide past one another (the unbonded condition), a coefficient of friction of 0.3 was inputted in the model. Since the CFRP was considered to be fully bonded to the mortar blocks, common nodes were modeled as perfectly rigid. For geometric imperfections, an initial out-of-straightness was approximated by imposing a half-sine curve on the steel bar member with an amplitude of $L/1000$. Three full-sine curves were then superimposed onto the global buckling curve

with an amplitude of $L/5000$ to allow higher modes of buckling. For material non-linearity, a piecewise linear J2 plasticity model was used to model the steel member and the mortar blocks. The model for the compressive stress-strain curve for the steel was calibrated by scaling down tensile coupon test results to better match experimental results. The CFRP was assigned elastic-brittle material properties in both longitudinal and transverse directions. One very innovative attribute of the model was that brittle CFRP finite elements that exceeded the tensile strength of the material were removed from the model to simulate crack propagation. The final FEA was reported to be successful in predicting all final failure modes and reasonably accurate in predicting load-displacement response.

A divergence in modeling technique, and complexity, for an all-steel BRB concept was reported that employed Timoshenko beam elements (Usami, Ge, & Kasai, 2008). Symmetry was used in order reduce the model to half of the brace length. Two beam elements each were used for both the steel core and the restraining members. All four of these beam elements were connected with very short rigid bars (15 along the half-length). The rigidity of the unbonding material wrapped around the steel core was neglected in this rigid bar analogy. All materials were defined with an elasto-plastic stress-strain relationship and global geometric imperfections were simulated with an unspecified initial deflection following a sinusoidal pattern. Loading eccentricity of the axial force was also considered in the model. The model successfully simulated the global buckling behavior of the tested BRBs.

A numerical model investigated primarily the local buckling effects of mortar-filled tube BRBs (Takeuchi, Hajjar, Matsui, Nishimoto, & Aiken, 2010). This model

considered the close proximity of the thin edge of the core plate to the tube wall neglecting the mortar thickness. Shell elements with a one to one aspect ratio for the core plate were modeled as directly touching those of the tube wall which was taken as a fixed end supported plate that spans the distance of the width of the tube. The deformation of the core plate about its weak axis and rotation of the core plate were restrained. Initial geometric imperfections were established within the clearance between the core plate edge and the mortar. The half-length of the local buckling wave was kept to around $3.5B_c$ to $4B_c$ where B_c is the width of the core plate. Material non-linearity considered a combination of isotropic and kinematic hardening as shown below in Equations 18 and 19 where σ_{ys} is the yield surface stress for isotropic hardening, $\sigma|_{ys}$ is the yield surface stress at zero plastic strain, σ_{pl} is the backstress for kinematic hardening, C_1 and C_2 are material parameters calibrated by tensile coupon tests, and ε_{pl} is the plastic strain.

$$\sigma_{ys} = \sigma|_{ys} + \sigma_{pl} \quad (18)$$

$$\text{Where } \sigma_{pl} = \frac{C_1}{C_2} (1 - e^{-C_2 \varepsilon_{pl}}) \quad (19)$$

Hysteretic Modeling of Steel Braces

Examples of hysteretic modeling of steel braces that were not restrained from buckling but were expected to undergo dissipative yielding are also present in the literature. One recent report specifically described many of the phenomena involved in this complex interaction including yielding in tension, growth effect, inelastic buckling in compression, deterioration of the buckling capacity due to the Bauschinger effect, and the residual kink effect (Diceli & Calik, 2008). The authors divided the models into either finite element, phenomenological, or physical for the purposes of their discussion. It was

their opinion that finite element models tend to be computationally expensive and cumbersome while the much simpler phenomenological models involve numerous empirical coefficients that require substantial test data for each specific brace. Physical models are said to combine the advantages of finite element modeling and the phenomenological model thus achieving a universal and more computationally efficient hybrid. These physical models have been reported by various researchers as a simple structural system generally made up of two elastic beam members and a plastic hinge. This study developed a more efficient and broadly applicable theory based on the dummy load method and incorporated many of the phenomena listed above through semiempirical analytical equations. The hysteresis was broken up into six separate behavioral zones and each was treated discretely with easily understood physical models. The analytical model developed in this study correlated reasonably well with previous experimental hysteresis loops for both load-axial displacement and load-transverse displacement scenarios.

Cumulative Plastic Ductility Demand and Deformation Capacity

The concepts of maximum and cumulative plastic ductility (CPD) demand, defined as μ_{max} and μ_c , respectively, have been used by countless researchers and practitioners alike to quantify BRB performance in the ductile range. Equations 20 and 21 give formulas for both where Δ_{max} is BRB maximum deformation, Δ_{by} is BRB yield deformation, and $\Delta_{plastic}$ is BRB plastic deformation (Fahnestock, Ricles, & Sause, 2007).

$$\mu_{max} = \frac{\Delta_{max}}{\Delta_{by}} \quad (20)$$

$$\mu_c = \frac{\sum \Delta_{plastic}}{\Delta_{by}} \quad (21)$$

A comparison of ductility demands that have been imposed on previous BRB test specimens was presented. These values ranged from 10 to 25 for μ_{max} and 50 to 1,000 for μ_c . Given this large range, it could be seen that most test specimens have been able to achieve high levels of cumulative ductility before failure. Higher values of μ_c were achieved when μ_{max} was kept in the range of 10 to 15 suggesting that a higher plastic deformation range significantly reduced cumulative plastic ductility (CPD) potential.

3.0 MODEL BUILDING

3.1 *Objective*

A well-defined model building is selected prior to exploring design concepts for the ultra-lightweight buckling-restrained brace. The selected model building is fit with a concentrically braced frame (CBF) seismic lateral force resisting system in each orthogonal direction that utilizes the ULWBRB for the diagonal bracing members. This configuration is classified as a buckling-restrained braced frame (BRBF) as presented in the literature review. The purpose of the model building is to create sufficient context for the ULWBRB component for the primary goal of determining brace seismic demand (i.e. axial forces and displacement). In addition, geometric properties are determined including brace length, brace angle, and a general idea of brace end connections to the BRBF.

3.2 *Selection Criteria*

Development of the ULWBRB primarily concerns component-level seismic demand. However, knowledge of the system-level behavior at the individual frame or entire building level has been proven important by various researchers (Sabelli, Mahin, & Chang, 2003). Typically, dynamic analyses, non-linear analytical and numerical modeling, and several suites of ground motion time histories were applied at the system-level in such endeavors. Detailed statistical information on behavior such as interstory drifts, soft-story performance, and failure modes can be gleaned from such analyses.

However, in this program the basic seismic demands on the brace are extracted from a simplified linear-elastic equivalent lateral force analysis leaving this system-level performance to subsequent research. Therefore, a symmetrical model building without horizontal or vertical structural irregularities is desired. This serves to minimize activation of coupled translational-rotational motion.

Since the most-likely application for a ULWBRB is in retrofit applications of small to medium sized buildings with office, commercial, residential, or institutional-type occupancies, the model building should be similar. The building should also be low-rise, consisting of one to six stories, to lessen the susceptibility to dynamic effects from higher modes. The floor plates should be no larger than 200 feet by 200 feet in order to allow placement of only perimeter frames in each direction and still maintain rigid diaphragm action. Ideally, the model building should have equal sized bays in each direction that allow a single BRBF geometry throughout the building. These bays are proportioned with story heights in such a way as to permit reasonable brace angles. Many CBF systems utilize approximately 45 degree brace angles in order to maximize efficiency of gusset plates and connections to the columns, beams, and braces. Lastly, the building should be located in an area of high seismicity as BRBFs are expected to perform inelastically under high lateral loads. The fulfillment of these selection criteria leads to a system that can be analyzed with the chosen simplified method.

A summary of literature reports on system-level BRBF or CBF model building structures is given in Table 3. It can be seen that there is consistency between several completed research programs as far as the size of building floor plate, bay size, story height, and number of stories is concerned. The model building used in this project

should exhibit similar qualities in order to easily compare performance results with previously reported BRB concepts already in the literature. A direct comparison between moment frame, CBF, and BRBF system performance for the same model building and ground motion parameters is cited as advantageous (Sabelli, Mahin, & Chang, 2003). This project attempts to follow this precedent.

Table 3 – Summary of Model Buildings in the Literature						
Reference	Floor Plates	Lateral Force Resisting System	Stories	Story Height	Bay Size	Location/ Design Spectral Acceleration
(Federal Emergency Management Agency, 2000)	120' x 180'	moment frames	3	13'	30' x 30'	Los Angeles, Seattle, Boston
(Sabelli, Mahin, & Chang, 2003)	120' x 180'	SCBF, BRBF	3	13'	30' x 30'	Los Angeles
(Fahnestock, Sause, Ricles, & Le-Wu, 2003)	180' x 180'	BRBF	4	12.5'	30' x 30'	Los Angeles
(Kim & Choi, 2005)	98.4' x 98.4'	CBF	3 - 21	11.8'	32.8' x 32.8'	$S_{DS} = 0.5g$ $S_{D1} = 0.3g$
(Yang, Moehle, & Stojadinovic, 2009)	196' x 196'	SCBF	3	14'	28' x 28'	$S_{DS} = 1.27g$ $S_{D1} = 0.71g$

3.3 SAC Model Building

The SAC 3-story model building shown in Figures 5 and 6 is found to exhibit many of the desired qualities described above and has effectively been modified by previous researchers into a braced frame configuration, as shown in Table 3. SAC buildings of 3, 9, and 20-stories were originally designed as part of a joint study on welded moment resisting frames following the Northridge earthquake of 1994 (Federal Emergency Management Agency, 2000). They were designed per the local building code

requirements by three commissioned independent design firms to be representative of typical office buildings set in Boston, Seattle, and Los Angeles for comparison across differing regions of seismicity. The SAC buildings provide a context for the development of the ULWBRB that is well defined in terms of geometry, building mass, seismicity of location, and occupancy and are also well known within the seismic design community. The floor plates are constructed of concrete topping on 3-inch metal deck which serve as a idealized rigid diaphragm. The shaded area shown in Figure 5 represents a roof penthouse.

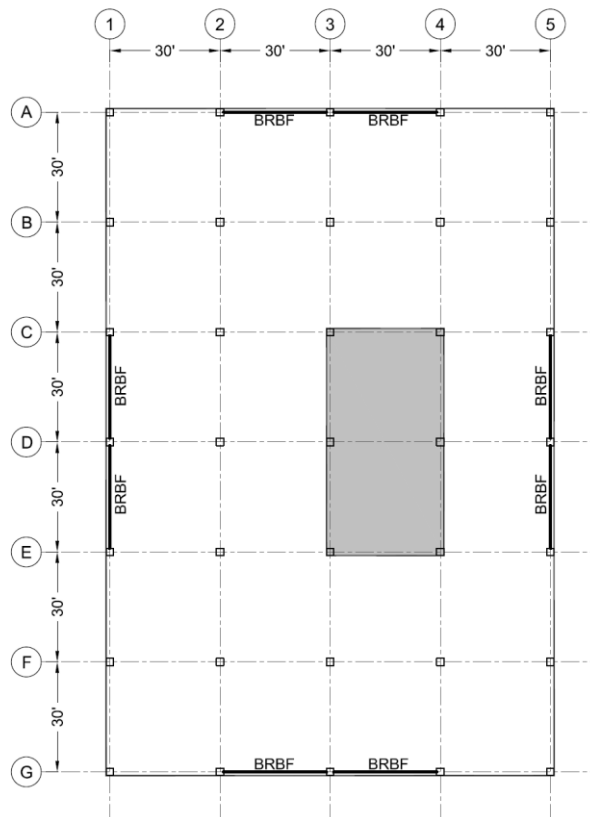


Figure 5 - Modified SAC 3-story model building plan

For the purposes of this project, the SAC perimeter moment resisting frames have been replaced with adjacently and symmetrically placed chevron, or v-braced, BRBFs as

shown in Figure 6. The inclusion of two bays of BRBFs on each perimeter column line in each direction serves to provide adequate redundancy for the system should any one brace fail during a seismic event. This strategy is effective in decreasing the code prescribed strength level forces by limiting the redundancy factor (ρ) to 1.0 in lieu of 1.3. A summary of the building's mass characteristics as given by SAC is shown in Table 4. These mass characteristics include the dead load mass of steel framing, slabs, partition walls, exterior walls, roofing, ceilings, and mechanical and electrical equipment.

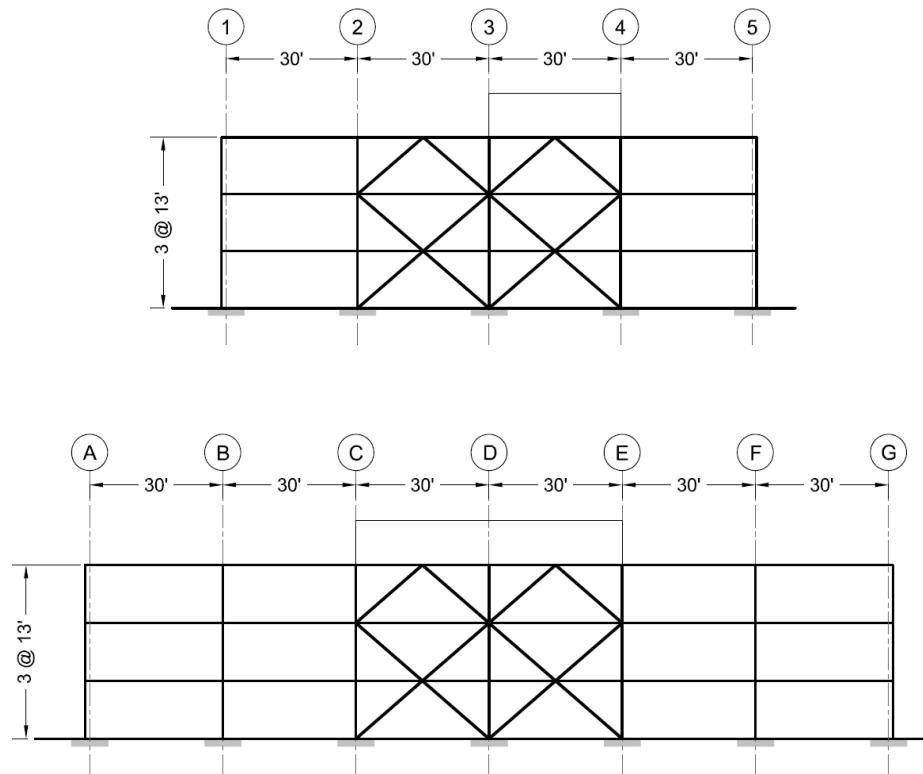


Figure 6 - Modified SAC 3-story model building elevations

Table 4 – Building Mass/Weight by Level		
Level	Seismic Mass (kip-sec²/ft)	Seismic Weight (kips)
Roof (including penthouse)	70.90	2,282
Third	65.53	2,110
Second	65.53	2,110
Total	201.96	6,502

3.4 Equivalent Lateral Force Analysis

The requirements of the *2009 International Building Code* are now used to determine the seismic loads on the SAC model building (International Code Council, 2009). The following design coefficients are determined per the *ASCE 7-05 Design Loads for Buildings and Other Structures* (American Society of Civil Engineers, 2005) using an assigned seismic force-resisting system of “Buckling-restrained braced frames, non-moment-resisting beam-column connections.” All specific references given are for this document.

- Occupancy Category II (Table 1-1)
- Seismic Importance Factor (I_e) = 1.0 (Table 11.5-1)
- Site Class = D - Stiff Soil (Table 20.3-1)
- Redundancy Factor (ρ) = 1.0 (Table 12.3-3)
- Response Modification Coefficient (R) = 7.0 (Table 12.2-1)
- System Overstrength Factor (Ω_o) = 2.0 (Table 12.2-1)
- Deflection Amplification Factor (C_d) = 5.5 (Table 12.2-1)

Spectral response acceleration parameters for short and 1.0 second periods for the

Maximum Considered Earthquake (MCE) ground motion with 5% of critical damping are taken from the mapped values for downtown Seattle and Los Angeles locations at the listed zip code as shown in Table 5. The US Geological Survey website is used to obtain accurate values of these spectral accelerations. The values represent an earthquake with an approximately 2500-year return period, or 2% probability of exceedance in 50 years, or the largest deterministic earthquake that can be generated by known seismic forces, as is the case in coastal California. Design Spectral Acceleration (S_{DS} , S_{D1}) values represent 2/3 of the soil modified MCE acceleration values and are recognized as a lower-bound margin of safety by the building code. They represent an earthquake with an approximately 475-year return period, or 10% probability of exceedance in 50 years.

Table 5 – Seismic Design Criteria									
Location	0.2 sec spect. resp. accel. (%g) S_s	1.0 sec spect. resp. accel. (%g) S_1	Long-period trans. (sec) T_L	Site coeff. F_a	Site coeff. F_v	Design spect. accel. (%g) S_{DS}	Design spect. accel. (%g) S_{D1}	SDC short period	SDC 1 sec. period
Seattle 98101	1.435	0.485	6	1.0	1.6	0.957	0.517	D	D
Los Angeles 90013	2.149	0.721	8	1.0	1.5	1.43	0.721	D	D
Reference (ASCE 7-05)	Figure 22-3	Figure 22-4	Figure 22-16	Table 11.4-1	Table 11.4-2	Eqn. 11.4-3	Eqn. 11.4-4	Table 11.6-1	Table 11.6-2

The equivalent lateral force procedure is used to determine the seismic base shear and vertical distribution of the seismic forces to the individual stories. The directions of application of the seismic forces are based on the orthogonal combination procedure of *ASCE 7-05*. An accidental eccentricity of 5% for each loading direction is included in the

analysis which gives a horizontal offset between the geometric and mass centroid of 6 and 9 feet for the north-south and east-west loading directions, respectively. For determination of seismic loads for use in sizing of the core and restrainer members, the approximate fundamental period of the SAC building is calculated by the procedure of the *ASCE 7-05* rather than employing a more rigorous dynamic analysis. The seismic base shear information is summarized in Table 6 for both Seattle and Los Angeles.

Table 6 – Seismic Base Shear Calculation			
Location	Approx. fundamental period (sec) T_a	Seismic response coeff. C_s	Seismic base shear (kips) V_b
Seattle	0.312	0.137	891
Los Angeles	0.312	0.204	1,326
Reference (ASCE 7-05)	Eqn. 12.8-7	Eqn. 12.8-2	Eqn. 12.8-1

A linear vertical distribution of horizontal lateral forces as calculated by Equation 22 with “k” equal to one for structures having a period of 0.5 seconds or less is used to determine the effective seismic forces at each level. This is summarized in Table 7 for both the Seattle and Los Angeles locations. Appropriate references in the *ASCE 7-05* are given. Each of the story forces in both the north-south and east-west directions are distributed into the BRBFs on each side of the building by using a rigid diaphragm assumption. The resultant lateral seismic forces for the maximum frame loading condition in either orthogonal direction are given in Figure 7 for both locations.

$$C_{vx} = \frac{w_x h_x^k}{\sum_{i=1}^n w_i h_i^k} \quad (22)$$

A single 3-story braced frame is then analyzed in order to determine the brace forces. All beam to column and column bases are considered as released in order to achieve full vertical pinned truss behavior. The elastic analysis of the frames assumes equal tension and compression stiffness of the BRBs in the distribution of axial force. This equal distribution is not the true behavior of BRBF systems. In reality, an unbalanced tension and compression force will occur. This unbalance has been reported in the literature as 10% higher brace axial strength in compression than in tension (Sabelli, Mahin, & Chang, 2003). This unbalanced brace force at the beam's mid-span needs to be figured into the beam design calculations similar to as required for special concentrically braced frames (SCBF). The final seismic brace axial forces at the strength design level for the two locations are shown in Figure 8. Floor dead and live loads carried by the beams are not included in the brace axial loads as it is common practice to design the floor beams to span the full bay length.

Table 7 – Lateral Seismic Force Calculation					
Level	Effective seismic weight (kips) w_x	Story height (ft) h_x	Vertical dist. factor C_{vx}	Seattle lateral seismic force (kips) F_x	Los Angeles lateral seismic force (kips) F_x
Roof	2,282	13	0.520	463	690
Third	2,110	13	0.320	285	424
Second	2,110	13	0.160	143	212
Reference (ASCE 7-05)	12.8.3	12.8.3	Eqn. 12.8-12	Eqn. 12.8-11	Eqn. 12.8-11

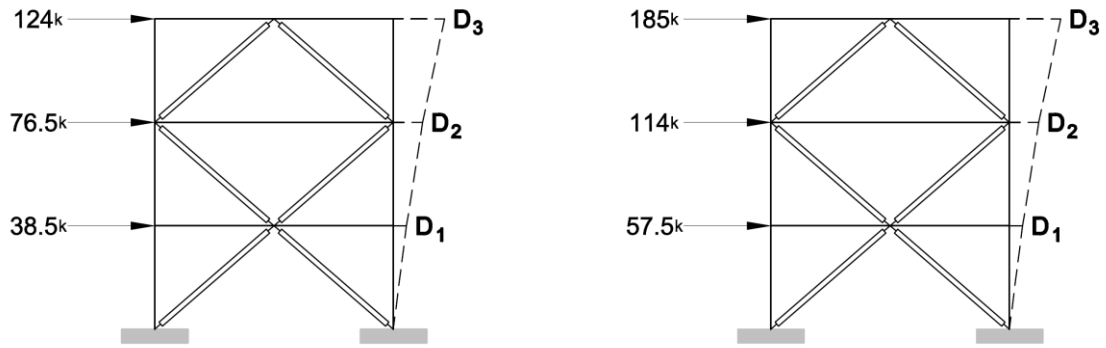


Figure 7 - BRBF lateral seismic forces by story, Seattle (left) and Los Angeles (right)



Figure 8 - Brace seismic axial forces (P_u), Seattle (left) and Los Angeles (right)

3.5 Final Frame and Brace Geometry

Finally, approximate BRBF beam, column, and gusset plate geometry is established to determine the actual length of the BRB as it would be installed in a realistic frame. The sizes of beams (W21x111) and columns (W14x176) are taken from a literature report on large-scale testing of BRBFs (Fahnestock, Ricles, & Sause, 2007) and used only as a guideline for member depths that ultimately establish the length of the brace. Length of the reduced core section is determined by the following analysis. This approximate method relates brace geometry to total axial strain and story drift.

Neglecting elastic axial deformation of the much stiffer beams and columns, the elastic story drift (D_{ie}) for a BRBF normalized by the story height (h_i) can be related to

brace axial deformation and the brace's inclination to the horizontal (θ) by Equation 23a where γ is the ratio of L_c/L_b and η is the ratio of A_1/A_3 . A_1 and A_3 are the section area at the reduced and unreduced section of the core, respectively (Tremblay, Bolduc, Neville, & DeVall, 2006). By solving this equation for γ to be used in calculating the required reduced core length, Equation 23b is given.

$$\frac{D_{ie}}{h_i} = \frac{\phi F_y}{E_c} \left[\frac{\gamma + \eta(1 - \gamma)}{\sin\theta \cos\theta} \right] \quad (23a)$$

$$\gamma = (1 - \eta)^{-1} \left[\frac{D_{ie} E_c \sin\theta \cos\theta}{\phi F_y h_i} - \eta \right] \quad (23b)$$

The maximum inelastic story drift ratio (D_i/h_i) for a regular building given by the building code is 2.5% (American Society of Civil Engineers, 2005). Inelastic drift is empirically converted to elastic story drift ratio for a given level “i” by using Equation 24 where C_d and I_e have previously been defined in the equivalent lateral force analysis.

$$\frac{D_{ie}}{h_i} = \frac{D_i/h_i}{C_d/I_e} = \frac{0.025}{5.5/1.0} \quad (24)$$

Using this equation to determine D_{ie}/h_i as 0.45% and using a brace angle of 40 degrees, resistance factor of 0.9, Young's modulus of 10,100 ksi, yield stress of 35 ksi, and a η ratio of 0.5 (this was taken as a reasonable value at this point), a value of 0.48 for γ is calculated using Equation 23b. For a brace end to end length of 190 inches, this gives an approximately 91 inch long reduced core length that is rounded up to an even 8 feet (96 inches) for the purposes of this project.

The average elastic strain at the reduced core section (ϵ_{ce}) is then calculated by subtracting the elastic axial deformation expected in the full core section at the nominal

design load from the total axial deformation of the brace at the maximum elastic story drift ratio and then dividing by the reduced section length. These are given as the second and first terms, respectively, in the numerator as shown in Equation 25.

$$\varepsilon_{ce} = \frac{D_{ie} \cos \theta - \left[\frac{\eta \phi F_y (L_b - L_c)}{E_c} \right]}{L_c} \quad (25)$$

Using this equation, the value of ε_{ce} is calculated as 0.0042 in/in for the BRBF shown. Elastic axial strain is then multiplied by the deflection amplification factor to arrive at an average inelastic strain at the core reduced section (ε_c) of 0.023 in/in (2.3%). This is slightly more than peak strain amplitudes of 0.01 – 0.02 reported in the literature for larger reduced core lengths and just below the 0.03 – 0.05 range reported for short core lengths (Tremblay, Bolduc, Neville, & DeVall, 2006). Ultimately, adjustment of the reduced section length can accommodate any target story drift desired by the designer.

The appropriate selection of reduced section length should consider the following. For aluminum alloys the core inelastic strain should be kept in the range of approximately 1%-2.5% in order to reduce the potential for premature fatigue failure. Minimum length subjected to plastic straining should be 2-3 feet, to allow for a sufficient length of prismatic core not subject to plane strain boundary conditions. The maximum value for L_c is limited by the requirement for the bolted connection to the gusset plates as well as a sufficient overlap length of the restrainer to an unreduced core section. Practically, this maximum value should be taken as 50% of the full brace end to end length.

Figure 9 shows the work-point to work-point (L_w), end to end (L_b), and reduced core (L_c) dimensions for the BRB at the typical level. These brace lengths are used throughout the development of the ULWBRB for calculations regarding unbraced length.

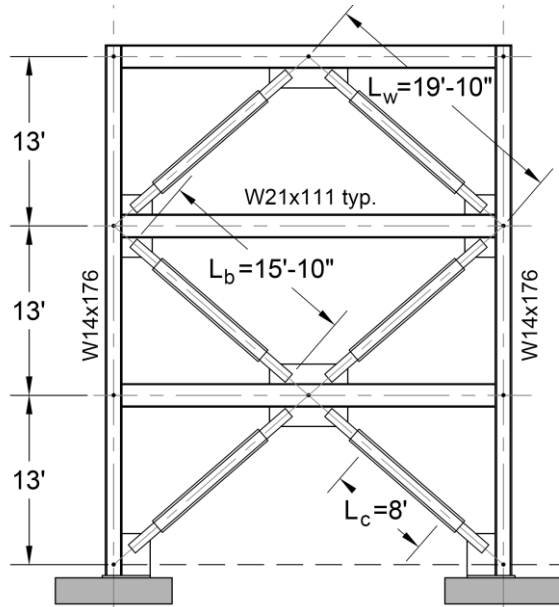


Figure 9 - BRBF and BRB geometry

4.0 BRACE CONFIGURATION

4.1 Objective

Configuration of the aluminum core section and FRP restrainer are developed using the required strength of the full-scale brace located in the more severe Los Angeles model building. Criteria for selection of the core members are first presented and used to establish the full-scale core section properties. Calculations are performed on the unrestrained core section limit states per the Load and Resistance Factor Design (LRFD) specification of the *Aluminum Design Manual* in order to highlight the weaknesses of the unrestrained core. Next, to account for the interaction of the core and restrainer, mechanical models are developed from elementary buckling models including single degree-of-freedom and the Euler column. This requires an understanding of the relative contribution of the core and restrainer on precluding global buckling. These models provide a simple design methodology for analytical design of the restrainer tubes. Lastly, FRP material properties are established and used to develop an analytical shear flow model to design the FRP wrap. At this point, it is possible to complete the analytical design of the restrainer for any core configuration. This section concludes with the presentation of the final ULWBRB configuration and a comparison of BRB weights.

4.2 Core Concepts

To begin the process of selecting core concepts for further analytical exploration, the following criteria are established in order to satisfy lessons learned by previous researchers.

1. Make use of readily available extruded aluminum shapes that are commonly stocked by mill warehouses. Many of these sections are listed in the *Aluminum Design Guide, Part IV: Section Properties*.
2. The sections should be available in the commonly used structural aluminum specification 6061-T6.
3. The core should be doubly symmetrical in cross section.
4. No welding at any point along the core should be required.
5. Since the FRP restrainer elements are comprised of wrapped pultruded FRP tubes, the aluminum core section should also have non-tapered outstands that allow a tight fit without gaps or required shimming.
6. All core element outstands should be restrained with an FRP tube or plastic spacer on both sides to prevent severe rippling.
7. Sufficient space should be provided at the tip of all core element outstands in order to allow for Poisson expansion during compression cycles.
8. The core configuration should allow varying sizes of FRP tubes since the exact required size of the restrainer has not yet been determined.
9. The unrestrained portion of the core shall be sufficiently robust and stiffened to prevent torsional or local buckling.
10. The core section area should be sufficient to carry the strength-level seismic loads as calculated for the model building. The available tensile strength based on specified yield stress shall not exceed the required strength by more than 10 percent to ensure yielding occurs during the design earthquake.

Four back-to-back equal leg angles and two back-to-back T-sections cut from I-beams are selected and meet the above criteria. The core sections are shown in Figure 10 along with their calculated section properties for individual angles. Properties for the torsional and flexural-torsional buckling limit states have been provided according to the following method. St. Venant's torsional constant (J) for a section composed of thin rectangles may be approximated as the sum of the values for the individual components neglecting the fillet regions as given in Equation 26 where b is the width dimension and t is the thickness dimension of the individual rectangular elements. This equation is used on both section shapes.

$$J = \sum \frac{1}{3} \left(b - \frac{t}{2} \right) t^3 \quad (26)$$

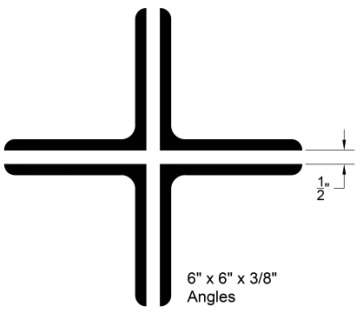
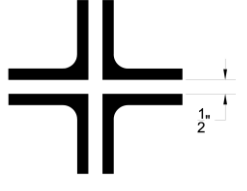
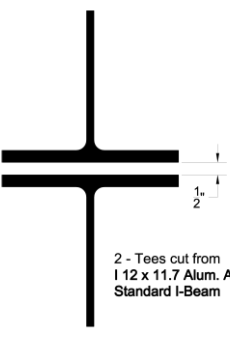
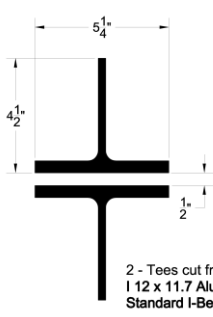
The torsional warping constant (C_w) may be calculated for four back-to-back angles acting compositely as given in Equation 27 where b is the outstand width, t is the outstand thickness, and g is the gap between back to back legs (Murtha-Smith & Adibjahromi, 1988).

$$C_w = \frac{8t}{3} \left(\frac{g+t}{2} \right)^2 \left(b - \frac{t}{2} \right)^3 \quad (27)$$

It may similarly be calculated for single angle and tee sections by Equations 28 and 29, respectively. For the tee section, b_f and t_f are the width and thickness of the flange and b_w and t_w are the width and thickness of the web, respectively.

$$C_w = \frac{t^3}{18} \left(b - \frac{t}{2} \right)^3 \quad (28)$$

$$C_w = \frac{1}{36} \left(\frac{b_f^3 t_f^3}{4} + \left(b_w - \frac{t_w}{2} \right)^3 t_w^3 \right) \quad (29)$$

Figure 10 - Full-scale Core Section Properties			
Full-Section		Reduced-Section	
 <p>6" x 6" x 3/8" Angles</p>	<p>Per Angle: $A_3 = 4.35 \text{ in}^2$ $b_o = 4.13 \text{ in}$ $t_o = 0.375 \text{ in}$ $I_z = 6.07 \text{ in}^4$ $r_z = 1.18 \text{ in}$ $J = 0.204 \text{ in}^4$ $C_w = 0.575 \text{ in}^6$</p>	 <p>2 3/4" x 2 3/4" x 3/8" Angles</p>	<p>Per Angle: $A_1 = 1.98 \text{ in}^2$ $b_o = 1.88 \text{ in}$ $t_o = 0.375 \text{ in}$ $I_z = 0.725 \text{ in}^4$ $r_z = 0.605 \text{ in}$ $J = 0.090 \text{ in}^4$ $C_w = 0.0492 \text{ in}^6$</p>
 <p>2 - Tees cut from I 12 x 11.7 Alum. Assoc. Standard I-Beam</p>	<p>Per Tee: $A_3 = 4.96 \text{ in}^2$ $b_o = 5.13 \text{ in}$ $t_o = 0.290 \text{ in}$ $I_x = 13.9 \text{ in}^4$ $I_y = 13.5 \text{ in}^4$ $r_x = 1.67 \text{ in}$ $r_y = 1.65 \text{ in}$ $J = 0.289 \text{ in}^4$ $C_w = 0.377 \text{ in}^6$</p>	 <p>2 - Tees cut from I 12 x 11.7 Alum. Assoc. Standard I-Beam</p>	<p>Per Tee: $A_1 = 3.71 \text{ in}^2$ $b_o = 3.63 \text{ in}$ $t_o = 0.290 \text{ in}$ $I_x = 5.66 \text{ in}^4$ $I_y = 5.68 \text{ in}^4$ $r_x = 1.24 \text{ in}$ $r_y = 1.24 \text{ in}$ $J = 0.216 \text{ in}^4$ $C_w = 0.157 \text{ in}^6$</p>

Calculations are performed for the following limit states in order to examine the available axial strength of the unrestrained reduced-section of the core for both configurations. These limit states include: tension gross section yielding (ϕT_{L1}), tension net section fracture (ϕT_{L2}), compression global elastic buckling (ϕP_{L3}), compression torsional buckling (ϕP_{L4}), compression flexural-torsional buckling (ϕP_{L5}), and compression component local buckling (ϕP_{L6}). A summary of these values for the two core configurations are given in Table 8 for pinned supports ($K = 1$). All values are calculated for a single angle or tee and multiplied by the number of elements to give a total value. Effective length (KL_c/r) and largest controlling outstand width to thickness ratio (b_o/t_o) are also included as they are implicit in the preceding calculations. The

appropriate references for these calculations are given for the *Aluminum Design Manual LRFD Specification* (Aluminum Association, 2000) and can be found in Appendix C.

Table 8 – Full-scale Available Strength of Unrestrained Core			
Parameter	Four Angles	Two Tees	Reference (Aluminum Association, 2000)
L_c (in)	96	96	-
KL_c/r	159	77.6	-
b_o/t_o	5.0	12.5	-
ϕT_{L1} (kips)	263	247	Eq. 3.4.1-1
ϕT_{L2} (kips)	256	240	Eq. 3.4.1-2
ϕP_{L3} (kips)	30	96	Eq. 3.4.7-4
ϕP_{L4} (kips)	218*	206	Eq. 3.4.7-4
ϕP_{L5} (kips)	29*	81	Eq. 3.4.7-4
ϕP_{L6} (kips)	251	163	Eq. 3.4.8-3
* Indicates rational analysis used for nonsymmetrical sections.			

The inclusion of compression limit state values begins to examine the amount of demand on the buckling restraint system for different failure modes. The susceptibility of the core member to global or local outstand buckling can be seen by the indication of lower available strength for these failure modes. Although, increased susceptibility to a given failure mode does not directly indicate increased force demand on the restraining member as the force exerted by core member is reduced with less stiff profiles. This can be rationalized by treating the restraining force required to prevent the buckling of the core member as equal and opposite to the buckling force itself. A diagram of this global force interaction is given in Figure 11. Global demand on the restrainer should be

quantified analytically in order to allow preliminary design of the FRP tubes and wrap.

4.3 Restrained Brace Mechanical Models

In order to develop a crude analytical method for preliminary sizing of the restrainer to prevent global buckling, a simple mechanical model is created for each of the buckling modes likely to be present in the four-angle core configuration. It is recognized that transverse displacement of the slender core member produces a transverse bending effect on the restrainer through application of a load with an unknown distribution function $w(x)$ as shown in Figure 11. This flexure causes the restrainer tubes to act much like a simple span beam when buckling initiates during the compressive portion of the cyclic load. Flexural stiffness of the restrainer serves to prohibit the core transverse displacement from reaching the point of instability which would eventually lead to plastic hinging in the core member and subsequent large transverse displacement.

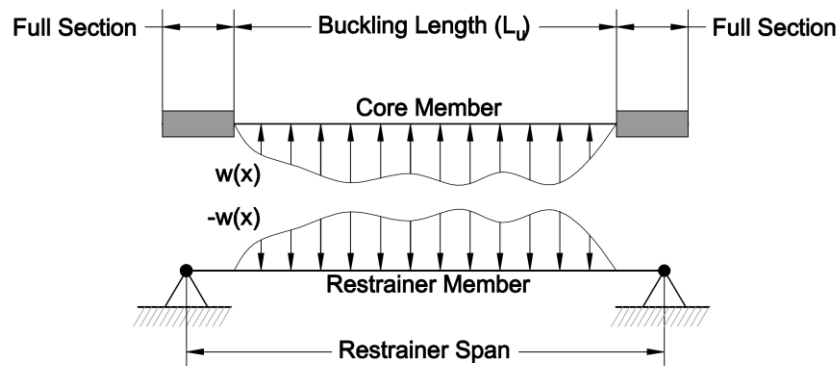


Figure 11 - Unknown force interaction between core and restrainer

Figure 12 shows the brace core and restrainer dimensions for the purpose of establishing the simple span restrainer beam analogy. Given the rigidity of the bolted connection to the gusset plate and the greater stiffness of the core full section as compared to the reduced section, the overlap length (L_o) can be used as the simple span

support of the restrainer. The full section will exhibit a much higher stiffness than the reduced section due to its higher moment of inertia, greater cross-sectional area, and ability to maintain material stresses well within the elastic range as the reduced section undergoes plasticity. Ability of the full section to cantilever from a rigid bolted gusset plate connection is the assumption that allows the pinned end support to be used in the simple span analogy.

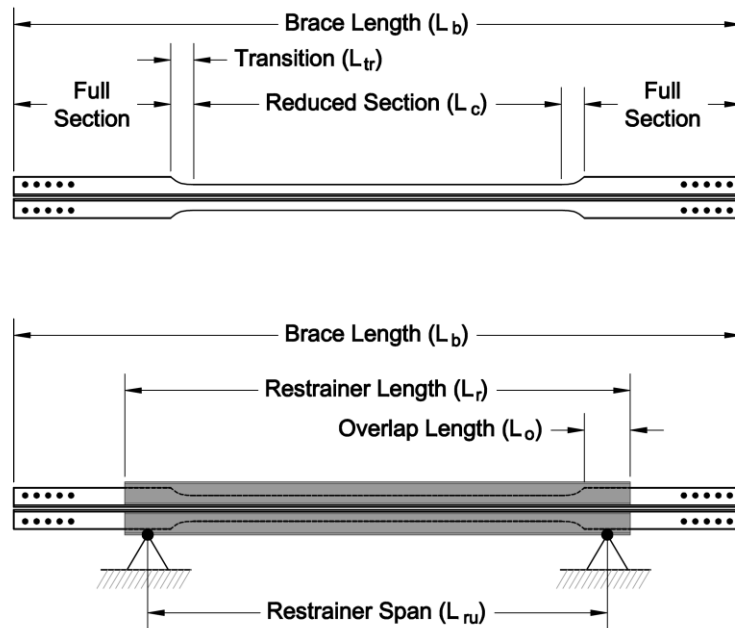


Figure 12 - Brace dimensions, unrestrained core (top) restrained core (bottom)

Typically, global elastic buckling load for deformable long slender columns is determined with a classical Euler method which assumes that the column is perfectly straight, no load eccentricity exists, plane cross-sections remain plane after deformation, transverse shear deformation is ignored, the material obeys Hooke's Law, and the displacement of the member is small. Internal moment at any position along the length is given as the curvature (second derivative of the sine wave lateral displacement equation) multiplied by the elastic stiffness of the core member $E_c I_c$ as shown in Equation 30. The

assumed lateral displacement equations at buckling for pinned-pinned columns and fixed-fixed columns are given in Equations 31 and 32, respectively, where x is the position along the column's length, δ is the maximum displacement at mid-length, L_u is the buckling length, M_{FEM} is the column fixed end moment, M_{int} is the internal moment at the cut, and P is the axial load. A well-known diagram of this Euler column is shown in Figure 13 for the pinned-pinned end condition.

$$M_{int} = -E_c I_c y'' \quad (30)$$

$$y(x) = \delta \sin\left(\frac{\pi x}{L_u}\right) \quad (31)$$

$$y(x) = \frac{M_{FEM}}{P} \left(1 - \cos\frac{2\pi x}{L_u}\right) \quad (32)$$

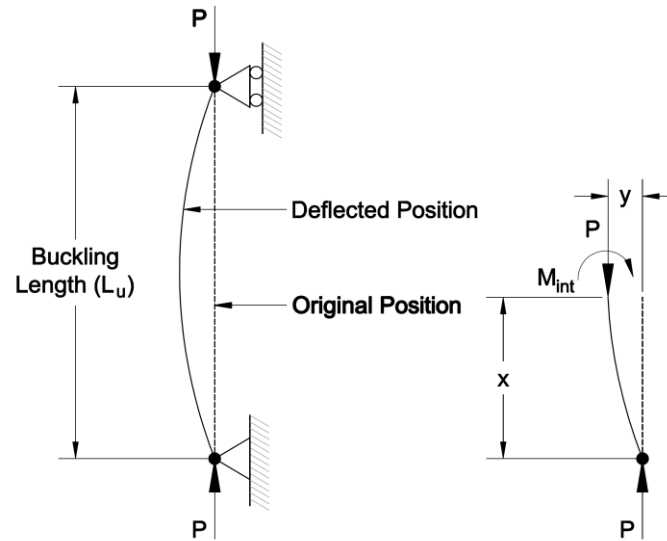


Figure 13 - Diagram of force and moment equilibrium for development of the differential equation

Single Degree-of-Freedom Model

In the following discussion, it is shown that a simple mechanical model neglecting the core's internal moment and converting the distributed core-restrainer force

interaction into a single point load applied at the mid-span of the restrainer may effectively simulate the behavior of the brace at the onset of buckling. This model also assumes that the system is energy conservative and accounts for core member geometric imperfections caused by member initial out-of-straightness and eccentricity of the applied load. The simplest model that can be used is a single degree-of-freedom (SDOF) system consisting of two undeformable truss members connected with frictionless hinges and supported by a linear spring at the center hinge as shown in Figure 14. This linear spring is responsible for providing buckling restraint and is analogous to the flexural stiffness provided by the BRB restrainer beam that remains elastic. The classical bifurcation method may be used to determine the critical load (P_{cr}) at which the system will buckle if it is given an initial deflected position (Δ_i) equal to zero (perfect column).

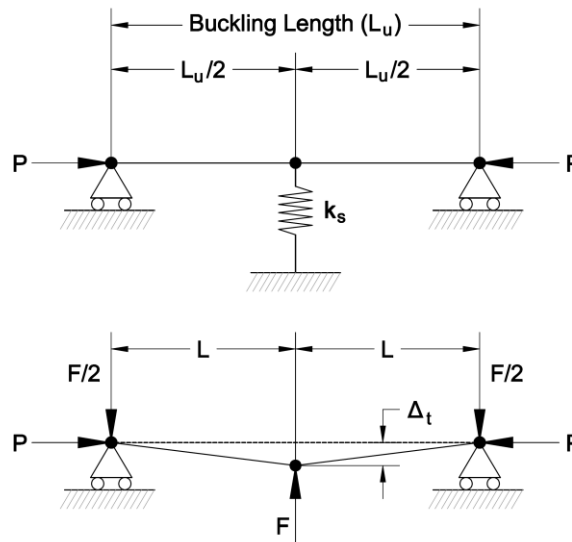


Figure 14 - Single degree-of-freedom mechanical model, undeformed (top) deformed (bottom)

It should be shown first that the internal moment in the core element may be neglected from the model in the presence of much stiffer restraining tubes thus justifying the mid-length hinge. This may be done by comparing the core's internal moment at the

mid-length of the fully elastic Euler column with the equivalent resisting moment provided by the restrainer force F at a given deflection Δ_t . Substituting $L_u/2$ for x in Equation 31, differentiating twice, and substituting Equation 31 into 30 gives the internal moment in the elastic column (M_{int}^e) at mid-length for the pinned-pinned condition as shown in Equation 33a.

Since the premise of the BRB is to undergo plastic straining at high axial loads, material non-linearity must also be considered. Axial stress beyond the proportional limit causes a progressive decrease in the elastic bending stiffness $E_c I_c$. Furthermore, if significant transverse displacements are present, the interaction of axial plus flexural stresses across the cross-section require a nonlinear bending analysis. (This will be examined shortly.) A simplified adjustment of the solution for M_{int}^e to account for material non-linearity can be made by referencing rational modifications made to the elastic buckling equation in derivation of the inelastic tangent modulus formula (Brush & Almroth, 1975). The modified formula for M_{int}^p is shown in Equation 33b where E_c is replaced with E_{ct} which represents the local slope of the stress-strain curve in the inelastic range. Since the value for E_{ct} is taken at a specific locality along the curve, the value changes incrementally along with stress. For the purposes of this study, the sharp transition from elastic to plastic behavior that is common in most structural alumina will be utilized by assigning a constant E_{ct} equal to 5% post-yield hardening in lieu of an incremental approach. (This property of aluminum will be shown later in the Coupon Testing section.)

$$M_{int}^e \left(\frac{L_u}{2} \right) = \frac{\pi^2 \Delta_t}{L_u^2} E_c I_c \quad (33a)$$

$$M_{int}^p \left(\frac{L_u}{2} \right) = \frac{\pi^2 \Delta_t}{L_u^2} E_{ct} I_c \quad (33b)$$

The equivalent resisting moment (M_{res}) provided by the restrainer is then calculated using moment equilibrium on the column's half-length without axial load as shown in Figure 15. Restrainer force F is calculated by applying a known displacement Δ_t to the mid-length of the restrainer modeled as a simple span beam as shown in Equation 34 where L_{ru} , E_r and I_r are the span length, Young's modulus, and moment of inertia of the restrainer assembly, respectively.

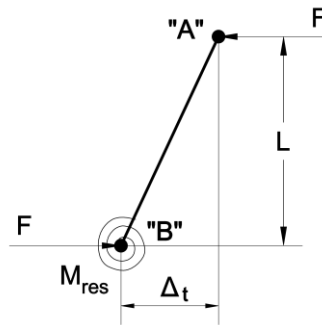


Figure 15 - Exaggerated free body diagram of column half-length

$$F = \frac{48E_r I_r \Delta_t}{L_{ru}^3} \quad (34)$$

Span length (L_{ru}) of the restraining tube assembly can be estimated by adding the length of the reduced core (L_c), transitions (L_{tr}), and one-half the overlap (L_o) for each end as shown in Equation 35. The amount of expected axial inelastic deformation of the core should be considered when determining the overlap length as repeated tension and compression excursions should not compromise the overlap. Expected strain values, previously given on page 69, result in 2 inches of elongation at each end of the core. At this early stage, the overlap length will be taken as a minimum of 12 inches.

$$L_{ru} = L_c + 2L_{tr} + L_o \quad (35)$$

Then M_{res} may be calculated by summing moments about joint “A” to give Equation 36.

$$M_{res} = FL \quad (36)$$

Using Pythagorean’s theorem, L may be calculated for a large transverse displacement (Δ_t). This value for L and F may then be substituted into Equation 36 to give the equivalent resisting moment in terms of restrainer stiffness $E_r I_r$, total transverse displacement Δ_t , core unbraced length L_u , and restrainer span length L_{ru} as shown in Equation 37.

$$M_{res} = \frac{48E_r I_r \Delta_t}{L_{ru}^3} \sqrt{\left(\frac{L_u}{2}\right)^2 - \Delta_t^2} \quad (37)$$

In order to examine the relative contributions of M_{int} and M_{res} to the equilibrium of the system, further assumptions are made. First, a realistic ratio of restrainer stiffness to elastic core stiffness is established. A $E_r I_r / E_c I_c$ ratio of 4.54 and a $E_r I_r / E_{ct} I_c$ ratio of 90.8, considering the 5% post-yield hardening, is used for this exercise. These values are governed primarily by brace geometry and material modulus as will be explained in subsequent sections. Second, a limiting value for transverse displacement of the core and restrainer is determined that considers the maximum flexural stress on the restrainer tubes at a given displacement. Section modulus of the restraining tubes (S_r) is defined in Equation 38 where c is the distance from the neutral axis to the extreme fiber.

$$S_r = \frac{I_r}{c} \quad (38)$$

Section modulus is related to allowable restrainer bending stress (f_b) through the relationship shown in Equation 39 where M_r is the moment at the mid-span of the restrainer.

$$f_b = \frac{M_r}{S_r} \quad (39)$$

The moment at the mid-span of the restrainer is calculated as shown in Equation 40. By solving for M_r in Equation 39 and substituting this and Equation 38 into Equation 40, the relationship between transverse load (F) and allowable restrainer bending stress (f_b) is discovered for a given length and moment of inertia of the restrainer in Equation 41.

$$M_r = \frac{FL_{ru}}{4} \quad (40)$$

$$F = \frac{4f_b I_r}{cL_{ru}} \quad (41)$$

Equation 41 is then substituted into Equation 34 and after cancelling like terms Equation 42 is given that shows maximum transverse displacement for a given allowable restrainer bending stress, restrainer span length, distance from the neutral axis to the extreme fiber, and restrainer Young's modulus.

$$\Delta_t = \frac{4f_b L_{ru}^2}{48cE_r} \quad (42)$$

A plot of core internal moment and equivalent restrainer moment versus core unbraced length at the maximum transverse displacement is shown in Figure 16 for both the M_{int}^e and M_{int}^p cases. Allowable bending stress of the pultruded FRP tubes is taken as one-half the ultimate bending stress. This gives a constant value of $f_b = 15$ ksi. The modulus of elasticity for the pultruded sections is taken as 2,800 ksi. (Tables showing typical FRP material properties are given in the following section.) For simplicity, the distance “ c ” is approximated as 5 inches. The same constants for f_b , E_r , and c are used in all plots. Figure 17 shows a normalized plot of M_{res}/M_{int} versus core unbraced length for both the elastic column and fully plastic column. It can be seen that for reasonable values

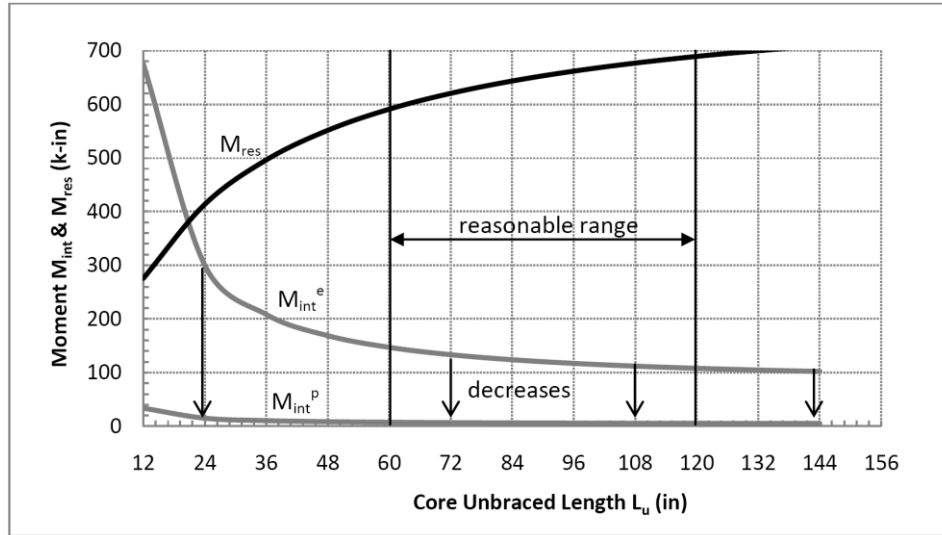


Figure 16 - Plot of core internal moment and equivalent restrainer moment versus unbraced length

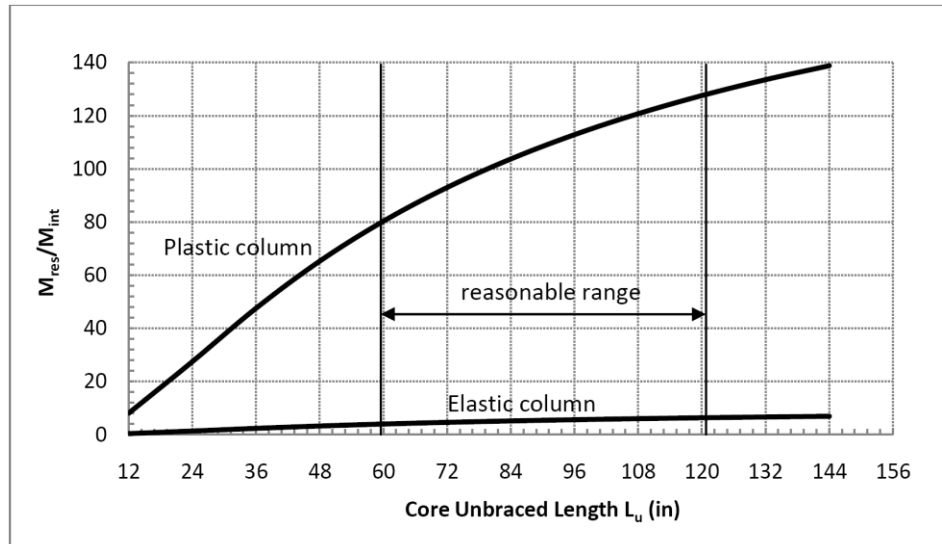


Figure 17 - Plot of ratio of equivalent restrainer moment to core internal moment versus unbraced length of core unbraced length in the 60 inch to 120 inch range, the equivalent restrainer moment is from 4 to 6.4 times the value of the internal moment in the core of the elastic column. Similarly, values of 80 to 128 are achieved for the fully plastic column. These values approach two orders of magnitude greater stiffness which correlates well with assumptions described by Black et al. (2002). Additionally, the reduction in flexural

stiffness of a steel core undergoing axial yielding has been reported to be 25-30% of the elastic value (Tremblay et al. 2006). This higher value is not applicable for aluminum since steel typically has a much higher stiffness above the proportional limit.

The point of bifurcation instability for elastic columns is defined in many textbooks as the sudden transition between the column displacing axially in the direction of the applied load, also defined as the primary path, to an alternative transverse displacement path, defined as the post-buckling path (Simitises, 1986). Because of the presence of the BRB's restrainer, the post-buckling path may not be fully realized. In perfect "ideal bars" the restrainer is not required to resist appreciable transverse load until the point of bifurcation is reached. Conversely, in imperfect "industrial bars" that exhibit load eccentricity either through non-centroidal load application or initial out-of-straightness, the bifurcation load cannot be reached. Figure 18 shows plots of load versus displacement curves for perfect and imperfect slender columns with two degrees of initial

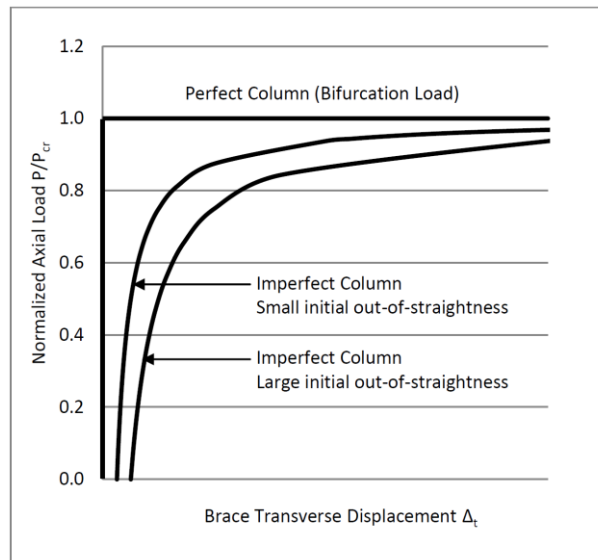


Figure 18 - Load-displacement curves for perfect and imperfect Euler columns

out-of-straightness. It can be seen that the bifurcation approach provides a critical load

only for the mathematically ideal case. This solution is commonly provided by a traditional eigenvalue analysis of the system's stiffness matrix in which the lowest eigenvalue, and associated eigenvector, represent the critical load for the system. For imperfect systems the curves run asymptotically to the critical load while never reaching it. The total transverse displacement (Δ_i) also begins immediately at initial axial load application rather than suddenly as shown by the ideal case.

Since real world BRB core members often exhibit both initial out-of-straightness and load eccentricity, they require a second-order stability analysis focusing on convergence in order to determine the required stiffness of the restrainer element. This is the geometrically non-linear portion of the analysis. The value of maximum out-of-straightness allowed by the *AISC Code of Standard Practice for Steel Buildings and Bridges* is $L/1000$ can thus be taken as a realistic starting point for analysis of the "industrial bar". It has also been presented in the literature that this represents a realistic value based on measurement of actual HSS column specimens (Shaat & Fam, 2009).

Application of the SDOF model to the actual BRB is shown in Figure 19 which assumes the reduced section of the core will act like a pinned-pinned column during the commencement of buckling and all four core angles buckle in the same direction about their principal axes. A presentation of equilibrium in Equations 43 – 45 for the free body of reduced core half-length shows the resulting lateral restraint force (F_A) for a given axial load (P), reduced core length (L_c), initial transverse displacement (Δ_i), and an additional transverse displacement due to second order load-deflection effects (Δ). The total lateral force exerted at the mid-length of the restrainer is calculated by multiplying F_A by two to account for the half-height free body used in the equilibrium equation and

again by four to account for the equal buckling of all angles in the same direction. This gives a total lateral force of $8F_A$ as shown in Figure 19.

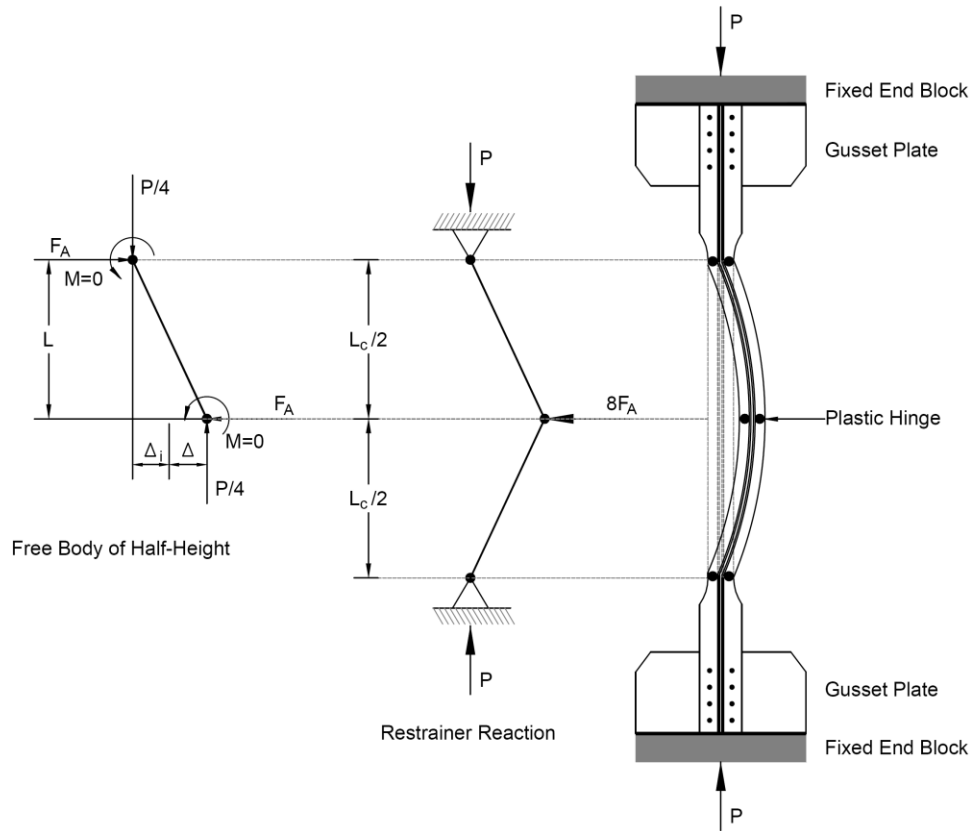


Figure 19 - Four-angle core mechanical model – pinned ends/one-way/in-plane (mode A)

In this buckling case application of the load occurs concentrically at the section's centroid. This is explained in Figure 20 which shows a section view of the gusset plate and angle bolting. Loading in this idealized buckling model does not consider in-plane bending moments created by BRBF drift during high lateral loads. End moments induced by frame deformation were addressed in the literature review and will be incorporated into the final restrainer design methodology. At this time, they are ignored for simplicity. Additionally, material nonlinearity in the core is not required to be considered since the justification of the plastic hinge has been made.

$$\sum M = 0 = -\frac{P}{4}(\Delta_i + \Delta) + F_A L \quad (43)$$

$$\text{Where } L = \sqrt{\left(\frac{L_u}{2}\right)^2 - (\Delta_i + \Delta)^2} \quad (44)$$

$$F_A = \frac{P/4(\Delta_i + \Delta)}{\sqrt{\left(L_c/2\right)^2 - (\Delta_i + \Delta)^2}} \quad (45)$$

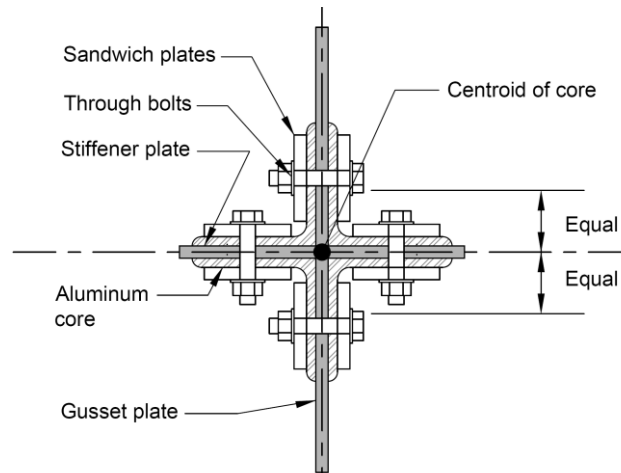


Figure 20 - Centroidal loading of four-angle core

An example convergence plot for a constant axial load of 100 kips and initial out-of-straightness, or eccentricity, of $L/1000$ is shown in Figure 21 for a reduced core length of 120 inches and restrainer span length as defined in Equation 35. Convergence must occur before the allowable transverse displacement as given in Equation 42 is reached. It can be seen that the brace reaches stable equilibrium at a transverse displacement of 1.58 inches at approximately 40 iterations of successive load-deflection ($P-\Delta$) analysis using Equation 45 when a restrainer stiffness of $280,000 \text{ k-in}^2$ was used. A second convergence study is also shown in Figure 22 where the brace is allowed to displace transversely as much as necessary to achieve equilibrium. Convergence is reached at a

transverse displacement of 4.2 inches after approximately 200 iterations using a restrainer stiffness of 272,000 k-in² which is only slightly less than the previous case. This method may not follow the assumptions of small displacement theory, so it is included only for comparison. In addition, this large transverse displacement would be beyond the stress limits of the pultruded restrainer sections.

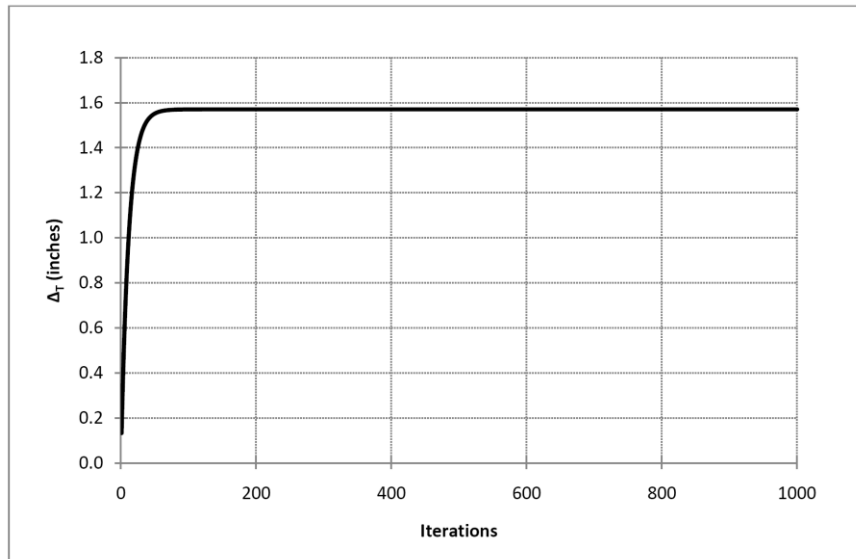


Figure 21 - Example SDOF model convergence plot with restrainer flexural stress constraint

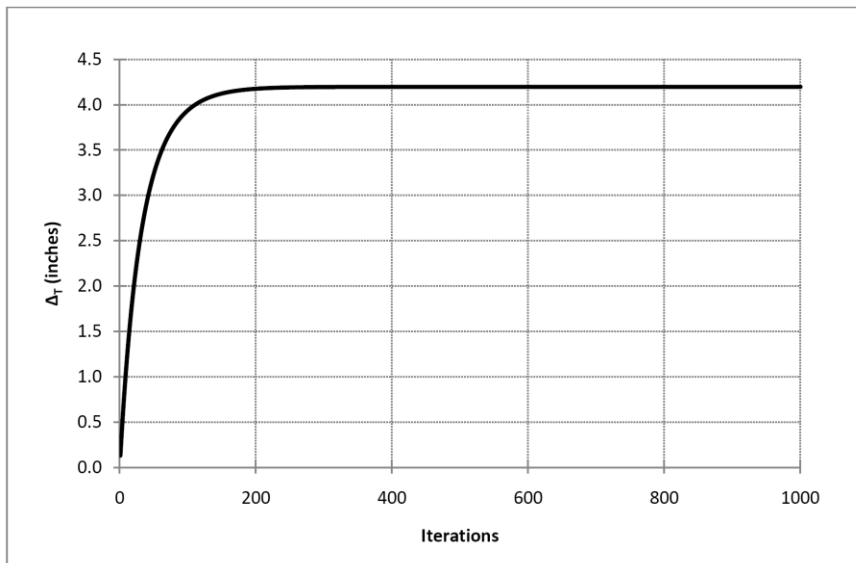


Figure 22 - Example SDOF convergence plot without restrainer flexural stress constraint

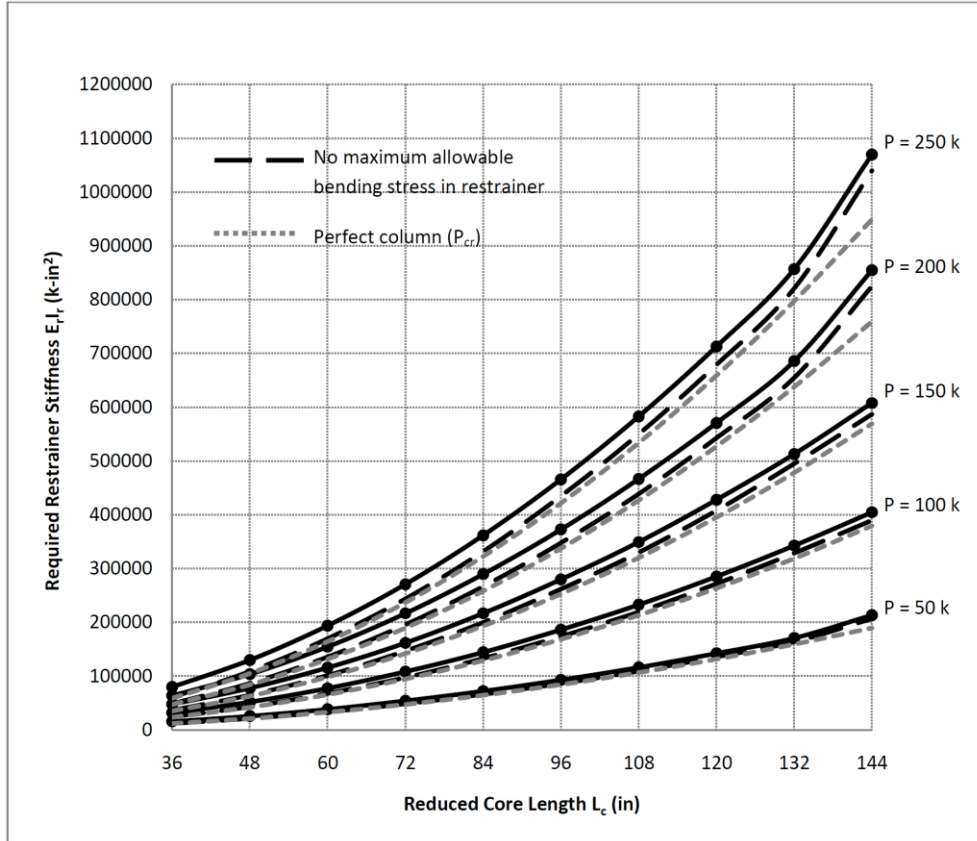


Figure 23 - BRB restrainer design plot for four-angle core configuration mode A buckling

A single convergence study is then made for several different reduced core lengths and axial loads in order to plot a single point on the design plot constructed in Figure 23. This plot can be used to select the required restrainer stiffness for a known axial load and reduced core length. The dashed lines in this plot indicate convergence irrespective of the allowable bending stress of the restrainer tubes. It can be seen that this yields slightly unconservative lower values of required restrainer stiffness.

The values of critical bifurcation load (P_{cr}) for a perfect column are also shown in Figure 23 for comparison. This critical bifurcation load is given in Equation 46 where k_s is taken as the stiffness of the simple span restrainer loaded at mid-length in kips/inch, and l is the half length of the SDOF system. This critical bifurcation load can be

determined using an eigenvalue analysis. It is clear that the design method for perfect columns yields slightly unconservative lower values for required restrainer stiffness.

$$P_{cr} = \frac{k_s l}{2} = \frac{12E_r I_r L_c}{L_{ru}^3} \quad (46)$$

Another possible SDOF buckling mode where the ends of the reduced section behave as fixed supports and all core angles buckle in the same direction is shown in Figure 24. This mode also exerts a point load at the mid-span of the restrainer albeit to a lesser effect due to the presence of the fixed end moment. The flexural plastic moment of an axially loaded member is reduced below the value of $F_y Z$ since the sum of axial forces across the section is not zero and the neutral axis shifts away from the equal area axis as shown in Figure 25. Therefore, if the reduced section of the core is considered when all four core angles act compositely by shear transfer occurring at the bolted end connections the available plastic moment of the reduced section of the core (M_p) can be calculated. The least available plastic section modulus about axes x, y, or z is used in this calculation with axes defined in Figure 26. There will always be a small amount of available plastic moment due to the resistance factor (ϕ) and unavoidable slight oversizing of the core element to meet design force (P_u) requirements. Values for M_p for each core configuration about the least bending axis are shown in Table 9 using the section properties given in Figure 10.

Table 9 – Available Plastic Moment of Reduced Section of Core							
Core Configuration	F_y (ksi)	P (kips)	A=P/F_y (in²)	d₁ (in)	d₂ (in)	Z (in³)	M_p (k-in)
Two-Tees	35	250	7.14	4.97	5.11	0.715 (Z _y)	25.0
Four-Angles	35	250	7.14	4.23	4.68	1.83 (Z _z)	63.9

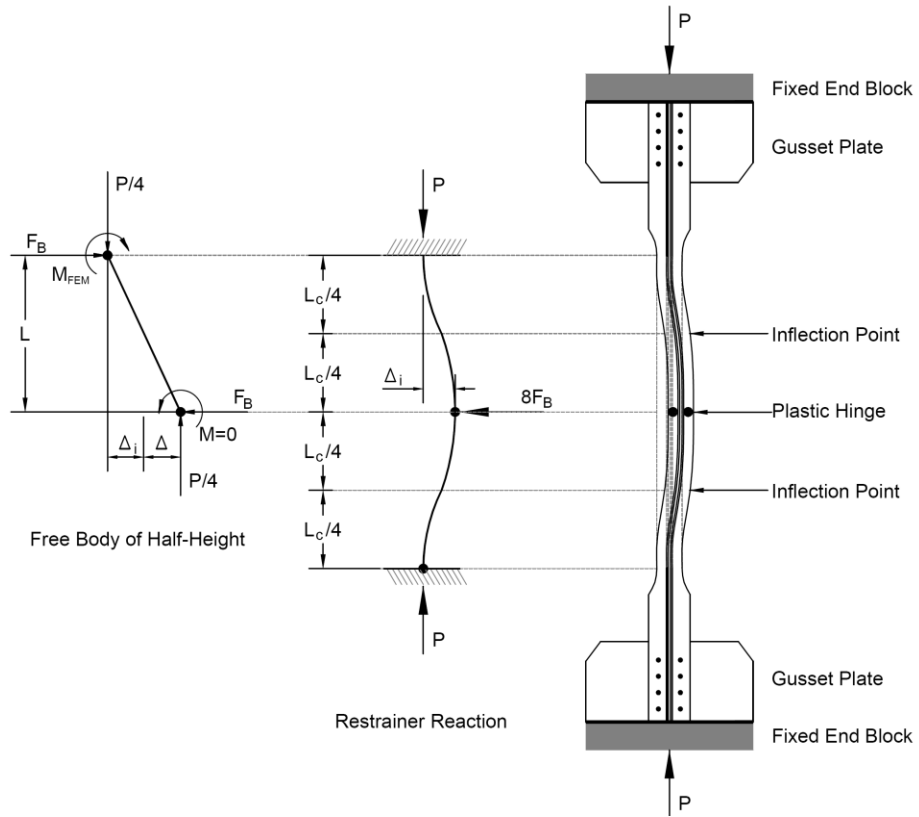


Figure 24 - Four-angle core mechanical model - fixed ends/one-way/in-plane (mode B)

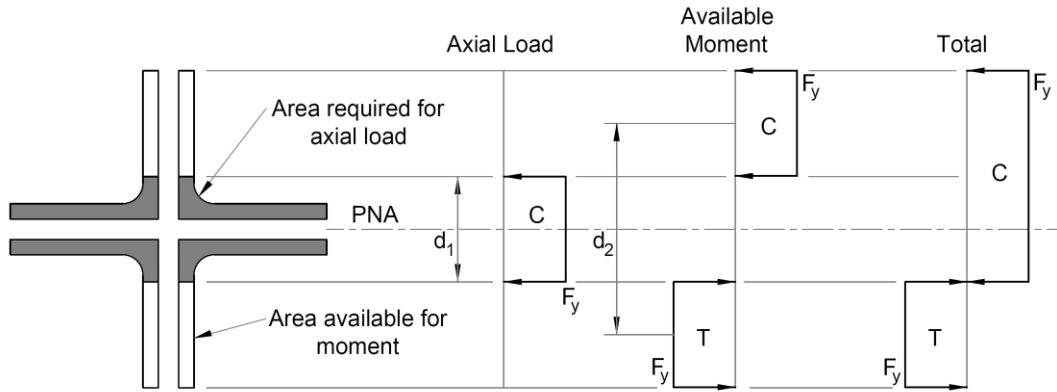


Figure 25 - Interaction of axial load and available moment for composite section

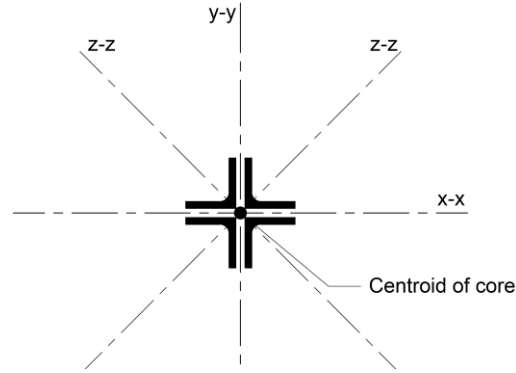


Figure 26 - Four-angle core axes definition (x-x, y-y are geometric axes, z-z are principal axes)

Moment equilibrium is used again to determine the required restrainer force on the reduced core half-length. The eccentricity is made up of the initial out-of-straightness (Δ_i) and an additional transverse displacement due to second order load-displacement effects (Δ). Equation 47 gives the lateral restraint force F_B on an individual core angle half-length for a given core length and transverse deflection. This gives a total lateral force of $8F_B$ for all four full-length angles as shown in Figure 25.

$$F_B = \frac{P/4 (\Delta_i + \Delta) - M_{FEM}}{\sqrt{\left(L_c/2\right)^2 - (\Delta_i + \Delta)^2}} \quad (47)$$

An identical convergence study approach is used to create design plots for the four-angle core configuration. A plot of required restrainer stiffness versus reduced core length is shown in Figure 27 as a dashed line for an axial design load of 250 kips. It can be seen that when high axial stress is considered, the contribution of the core end fixity is negligible as compared to the pinned case which is shown with a solid line. Since similar convergence behavior is witnessed with the same restrainer stiffness for cores with pinned or fixed ends, the minimal effect of the available end moment at high axial stress may be neglected when designing the brace restrainer.

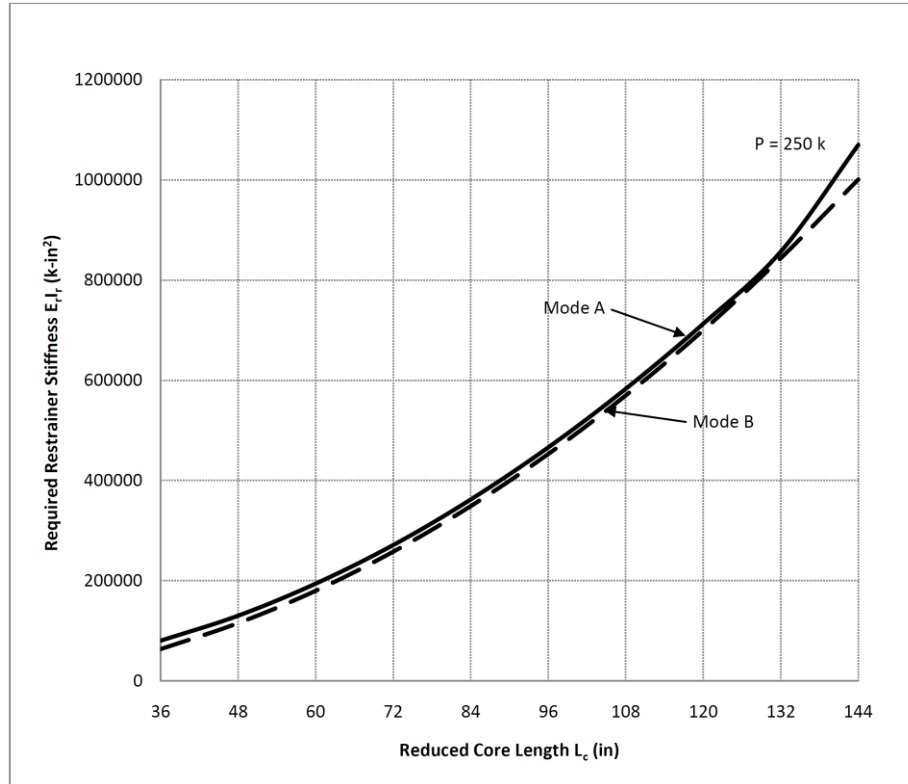


Figure 27 - BRB restrainer design plot for four-angle core configuration mode B buckling

To capture the possibility of the four-angle core members buckling outward symmetrically from one another about their principal axes, buckling mode C is developed as shown in Figure 28. This mode results in application of a hoop force on the FRP restrainer wrap and due to symmetry does not apply bending load to the restrainer as in the previous cases. Due to the relatively high stiffness of the FRP wrap in the hoop direction, as compared to the restrainer bending cases, a second order convergence study is not required to calculate the increasing transverse deflection from successive (P- Δ) iterations. Instead, an analysis of the required FRP wrap strength in the hoop direction for a given initial core out-of-straightness (Δ_i) and load eccentricity with respect to the angle's principal axis (e_z) suffices. Equation 48 gives the expected lateral restraint force (F_C) for mode C.

$$F_C = \frac{P/4 (\Delta_i + e_z)}{\sqrt{(L_c/2)^2 - (\Delta_i + e_z)^2}} \quad (48)$$

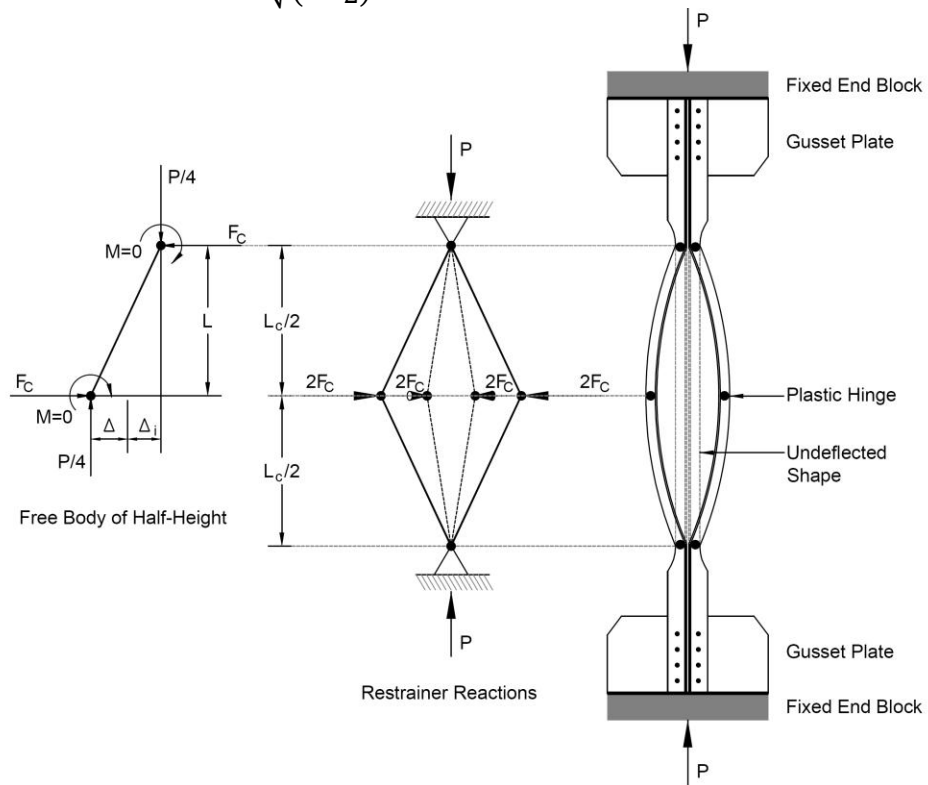


Figure 28 - Four-angle core mechanical model - pinned ends/all-ways (mode C)

Figure 29 shows the hoop force diagram for buckling mode C at a cross-section of the brace's mid-length shown in Figure 30. The hoop stress (σ_h) acting on an arbitrary length section (L_t) of the transversely oriented wrap is calculated using Equation 49.

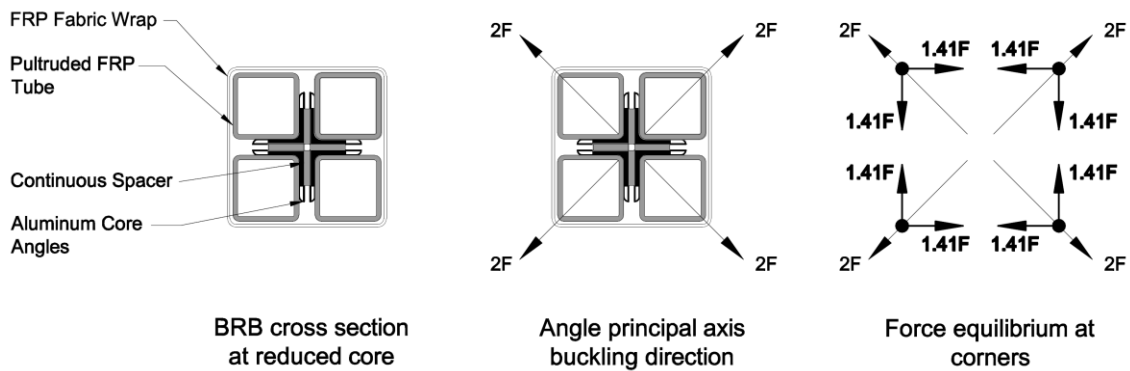


Figure 29 - Hoop force diagrams for mode C buckling

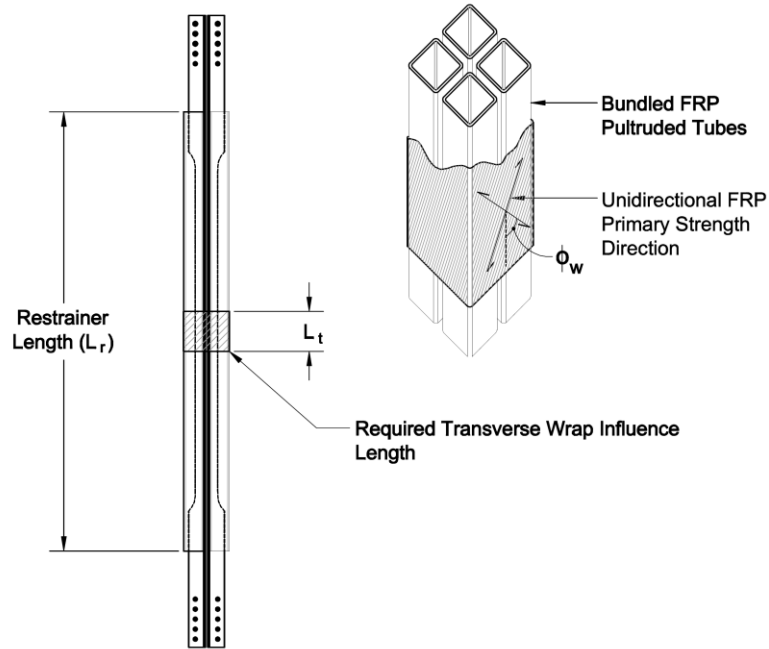


Figure 30 - Transverse FRP wrap influence area for mode C buckling

$$\sigma_h = \frac{1.41F_c}{L_t t_L} \quad (49)$$

Equation 48 can be substituted into Equation 49 to find the calculated hoop stress at a given axial load (P), total eccentricity ($\Delta_i + e_z$), influence length (L_t), and wrap laminate thickness (t_L). Influence length is only an approximation of how much of the wrap is required to prevent over-stressing. To calculate the required length of transverse FRP layers to prevent the blow-out failure mode, these equations can be solved for L_t as shown in Equation 50. Note that hoop stress has been replaced with the wrap material ultimate tensile strength in the lengthwise direction F_{wLW} at an angle ϕ_w . (The following section presents tables on different manufacturer's FRP wrap material properties.)

$$L_t = \frac{0.353P(\Delta_i + e_z)}{\sin \phi_w F_{wLW} t_L \sqrt{\left(\frac{L_c}{2}\right)^2 - (\Delta_i + e_z)^2}} \quad (50)$$

Plots of required transverse wrap influence length divided by core reduced section length (L_t/L_c) versus total eccentricity ($\Delta_1 + e_z$) for varying axial loads are shown in Figure 31. It can be seen that the required influence length is on the order of zero to 0.8% of the reduced core length for a wrap with F_{wLW} equal to 84.4 ksi placed with its primary strength axis at a 45 degree angle to the longitudinal axis of the brace, and a single laminate thickness of 0.05 inches. Therefore, required influence length is negligible with reasonably small values of load eccentricity and begins to show the small effect of this buckling mode as compared to the bending modes previously discussed.

Lastly, Figure 32 shows a mode that may occur out-of-plane to the frame and gusset. This results in a bending load application to the restrainer without the stationary pinned ends as is present in in-plane buckling modes A and B. This mode is not considered as imparting flexural forces to the restrainer because large gusset plates can, and should, be fit with transverse stiffeners to control out-of-plane buckling.

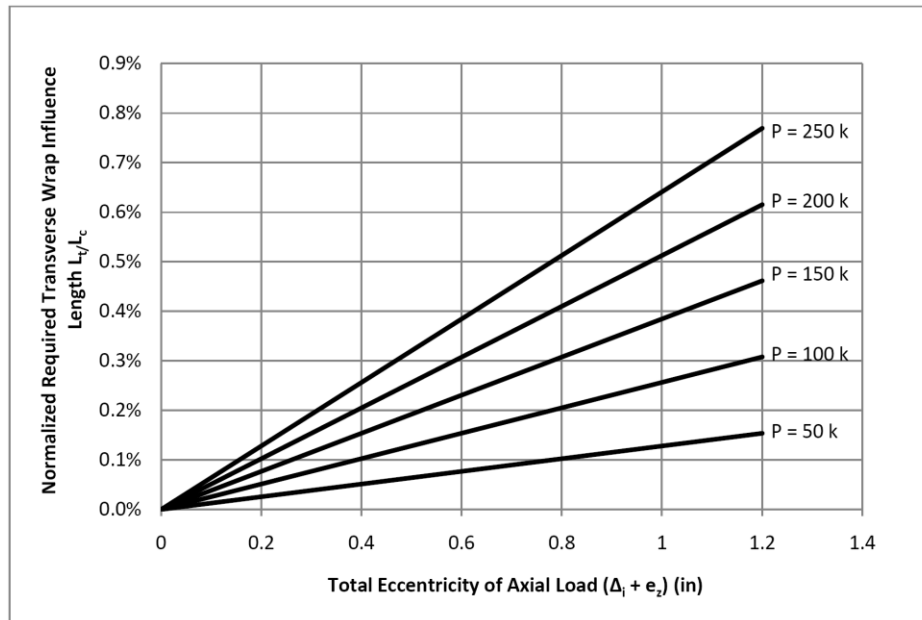


Figure 31 - Plot of normalized required transverse wrap influence length for mode C buckling ($\phi_w = 45^\circ$)

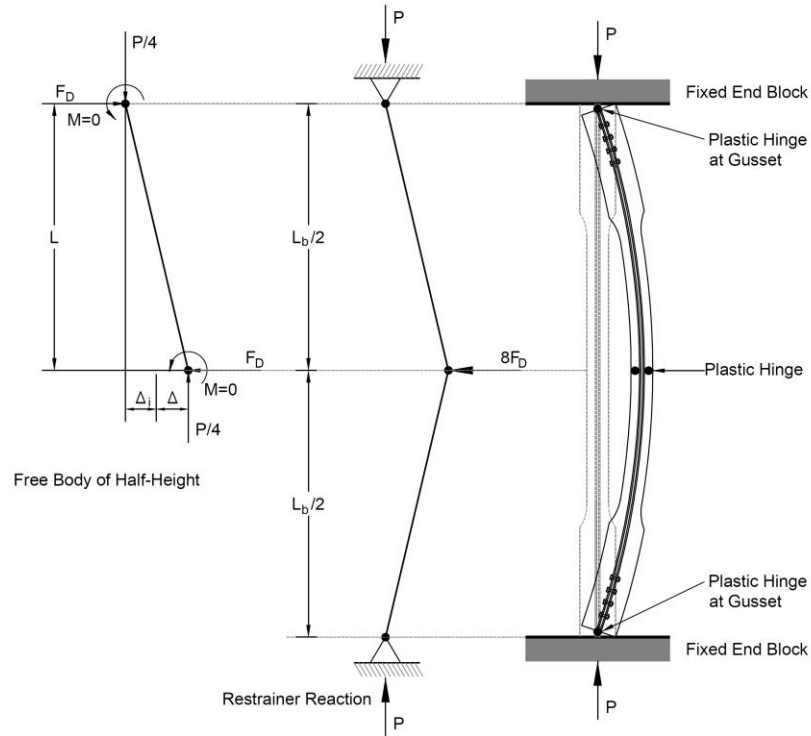


Figure 32 - Four angle mechanical model - pinned ends/out-of-plane (mode D)

Global Stability Modeled with an Euler Column

A mechanical model that more closely approximates the force interaction between the restrainer tubes and the buckling core has been presented (Black & Aiken, 2002; Xie, 2005). This model uses the classical Euler column with an additional transverse distributed force applied by the restrainer previously shown in Figure 11. In this case, the FRP restrainer tubes can be thought of as a continuous elastic foundation providing support to the reduced section of the core over its entire length instead of just at a single point as in the rudimentary SDOF model. The stiffness of the restrainer is taken as a constant “w” or any function of the position along the length of the column $w(x)$. This model promises less conservative results as compared with the SDOF model since the FRP tube restrainer is expected to provide continuous elastic support to the core member thus reducing flexural moment demand.

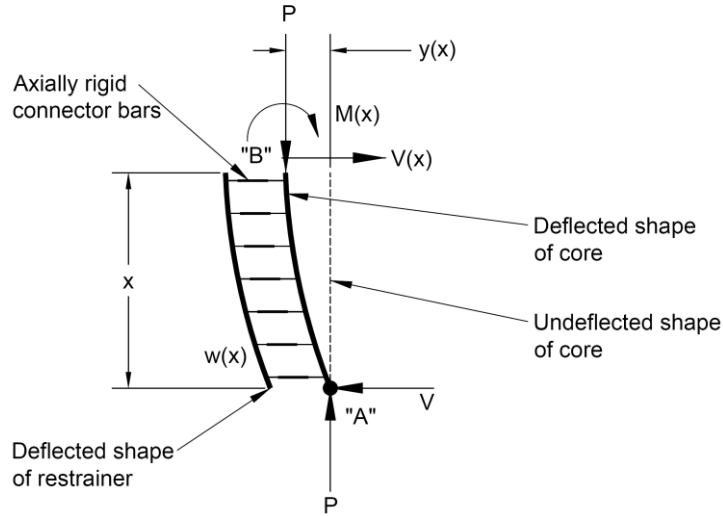


Figure 33 - Free Body Diagram of partial Euler column with restrainer force

Figure 33 shows the free body diagram of the partial length Euler column cut at a distance “x” from the bottom pin support at “A”. In Equation 51, moment equilibrium is written summing about point “A” (clockwise moments are positive).

$$\sum M_A = -Py(x) + V(x)x + M(x) + \int_0^x w(x)x \, dx = 0 \quad (51)$$

Since the shear at the cut $V(x)$ is unknown, force equilibrium is written in the y-direction to give Equation 52 (forces are positive to the right). The distributed force $w(x)$ is assumed to be symmetrical about the mid-height of the column for the BRB undergoing the global buckling mode. Therefore, the reaction (V) is simply one-half the integral of $w(x)$ over the total buckling length of the Euler column (L_u) as shown in the third term.

$$\sum F = \int_0^x w(x) \, dx + V(x) - \frac{1}{2} \int_0^{L_u} w(x) \, dx = 0 \quad (52)$$

Equations 51 and 52 are combined to give Equation 53.

$$-Py(x) + \frac{1}{2}x \int_0^{L_u} w(x) \, dx - x \int_0^x w(x) \, dx + M(x) + \int_0^x w(x)x \, dx = 0 \quad (53)$$

By assuming the same sine wave displacement function given in Equation 31, and

differentiating four times with respect to x , Equations 54-58 are given. Where δ is the maximum displacement amplitude at the mid-length of the column.

$$y(x) = \delta \sin \pi x / L_u \quad (54)$$

$$\frac{dy(x)}{dx} = \delta \frac{\pi}{L_u} \cos \pi x / L_u \quad (55)$$

$$\frac{d^2y(x)}{dx^2} = -\delta \frac{\pi^2}{L_u^2} \sin \pi x / L_u \quad (56)$$

$$\frac{d^3y(x)}{dx^3} = -\delta \frac{\pi^3}{L_u^3} \cos \pi x / L_u \quad (57)$$

$$\frac{d^4y(x)}{dx^4} = \delta \frac{\pi^4}{L_u^4} \sin \pi x / L_u \quad (58)$$

Substituting the above values into the elastic formulas given in Equations 59-61 and then substituting these values back into Equation 53 gives the final equilibrium equation in terms of the assumed displacement function $y(x)$ as shown in Equation 62. Note that Equation 61 represents the distributed force reaction provided by the restrainer and uses the stiffness of the restrainer ($E_r I_r$) instead of the core.

$$M(x) = E_c I_c \frac{d^2y(x)}{dx^2} \quad (59)$$

$$V(x) = E_c I_c \frac{d^3y(x)}{dx^3} \quad (60)$$

$$w(x) = -E_r I_r \frac{d^4y(x)}{dx^4} \quad (61)$$

$$\begin{aligned} \sum M_A = & -P\delta \sin \frac{\pi x}{L_u} - \frac{1}{2} x E_r I_r \delta \frac{\pi^4}{L_u^4} \int_0^{L_u} \sin \frac{\pi x}{L_u} dx + x E_r I_r \delta \frac{\pi^4}{L_u^4} \int_0^x \sin \frac{\pi x}{L_u} dx \\ & - E_c I_c \delta \frac{\pi^2}{L_u^2} \sin \frac{\pi x}{L_u} - E_r I_r \delta \frac{\pi^4}{L_u^4} \int_0^x x \sin \frac{\pi x}{L_u} dx = 0 \end{aligned} \quad (62)$$

After evaluating the integrals and simplifying like terms in Equation 62, Equation 63 is given. Then substituting back in for $y(x)$ and d^2y/dx^2 Equation 64 is given.

$$P\delta \sin \frac{\pi x}{L_u} + E_c I_c \delta \frac{\pi^2}{L_u^2} \sin \frac{\pi x}{L_u} + E_r I_r \delta \frac{\pi^2}{L_u^2} \sin \frac{\pi x}{L_u} = 0 \quad (63)$$

$$P y(x) + E_c I_c \frac{d^2 y(x)}{dx^2} + E_r I_r \frac{d^2 y(x)}{dx^2} = 0 \quad (64)$$

Lastly, by differentiating $y(x)$ twice with respect to x on both sides of Equation 64, we arrive at the homogeneous differential Euler equation shown in Equation 65.

$$P \frac{d^2 y(x)}{dx^2} + E_c I_c \frac{d^4 y(x)}{dx^4} + E_r I_r \frac{d^4 y(x)}{dx^4} = 0 \quad (65)$$

This equation can be rearranged to give Equation 66.

$$\frac{d^4 y(x)}{dx^4} + \frac{P}{E_c I_c + E_r I_r} \frac{d^2 y(x)}{dx^2} = 0 \quad (66)$$

After solving the differential equation, the critical load for a brace with reduced core length (L_c) is given in Equation 67 where K is the effective length factor. As was previously presented, the equivalent buckling resistance of the restrainer is 80 to 128 times that of the plastic core which allows the $E_c I_c$ term to be eliminated. The derivation of this equation brings us to same equation as is presented in the literature. Since the $E_c I_c$ term has been removed from the equation and only the linear-elastic restrainer stiffness remains, an incremental analysis considering material non-linearity is not required.

$$P_{cr} = \frac{\pi^2}{(KL_c)^2} (E_c I_c + E_r I_r) \quad (67)$$

A plot of the required stiffness of the restrainer element versus reduced core length for axial loads of 50-250 kips for the pinned case is shown in Figure 34 where

required $E_r I_r$ has been normalized by L_{ru}^3 to give actual flexural stiffness in units kips/in. The SDOF mode A model and Euler model plots are presented alongside for comparison. It can be seen that the Euler model with its distributed restrainer reaction force is indeed less conservative than the SDOF model. Fixed end results are taken as unconservative since the high axial stress present at the ends of the reduced section is expected to promote plastic hinging allowing minimal rotational stiffness. Figure 35 shows that required restrainer stiffness for the SDOF mode A buckling model normalized by the pinned Euler model is indeed conservative by a factor of two for lengths of 60-144 in.

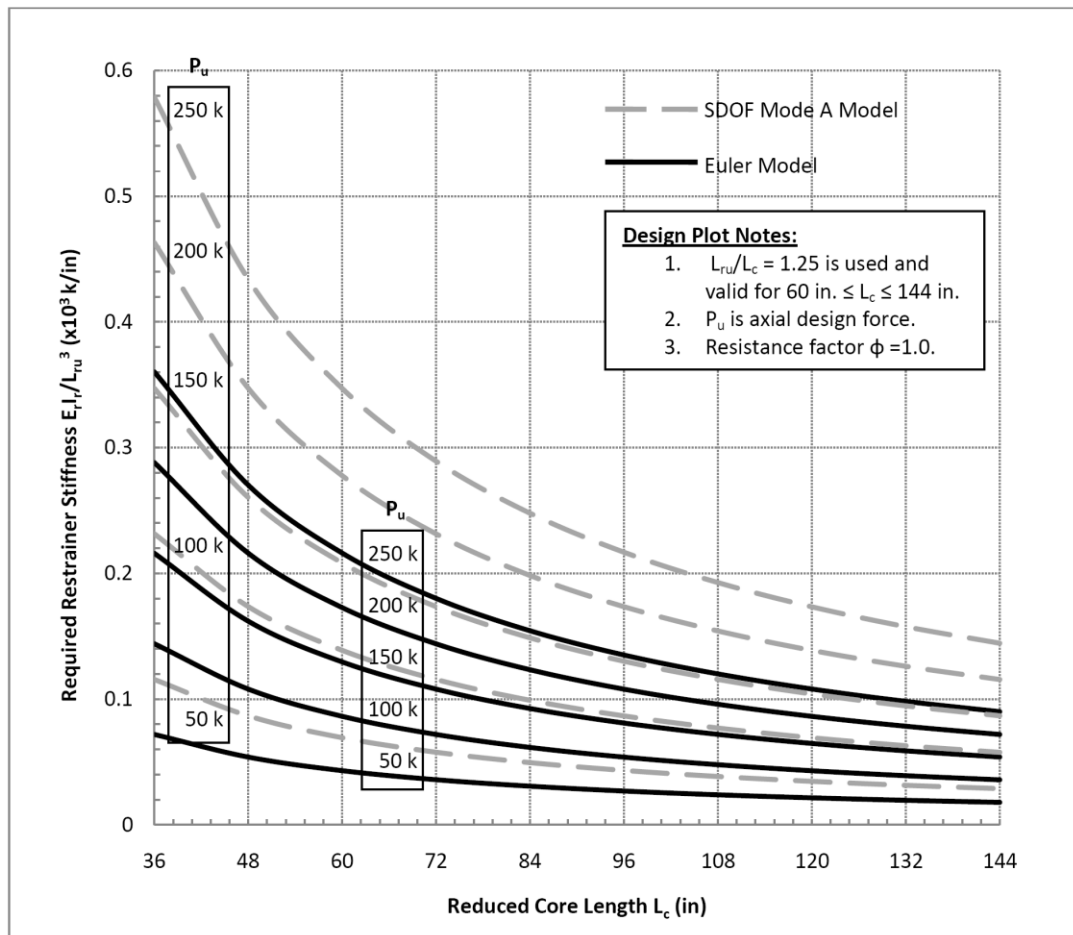


Figure 34 - Comparison of required restrainer stiffness for Euler column model to SDOF mode A model

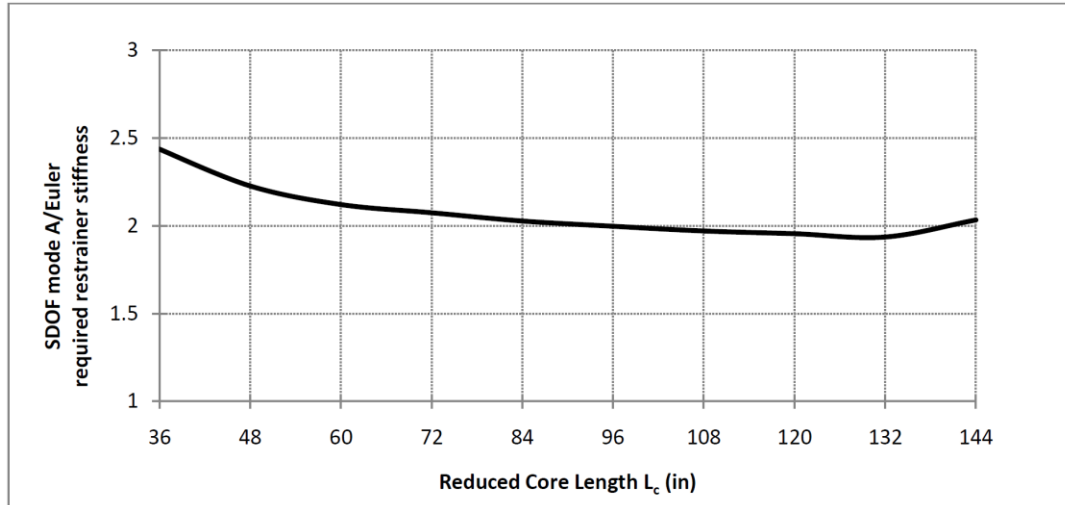


Figure 35 - Degree of conservatism of SDOF mode A model compared to Euler column model

4.4 Full-scale Restrainer Design

Now that analytical methods for determining required restrainer stiffness for the ULWBRB are established, the FRP restraint system can be designed. This design process first requires establishing material properties for both the FRP tubes and wrap. Secondly, a discussion of the composite behavior of the FRP restrainer assemblage serves to clarify the assumptions used in calculation of its section properties. Lastly, the restrainer tubes and wrap are designed using both mechanical models developed in the preceding section and presented in the literature review. Presentation of these restrainer configurations and their section properties completes the analytical design of the ULWBRB.

FRP Material Properties

Material properties of structural grade pultrusions reported by a sampling of three manufacturers are provided in Table 10. Typically, FRP pultrusions used in building construction are composed of glass fiber roving in the principal pultrusion direction and fiberglass mat in the transverse direction bonded together with a resin matrix. Different

resin formulations are available from the manufacturers depending on desired fire, ultraviolet, and chemical resistance. An isophthalic polyester resin formulation providing a low flame spread rating of 25 or less according to the tests of ASTM E-84 is selected recognizing that installation in building structures will require additional sprayed fireproofing. It can be seen that there is a consistency between manufacturers on critical material property values. Most material suppliers offer square, rectangular, and circular structural tube shapes that meet the requirements of the ULWBRB conceptual configuration.

Table 10 – Summary of Pultruded GFRP Structural Shape Material Properties			
Property (ksi)	Manufacturer		
	Strongwell EXTREN® Series 525	Creative Pultrusions Pultex® Series 1525	Fibergrate Composite Structures Dynaform® ISOFR
Ultimate Tensile Stress LW (F_{ptLW})	30.0	33.0	30.0
Ultimate Tensile Stress CW (F_{ptCW})	7.0	7.5	7.0
Ultimate Compressive Stress LW (F_{pcLW})	30.0	33.0	30.0
Ultimate Compressive Stress CW (F_{pcCW})	15.0	16.5	15.0
Ultimate Flexural Stress LW (F_{pbLW})	30.0	33.0	30.0
Ultimate Flexural Stress CW (F_{pbCW})	10.0	11.0	10.0
Young's Modulus Full Section (E_p)	2,600	3,200	2,800
Flexural Modulus Crosswise (E_{cw})	800	800	800
Shear Modulus (G_p)	425	420	450
"LW" indicates lengthwise to principal fiberglass roving direction. "CW" indicates crosswise to principal fiberglass roving direction.			

Likewise, material properties for GFRP composite laminate systems commonly used in structural strengthening applications are shown in Table 11. All of the products listed are comparable unidirectional e-glass and aramid fabric reinforcing systems to be used with epoxy resin. The glass material is orientated in the 0 degree direction and the aramid fibers are at 90 degrees. All systems use a two-component epoxy matrix material and are workable in a wet hand-layup process. The e-glass was selected over stronger and higher modulus carbon fiber products due to its lower cost and lower susceptibility to galvanic corrosion in the presence of aluminum.

Table 11 – Summary of GFRP Fabric/Resin System Material Properties			
Property	Manufacturer		
	FYFE Tyfo® SEH-51/ Tyfo® S epoxy	SikaWrap Hex® 100G/ SikaDur® 300 epoxy	QuakeWrap® VU20G/QuakeBond® J300R epoxy
Ultimate Tensile Stress LW (F_{wLW}) (ksi)	84.4	88.8	63.7
Ultimate Tensile Stress CW (F_{wCW}) (ksi)	6.25	4.40	N/A
Tensile Modulus (E_w) (ksi)	3,790	3,790	2,940
Laminate Thickness (t_L) (in)	0.05	0.04	0.037
“LW” indicates lengthwise to principal fiberglass direction. “CW” indicates crosswise to principal fiberglass direction.			

Composite Behavior of FRP Assemblage

The bundled pultruded FRP tubes shown previously in Figures 29 and 30 have the potential to work compositely with each other if shear flow between the members can be maintained. This composite section has a considerably higher stiffness than tubes working individually. Shear flow between the tubes can be accomplished by orienting the exterior FRP wrap at an angle ϕ_w to the longitudinal axis of the brace and using the

unidirectional glass fibers only in tension to prevent compression buckling of the unsupported wrap when the tubes slide axially past each other as depicted in Figure 36 (left). Tension only configuration requires the wrap to be laid in two layers perpendicular to each other as shown in Figure 36 (right).

Shear flow (q) per unit length between the FRP members can be calculated using solid mechanics for a beam made up of more than one ply as shown in Equation 68 where $V(x)$ is the shear force perpendicular to the neutral axis at a given location along the span “ x ” and Q and I_r are the first and second moment of area about the neutral axis, respectively.

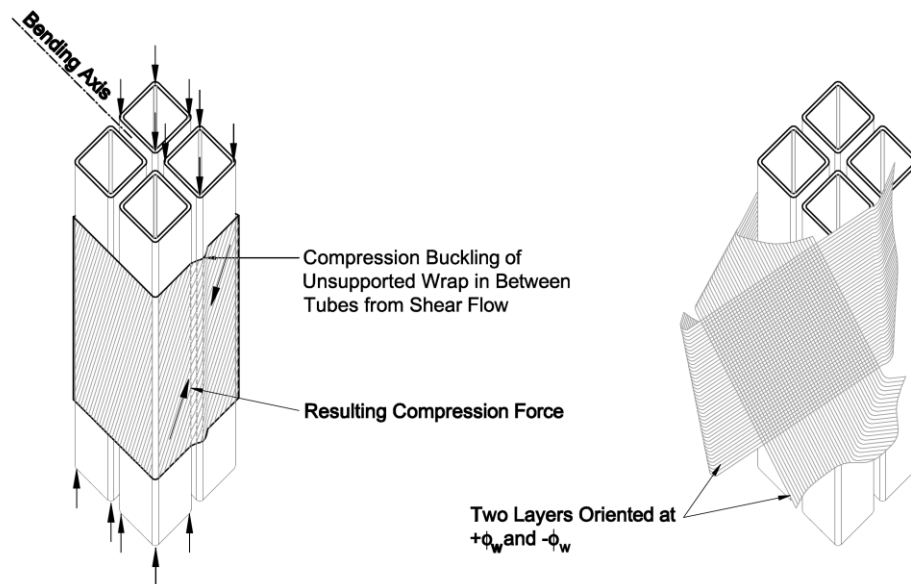


Figure 36 - Possible compression buckling of restrainer wrap (left) and proposed layer orientation (right)

$$q(x) = \frac{V(x)Q}{I_r} \quad (68)$$

For a simple span beam, shear flow is the greatest at the ends because this is the location of the greatest internal shear. Shear along the length can be determined using force equilibrium on the partial Euler column as previously shown in Figure 33. Starting with

the y-direction force equilibrium Equation 52, solving for $V(x)$ and then substituting in Equation 61 for $w(x)$ and differentiating gives Equation 69.

$$V(x) = \frac{E_r I_r \delta \pi^4}{2L_u^4} \int_0^x \sin\left(\frac{\pi x}{L_u}\right) dx - \frac{E_r I_r \delta \pi^4}{2L_u^4} \int_0^{L_u} \sin\left(\frac{\pi x}{L_u}\right) dx \quad (69)$$

Then evaluating the integrals and simplifying like terms gives Equation 70 for the assumed displacement function previously established in Equation 31.

$$V(x) = -\frac{E_r I_r \delta \pi^3}{L_u^3} \cos\left(\frac{\pi x}{L_u}\right) \quad (70)$$

The first moment of area about the neutral axis can be calculated as shown in Equation 71 where y_{ti} is the distance from the centroid of the part “i” to the composite neutral axis and A_{ti} is the cross sectional area of the part “i”.

$$Q = \sum y_{ti} A_{ti} \quad (71)$$

Substituting Equations 70 and 71 into 68 and defining L_c for L_u , Equation 72 gives shear flow at the composite neutral axis where y_t and A_t are shown in Figure 37 for a typical ULWBRB configuration.

$$q(x) = 2 \frac{y_{ti} A_{ti} E_r \delta \pi^3}{L_c^3} \cos\left(\frac{\pi x}{L_c}\right) \quad (72)$$

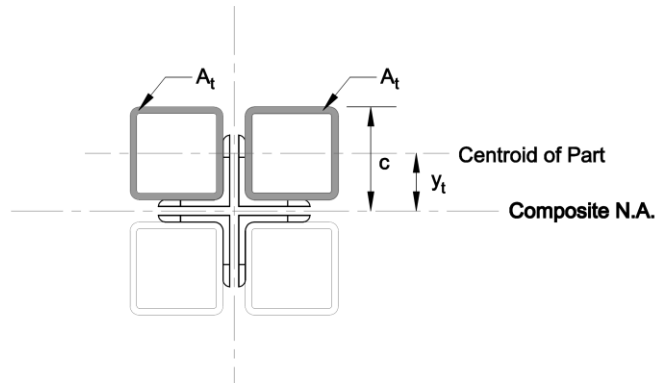


Figure 37 - Cross section of ULWBRB showing definition of shear flow variables

Equation 72 contains five variables of which four will be readily known at the time of design (y_t , A_t , L_c , and E_r). The remaining variable δ needs to be determined using a previously defined relationship relating to the allowable bending stress in the restrainer tubes to the maximum expected transverse deflection. This was given in Equation 42 and is shown again in Equation 73.

$$\delta = \Delta_t = \frac{4f_b L_{ru}^2}{48cE_r} \quad (73)$$

Combining Equations 72 and 73 gives the maximum shear flow all in terms of known variables.

$$q(x) = \frac{y_t A_t f_b \pi^3 L_{ru}^2}{6cL_c^3} \cos\left(\frac{\pi x}{L_c}\right) \quad (74)$$

Shear flow is then calculated for a given restrainer design and compared to the maximum allowable shear flow force per unit length (F_{ϕ_w}) acting at an angle ϕ_w to the composite neutral axis as given in Equation 75 where FS is a pre-determined factor of safety. Note that the factor two occurs in the numerator to account for wrap on two sides.

$$F_{\phi_w} = \frac{2F_w L W t_L}{(FS) \cos \phi_w} \geq q(x) \quad (75)$$

Analytical Design of Restrainer Tubes

The required restrainer stiffness $E_r I_r$ has been proposed as the most important design consideration for precluding global brace buckling. Before total demand on the restrainer can be calculated, BRBF in-plane drift and its ability to introduce end moments into the BRB needs to be examined. This effect causes additional flexural demand on the restrainer above and beyond that caused by the mechanical idealizations of Euler buckling. A conservative upper bound end moment that utilizes the available plastic

moment in the unrestrained section will be used in the design equation proposed by Palazzo et al. as follows.

Equation 8 given by Palazzo et al. has not been converted into a form useable for this design. This can be accomplished by first replacing the notation $E_{ca}I_{ca}$ for $E_r I_r$ and solving for this combined variable as shown in Equation 76. M_1 is also replaced with M_r to remain consistent with previously defined variables.

$$E_r I_r = \frac{P M_r}{\frac{M_r \pi^2}{(K L_c)^2} - \frac{P e_1 \pi^2}{(K L_c)^2}} \quad (76)$$

All of these variables are predetermined except M_r which can be set to a maximum value dependent on the allowable bending stress in the restrainer defined as $M_r = S_r f_b$. After substituting these values into Equation 76, Equation 77 is given.

$$E_r I_r = \frac{P S_r f_b}{\frac{S_r f_b \pi^2}{(K L_c)^2} - \frac{P e_1 \pi^2}{(K L_c)^2}} \quad (77)$$

The elastic section modulus of the restrainer is not known at the time of determining the required restrainer stiffness as they are mutually dependent, so a simple relationship $S_r = I_r/c$ is substituted into Equation 77. This gives Equation 78 which is all in terms of known variables.

$$E_r I_r = \frac{P I_r f_b}{\frac{I_r f_b \pi^2}{(K L_c)^2} - \frac{P e_1 \pi^2 c}{(K L_c)^2}} \quad (78)$$

This equation is converted algebraically by solving for I_r only as shown in Equation 79 which represents a direct superposition of Euler effect and eccentricity effect.

$$I_r = \frac{P(K L_c)^2}{E_r \pi^2} + \frac{P e_1 c}{f_b} \quad (79)$$

Lastly, for conservative design of the restrainer, an upper bound for the load eccentricity (e_1) is determined. This value takes into account both the initial out-of-straightness of the core member plus the influence of the in-plane end moment imparted to the brace resulting from frame lateral drift. This has been presented in the literature by Tremblay et al. (2006) and is depicted conceptually in Figure 38. The moments at the end of the brace increase with frame drift but cannot exceed the plastic moment of the unrestrained portion of the core itself. The smallest plastic moment outside of the restrained portion of the core is found at the intermediate section (L_{c2}) shown in Figure 40 and must be reduced to account for the axial stress present. Table 12 shows the available plastic moment (M_p') at this portion of the core for the two core configurations using axial yield force at the nominal specified strength. It can be seen that these values are larger than those previously calculated in Table 9 given the larger section size at the intermediate section. Note that bending about x-x axis was considered in lieu of z-z since end moments act in the plane of the frame which is orthogonal to the x-x axis.

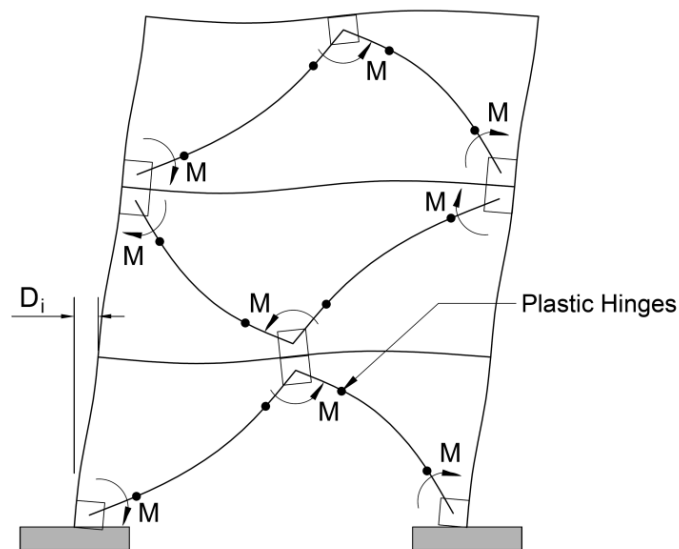


Figure 38 - In-plane moments for typical BRBF

Table 12 – Available Plastic Moment of Intermediate Section of Core							
Core Configuration	F_y (ksi)	P_y=A₁F_y (kips)	A=P_y/F_y (in²)	d₁ (in)	d₂ (in)	Z_x (in³)	M_p' (k-in)
Two-Tees	35	260	7.42	4.50	5.75	7.19	252
Four-Angles	35	277	7.91	3.32	6.16	13.1	459

If the available plastic moment at the intermediate section of the core is known, it can be used in place of the relationship shown in Equation 80.

$$M_p' = P e_1 \quad (80)$$

This equation can then be substituted into Equation 79 to give Equation 81. This final equation is used in creating the values shown in Table 13.

$$I_r = \frac{P(KL_c)^2}{E_r \pi^2} + \frac{M_p' c}{f_b} \quad (81)$$

Table 13 – Full-scale Required Restrainer Stiffness E_rI_r (k-in²)			
Method	Two Tees	Four Angles	Reference
Ratio P _E /P _y > 1.9	745,000	794,000	(Kimura, Takeda, Yoshioka, Furuya, & Takemoto, 1976)
Euler Buckling Model	225,000	225,000	(Black, Makris, & Aiken, 2004)
Modified Euler Model	460,200	653,400	(Palazzo, Lopez-Almansa, Cahis, & Crisafulli, 2009)
SDOF Mode A	449,300	449,300	Figure 22

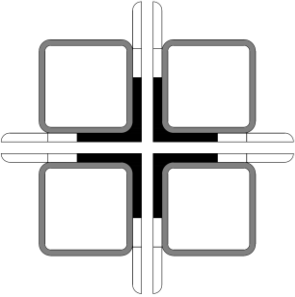
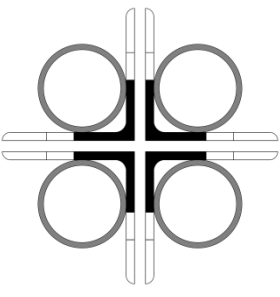
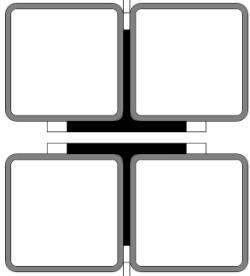
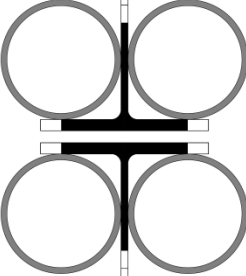
Results shown in Table 13 use previously determined values for L_c = 96 inches, F_y = 35 ksi, P_u = 241 kips, and effective length factor K = 1. Furthermore, restrainer properties include restrainer span length, L_{ru} = 122 inches, allowable restrainer bending stress, f_b = 15 ksi, distance from composite neutral axis to extreme fiber, c = 5 inches, and Young's

modulus, $E_r = 2,800$ ksi. For SDOF Mode A, the initial eccentricity of load (Δ_i) is taken to be $L/1000$ at the mid-length of the reduced core section. The factor of safety for all $E_r I_r$ values is set equal to one.

It can be seen that when accounting for load eccentricity the values for $E_r I_r$ proposed by Palazzo et al. are approximately 2-3 times higher than those in the method proposed by Black et al. This approach of introducing M_p' as an upper bound into Equation 83 appears to be overly conservative. However, it is important to protect the core experiencing high frame drift when significant end moments from frame deformation and rotation are present. Palazzo et al. has mentioned that accounting for eccentricity may be able to reduce the safety factor proposed by Black et al. for the ideal column method. As for the SDOF model, the values for the method proposed by Kimura et al. are approximately 1.8 times greater. This correlation has no mathematical basis as the P_E/P_y rule-of-thumb method was based solely on experimental observation. The SDOF method does inherently incorporate initial eccentricity but not end moments. The SDOF mathematical model provides values for $E_r I_r$ approximately twice that of the method proposed by Black et al.

Figure 39 shows the cross sectional view of the proposed core-restrainer configurations and composite section properties to be used in calculation of maximum shear flow. A square tube and round tube option is provided for comparison. At this time, it is hypothesized that the round tubes may be able to use arching action to restrain core outstand rippling instead of fixed-fixed tube wall bending as in the rectangular case. This fixed-fixed beam tube wall analogy was previously developed by other researchers (Takeuchi, Hajjar, Matsui, Nishimoto, & Aiken, 2010). The round tubes also provide a

lower moment of inertia.

Figure 39 - Full-scale Restrainer Configurations			
Square Tubes		Round Tubes	
	<p>4"x4"x1/4" Square Tubes</p> <p>FRP Group: $I_{x,y} = 138 \text{ in}^4$ $S_{x,y} = 29.8 \text{ in}^3$ $c = 4.63 \text{ in}$ $A_t = 7.48 \text{ in}^2$ $y_t = 2.63 \text{ in}$</p> <p>$E_r I_r = 386,400 \text{ k-in}^2$</p>		<p>4" dia. x 1/4" Round Tubes</p> <p>FRP Group: $I_{x,y} = 102 \text{ in}^4$ $S_{x,y} = 22.0 \text{ in}^3$ $c = 4.63 \text{ in}$ $A_t = 5.88 \text{ in}^2$ $y_t = 2.63 \text{ in}$</p> <p>$E_r I_r = 285,600 \text{ k-in}^2$</p>
	<p>5.2"x5.2"x1/4" Square Tubes</p> <p>FRP Group: $I_y = 223 \text{ in}^4$ $S_y = 41.5 \text{ in}^3$ $c = 5.38 \text{ in}$ $A_t = 9.58 \text{ in}^2$ $y_t = 2.75 \text{ in}$</p> <p>$E_r I_r = 624,400 \text{ k-in}^2$</p>		<p>5" dia. x 1/4" Round Tubes</p> <p>FRP Group: $I_y = 150 \text{ in}^4$ $S_y = 28.9 \text{ in}^3$ $c = 5.13 \text{ in}$ $A_t = 7.46 \text{ in}^2$ $y_t = 2.63 \text{ in}$</p> <p>$E_r I_r = 420,000 \text{ k-in}^2$</p>

Since the restrainer configurations are not large enough in section to allow circumferential wrapping of the bundled tubes without interfering with the full-section outstands, a double stepped reduced core is developed. This is a refinement of the initial reduced core shown in Figure 12 and allows more compact restrainer geometry. The refined core dimensions are shown in Figure 40 along with the longitudinal positioning of the restrainer. Enough clearance is left for axial deformations without tearing of the FRP wrap. This results in dimensions of 190 inches for L_b , 134 inches for L_r , 96 inches for L_c , 13 inches for L_o , 6 inches for L_{tr} , 28 inches for L_{c2} , and 19 inches for L_{c3} . By using Equation 35, the restrainer span (L_{ru}) remains at 122 inches. A 10 inch extension of the unwrapped tubes is provided to prevent local buckling of the intermediate section while

still allowing the full section to slide through. Extended tubes cantilever out from the last section of transverse wrap and leave a clearance of 6 inches to the first bolt. The wrap should be reinforced in this area to provide additional strength.

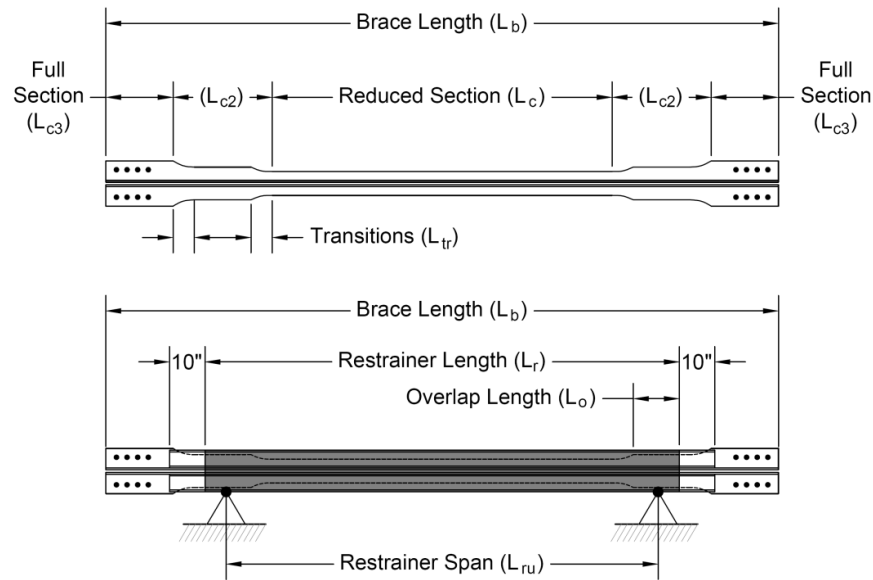


Figure 40 - Refined brace dimensions unrestrained core (top) restrained core (bottom)

When designing the longitudinal dimensions of the brace, attention should be paid to possible walking of the restrainer to one end of the intermediate section of the core. This could occur during repeated tension/compression cycles and cause the restrainer to lose its pinned support on one end leading to buckling. The overlap length should be long enough to prevent the restrainer from losing support if walking should occur. Figure 40 also indicates drilled holes for bolted end connections. These bolted connections shall be designed considering the adjusted brace strength and required connection strength as given in the *Provisions*. This methodology accounts for axial force exceeding yield strength. This is due to strain and cyclic hardening and actual material yield strength exceeding nominal specified F_y . The values for over-strength factors β , ω , and R_y are not currently available for structural aluminum, so values given for ASTM A36 steel are

used. Calculations for connections are provided in Appendix A.

Analytical Design of Restrainer Wrap

Shear flow through the wrap can now be examined in order to determine the number of layers required. Table 14 shows the results of using the restrainer section properties in Equations 74 and 75 where f_b is equal to 30 ksi. It can be seen that higher maximum shear flow is expected for square tube restrainer sections that possess a greater area, but this is only due to overdesign of the restrainer.

Table 14 – Full-scale Wrap Shear Flow Analysis					
Parameter	Two Tees		Four Angles		Reference
	Square	Round	Square	Round	
q(x) maximum (kips/in)	12.8	9.97	16.2	8.70	Equation 76
F_{ϕ_w} per layer (kips/in) ($\phi_w = 45^\circ$, $t_L = .05$ in)	11.9	11.9	11.9	11.9	Equation 77
Number of Layers Required at End	2	1	2	1	-
Factor of Safety Provided	1.85	1.19	1.46	1.37	-
Max. Out-of-Plane Displacement (in)	2.47	2.60	2.87	2.87	Equation 75

For the selected wrap product, one or two layers in both the +45 and -45 degree directions accommodate the maximum expected shear flow at the end of the member.

Since shear flow is decreasing as “x” approaches the mid span of the brace, a reduction of wrap layers is appropriate. Figure 41 shows a plot of the required number of layers along the length of the brace for the four angle square tube configuration. This plot is constructed by dividing Equation 74 by Equation 75 along the length. The diagram of the brace in Figure 41 shows a possible distribution of layers over the length. Adding

another layer in the 90° (transverse) direction at the ends helps prevent tearing if localized tensile or shearing stresses occur during loading. Tearing of the FRP wrap at the ends of the FRP restrainer has been reported in pilot tests (Dusicka & Wiley, 2008). Reinforcement of vulnerable ends is also suggested by El-Tawil & Ekiz (2009).

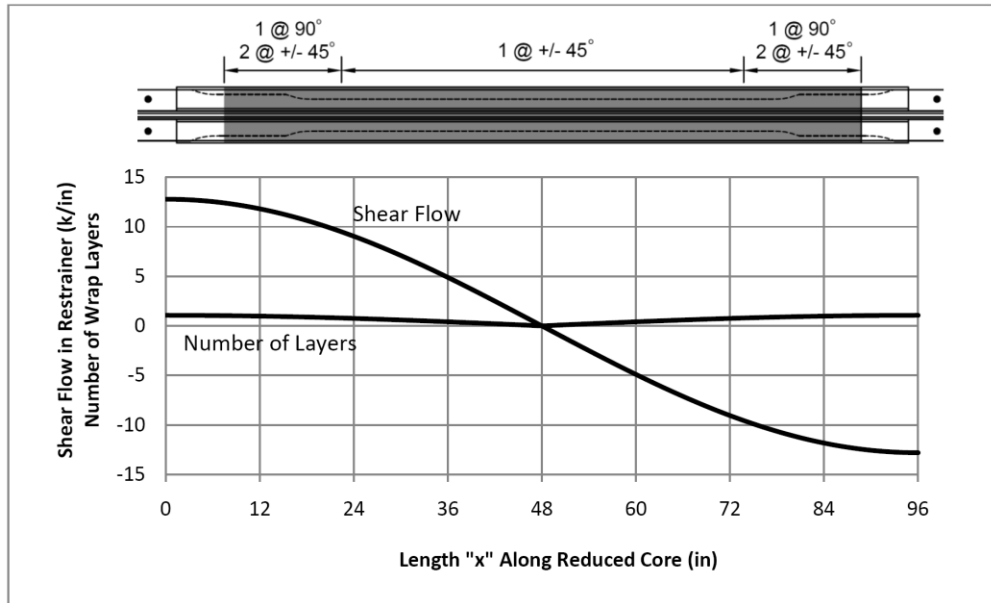


Figure 41 - Shear flow and required number of layers of wrap for four angles with square tube restrainer

Core Spacer Consideration

Figure 29 showed that spacers are required between the back to back angle legs to prevent local buckling inward during compression load cycles. This has been a problem in many tests reported in the literature and should be remedied with a sufficiently stiff elastic medium placed continuously between the angle legs. Since the ULWBRB must economize on weight, hard plastic spacers serve this purpose most effectively.

In order to select a material with sufficient compressive modulus, Table 15 presents manufacturer's data from several different formulations of commonly used plastic sheets. It can be seen that FRP composite plate material provides the highest strength and modulus, obviously a result of the reinforcement provided to the resin by the

glass fibers. However, there are plastics available that can provide a similar strength and modulus with less cost. Commercially available polystyrene and acrylic sheets give reasonably high values of compressive yield stress and modulus. An interesting comparison is made by dividing the compressive modulus by the density of the plastic to give what can be considered an elastic medium weight efficiency ratio.

Table 15 – Mechanical Properties of Common Plastics				
Material	Compressive Modulus ISO 604/ASTM D695 (ksi)	Compressive Yield Stress ISO 604/ASTM D695 (ksi)	Density ASTM D792 (lbs/in³)	Efficiency Ratio (col A:col C) (x 10⁶ in)
Polyethylene Terephthalate (PET)	145	11.6	0.050	2.9
High-Density Polyethylene (HDPE)	102	2.90	0.034	3.0
Polyvinyl Chloride (PVC)	307	8.3	0.051	6.0
Polypropylene (PP)	218	5.80	0.032	6.8
Polystyrene (PS)	363	10.1	0.038	9.6
Acrylic	435	13.8	0.043	10.1
FRP <i>Strongwell Extren 525</i>	800 (CW)	15.0 (CW)	0.066	12.1
CW indicates crosswise loading to extrusion direction.				

Both polystyrene and acrylic approach the efficiency of the more expensive FRP. Another point worth mentioning is very inexpensive recycled plastic materials are available in the marketplace that may be of use in this compression application. Specifically, polyethylene terephthalate (PET) can be recycled from used plastic pop bottles. The required stiffness of this elastic medium to control local buckling is suggested as a future research topic since the effect of local buckling is not part of this

study. Friction and fire resistance properties are among the others that must be considered.

Weight Comparison between BRBs

Weight savings of the ULWBRB as compared to a mortar-filled tube and all-steel BRB are given in Table 16. For the weight calculation, all braces are taken to be 190 inches for the total length (L_b) and have similar core and restrainer dimensions as given for the ULWBRB. Since the nominal yield stress of ASTM A36 steel is almost identical to that of the 6061-T6 aluminum, similar core section sizes are assumed for this rudimentary comparison. The unit weight for mild steel and aluminum is taken as 490 and 165 pounds per cubic foot, respectively.

Table 16 – Weight Comparison Between BRBs			
Component	Mortar-filled Tube	All-Steel	Aluminum/FRP (Ultra-Lightweight)
Core (lbs.)	570	570	192
Restrainer (lbs.)	314	420	213
Mortar (lbs.)	841	-	-
Total (lbs.)	1,725	990	405
Weight Ratio ULWBRB/BRB	24%	41%	-

As for the restrainer sizes, a typical mortar-filled BRB is taken from a literature report by Tremblay et al. (Tremblay, Bolduc, Neville, & DeVall, 2006). In these experiments, a 10 3/4 inch by 1/4 inch round steel tube restrainer size was used. The concrete mortar is assumed to have a unit weight of 150 pounds per cubic foot. For the typical all-steel BRB, the same restrainer tube configuration developed for the ULWBRB is used. These 4 x 4 x 1/4 inch tubes are converted from FRP to steel. Various bolted connection plates

are undoubtedly required for connection of the tubes; however, they are not included in the weight comparison. This comparison serves to highlight the considerable weight savings that can be realized with the ULWBRB.

Conclusion

Now that the ULWBRB core and restrainer are developed to the point where their geometry and construction are well defined, practical conclusions can be drawn which will shape subsequent steps of this project. Interplay of the core-restrainer geometry and availability of stock shapes influence the design of the final brace configuration irrespective of the analytical method. These constraints must be balanced with the results of the calculations in choosing the optimum solution as is the case with most design endeavors.

For instance, the two tee and four angle cores show that it may be difficult to select stock tees or tees cut from I-shaped beams that provide outstand dimensions which lead to a compact cross section. This can be seen in the two tee configuration where the restrainer stiffness provided is approximately twice that of the four angle configuration. The more compact four angles allow the restrainer size to be chosen based on the required stiffness rather than geometry. Thus this configuration lends itself to greater efficiency through customization as many single angle sizes are readily available.

In addition, the round FRP tubes are difficult to size in order to prevent core outstand rippling as the tangent point of the tube must coincide with the faying surface near the end of the outstand. This geometric requirement is taken as the controlling factor on both configurations. Due to the unavailability of stock round section shapes with thicker tube walls, the required restrainer stiffness was not able to be satisfied. Also,

the round tubes leave a large unsupported area on the core outstands that may lead to local buckling problems.

It can be assumed that a high degree of customization potential for both the core and the restrainer is desired. It is evident that the four angle core with square FRP tubes is the most promising of the four alternatives explored in this design. It is recognized that special order sections are commonly requested from suppliers in both aluminum extrusions and FRP pultrusions. Through this, manufacturers would have the ability of fine-tuning the design for a specific application. For example, a single piece cruciform shaped core and restrainer tubes that exactly fit the core dimensions have the potential for minimizing the amount of material used and eliminating required plastic spacers in between the angle legs. This type of customization would be beneficial to a large producer of ULWBRBs. However, for the purposes of this project, the four angle core with square restrainer tubes proves to be the most promising for the upcoming numerical study and future experimental test programs.

It is also found that the guidance provided on selecting the reduced section length of the core was maximized in this design. The selected value of 96 inches for L_c left only 47 inches for the full-section gusset plate connection, intermediate section overlap length, and a sufficient amount of length for axial shortening of the core. Therefore, the use of $L_c/L_b = 0.5$ as a design guideline appears to be appropriate.

5.0 BRACE SCALING

5.1 Objective

A partial-scale prototype brace is desired for numerical and future laboratory testing. Dimensions of the partial-scale brace and seismic demand on it cannot be determined by creating a small-scale prototype building as was done in the previous section since this small of a structure would be unrealistic. Therefore, a proportional scaling method is applied at the component level. The partial-scale available strength is calibrated to the full-scale core in order to examine scaling effects. After scaling of the core is complete, the partial-scale restrainer assemblage is designed using the analytical methods previously developed.

5.2 Core Scaling

To begin the scaling process, section geometries are developed for the four-angle and two-tee configurations similar to what was done for the full-scale brace. The following parameters are considered when choosing the core geometry.

1. Brace end to end length is selected as 120 inches giving a reduced core length of 60 inches in order to maintain a γ ratio of 0.5.
2. Cross-sectional area of the reduced core section is set to be approximately 50% of the full-scale brace in order to maintain available tension strength of 128 kip (half that of the full-scale brace).
3. Effective length (KL_c/r) of the reduced core is set equal to the full-scale

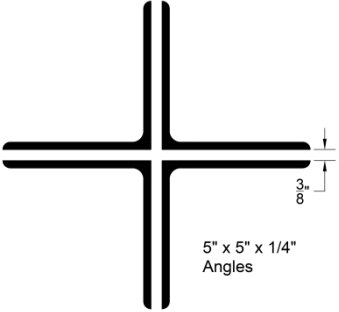
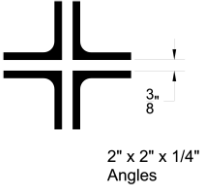
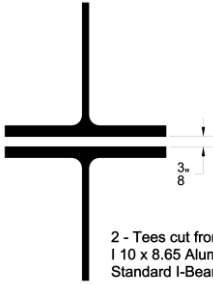
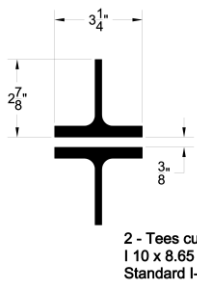
brace as this is thought to be most influential for global buckling. The radius of gyration is manipulated in order to achieve this equality.

4. Width-thickness ratio (b_o/t_o) of the core outstands should not vary greatly from the full-scale brace as this affects local buckling potential.
5. Core individual elements shall still fit integrally with proposed square or circular FRP tube restrainer elements.

The target scaling ratio also considers the following laboratory parameters:

1. Maximum cyclic load application potential of laboratory equipment is set at 120 kips tension or compression to allow for ample reserve capacity to account for R_y , β , and ω .
2. Available laboratory floor space sets end to end length of brace at 120 inches.
3. Connection regions of the core to test apparatus must accommodate minimum 1/2 inch diameter bolts in a single line and a minimum gusset plate thickness of 3/8 inch.
4. Minimum outstand thickness should not be less than 1/4 inch in order to allow reasonable bolt bearing stress.

Figure 42 shows the selected core section configurations along with their relevant section properties. Selection of the section sizes is made by trial considering the above parameters and stock section availability. Throughout this process, equations provided in the *Aluminum Design Manual* for tension and compression limit states are calculated for the bare unrestrained partial-scale core and compared with the full-scale results until target scaling ratios were achieved.

Figure 42 - Partial-scale Core Section Properties			
Full-Section		Reduced-Section	
 <p>5" x 5" x 1/4" Angles</p>	<p>Per Angle: $A_3 = 2.45 \text{ in}^2$ $b_o = 4.38 \text{ in}$ $t_o = 0.25 \text{ in}$ $I_z = 2.415 \text{ in}^4$ $r_z = 0.993 \text{ in}$ $J = 0.0508 \text{ in}^4$ $C_w = 0.0042 \text{ in}^6$</p>	 <p>2" x 2" x 1/4" Angles</p>	<p>Per Angle: $A_1 = 0.97 \text{ in}^2$ $b_o = 1.38 \text{ in}$ $t_o = 0.250 \text{ in}$ $I_z = 0.140 \text{ in}^4$ $r_z = 0.390 \text{ in}$ $J = 0.0195 \text{ in}^4$ $C_w = 0.0016 \text{ in}^6$</p>
 <p>2 - Tees cut from I 10 x 8.65 Alum. Assoc. Standard I-Beam</p>	<p>Per Tee: $A_3 = 3.68 \text{ in}^2$ $b_o = 4.18 \text{ in}$ $t_o = 0.250 \text{ in}$ $I_x = 6.96 \text{ in}^4$ $I_y = 7.39 \text{ in}^4$ $r_x = 1.38 \text{ in}$ $r_y = 1.42 \text{ in}$ $J = 0.163 \text{ in}^4$ $C_w = 0.151 \text{ in}^6$</p>	 <p>2 - Tees cut from I 10 x 8.65 Alum. Assoc. Standard I-Beam</p>	<p>Per Tee: $A_1 = 2.02 \text{ in}^2$ $b_o = 2.06 \text{ in}$ $t_o = 0.250 \text{ in}$ $I_x = 1.20 \text{ in}^4$ $I_y = 1.18 \text{ in}^4$ $r_x = 0.770 \text{ in}$ $r_y = 0.770 \text{ in}$ $J = 0.0886 \text{ in}^4$ $C_w = 0.0247 \text{ in}^6$</p>

Limit state available strengths are shown in Table 17 along with their respective scaling ratios per Appendix D. It can be seen in this table that the length of the reduced section of the core is 63% of the full-scale brace due to the chosen L_c of 60 inches. The area of the reduced section for the four-angle configuration has been scaled to approximately 50% giving a tension available strength of 125 kips, as intended. The slenderness ratios remain essentially the same which gives an equal available stress for the global elastic buckling limit state. However, since the reduced core area is approximately 50% of the full-scale brace, the resulting scaling factor is 0.52. Outstand width to thickness scaling ratio is able to be held close to 1.0 for the four-angle configuration which gives similar available stress for the component local buckling limit state. The scaling factor for limit strength is again controlled by the reduced core area

scaling ratio of approximately 50%. It should be noted that the two-tee configuration is not able to achieve a one to one scaling of the width to thickness ratio because available section size and manipulation of the radius of gyration for global buckling imposes too many constraints on the scaling parameters. It is hypothesized that this would lead to a smaller likelihood of component local buckling as compared with the full-scale configuration for the two-tees. This can be seen by the 0.68 scaling ratio for ϕP_{L6} .

Table 17 – Partial-scale Available Strength of Unrestrained Core					
Parameter	Four Angles		Two Tees		Reference (Aluminum Association, 2000)
	Partial-scale Value	Partial- scale to Full-scale ratio	Partial- scale Value	Partial- scale to Full-scale ratio	
L_c (in)	60.0	0.63	60.0	0.63	-
KL_c/r	154	0.97	78.4	1.01	-
b_o/t_o	5.5	1.10	8.2	0.66	-
ϕT_{L1} (kips)	129	0.49	134	0.54	Eq. 3.4.1-1
ϕT_{L2} (kips)	125	0.49	130	0.54	Eq. 3.4.1-2
ϕP_{L3} (kips)	16	0.52	52	0.54	Eq. 3.4.7-4
ϕP_{L4} (kips)	99*	0.41	119	0.58	Eq. 3.4.7-4
ϕP_{L5} (kips)	15*	0.50	47	0.58	Eq. 3.4.7-4
ϕP_{L6} (kips)	121	0.48	111	0.68	Eq. 3.4.8-3
* Indicates rational analysis used for nonsymmetrical sections.					

5.3 Partial-Scale Restrainer Design

Now that the scaled brace core geometry has been determined, analytical design of the restrainer assemblage can be completed. The same methodology is used as

described for the full-scale brace. Again, the available plastic moment for the composite section is calculated in Table 18. These plastic moments are used to introduce an upper bound end moment M_p' in the method proposed by Palazzo et al.

Table 18 – Available Plastic Moment of Intermediate Section of Core							
Core Configuration	F_y (ksi)	$P_y=A_1F_y$ (kips)	$A_{req}=P_y/F_y$ (in²)	d_1 (in)	d_2 (in)	Z_x (in³)	M_p' (k-in)
Two-Tees	35	141	4.04	4.10	5.05	4.20	147
Four-Angles	35	136	3.89	2.39	4.50	4.77	167

Table 19 shows the required restrainer stiffness for the different design methods using 60 inches for L_c , 35 ksi for F_y , 120 kips for P_u , and effective length factor $K = 1$. Restrainer parameters are 74 inches for L_{ru} , 15 ksi for f_b , 4 inches for c , and 2,800 ksi for E_r . For SDOF Mode A, the initial eccentricity of load (Δ_i) is taken to be $L/1000$ at the mid-length of the reduced core. The factor of safety for these values is set equal to one. As before, the design values for the method proposed by Palazzo et al. are used to design the restrainer. It can be seen that the required stiffness for this method is approximately 4 times greater than that proposed by Black et al. Therefore, introduction of this upper bound end moment (M_p') should be thought of as an extremely conservative design method that accounts for BRBF drifts and gusset plate rotation higher than those expected by design. It should be the judgment of the designer to introduce a smaller end moment based on maximum expected story drift and relative stiffness of the brace vs. the frame. This upper bound end moment is expected to be unrealistically large once actual moments in a BRBF are analyzed. Therefore, only a percentage of M_p' is anticipated to be used in subsequent numerical modeling sections.

Table 19 – Partial-scale Required Restrainer Stiffness $E_r I_r$ (k-in²)			
Method	Two Tees	Four Angles	Reference
Ratio $P_E/P_v > 1.9$	149,000	143,000	(Kimura, Takeda, Yoshioka, Furuya, & Takemoto, 1976)
Euler Model	43,800	43,800	(Black, Makris, & Aiken, 2004)
Modified Euler Model	153,500	168,500	(Palazzo, Lopez-Almansa, Cahis, & Crisafulli, 2009)
SDOF Mode A	83,500	83,500	Figure 22

Figure 43 shows the cross sectional view of the proposed restrainer assemblies for the partial scale brace. Just like in the restrainer design of the full-scale brace, it is difficult to provide exactly the required amount of stiffness. Geometric constraints and stock section availability cause the two tee configuration to have $E_r I_r$ values up to 212% of that required. $E_r I_r$ much closer to that required is able to be provided on the four angle configurations. Note that the four angle, round tube configuration is less than required due to the required tangent point between the tube and angle leg.

A similar analysis of shear flow through the restrainer elements is now completed in order to determine the required number of wrap layers. The results of this analysis are presented in Table 20. A plot of shear flow and required number of layers for the four angle, square tube configuration are shown in Figure 44. Only one layer of FRP wrap is required due to the short length of the restrainer span and reduced section. In the partial-scale case, the number of layers shall not be governed by shear flow, but by robustness of the ends of the restrainer and their ability to resist tearing. Therefore, a second wrap layer at 90 degrees is recommended.

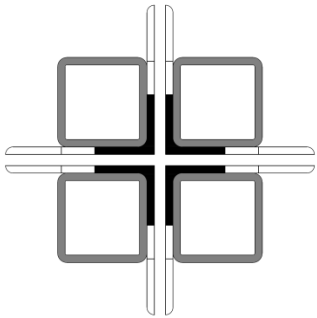
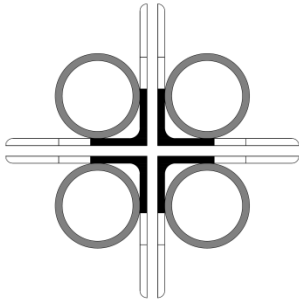
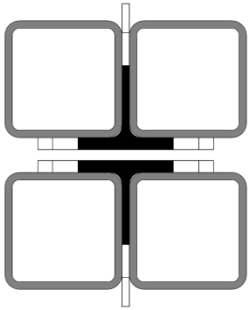
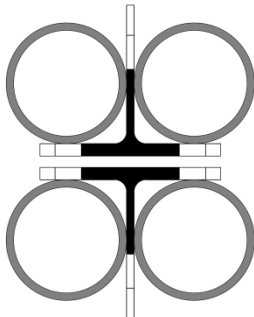
Figure 43 – Partial-scale Restrainer Configurations			
Square Tubes		Round Tubes	
	3"x3"x1/4" Square Tubes FRP Group: $I_{x,y} = 55.0 \text{ in}^4$ $S_{x,y} = 16.0 \text{ in}^3$ $c = 3.44 \text{ in}$ $A_t = 2.74 \text{ in}^2$ $y_t = 1.94 \text{ in}$ $E_r I_r = 154,000 \text{ k-in}^2$		3" dia. x 1/4" Round Tubes FRP Group: $I_{x,y} = 40.7 \text{ in}^4$ $S_{x,y} = 11.8 \text{ in}^3$ $c = 3.44 \text{ in}$ $A_t = 2.16 \text{ in}^2$ $y_t = 1.94 \text{ in}$ $E_r I_r = 114,000 \text{ k-in}^2$
	4"x4"x1/4" Square Tubes FRP Group: $I_y = 103 \text{ in}^4$ $S_y = 25.0 \text{ in}^3$ $c = 4.13 \text{ in}$ $A_t = 3.74 \text{ in}^2$ $y_t = 2.13 \text{ in}$ $E_r I_r = 288,400 \text{ k-in}^2$		4" dia. x 1/4" Round Tubes FRP Group: $I_y = 73.9 \text{ in}^4$ $S_y = 17.9 \text{ in}^3$ $c = 4.13 \text{ in}$ $A_t = 2.94 \text{ in}^2$ $y_t = 2.13 \text{ in}$ $E_r I_r = 206,900 \text{ k-in}^2$

Table 20 – Partial-scale Wrap Shear Flow Analysis					
Parameter	Two Tees		Four Angles		Reference
	Square	Round	Square	Round	
q(x) maximum (kips/in)	7.58	5.96	6.07	4.79	Equation 76
F_{ϕ_w} per layer (kips/in) ($\phi_w = 45^\circ$, $t_L = .05 \text{ in}$)	11.9	11.9	11.9	11.9	Equation 77
Number of Layers Required at End	1	1	1	1	-
Factor of Safety Provided	1.57	2.0	1.96	2.48	-
Max. Out-of-Plane Displacement (in)	1.18	1.18	1.42	1.42	Equation 75

The refined core geometry is shown in Figure 45 and utilizes the same two step configuration as the full-scale brace. Dimensions shown are 122 inches for L_b , 82 inches

for L_r , 74 inches for L_{ru} , 7 inches for L_o , 4 inches for L_{tr} , 16 inches for L_{c2} , and 15 inches for L_{c3} . The tubes are extended without wrap for a distance of 6 inches leaving 4 inches between the end of the tubes and the first bolt to prevent local buckling of the intermediate section while still allowing the full-section outstands to slide independently between the tubes. Appendix B shows design of the end connections.

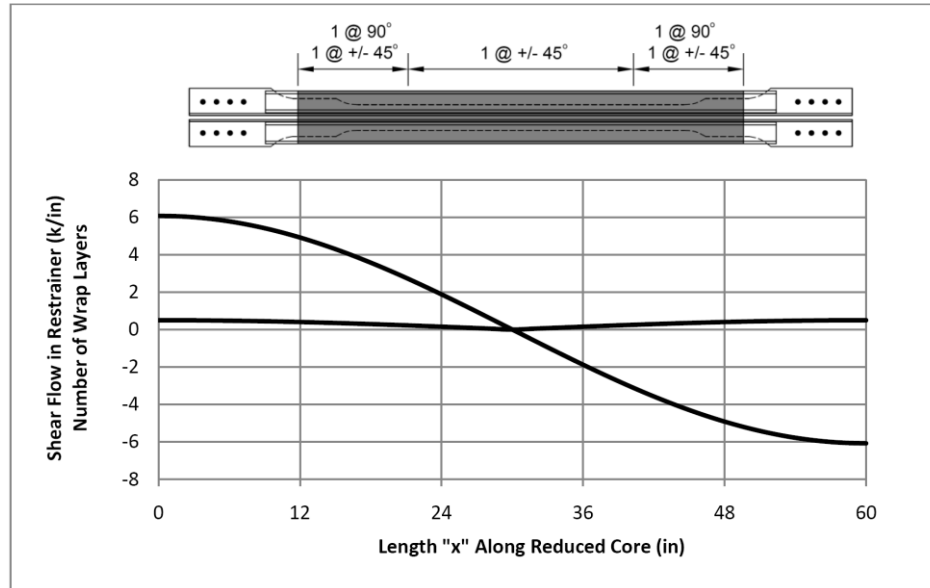


Figure 44 - Shear flow and required number of layers of wrap for four angles with square tube restrainer

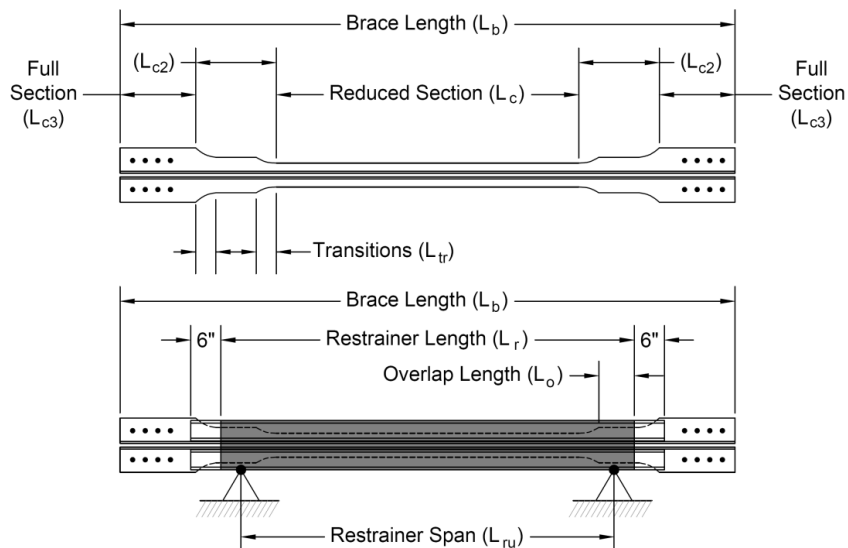


Figure 45 - Refined partial-scale brace dimensions

6.0 COUPON TESTING

6.1 Objective

The literature review showed that there is a push towards applying aluminum alloys in yielding components of seismic energy dissipating systems, but its plastic cyclic behavior remains largely unreported. Much of the research on cyclically loaded aluminum has been on high-cycle fatigue directed toward understanding the life-span of aluminum components designed to perform well within their elastic limit (e.g. in airframes). Yet, there are limited reports of low-cycle fatigue (LCF) testing of aluminum coupons that begin to shed light on how it would behave in seismic applications. In the ULWBRB core the material is expected to perform in a predictable and stable manner without fracture when loaded repeatedly past its elastic limit approaching 2 to 3% plastic strain. Consequently, further LCF testing of structural aluminum coupons is warranted.

Coupon testing reveals both the tensile monotonic ductility and fully reversed cyclic behavior of the chosen aluminum alloy 6061 with a T6511 heat treatment under uniaxial stress. From the test data, yield stress, tangent modulus, elongation at yield and ultimate, stress-strain hystereses, and information on cyclic hardening or softening are gleaned. Hysteresis data subsequently is used to create the constitutive model for use in the numerical analysis. The goal of these tests is to enhance what is known about the in-elastic and cyclic behavior of structural aluminum.

6.2 ASTM Test Methods

To begin, there are two ASTM test methods that are useful in defining the

specimen dimensions for the proposed tests. *ASTM E 8 Standard Test Methods for Tension Testing of Metallic Materials* (ASTM, American Society for Testing & Materials, 2008) provides standard round specimen geometry that uses a gage to diameter ratio (A/D) of four that allows tensile necking to occur independent of the larger diameter boundaries. This allows the Poisson effect to occur while minimizing plane-strain behavior that can be set up by the boundary conditions. Of course, this test only loads the specimen in tension, so compression buckling of the relatively slender reduced section is not a concern.

An examination of gage to diameter ratio is important since cyclic testing loads the coupons in compression as well as tension. *ASTM E 606 Standard Practice for Strain-Controlled Fatigue Testing* (ASTM, American Society for Testing & Materials, 2004) provides uniform gage round specimen limitations to control buckling of the reduced section that is considerably less slender. This test method is meant to determine fatigue properties of material specimens subjected to uniaxial stress under fully-reversed, push-pull constant amplitude cycling. The recommended gage to diameter ratio (A/D) ranges from two to four. It is noted in the standard that the uniform gage specimen is suitable for strain ranges to about 2% while the standard hourglass specimen may be necessary for strain ranges greater than 2%. These ratios provide a starting point for determining the cyclic coupon dimensions.

6.3 Tensile Coupon Tests

The first tests measure the elastic modulus (E), yield strength at 0.2% offset ($f_{0.2}$), ultimate tensile strength (f_{tu}), elongation at yield (ϵ_y), and elongation at fracture (ϵ_u). A CNC machined round specimen test coupon is shown in Figure 46 that follows the

ASTM E 8 standard specimen geometry. The parent material was a 7/8 inch extruded round bar with chemical composition: 0.15-0.40% Cu, 0.04-0.35% Cr, 0-0.70 % Fe, 0.8-1.2% Mg, 0-0.15% Mn, 0.4-0.8% Si, 0-0.15% Ti, and 0-0.25% Zn.

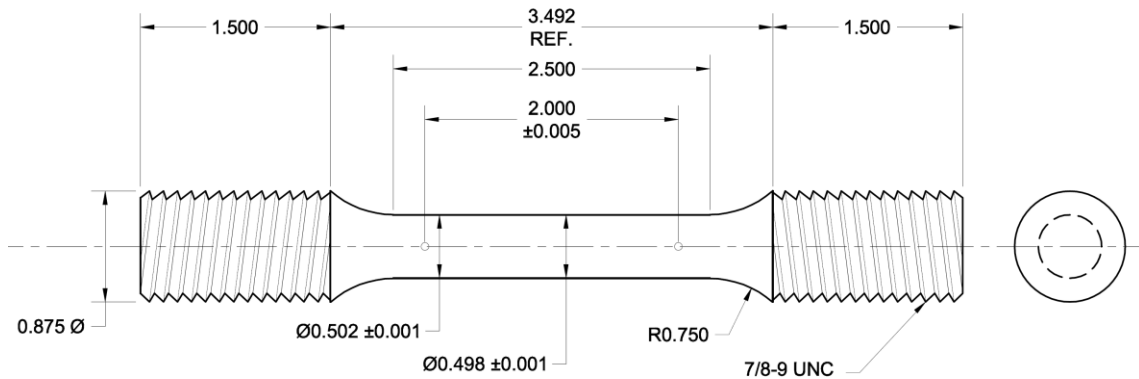


Figure 46 - ASTM E 8 coupon dimensions (all dimensions in inches)

A Minnesota Testing Systems servo-hydraulic load frame with a +/- 110 kip capacity interfaced to a computer for control and data acquisition was used for the tests. Threaded ends with double nuts were used to mount the round specimens into HSS fixtures hard mounted between the actuator and the load cell. A laser extensometer recorded the displacement of the gage length and a load cell with a capacity of 100 kips recorded applied load at a sampling rate of 20 Hz. Load was applied using displacement control at a strain rate of 0.006% per second using the LVDT. Reflective tape for the laser extensometer was applied to the section at a gage length of approximately one inch for both Coupon T1 and C1 which allowed necking to occur within. A photo of the test setup for the tension test is shown in Figure 47. The double nuts were custom made from flat plate to allow a greater contact area against the HSS fixture. In cyclic tests the top HSS fixture was attached directly to the load cell without the center threaded rod to minimize eccentricity.

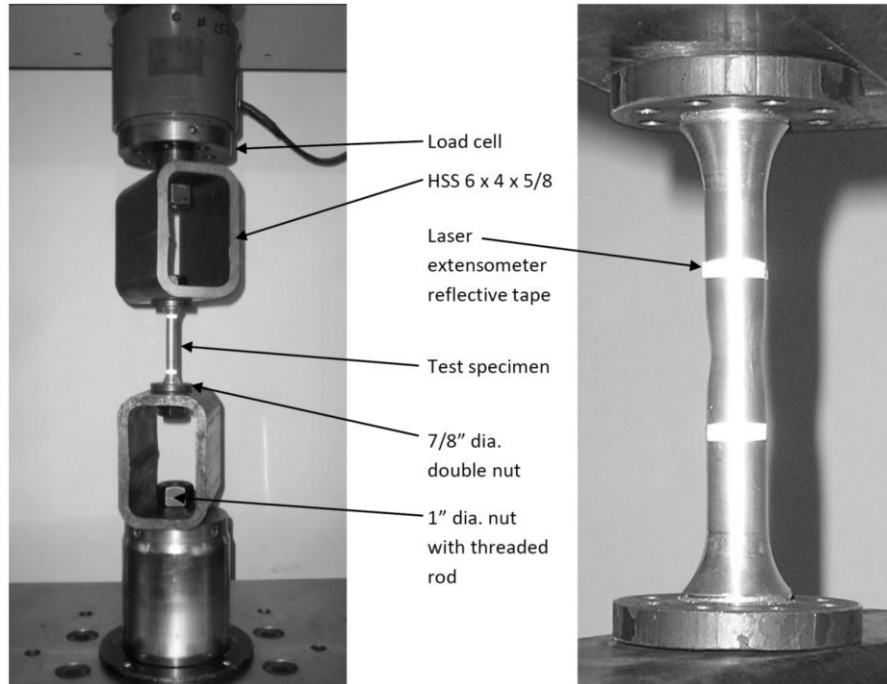


Figure 47 - Photo of tension test setup (left), tension necking of coupon (right).

Figure 48 shows the plot of the monotonic tension test data for both specimens T1 and C1. The difference in the two curves can possibly be attributed to boundary effects present in the cyclic test coupon where a long gage length was not used. Both specimens exhibited plastic necking at the center of the gage length up until fracture indicating good ductility. Strain hardening occurred up until 5% elongation and was followed by softening up until fracture at 22% elongation. Table 21 shows the material properties calculated from the tension tests. These values indicate that the experimental yield strength exceeds the minimum nominal yield strength by approximately 25%.

Table 21 – Tension Test Results										
Coupon ID	Gage Length (in)	Dia. (in)	Area (in ²)	f _{0.2} (ksi)	f _u (ksi)	ε _y (%)	ε _u (%)	E (ksi)	Area at Failure (in ²)	Failure Stress (ksi)
T1	1.117	0.5005	0.1967	42.9	46.0	0.38	21.9	11,200	0.0831	60.1
C1	0.9291	0.5016	.01976	43.5	46.5	0.33	22.3	13,200	0.0823	54.8

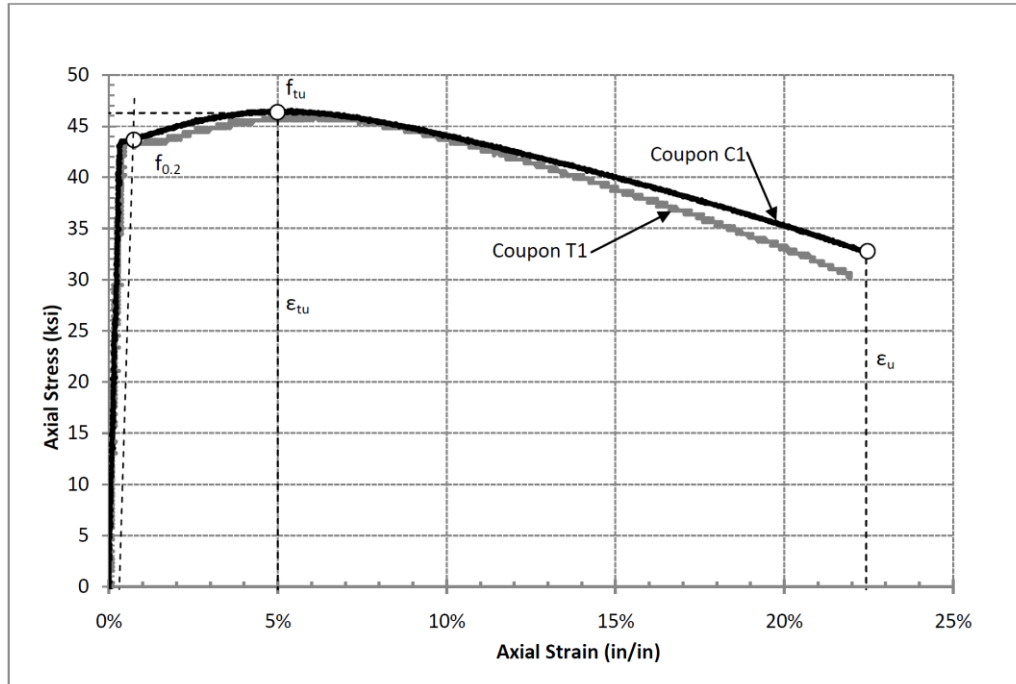


Figure 48 - Monotonic tension test stress-strain plot

6.4 Cyclic Coupon Tests

The cyclic tests were executed in the same test apparatus. Four coupons were CNC machined from 7/8 inch round bar stock with dimensions as shown in Figure 49 of which one was used for the monotonic tension test (C1) and three for cyclic tests of constant strain amplitudes of 2%, 3%, and 4% (C2-C4). The coupons had an A/D ratio of 1.5 to control buckling. This ratio is slightly less than the minimum ratio of two given in the ASTM standard, but has successfully been used in similar tests on low yield point steel (Dusicka, Itani, & Buckle, 2007). A uniform gage specimen was used in lieu of an hourglass section to create a short prismatic section for the yielding mechanism to occur. Load was applied in manual displacement control to achieve constant total strain amplitude by application of a triangular waveform. Straining began with a tensile excursion and was carried out until tensile fracture failure or reversal stress that did not

achieve 50% of the maximum recorded cyclic stress (compression failure).

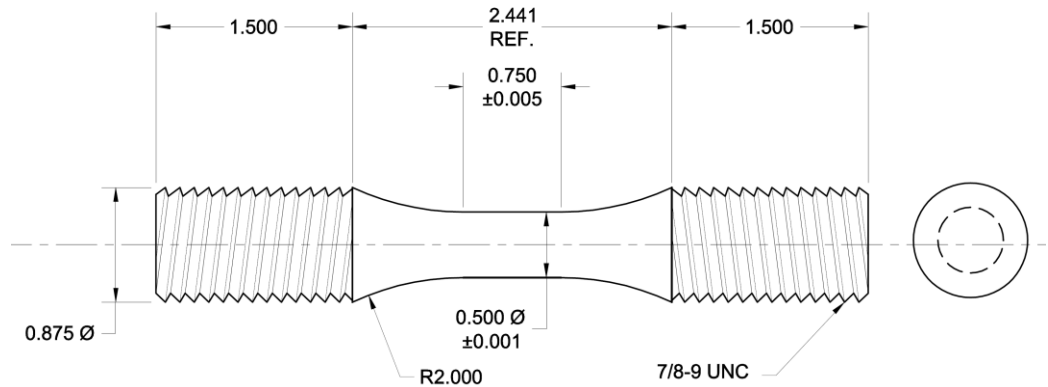


Figure 49 - Cyclic test coupon dimensions (all dimensions in inches)

Rapid plastic working of the aluminum has the potential of increasing the temperature significantly above ambient conditions. This can influence the mechanical properties of the material which is not the intent of these tests. Previous research has recognized the heat-sink capability of the surrounding structure in contact of the plastic section since it is generally much larger. The heat sink in the ULWBRB is expected to be the intermediate and full-section cores since the FRP restrainer is not able to provide the same heat absorbing function as the mortar-filled tube or all-steel BRB configurations. Taking this into account, the plastic strain rate was set at 0.1% per second to match what has been reported in the literature. For example, tests on 6060 coupons using a sinusoidal wave and strain amplitude of 1.2% used a strain rate 0.1% per second (Hopperstad, Langseth, & Remseth, 1995). Similarly, 6060 coupons were tested with a triangular wave to maximum strain amplitude of 1.5% using 0.8% per second (Borrego, 2004).

The results for the cyclic tests are shown in Table 22. It can be seen that increasing the strain amplitude had a linear effect on the number of cycles the coupon was able to endure before tension fracture. In all tests slight cyclic softening was

witnessed after the first few cycles. Images of the progression of Coupon C3 are shown in Figure 50. Stress fatigue cracking can be seen at the center of the reduced section in cycle 14 and bulging of the entire reduced section can be seen in the compression portion of the same cycle. This specimen failed by tensile fracture during cycle 19.

Table 22 – Cyclic Test Results						
Coupon ID	Gage Length (in)	Diameter (in)	Area (in ²)	Strain Amplitude (%)	Full Cycles Prior to Failure	Failure Mode
C2	0.9306	0.5024	0.1982	2	24	Tensile Fracture
C3	0.9402	0.5026	0.1984	3	18	Tensile Fracture
C4	0.8918	0.5016	0.1976	4	11	Tensile Fracture

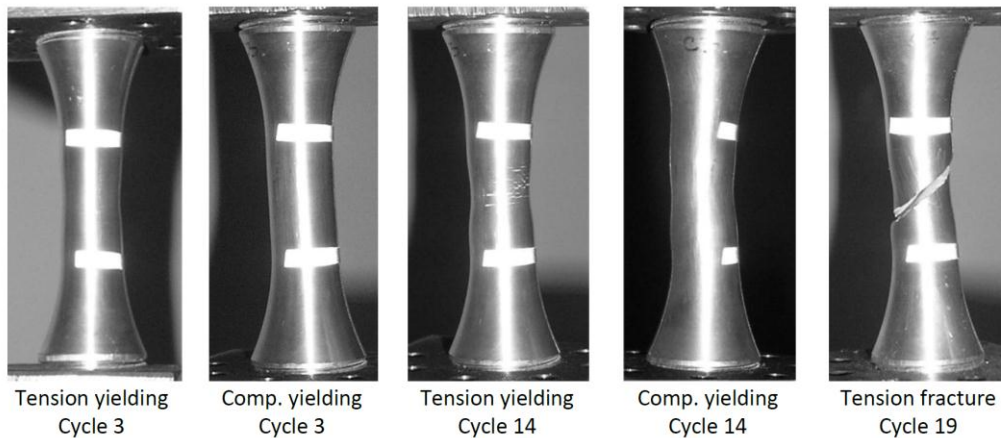


Figure 50 - Images of coupon C3

Hystereses for the cyclic tests are shown in Figures 51-53. Final degradation cycles are hidden for clarity. The loops have a bi-asymptotic shape and are composed of a linear elastic, smooth non-linear elastic-plastic transition, and an approximately linear plastic region. Transitions between the elastic and plastic regions are less abrupt for the cyclic tests as compared to the monotonic primarily due to the Bauschinger effect. Small

bumps at the zero stress level can be attributed to looseness in the double nuts holding the specimens in the fixture. Closeness of the loops indicates that cyclic softening occurred at a very low rate, especially for the specimen cycled at 2% strain. This is better shown in Figure 54, a plot of maximum cyclic stress vs. number of reversals. The rate of softening does increase slightly for the 3% and 4% specimens and the change in slope of this line appears to relate to strain amplitude. Consequently, cyclic (isotropic) hardening is relatively slow compared with kinematic hardening. This was witnessed in tests of 6060-T6 aluminum tested to strain amplitudes of +/- 0.4%, 0.8%, and 1.2% by previous researchers (Hopperstad, Langseth, & Remseth, 1995). The small amount of stress degradation in the 2% test is highlighted by the curve representative of the first quarter cycle of loading. This curve still remains lower than the stable cyclic loops until failure.

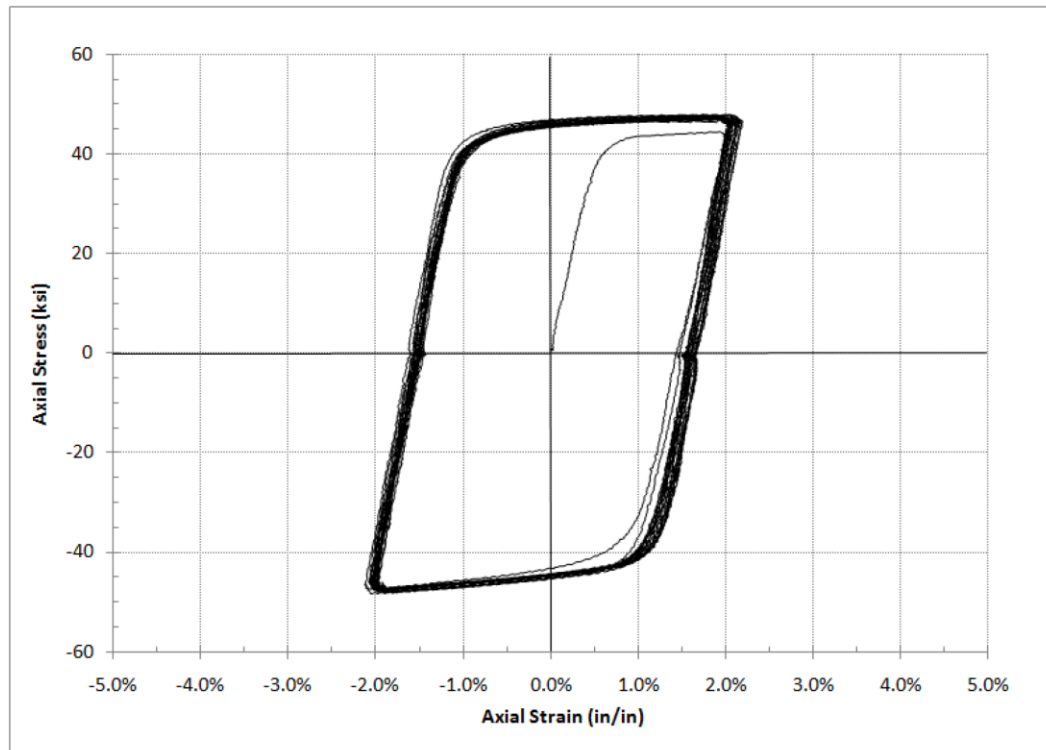


Figure 51 - Hysteresis for 2% axial strain

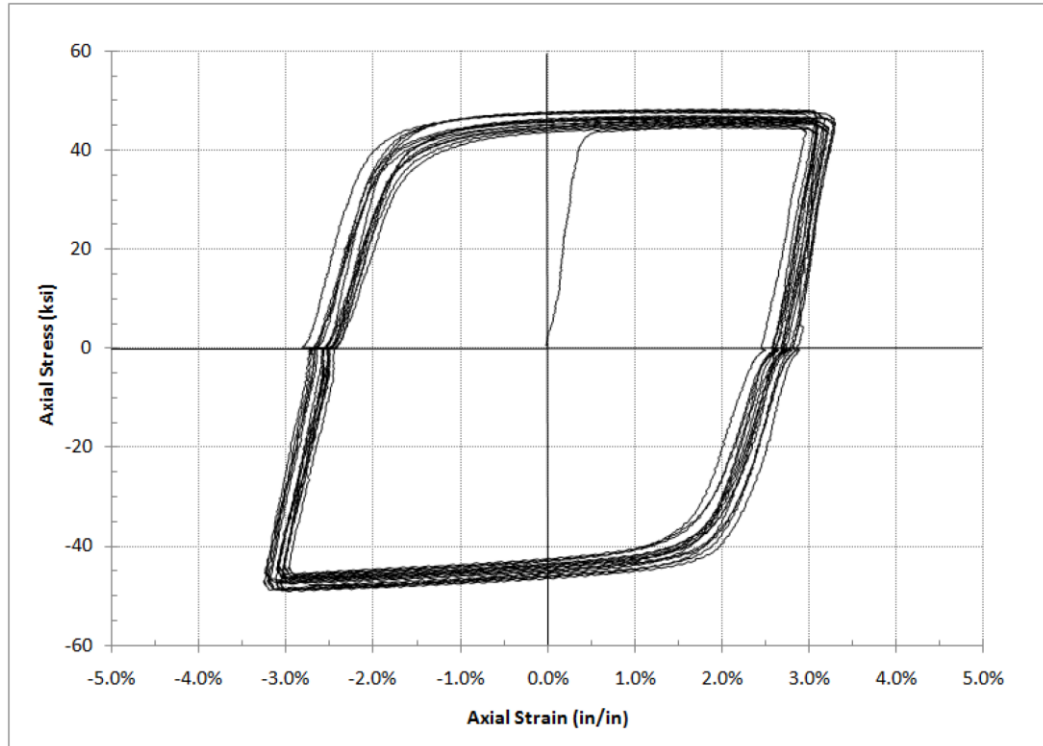


Figure 52 - Hysteresis for 3% axial strain

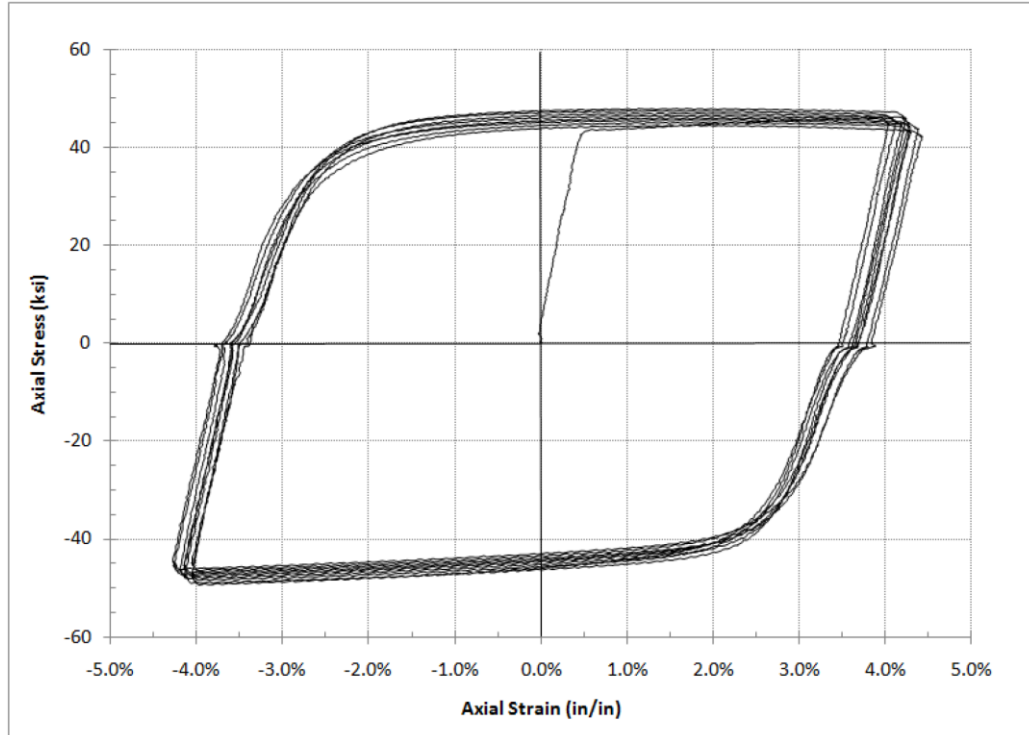


Figure 53 - Hysteresis for 4% axial strain

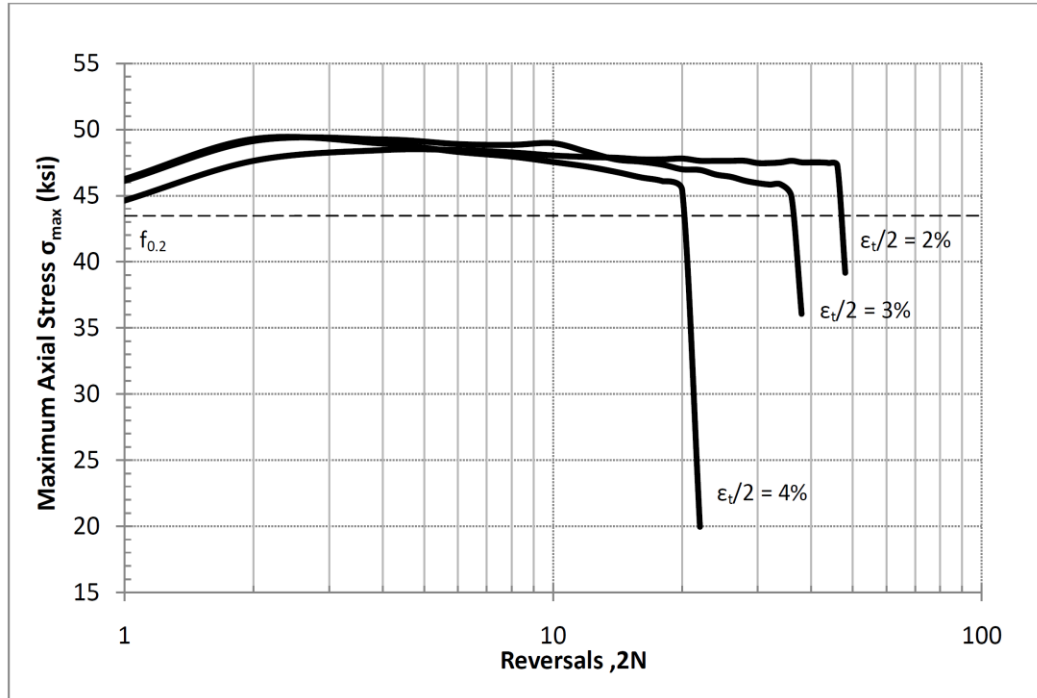


Figure 54 - Maximum cyclic stress plot

6.5 Comparison with Other Materials

The test results must be compared with those reported for other aluminum and steel alloys. Table 23 shows information available on cycles to failure and cyclic hardening for other structural alumina and low yield point steel. 6061-T651 aluminum alloy has been successfully tested to greater than 70 cycles at total strain amplitude of +/- 2.5% (Brodrick & Spiering, 1972). The fatigue life of 6061-T6 at 2-3% amplitude has been shown in the present tests as significantly less which may be a result of slight bending of the reduced section causing non-uniform strain distribution across the cross section. Because of this inconsistency between research, further testing of the 6061 alloys is required to determine if this alloy is indeed desirable for LCF applications.

Table 23 – LCF Comparison of Metallic Materials					
Material	f_{0.2} (ksi)	Strain Amplitude	Cycles to Failure	Cyclic Behavior	Reference
5454-O	16.8	1.5% 2.5%	376 92	H H	(Brodrick & Spiering, 1972)
5454-H34	37.2	1.5% 2.3%	211 73	H-S H-S	(Brodrick & Spiering, 1972)
6061-T651	40.1	1.45% 2.5%	282 71	H-S H-S	(Brodrick & Spiering, 1972)
6060-T6	34.8	1.0% 1.4%	~14 ~5	H-S H	(Borrego, 2004)
6060-T4	10.4	0.8% 1.2%	>40 >40	H H	(Hopperstad, Langseth, & Remseth, 1995)
6060-T6	30.9	0.8% 1.2%	>40 >40	H-S H-S	(Hopperstad, Langseth, & Remseth, 1995)
6082-T6	44.5	1.0% 1.5%	~100 ~80	H H-S	(Borrego, 2004)
6063-T	21	0.3% 1.0%	>1000 >100	H-S H-S	(Ma, Chen, Tian, Che, & Liaw, 2009)
7075-T6	73	0.4% 1.2%	>1000 >100	S S	(Li & Marchand, 1989)
LYP Steel BT-LP225	35.1	3% 4%	~60 ~40	H H	(Dusicka, Itani, & Buckle, 2007)
H indicates cyclic hardening until failure S indicates cyclic softening until failure H-S indicates initial cyclic hardening followed by stability or slight softening until failure					

For comparison, low yield point (LYP) steels have successfully been tested to higher strain amplitudes (>4%) and achieved at least 40 to 60 cycles before failure (Dusicka, Itani, & Buckle, 2007). Since steel is the most commonly used material in BRB cores and has undergone numerous qualification tests to prove its viability, the proposed aluminum alloy must sustain a similar number of cycles to be considered as a viable candidate material. An exploration of these other materials is therefore warranted.

Preliminary research indicates two candidate materials for similar testing. 6061-T6 alloy may be able to achieve a greater number of cycles if it is annealed. The annealing process typically is used to soften the material to increase ductility thus providing improved cold-working properties. Annealed 6061, or 6061-O, has typical

yield strength of 8 ksi, tensile strength of 18 ksi, and an elongation at failure of 25-30%. However, the much lower yield strength would require considerable larger core section area in order to withstand the seismic design loads which would significantly increase the weight of the ULWBRB. Therefore, this option may be less than desirable.

Aluminum-magnesium alloy 5086 is readily available in temper –H111 in both extruded round rods and structural angles and is primarily used in marine environments where corrosion resistance, good workability, and weldability are desired. This is a non-heat-treatable, strain hardened alloy that has typical yield and ultimate tensile strength of 30 and 45 ksi, respectively. Elongation at fracture is typically 21% for round bars of ½ inch diameter indicating good ductility (Aluminum Association, 2000). This material is also available in annealed –O tempers with a typical yield and ultimate tensile strength of 17 and 38 ksi, respectively which exhibit excellent ductility to 22% elongation at fracture. LCF tests of strain hardened 5454-O and 5454-H34 alloy hourglass shaped coupons were reported to have achieved 92 and 73 cycles to failure, respectively, when tested to 2.5% strain (Brodrick & Spiering, 1972)

Additionally, aluminum-copper alloy 2024 is commonly used in aircraft structures requiring high fatigue resistance. 2024-O is the annealed designation with typical yield and ultimate tensile strengths of 11 ksi and 27 ksi, respectively. Elongation at fracture is typically 22% for round bars of ½ inch diameter (Aluminum Association, 2000). The heat treated –T3 temper is harder and stronger with typical yield and ultimate tensile strengths of 50 ksi and 70 ksi, respectively. Elongation at fracture is typically 18% for round bars of ½ inch diameter (Aluminum Association, 2000). This alloy is available in extruded shapes such as angles or round bars. However, standard structural angle sizes,

as used in the ULWBRB, are only available by custom extrusion.

6.6 Constitutive Model

A constitutive material model is required for the numerical cyclic tests. Accurate prediction of inelastic material behavior can be made by calibrating an accepted model with the experimental data. A general nonlinear combined kinematic-isotropic model is chosen as defined in Equation 85 where f is the yield function, α is the backstress tensor that describes how the center of the yield surface moves in stress space as plastic strains accumulate, and σ^0 is the yield stress that can change magnitude as plastic strains accumulate. The first term indicates the von Mises yield potential function. This model is capable of modeling the Bauschinger effect, cyclic hardening with plastic shakedown, and relaxation of the mean stress.

$$f = q(\sigma - \alpha) - \sigma^0 \quad (85)$$

Kinematic hardening in this combined model is governed by Equation 86 where C , σ_0 , and γ are all material parameters. The rate at which the kinematic hardening modulus decreases with plastic straining is controlled by γ .

$$\dot{\alpha} = C \frac{1}{\sigma^0} (\sigma - \alpha) \dot{\epsilon}^{pl} - \gamma \alpha \dot{\epsilon}^{pl} + \frac{1}{C} \alpha \dot{C} \quad (86)$$

This component can be defined in ABAQUS by either inputting the material parameters for initial yield stress at zero plastic strain ($\sigma|_0$), kinematic hardening parameter (C), and rate at which hardening modulus decreases with plastic straining (γ) directly or by using test data from the half-cycle of hysteresis data before any severe degradation of the stress-strain data occurred. Most accurate results are obtained if test data are provided for the specific strain range occurring in the simulation.

The isotropic component of the model can be defined by the exponential relationship given in Equation 87 where Q_∞ is the maximum change in the size of σ^0 and b is the rate at which σ^0 changes with plastic strain.

$$\sigma^0 = \sigma|_0 + Q_\infty \left(1 - e^{-b\bar{\varepsilon}^{pl}}\right) \quad (87)$$

This component can be defined in ABAQUS by inputting equivalent stress and equivalent plastic strain data from the backbone curve from the positive side of the hysteresis of a symmetric strain experiment. All data must first be converted from engineering stress and strain to true stress and logarithmic strain by using Equations 88 – 90.

$$\sigma_{true} = \sigma_{eng}(1 + \varepsilon_{eng}) \quad (88)$$

$$\varepsilon_{true} = \ln(1 + \varepsilon_{eng}) \quad (89)$$

$$\varepsilon_{pl} = \varepsilon_{true} - \frac{\sigma_{true}}{E} \quad (90)$$

Since plastic strain in the range of 2-3% is expected during full-scale brace simulations, data points from the 3% strain experiment are used. In order to remain consistent with previous assumptions on the yield stress of the material, the second half-cycle data is first adjusted to a nominal yield stress of 35 ksi by scaling all the stress data by the ratio: nominal yield stress/yield stress at the first quarter cycle. This equals 0.83. Adjusted stress values are shown on the right vertical axis of Figure 55. Seven data points are then plotted on the third quarter cycle beginning from the adjusted yield stress (σ_0). Plotted strain values are then modified to make the stress at point σ_0 that of zero plastic strain according to Equation 91 thus shifting the portion of the curve above σ_0 all into the positive side of the ordinate.

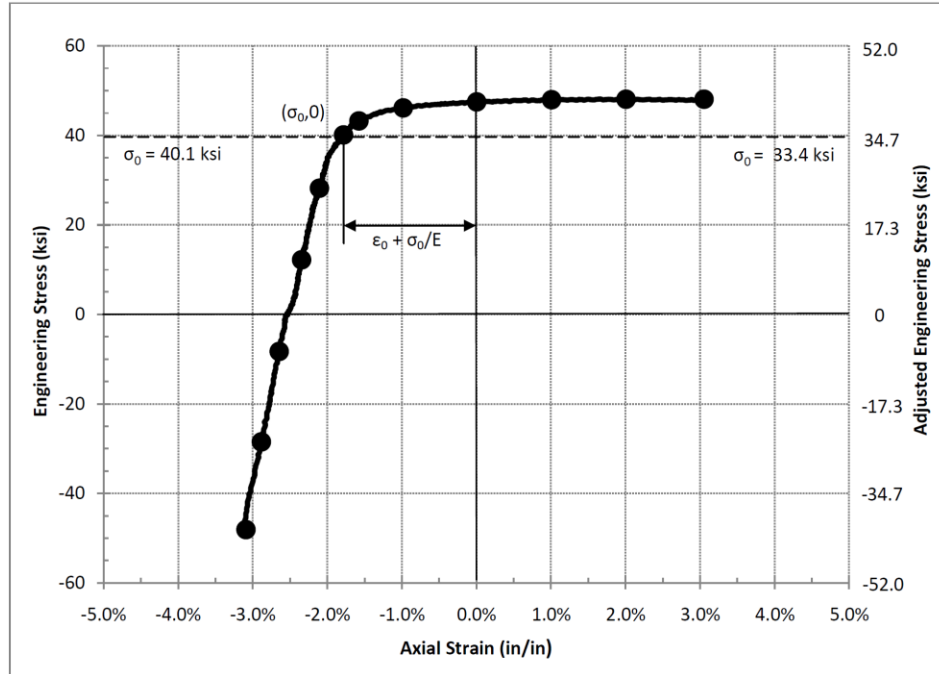


Figure 55 - Second half-cycle plot for 3% strain

$$\epsilon_{ABAQUS} = \epsilon_{true} - \frac{\sigma_0}{E} - \epsilon_0 \quad \text{Where } \sigma_0 = 33.4 \text{ ksi and } \epsilon_0 = 1.474\% \quad (91)$$

Table 24 shows the final stress and strain values for the third quarter cycle to be input into ABAQUS beginning with the adjusted true yield stress at zero plastic strain. This defines the kinematic hardening portion of the combined model and should give accurate results for the range of cycles to be tested. As previously stated, isotropic, or cyclic, hardening will be neglected since its effect is negligible.

6.7 Verification of Constitutive Model

Verification of the proposed hardening model is made by modeling the aluminum coupon in ABAQUS with an extra fine mesh of tetrahedral continuum elements. Figure 56 shows the finite element model mesh used as a result of the convergence study shown in Figure 57. The convergence study considered elastic strain of the center node when loaded with a small elastic displacement. Convergence of model stiffness is shown by

the lack of difference between the 50,258 and 99,004 element mesh.

Table 24 – Kinematic Hardening Stress-Strain Data					
Data Pt.	σ_{eng} (ksi)	ϵ_{eng} (%)	σ_{true} (ksi)	ϵ_{true} (%)	ϵ_{ABAQUS} (%)
1	33.42	-1.783	32.83	-1.799	0
2	36.02	-1.578	35.45	-1.590	0.209
3	38.48	-0.983	38.10	-0.987	0.812
4	39.58	0.0021	39.59	0	1.801
5	39.97	1.008	40.37	1.003	2.802
6	40.07	2.004	40.87	1.984	3.783
7	40.08	3.053	41.31	3.007	4.807

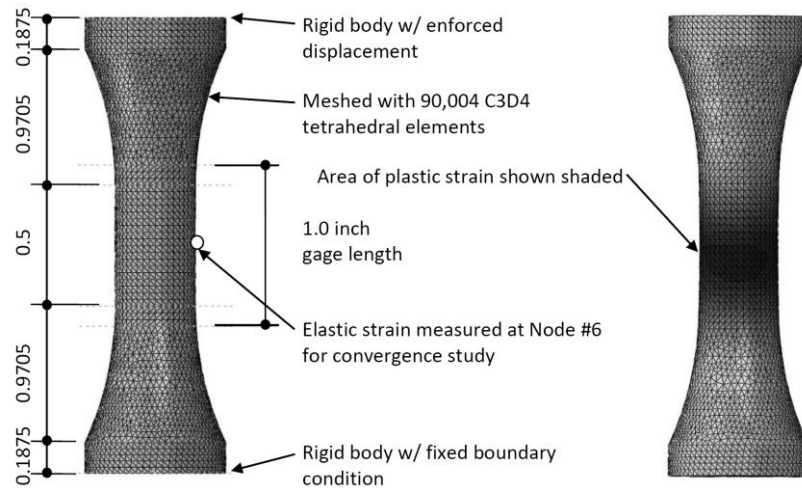


Figure 56 - Coupon FEA model

The kinematic hardening data is used in the model and allowed to run for two cycles. Superposition of three backstresses is used in order to better capture the shape of the experimental hysteresis loops in the Bauschinger region. Multiple backstresses help account for the strain ratcheting effect present in this problem. Figure 58 superimposes numerical data on the scaled experimental and indicates reasonably accurate calibration

for all strain amplitudes. The difference between the numerical and experimental loops is the greatest on the 4% strain case. The change in slope of the linear portion of the loop as the stress goes through zero causes a sharper elasto-plastic transition for the numerical data as compared to experimental. This can be attributed to a small amount of buckling during the compression excursions of the experimental tests causing the axial stiffness to diminish through mobilization of bending. The Bauschinger effect is effectively captured with a lower σ' value as compared to the first quarter cycle yield stress σ .

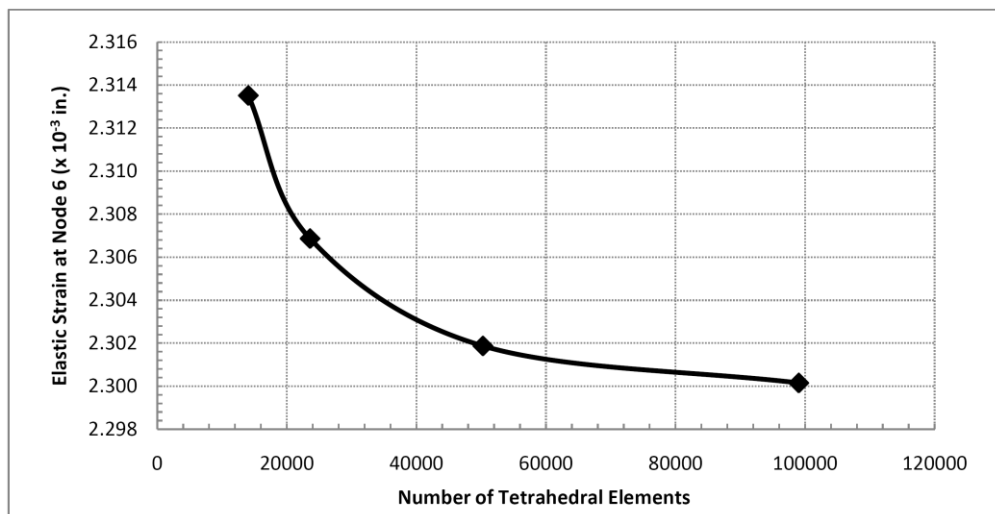


Figure 57 - Coupon FEA convergence study results

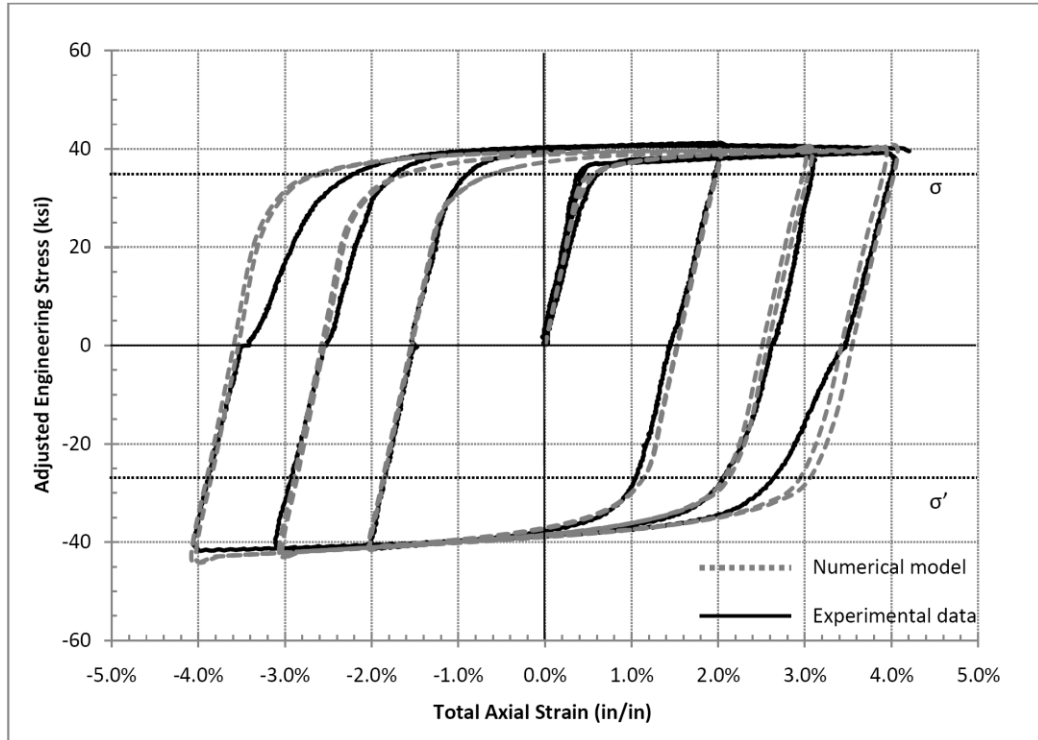


Figure 58 - Calibration of kinematic hardening model

7.0 NUMERICAL MODELING

7.1 Objective

Numerical modeling begins with a parametric study of monotonically loaded ULWBRB configurations with and without end moments for validation of the proposed analytical models. The four-angle core with square tube restraining elements serves as the test subject since it is envisioned as the most promising configuration. A successful monotonic test is defined as the ability of the core to yield in compression without buckling to the maximum axial deformation expected in the design seismic event. The study aims to capture primarily global buckling failure modes; however, local buckling is allowed to a limited extent.

After the monotonic tests, modeling focuses on a similar brace loaded cyclically. This study considers restrainer stiffness and its effect on global buckling as well as cyclic material behavior when loaded well past its yield point. Reliable and symmetric hysteretic numerical data should be achieved even when the brace is subjected to several cycles of high plastic deformation. This cyclic yielding should prove to be a stable mechanism to dissipate seismic energy. At the conclusion of this section, the feasibility of using the ULWBRB for such is assessed.

7.2 Numerical Model

Two test braces are selected for the numerical study that remain consistent with the partial and full-scale geometry and are shown in Figure 59. Two different reduced

core section lengths allows examination of the effect longer buckling length has on required restrainer stiffness as well as measure the proposed scaling method's accuracy.

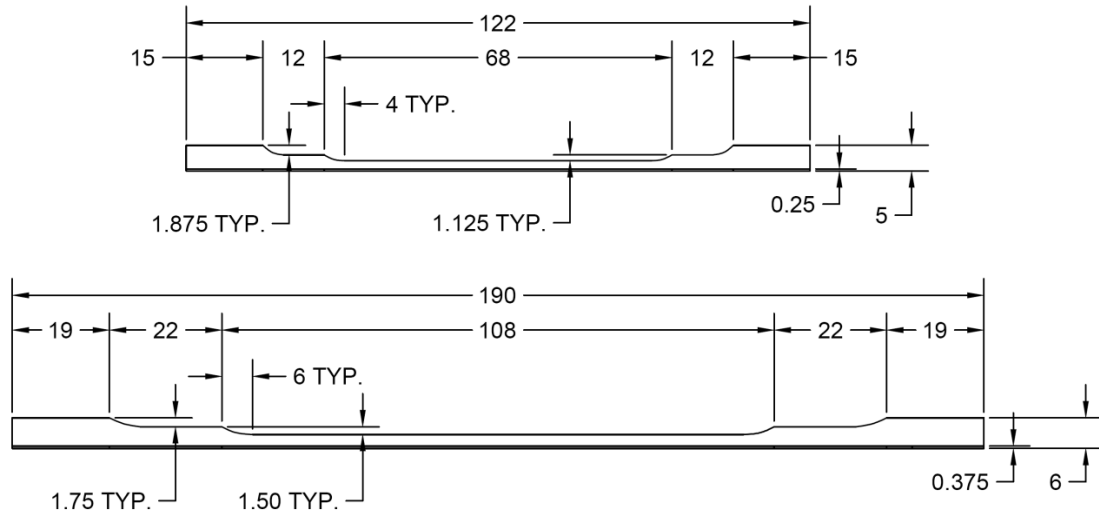






Figure 59 - Test brace geometry, partial-scale brace (top), full-scale brace (bottom) (all dimensions in inches)

Geometric Imperfections

For both the monotonic and cyclic tests, geometric imperfections are assigned to the four angle core and FRP tube. Introduction of out-of-straightness into the model is expected to have a lesser effect on buckling than induced in-plane end-moments from BRBF deformation. However, capturing the first four buckling modes and introducing scaled deformations into the mesh served to stimulate global buckling of the brace subjected to purely axial load as well as local buckling of the unrestrained portion of the intermediate section of the core. Figure 60 shows a graphical depiction of the first four mode shapes plus the 8th mode for the partial and full-scale brace when a linear perturbation was applied to the brace core with no restraint. Global buckling of the reduced section predominates, as expected. The pairs consisting of modes 1 & 2 and 3 & 4 have similar eigenvalues since the model is symmetrical.

Figure 60 - Linear Buckling Analysis Results	
Eigenmode Shape	Eigenvalue
1 st Mode - y-y bending 	Partial-scale P = 122 kips
	Full-scale P = 178 kips
2 nd Mode - x-x bending 	Partial-scale P = 122 kips
	Full-scale P = 178 kips
3 rd & 4 th Mode - z-z bending about both principal axes 	Partial-scale P = 160 kips
	Full-scale P = 322 kips
8 th Mode - twisting 	Partial-scale P = 226 kips
	Full-scale P = 447 kips

Scaling each of the buckling modes to represent realistic material and erection tolerances is crucial. It has been presented throughout the analytical modeling section that a maximum global out-of-straightness of $L/1000$ has been established as a workable tolerance for erection of building structures. This works out to 0.12 and 0.19 inches for the partial and full-scale braces, respectively. Therefore, the first two buckling modes are scaled to this value which should stimulate global buckling. The third and fourth modes exhibits two buckling waves - acting in the angle's principal axes and are scaled to $L/4000$, or 0.05 inches. The superposition of all four modes serves to stimulate buckling in the principal axis direction when no end moments are applied. Higher energy buckling modes consisting of torsional or local instability are found in modes five and higher. These modes are not introduced as geometric imperfection since local buckling are

continuously restrained by the restrainer in this model. An example of one of the higher modes is shown in Figure 60.

General Model Configuration

The numerical model uses ABAQUS/CAE 6.10-2 finite element analysis (FEA) software. Figure 61 shows the model setup for the full-scale brace with final element formulations and number of elements.

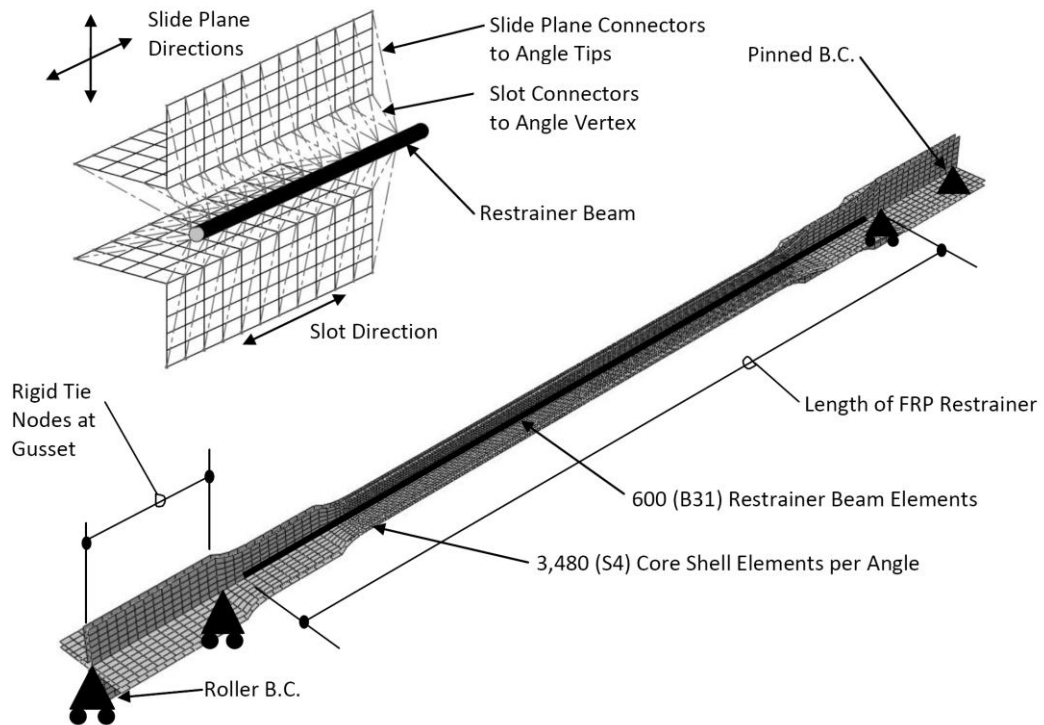


Figure 61 - Full-scale test brace finite element model

Nodes at the vertex and tips of the core angles are modeled with basic slotted or slide-plane connector elements to couple their degrees of freedom with the restrainer in the transverse bending direction while leaving the axial degree of freedom decoupled. Connectors are a realistic simulation of sandwiching the angle legs between FRP tubes and high compressive modulus plastic spacers that serve to prevent local buckling while

allowing for axial and Poisson effects. In each model, the spacing between slotted connectors is kept at a constant value of one inch. This leaves two unsupported nodes in between slotted connectors for the 3,480 element mesh where the axial dimension of the elements was 1/3 inch.

In future studies, local buckling of the core outstands should be considered by imposing a local buckling wave representative of a small amount of rippling in between the slotted connectors shown greatly exaggerated in Figure 62. Rippling along the core length has been reported in the literature for traditional BRBs and is expected to occur in the ULWBRB since support of the angle legs by plastic does not provide perfect restraint. A minor amount of rippling is a desirable energy dissipation mechanism if local instability can be controlled. Superposition of higher buckling modes on the four lowest modes is envisioned as a possible way to stimulate the desirable rippling effect. Research into local buckling phenomena on aluminum angles with thick plate (Mindlin) theory is currently under way (Mazzolani, Piluso, & Rizzano, 2011).

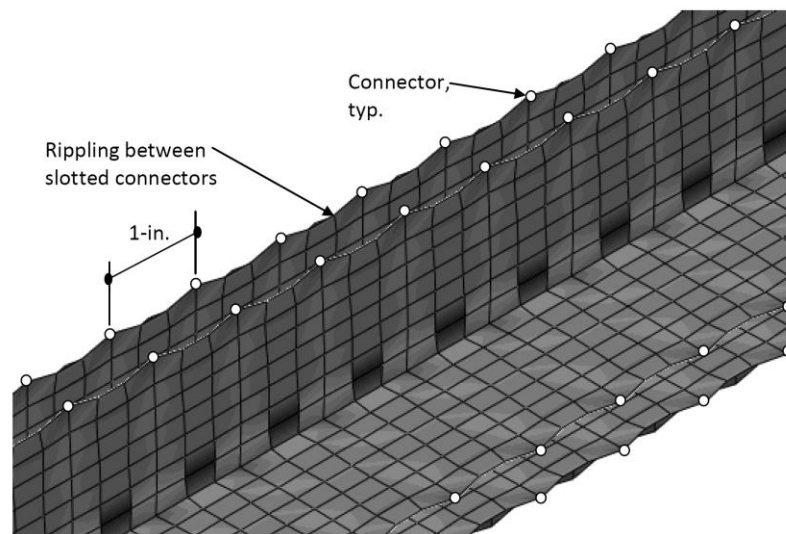


Figure 62 - Rippling in between slotted connectors for local buckling study

Convergence Study

The difference between thin and thick shell formulations must be considered in properly conducted convergence study. Determination of the type of shell problem is made by examination of the shell aspect ratios calculated by dividing the thickness by the characteristic length. Ratios less than 1/15 are typically considered thin shells. Since flexure may be occurring at the global or local level, this ratio is calculated for both in Table 25. It can be seen that transverse shear flexibility is not important for global flexure but may be for local or torsional flexure of the angle legs which has a much smaller characteristic length. The difference between reduced (S4R) and full (S4) integration 4-node general purpose shells and thin (S8R5) and thick (S8R) conventional 8-node shells are compared for a varying number of elements. General purpose 4-node shells capable of modeling large membrane strains are hypothesized to give reliable results with increased computational efficiency over the quadratic elements.

Table 25 – Shell Element Aspect Ratios					
Condition	Bending Axis	Thickness (in)	Characteristic Length (in)	Aspect Ratio (t/L)	Type of Shell
Global-PS	x-x, y-y	0.25	60	1/240	Thin
Local-PS	x-x (rippling)	0.25	2.0	1/8	Thick
Global-FS	x-x, y-y	.375	96	1/256	Thin
Local-FS	x-x (rippling)	.375	2.75	1/7.3	Thick

The optimum number of degrees of freedom for the core is determined by performing a convergence study using H & P-refinement of the shell mesh with 332, 680, 1092, 1,940, and 3,480 shell elements per angle. First, a pull test is run on each model in

displacement control in order to determine convergence of tension yield strength. An elasto-plastic material with 35 ksi yield and a 5% post-yield hardening is used to remain consistent with the analytical work provides numerical stability beyond yield. Enforced displacement was arbitrarily set at 2 inches for the convergence study.

Figure 63 shows the location of the nodes where strain and von Mises stress are read for each number of elements in order to construct a convergence plot. Two locations are selected in order to capture behavior at both the elastic and plastic regions. Figure 64 shows that von Mises stress at the elastic region converges from the top down and reaches stability at 1,940 elements. Maximum in-plane principal elastic strain (EE) appears to converge with as little as 332 elements as can be expected since strain usually converges quicker than stress. Equivalent plastic strain (PEEQ) and stress at the plastic region are unaffected by number of elements or element formulations. Rapid stress convergence is seen with the S4, S8R5, and S8R elements over the S4R.

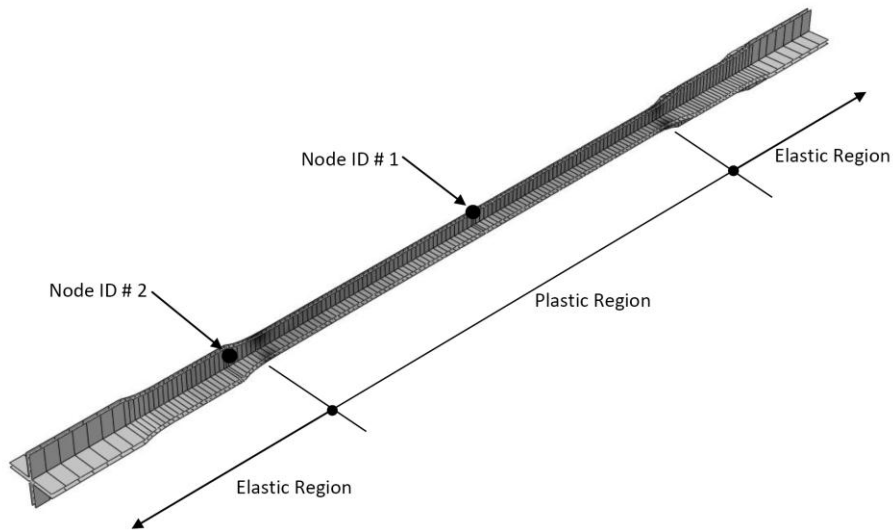


Figure 63 - Location of nodal stress values

Axial load vs. displacement curves for tension are plotted in Figure 65 to show

how the element formulation affects yield strength and post-yield stiffness. The 3,480 element mesh was used in all studies. Theoretical yield strength is calculated as 289 kips based on A_1F_y using the actual cross sectional area of the shell elements in the numerical model equal to 4.0 in². The model exhibits a yield strength of 283 kips, only 3% lower than theoretical. Both the general purpose thin/thick shells (S4R, S4) and conventional thick shell give similar results (S8R) while the conventional thin shell (S8R5) exhibits a slightly higher post-yield hardening. The tension tests are also run for the 332, 680, 1092, 1,940, and 3,480 element meshes. All results are similar indicating that membrane strains are independent of the mesh fineness.

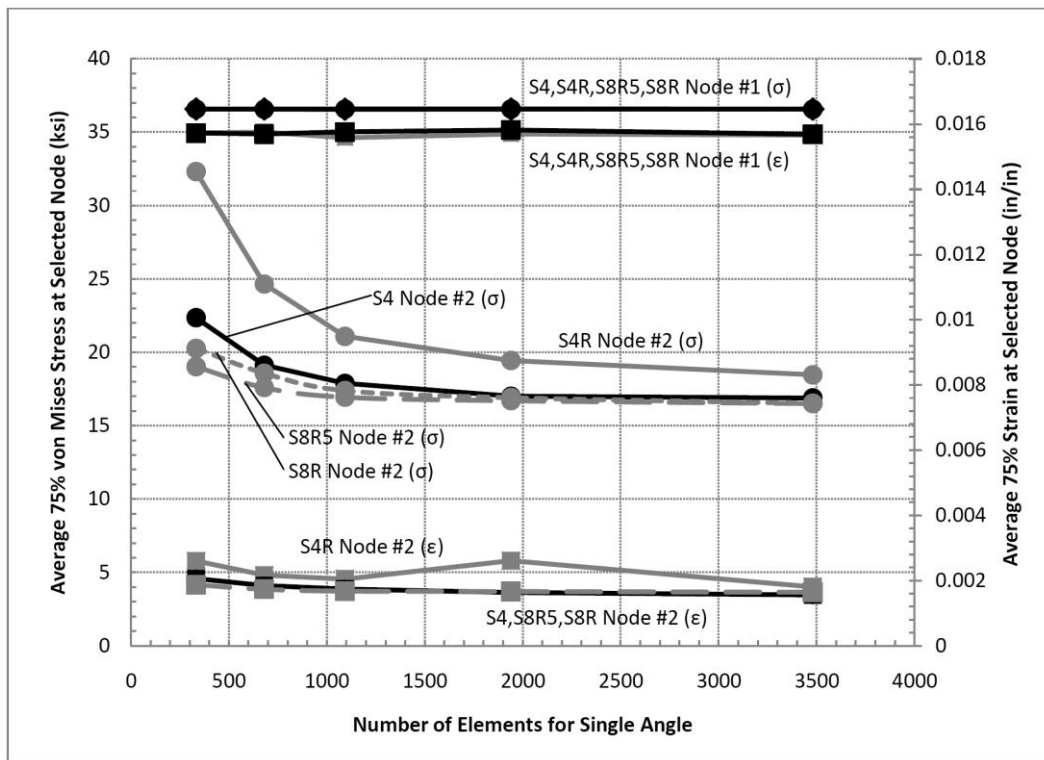


Figure 64 – Stress & strain convergence plots at selected nodes

The second element study is done in the compression regime as shown in Figure 65. Axial displacement is set at two inches with restrainer stiffness of 144,000 and

433,000 k-in². Two different restrainers are used in order to compare the element formulation on inadequately and adequately restrained cores. The element formulation is hypothesized to be more important for inadequately restrained cases where global buckling and flexure are present. Compression yield strength is shown to be symmetrical with tension for the adequately restrained case. Compression buckling of the inadequately restrained core occurs at approximately 270 kips for all element formulations in the principal z-z axis direction except the S4R brace that buckles in the geometric x-x axis. Elements appear to affect only post-buckling behavior which is dependent on the post-buckling path and severity of transverse bending. The post-buckling paths are all quite similar.

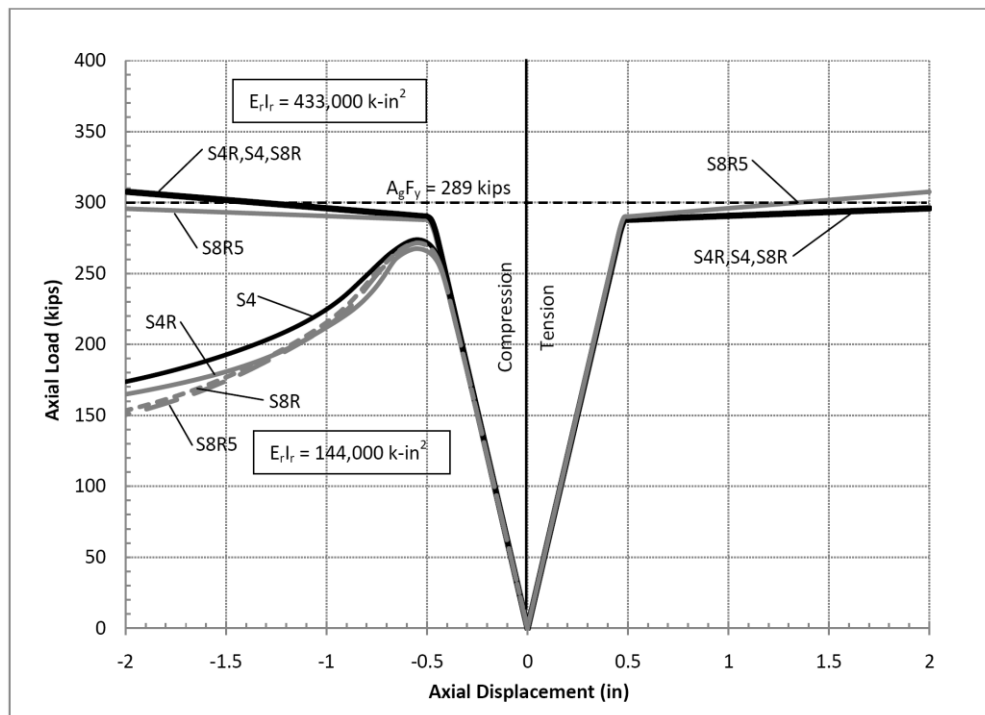


Figure 65 - Tension & compression comparison of element formulation

Table 26 shows the axial force, transverse displacement, and von Mises stress at the mid-length of the core for the four different element formulations with 3,480 elements

per core angle. The results show that varying the element formulations has a minimal effect on transverse bending and restrainer demand given that transverse displacement and angle stress are similar. The amount of post-buckling strength at 2 inches displacement is also similar between the elements. The S4 element achieved the highest value which is only 15% greater than the S8R5 element.

The results of the convergence study show that a relatively fine mesh of fully integrated general-purpose thin or thick shells is able to effectively capture yielding and buckling behavior of the brace with reasonable accuracy as compared to conventional quadratic shells. This indicates that shear flexibility is not a concern for the global buckling mode. The S4 element formulation is selected due to its capability of modeling large membrane strains which is expected to be the predominate behavior of an adequately restrained brace. The fine mesh is selected because future local buckling studies will require unsupported nodes as previously discussed. A similar convergence study is also run for the partial-scale brace with similar results. The selected number of elements are 3,314 (S4) for each core angle and 360 (B31) for the restrainer.

Table 26 – Results at 2-in Displacement (3,480 Elements)				
Element Formulation	Type of Shell	Axial Force (kips)	Mid-Length Transverse Y-Displacement (in)	Von Mises Stress at Mid-length of Angle (ksi)
S4R	Thin or thick	165	9.33 (x-x axis)	32.8
S4	Thin or thick	174	9.21 (z-z axis)	35.1
S8R5	Thin	151	9.14 (z-z axis)	29.6
S8R	Thick	154	9.13 (z-z axis)	30.3

7.3 Monotonic Tests

A series of monotonic axial tests are carried out in displacement control with the

same material and geometric imperfections assigned in the convergence studies. Table 27 shows the parameters for each of the test braces. Axial deformation representative of the maximum expected during cyclic testing is applied to the loading end and set at 2 and 4 inches for the partial and full-scale braces, respectively. An equivalent square tube section size is assigned to the beam elements to simulate the transverse bending stiffness of the four tube restrainer acting compositely.

Table 27 – Monotonic Test Brace Parameters							
Designation	Brace Scale	Equivalent FRP Restrainer Size (in)	Calculated Stiffness $E_r I_r$ (k-in²)	Ψ Ratio	P_c/P_y	P_{max}/P_y	$\Delta_{axial}/\Delta_{transverse}$
PS33	Partial	3 x 3 x ¼	9,770	0	0.13	0.84	0.251
PS4.54.5	Partial	4 ½ x 4 ½ x ¼	35,900	0	0.48	1.15	0.883
PS4.74.7	Partial	4 ¾ x 4 ¾ x ¼	42,700	0	0.57	1.18	5.78
PS4.54.5-M1	Partial	4 ½ x 4 ½ x ¼	35,900	0.41	0.48	1.10	0.500
PS55-M1	Partial	5 x 5 x ¼	50,100	0.41	0.66	1.15	0.832
PS5.75.7-M1	Partial	5 ¾ x 5 ¾ x ¼	77,800	0.41	1.03	1.18	4.20
PS55-M2	Partial	5 x 5 x ¼	50,100	0.82	0.66	1.11	0.511
PS66-M2	Partial	6 x 6 x ¼	88,900	0.82	1.18	1.15	1.88
PS7.57.5-M2	Partial	7 ½ x 7 ½ x ¼	178,000	0.82	2.36	1.18	4.09
FS77	Full	7 x 7 x ¼	144,000	0	0.34	1.00	0.716
FS88	Full	8 x 8 x ¼	216,000	0	0.52	1.12	0.564
FS9.29.2	Full	9 ¼ x 9 ¼ x ¼	340,000	0	0.81	1.31	8.70
FS88-M1	Full	8 x 8 x ¼	216,000	0.15	0.52	1.11	0.348
FS99-M1	Full	9 x 9 x ¼	313,000	0.15	0.75	1.24	0.585
FS9.79.7-M1	Full	9 ¾ x 9 ¾ x ¼	400,000	0.15	0.96	1.31	6.45
FS99-M2	Full	9 x 9 x ¼	313,000	0.30	0.75	1.21	0.426
FS1010-M2	Full	10 x 10 x ¼	433,000	0.30	1.04	1.28	0.976
FS10.210.2-M2	Full	10 ¼ x 10 ¼ x ¼	467,000	0.30	1.12	1.30	3.28

The third restrainer size in each of the sets is determined by running multiple analyses to find the minimum restrainer size required to preclude buckling. Since this

study measures only the effect of global buckling, torsional rigidity of the tube is not given an equivalent value. End moments about the y-y global axis are applied to simulate the effects from frame drift as previously shown in Figure 38. The end moment varies linearly with applied axial displacement and is shown in Table 27 as a ratio Ψ of applied end moment over available plastic moment of the intermediate section of core as previously given in Tables 12 and 18. Values of Ψ are determined by using a maximum end moment of 136 k-in for both the partial and full-scale brace. End moments are applied in opposite directions to cause single curvature flexure in the brace.

Each of the test braces has to pass two criteria in order to be considered adequately restrained from global buckling. First, target axial displacement is required to be achieved before buckling instability of the numerical model occurs. Inadequately restrained test braces exhibit a buckling progression as follows: 1) uniform axial stress with uniform yielding at the reduced section and only a slight amount of bending, 2) increasing transverse displacement and increasing bending stresses at the ends of the restrainer, 3) plastic local buckling of the core angle legs leading to hinging, and then 4) overall global buckling. Images of this failure progression are shown in Figure 66.

Global buckling occurs without hinging at the restrainer end in braces with a very small restrainer bending stiffness (PS33). For these, high bending stresses cause non-uniform yielding of the reduced section with yielding occurring only on the compressive side of the core neutral axis. Buckling occurs in the principal (z-z) axis of the composite core when no end moment is applied. This buckling direction is due to initial imperfections assigned equally in both transverse directions (about the x-x and y-y axes). Conversely, the test braces with applied end moment always buckle in the direction of the

moment (y-y axis). However, they do have a slight transverse deformation in the orthogonal direction (x-x axis) most likely a result of the initial imperfections.

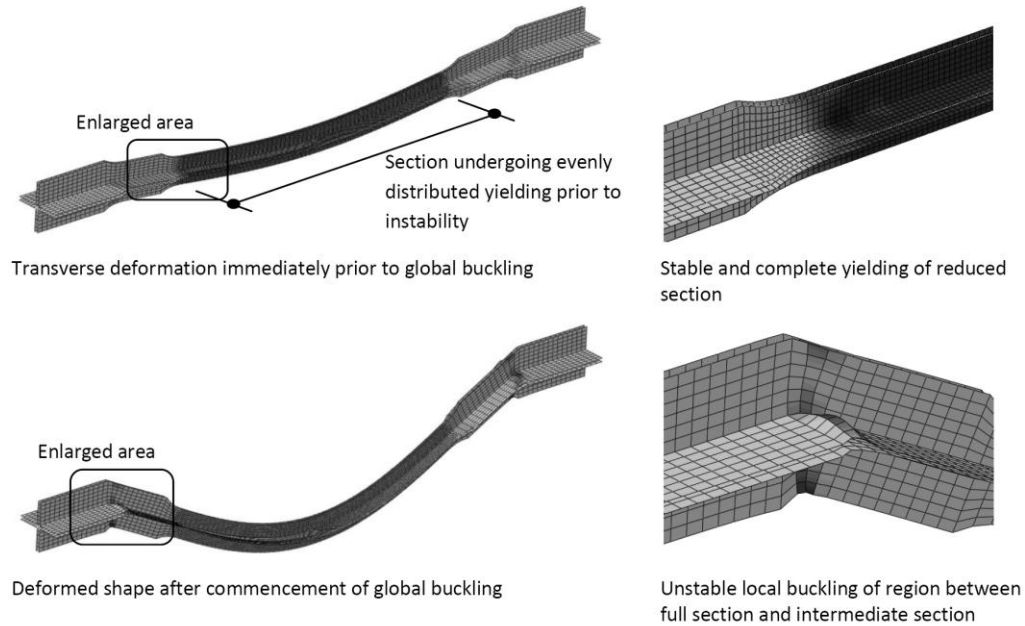


Figure 66 - Images of buckling for inadequately restrained core

The second criteria used to determine adequate buckling restraint is target axial displacement has to be reached without exceeding the allowable bending strength of the composite restrainer. This was assessed using the maximum allowable transverse displacement of the restrainer at its mid-length in the analytical modeling. The maximum transverse displacement of the FRP restrainer (Δ_t) before allowable flexural stress is achieved is calculated as 0.61 inches using Equation 42 estimating the distance from the neutral axis to extreme fiber (c) as 4 inches for the partial-scale brace. The full-scale brace used 1.33 inches for Δ_t and 5 inches for c . This allowable value intends to provide a reasonable limit to the bending stresses imparted to the FRP tubes and wrap in order to prevent stiffness and strength degradation over repeated cyclic loading. Obviously, the maximum deflection varies depending on the restrainer materials used.

Results of the numerical tests are combined into logarithmic plots of both axial displacement vs. axial load and transverse displacement at the mid-length of the restrainer vs. axial load. Plots show the load limits for the three different assigned restrainer stiffnesses. Figure 67 shows the partial-scale braces with geometric imperfections but no applied end moments while Figures 68 and 69 show the curves for end moment ratios $\Psi = 0.41$ and $\Psi = 0.82$, respectively. Solid filled markers indicate successful test braces that reached the target axial displacement before achieving either failure criterion. Unfilled markers indicate failure before the target. In many cases the theoretical yield strength of the core is exceeded even though the target displacement is not reached. This is due to the assigned 5% post-yield hardening which is necessary to keep the numerical model from reaching instabilities witnessed when using perfectly plastic material properties. Axial load at 2 inches compressive deformation was 165 kips with the post-yield hardening, only slightly above that achieved in monotonic tension tests. Load symmetry is a good indication of adequate buckling restraint since rippling, transverse displacement, and concentrated bending at the interface of the full and intermediate section are not present in the tension test.

Applied end moments have a large effect on the required restrainer stiffness for the test braces. The braces without are able to achieve axial displacements beyond the target value with 42,700 k-in² of restrainer stiffness. The required $E_r I_r$ for the remaining braces is 50,100 k-in², 78,800 k-in², 114,100 k-in², 178,000 k-in² for end moment ratios of $\Psi = 0.205, 0.41, 0.615, \text{ and } 0.82$, respectively. High sensitivity to end moments caused by BRBF deformation was also realized in the analytical modeling. End moments are certain during periods of high frame drift and must be incorporated into the design to

prevent unconservative results. Determination of the amount of end moment can be made with a nonlinear pushover analysis incorporating BRB geometric and material properties. Analysis shall assume that the core has minimal contribution in resisting bending since during compression or tension yielding its stiffness will be a fraction of the elastic stiffness. Since the quantification of end moments is not part of this study, the range studied is intended to capture those typical in design. Actual moments will be effected by frame geometry, member stiffness, BRB stiffness, rigidity of end connections, loading protocol, and the nonlinear behavior of BRB materials.

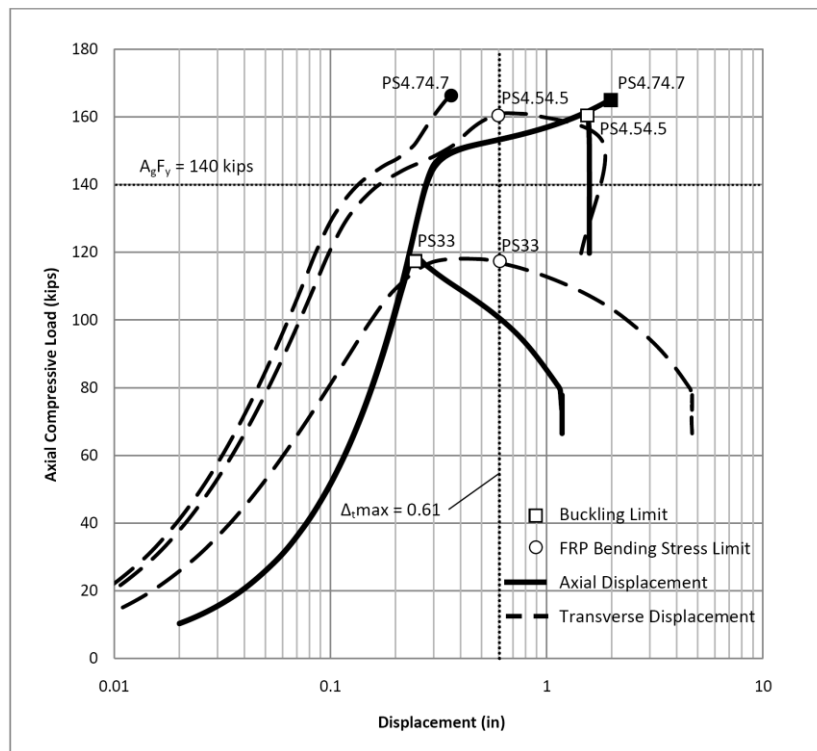


Figure 67 - Partial-scale load vs. displacement plot, $\Psi = 0$

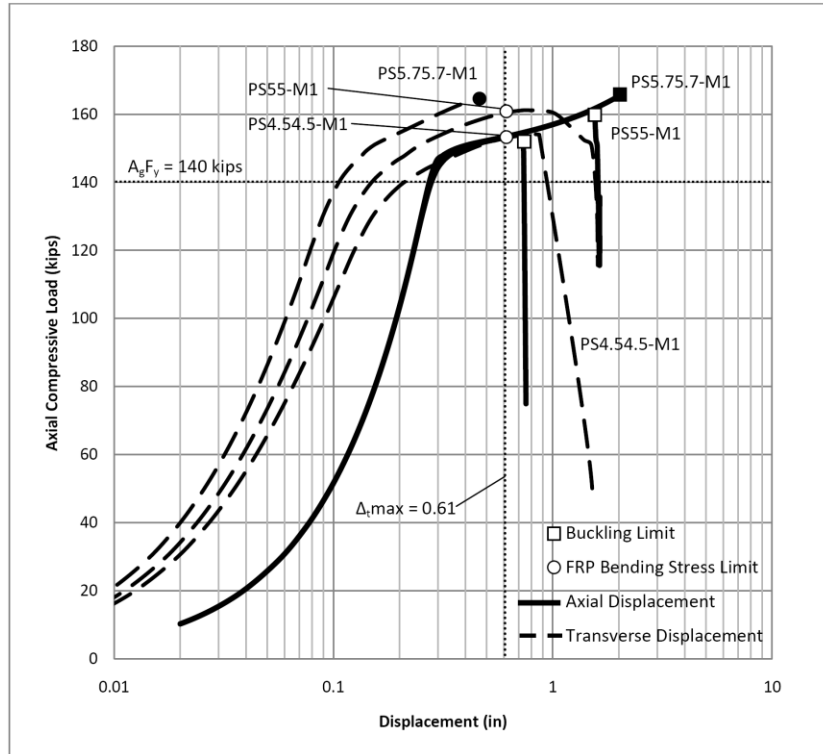


Figure 68 - Partial-scale load vs. displacement plot, $\Psi = 0.41$

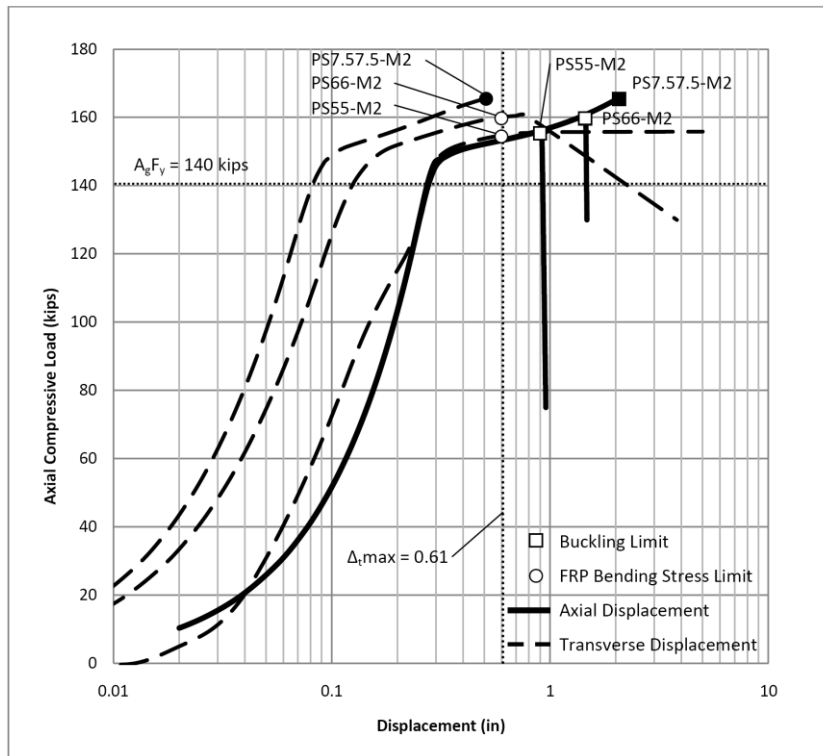


Figure 69 - Partial-scale load vs. displacement plot, $\Psi = 0.82$

A similar test program is run on full-scale braces to examine the influence of longer reduced core length on the results. The reduced section of the core has 6 approximately square shell elements across the angle leg dimension of $2\frac{3}{4}$ inches. Load vs. displacement plots are shown in Figures 70 – 72 for end moment ratios of $\Psi = 0, 0.15,$ and $0.30,$ respectively. In all plots the post-yield hardening is exaggerated due to the logarithmic displacement scale. The required restrainer stiffness for the braces is $340,000\text{ k-in}^2, 370,000\text{ k-in}^2, 400,000\text{ k-in}^2, 433,000\text{ k-in}^2, 467,000\text{ k-in}^2$ for end moment ratios of $\Psi = 0, 0.075, 0.15, 0.225,$ and $0.30,$ respectively. Note that two additional test braces with intermediate values of end moment are introduced to create a smoother data plot. Each step in end moment ratio leads to an approximately $30,000\text{ k-in}^2$ increase in required stiffness.

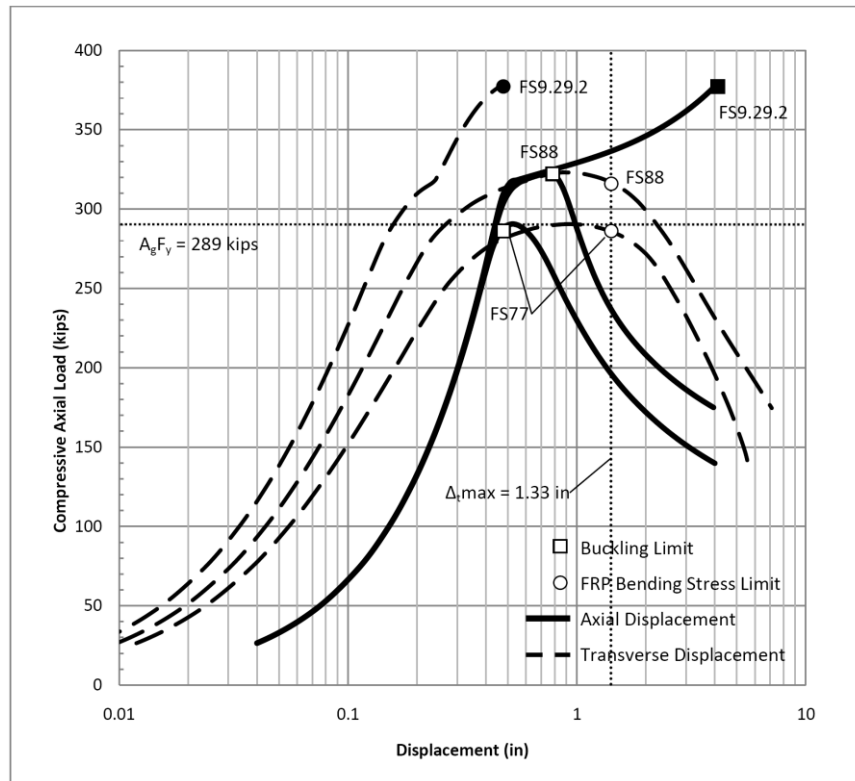


Figure 70 - Full-scale load vs. displacement plot, $\Psi = 0$

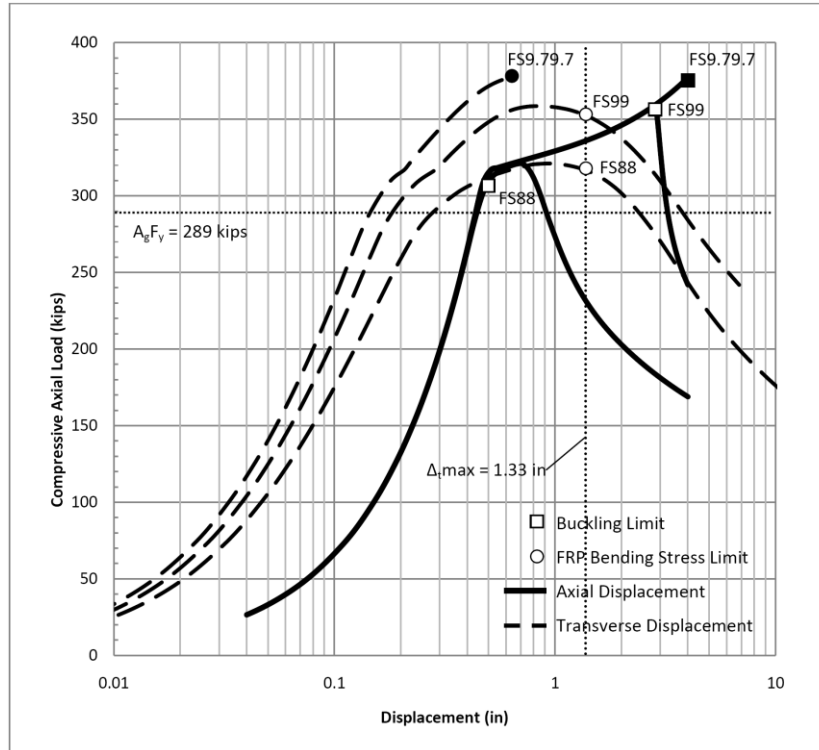


Figure 71 - Full-scale load vs. displacement plot, $\Psi = 0.15$

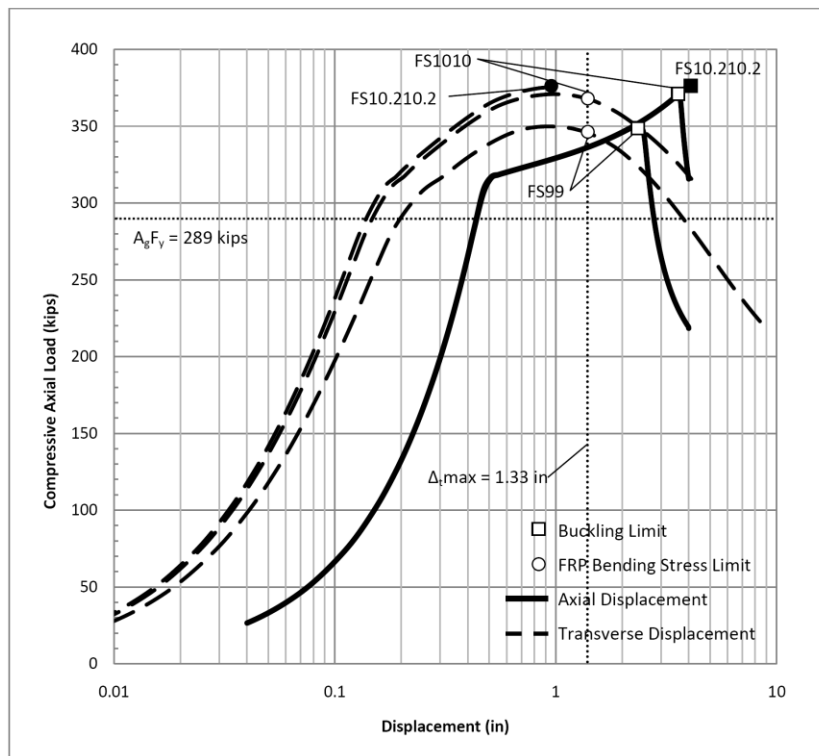


Figure 72 - Full-scale load vs. displacement plot, $\Psi = 0.30$

Comparison of end moment effect on numerical results is shown in Figure 73 where applied end moment is plotted against required restrainer stiffness for both the partial and full-scale brace (cyclic values are also shown which will be presented in the next section). The relationship is nearly linear with a slope of 932 k-in² and 977 k-in² per unit of end moment. Therefore, end moment effect appears to be independent of brace length and may be accounted for in design by superimposing the flexural demand from buckling and applied end moment similar to the analytical solution by Palazzo et al. For

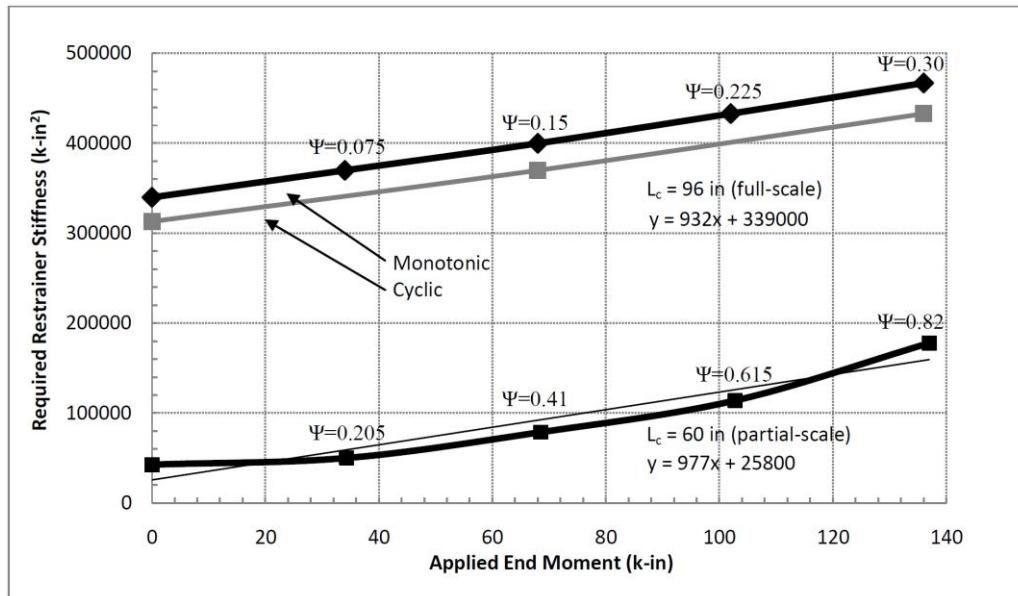


Figure 73 - Plot of end moment ratio vs. required restrainer stiffness

instance, if a nonlinear frame analysis indicates that the actual brace end moment at design story drift is 100 k-in, from 93,200 to 97,700 k-in² of additional restrainer stiffness is required. Since Ψ is dependent on the geometry of the intermediate section and somewhat arbitrary, a simple design rule cannot be applied to this variable. Therefore, the assumption of this ratio is made only to highlight the relative amount of end moment that is applied to the brace before the intermediate section would plastically hinge. The

values were selected by trial and error to give numerical results that were enveloped by the Euler model and P_e/P_y empirical method.

Comparison of Analytical and Numerical Results

Figure 74 shows a scatter plot of the required $E_r I_r$ for different end moment ratios for both brace scales. Analytical method results are shown alongside using theoretical yield strength ($A_1 F_y$) of 140 and 289 kips for the partial and full-scale braces. Theoretical yield strength is selected to remain consistent with the numerical results. The following list of observations is made:

1. There is excellent correlation between partial-scale numerical and modified Euler model results at $\Psi = 0.82$ and 43% lower numerical results when similarly compared at $\Psi = 0.41$. The numerical results for $\Psi = 0$ give 17% less required $E_r I_r$ than the Euler model.
2. The full-scale numerical results are consistently 20% greater than the modified Euler model at both $\Psi = 0.15$ and $\Psi = 0.30$. The numerical method with $\Psi = 0$ also gives 22% greater required $E_r I_r$ than the Euler model.
3. The SDOF model achieves values of required $E_r I_r$ that account for approximately $\Psi = 0.49$ and $\Psi = 0.20$ for the partial and full-scale braces, respectively, when the numerical method is compared.
4. The P_e/P_y empirical method correlates with $\Psi = 0.82$ for the partial-scale brace and is much higher than $\Psi = 0.30$ for the full-scale brace indicating that very high values of end moment can be accommodated when using this method.

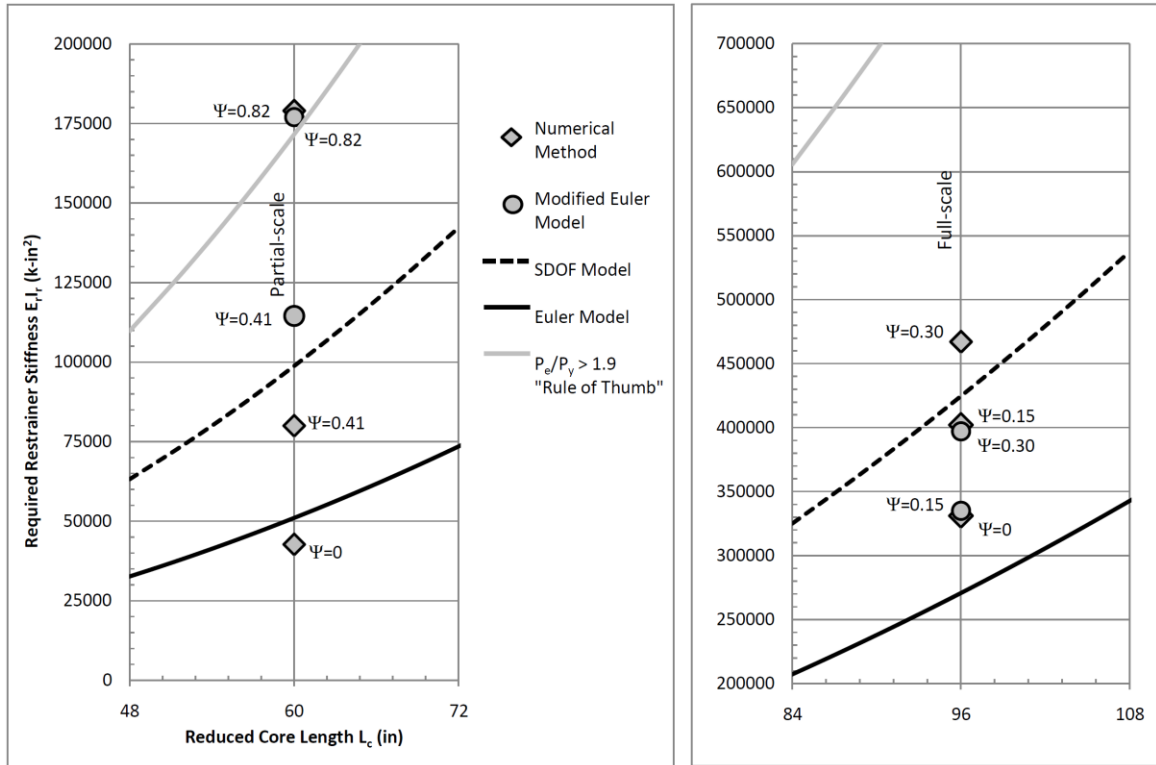


Figure 74 - Comparison of numerical and analytical methods

Generally, the Euler method gives what appear to be less conservative values of required $E_r I_r$ when significant end moments are applied. In addition, the proposed numerical method appears to be less conservative for the partial-scale brace and more conservative for the full-scale brace when compared to the modified Euler model. This lack of correlation between the models can be partially attributed to the following:

1. The numerical method considers both initial out-of-straightness and end moments while the analytical method proposed by Black et al. only considers bifurcation buckling of a perfect column. The numerical model, as well as the SDOF model, account for immediate brace transverse displacement on application of load representative of actual behavior.
2. Global buckling in the numerical model occurs over a longer unbraced

length that includes part of the intermediate section. The analytical methods assumed that the intermediate section would be able to cantilever rigidly past the gusset plate and provide support to the reduced section. Increasing the buckling length to include a portion of the intermediate section may be required to give more conservative analytical results.

3. Numerical results represent required restrainer stiffness in order to achieve a large amount of plastic axial deformation without buckling. Analytical results did not consider the higher axial load required to deform the brace through the region of post-yield hardening. This higher maximum axial load causes higher restrainer bending forces and transverse displacement.
4. Plastic local buckling of the unrestrained portion of the angle legs at the intermediate section increases susceptibility to global buckling once hinging is initiated. This leads to increased transverse brace displacement and thus greater restrainer demand.

This highlights the rudimentary nature of the analytical modeling and its applicability for preliminary design only. The numerical method presented within more effectively captures the likely global buckling failure mode but it is anticipated that a more in depth study of local and torsional buckling will uncover additional failure modes.

7.4 Cyclic Tests

The full-scale brace is selected to serve as the subject for cyclic testing. The objective of these tests is to assess energy dissipation potential and determine if the numerical model is capable of maintaining stability while undergoing repeated cycles of yielding. All tests use the constitutive material model calculated in the Coupon Testing

section with extended true stress-plastic strain data to account for numerical instabilities encountered if the strain of an individual element exceeds the maximum strain data.

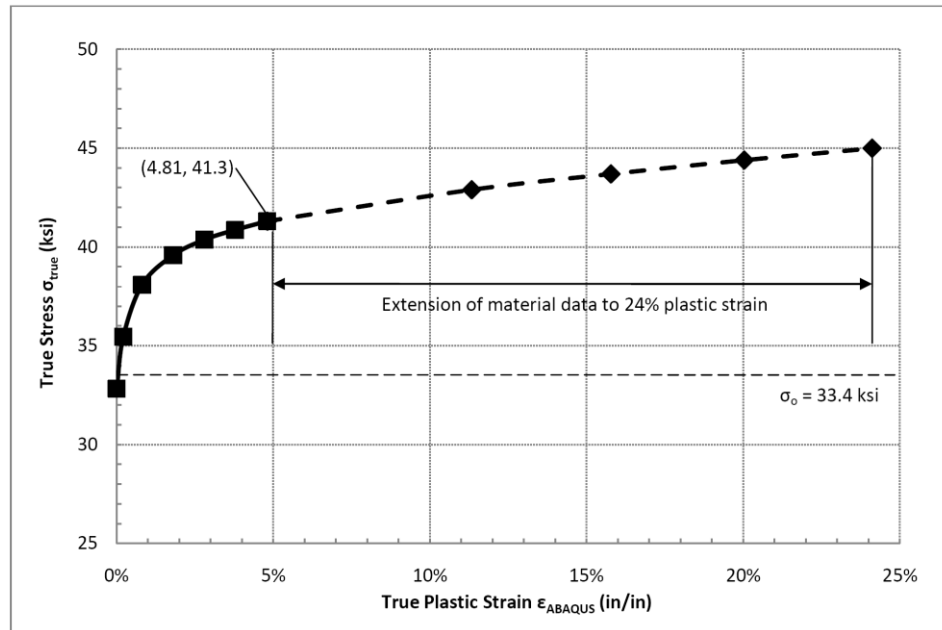


Figure 75 - Extended material data plot

If concentrated plasticity in a small number of elements results from introduction of initial imperfections, the plastic strain may exceed the maximum experimental data value of 4.81%. In this case ABAQUS treats additional strain as perfectly plastic which is not a suitable representation of actual behavior. Figure 75 shows the data extended to a very high plastic strain of 24% at a constant slope. The additional hardening shown by the extension should not be realized since the vast majority of shell element strains should not exceed 4% when subjected to the loading.

Loading Protocol

The loading protocol for the numerical modeling is taken from Appendix T “Qualifying Cyclic Tests of Buckling-Restrained Braces” of the *Provisions*. This cyclic loading sequence is based on the following two displacements given in Equations 92 and

93. Brace axial displacement at yield (Δ_{by}) is determined by inputting nominal P_y into the numerical model to remain consistent with previous results. Axial load at first yield (P_y) is equal to 289 kips using nominal yield strength ($F_{y,sc}$) of 35 ksi and a core section area (A_{sc}) of 8.25 in². Axial displacement at the design story drift (Δ_{bm}) is determined by applying the strength level design force of 241 kips to the numerical model to determine the elastic displacement (Δ_{be}) and then multiplying by C_d as shown in Equation 93.

Table 28 – Cyclic Test Displacement Protocol			
Cycle	Deformation (in)	Inelastic Deformation (in)	Cumulative Inelastic Deformation (Δ_{by})
2 @ Δ_{by}	0.467	0	0
2 @ $0.5\Delta_{bm}$	$0.5*2.00 = 1.00$	$2*2*(1.00 - 0.438) = 2.25$	$2.25/0.438 = 5.14$
2 @ Δ_{bm}	$1.0*2.00 = 2.00$	$2*2*(2.00 - 0.438) = 6.25$	$5.14 + 6.25/0.438 = 19.4$
2 @ $1.5\Delta_{bm}$	$1.5*2.00 = 3.00$	$2*2*(3.00 - 0.438) = 10.2$	$19.4 + 10.2/0.438 = 42.7$
2 @ $2.0\Delta_{bm}$	$2.0*2.00 = 4.00$	$2*2*(4.00 - 0.438) = 14.2$	$42.7 + 14.2/0.438 = 75.1$
11 @ $1.5\Delta_{bm}$	$1.5*2.00 = 3.00$	$2*11*(3.00 - 0.438) = 56.4$	$75.1 + 56.4/0.438 = 204$

At the design load level maximum in-plane strain at the reduced section of the core is 0.341%. Multiplying this by 5.5 to account for inelasticity gives an inelastic strain of 1.88% which is 18% lower than the 2.3% calculated by hand analysis using a maximum story drift of 2.5% as given in the Model Building chapter. Therefore, the design story drift at the first level is 2.61 inches which corresponds to a story drift ratio of 1.67% which is below the maximum.

$$\Delta_{by} = 0.438 \text{ in} \quad (92)$$

$$\Delta_{bm} = \Delta_{be}C_d = 0.3641(5.5) = 2.00 \text{ in} \quad (93)$$

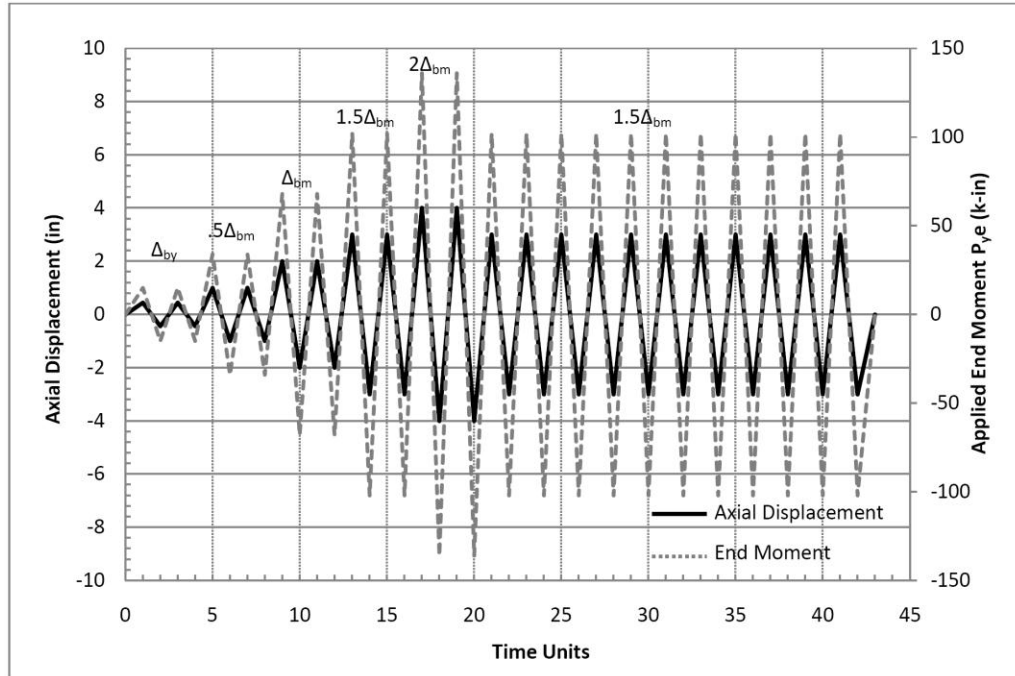


Figure 76 - Time vs. axial deformation plot

Table 28 shows the displacement protocol for the brace testing. Each loading cycle includes a full tension and full compression excursion to the prescribed displacement. Cumulative inelastic deformation for each step is calculated in accordance with Equation 21 giving eleven cycles required at $1.5 \Delta_{bm}$ in order to achieve the required cumulative inelastic deformation of 200 as prescribed by Appendix T. Figure 76 shows the applied axial displacement in plot form. Note that positive deformation values indicate tension and that the cyclic tests are initiated with a tensile excursion to yield strain. Applied end moments are also shown which are set directly proportional to axial displacement.

Testing Parameters & Results

Table 29 shows the parameters for the cyclic tests where the same values were used for Ψ to remain consistent with the monotonic tests. Five test braces are selected

with zero end moment in order to detect the gradual change in behavior for different restrainer stiffness. Restrainer sizes for end moment ratios of $\Psi = 0.15$ and 0.30 are chosen by trial and error to capture the range of behavior between inadequate and adequate restraint. Figures 77 – 86 show hysteresis loops of total axial displacement vs. axial force and total axial strain vs. axial force for the first group of braces with zero end moment. The strain reading is over a gage length of 1 inch at the mid-length of the core

Table 29 – Cyclic Test Brace Parameters						
Designation	Brace Scale	Equivalent FRP Restrainer Size (in)	Calculated Stiffness $E_r I_r$ (k-in²)	Geometric Imperfections	Ψ Ratio	P_e/P_y
FS77	Full	7 x 7 x ¼	144,000	Y	0	0.34
FS88	Full	8 x 8 x ¼	216,000	Y	0	0.52
FS8.58.5	Full	8 ½ x 8 ½ x ¼	262,000	Y	0	0.60
FS8.78.7	Full	8 ¾ x 8 ¾ x ¼	287,000	Y	0	0.66
FS99	Full	9 x 9 x ¼	313,000	Y	0	0.75
FS88-M1	Full	8 x 8 x ¼	216,000	Y	0.15	0.52
FS8.78.7-M1	Full	8 ¾ x 8 ¾ x ¼	287,000	Y	0.15	0.66
FS9.29.2-M1	Full	9 ¼ x 9 ¼ x ¼	340,000	Y	0.15	0.82
FS9.59.5-M1	Full	9 ½ x 9 ½ x ¼	370,000	Y	0.15	0.90
FS8.78.7-M2	Full	8 ¾ x 8 ¾ x ¼	287,000	Y	0.30	0.66
FS9.29.2-M2	Full	9 ¼ x 9 ¼ x ¼	340,000	Y	0.30	0.82
FS9.79.7-M2	Full	9 ¾ x 9 ¾ x ¼	400,000	Y	0.30	0.97
FS1010-M2	Full	10 x 10 x ¼	433,000	Y	0.30	1.04

and shows the amount of cyclic strain actually occurring in the core irrespective of transverse bending which is inclusive in the total axial displacement plots. Figures 87 – 94 show only axial displacement vs. axial force hysteresis for the braces with end moments. These plots also show transverse brace displacement at the mid-length in the direction of the applied end moment since this plot is an easy visual indicator of brace

success. End moment is applied in the same direction as the geometric imperfections in order capture the worst case effect.

The following results are compiled from an examination of the hysteresis plots:

1. The pinched hysteresis loops for the FS77 brace shown in Figure 77 indicate relatively short and uniform plastic plateaus only on the tension excursions with no compression yielding. Figure 78 further highlights the strain asymmetry with a lack of negative values and ratcheting of strain toward the tensile side. Figure 95 shows simulation images of angle leg local buckling during the compression excursions with insufficient $E_r I_r$.
2. The hysteresis loops for FS88 indicate compression yielding only for the first two cycles at $0.5\Delta_{bm}$ where after buckling occurred. Incrementally improved strain response can be seen in Figure 80 with the first two cycles in negative strain. The remainder of the loops exhibit strain ratcheting.
3. Brace FS8.58.5 indicates significantly improved strain symmetry up through the two cycles at $1.0\Delta_{bm}$ and approximately symmetrical strain where after buckling and loss of stiffness occurred. The remaining cycles exhibit strain ratcheting and pinched hysteresis loops. Brace FS8.78.7 remained devoid of buckling until first cycle of $2.0 \Delta_{bm}$.
4. Symmetrical strain response was first achieved in FS99 with full hysteresis loops for the full protocol. Figure 86 shows near strain symmetry with compressive strain at 90% of tensile. Qualitatively, this brace is determined to be capable of nearly symmetric and stable BRB performance. Compression buckling and strain ratcheting are absent.

5. It can be seen that the end moments have a significant effect on the shape of the hysteresis loops. The restrainer stiffness required to preclude buckling is 313,000, 370,000, and 433,000 for end moment ratios of $\Psi = 0, 0.15, \text{ and } 0.30$, respectively. These values are slightly lower than the monotonic tests due to the difference between the elasto-plastic and nonlinear kinematic hardening models used. A similar slope is shown in Figure 73 indicating that end moment has a linear superposition effect.
6. It can be seen that transverse deflection is great when too small of a restrainer is used and negligible when buckling is prevented. Large transverse deflections will exceed the flexural strength of the FRP.

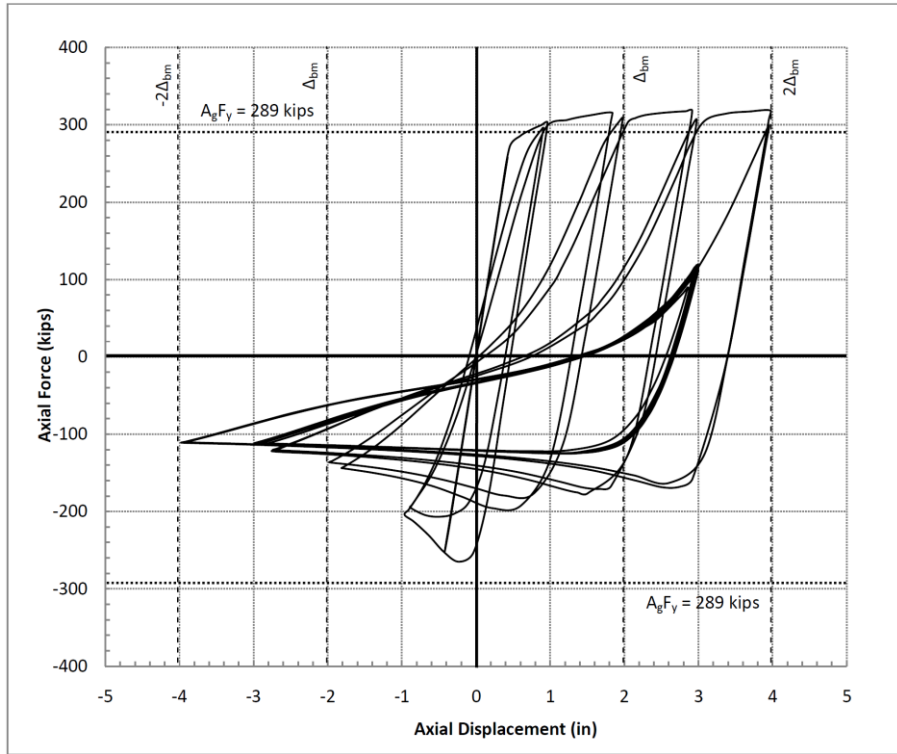


Figure 77 - Hysteresis for FS77, $\Psi = 0$

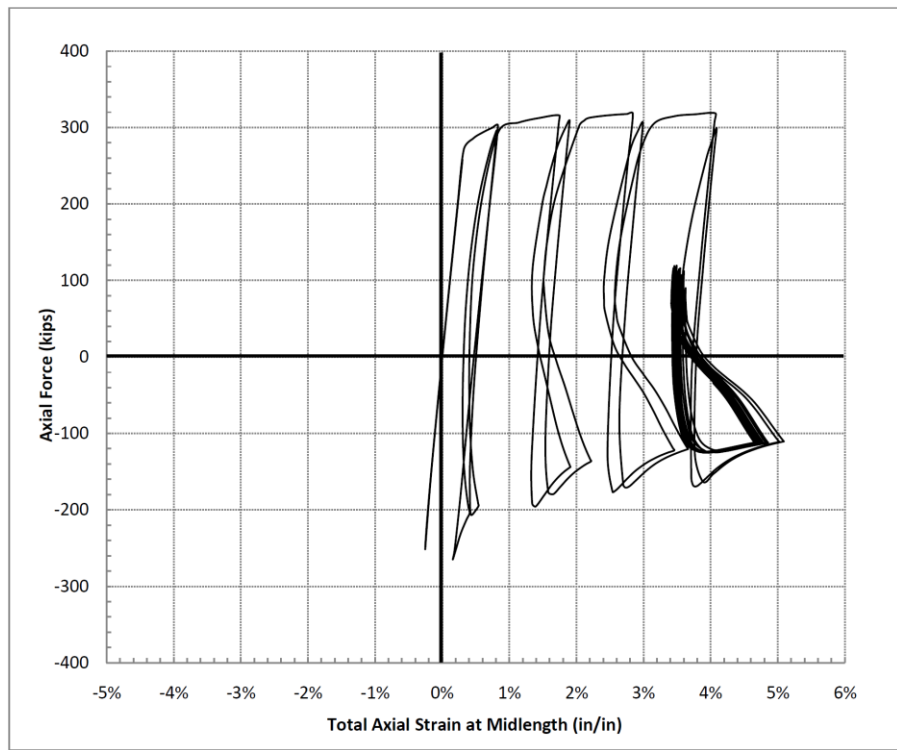


Figure 78 - Strain hysteresis for FS77, $\Psi = 0$

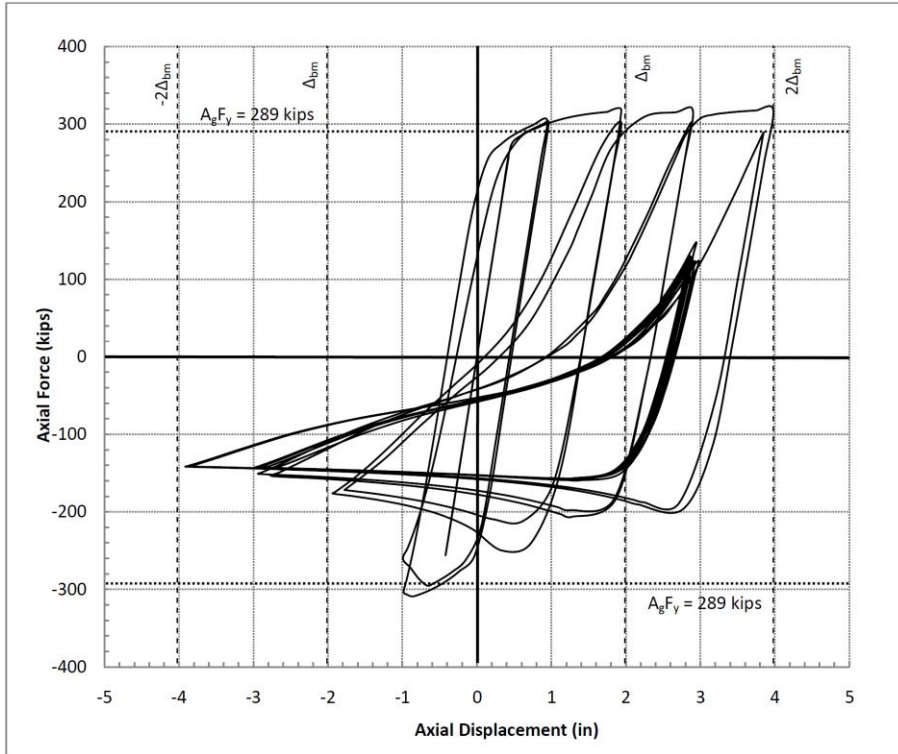


Figure 79 - Hysteresis for FS88, $\Psi = 0$

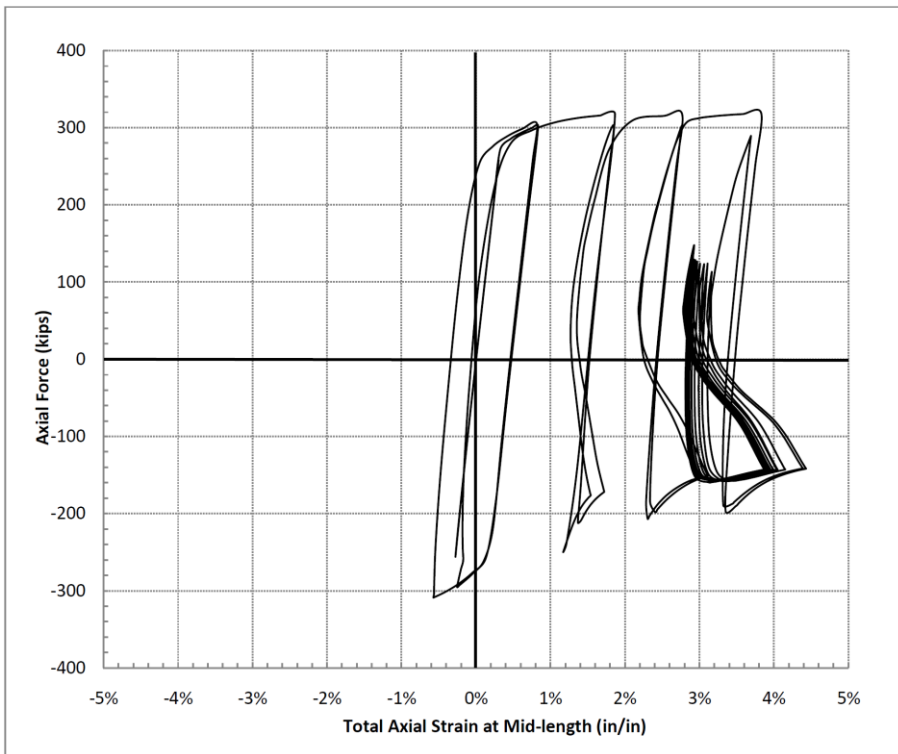


Figure 80 - Strain hysteresis for FS88, $\Psi = 0$

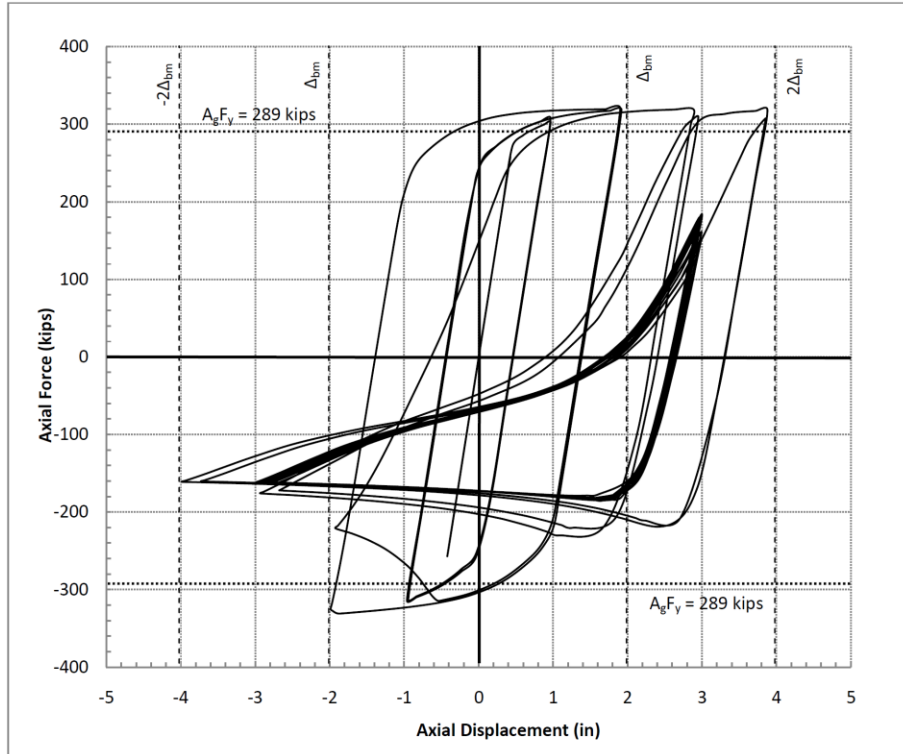


Figure 81 - Hysteresis for FS8.58.5, $\Psi = 0$

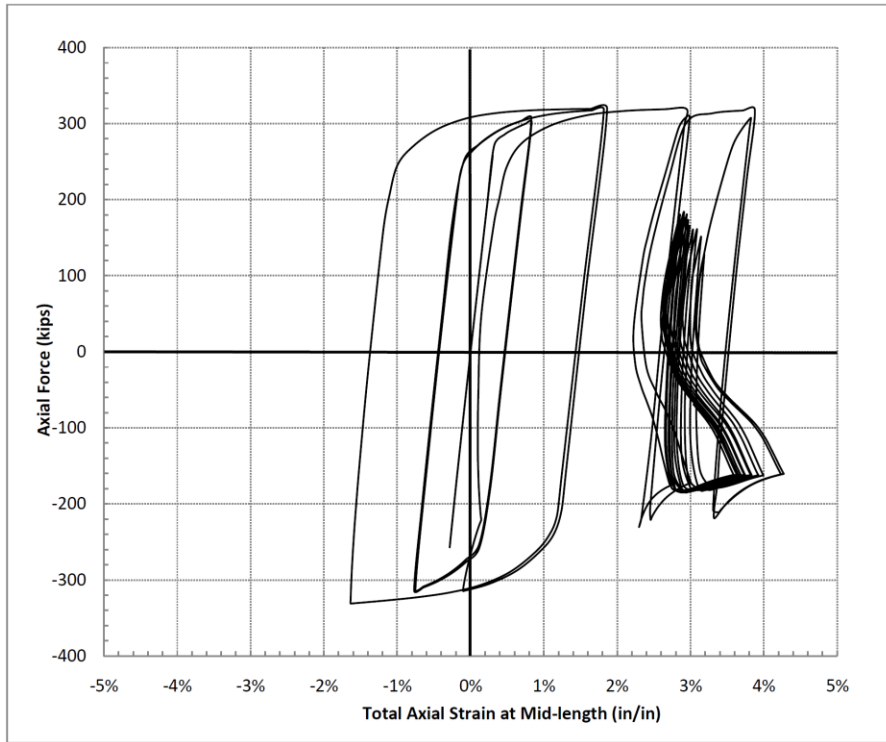


Figure 82 - Strain hysteresis for FS8.58.5, $\Psi = 0$

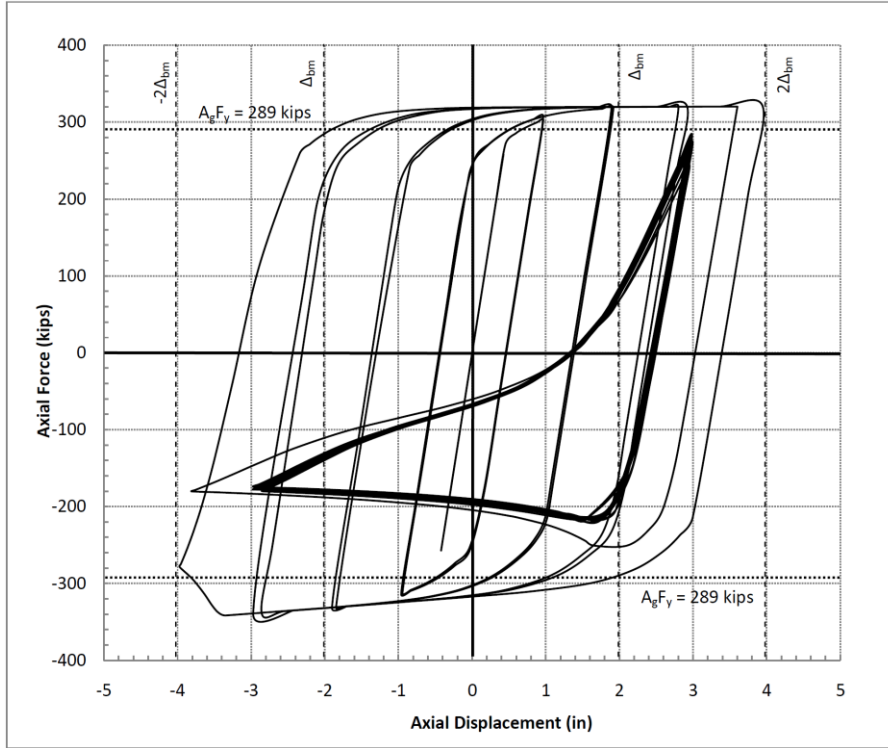


Figure 83 - Hysteresis for FS8.78.7, $\Psi = 0$

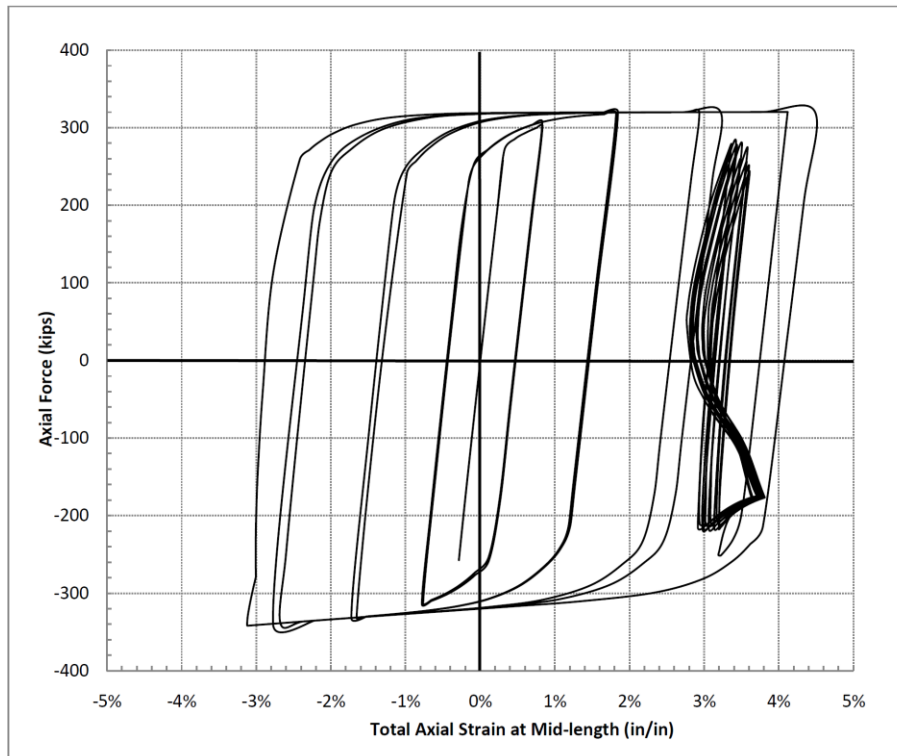


Figure 84 - Strain hysteresis for FS8.78.7, $\Psi = 0$

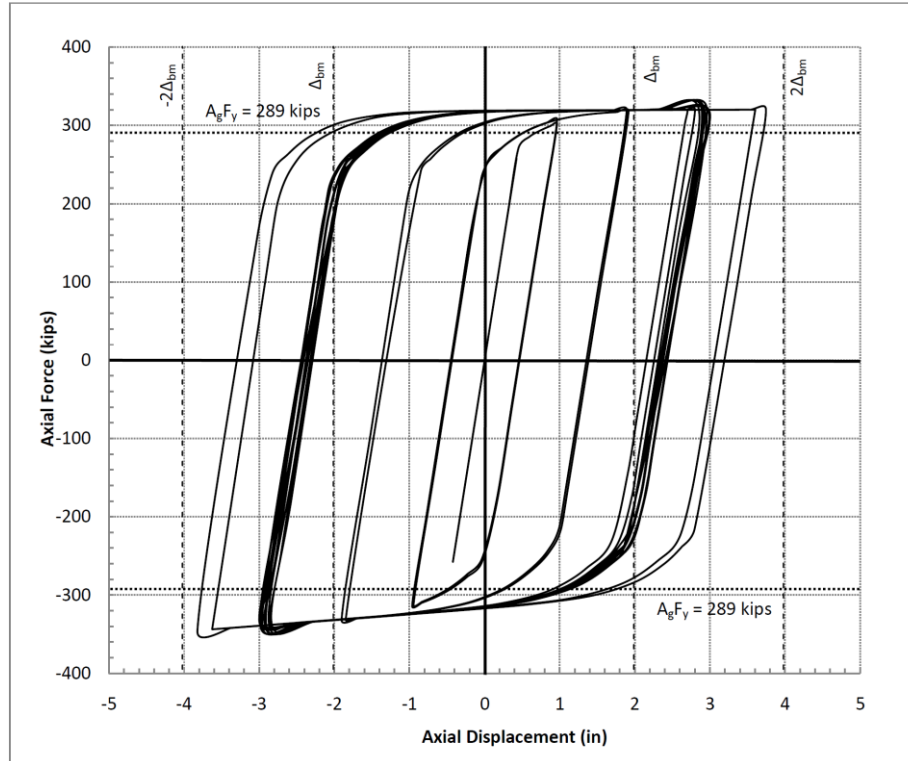


Figure 85 - Hysteresis for FS99, $\Psi = 0$

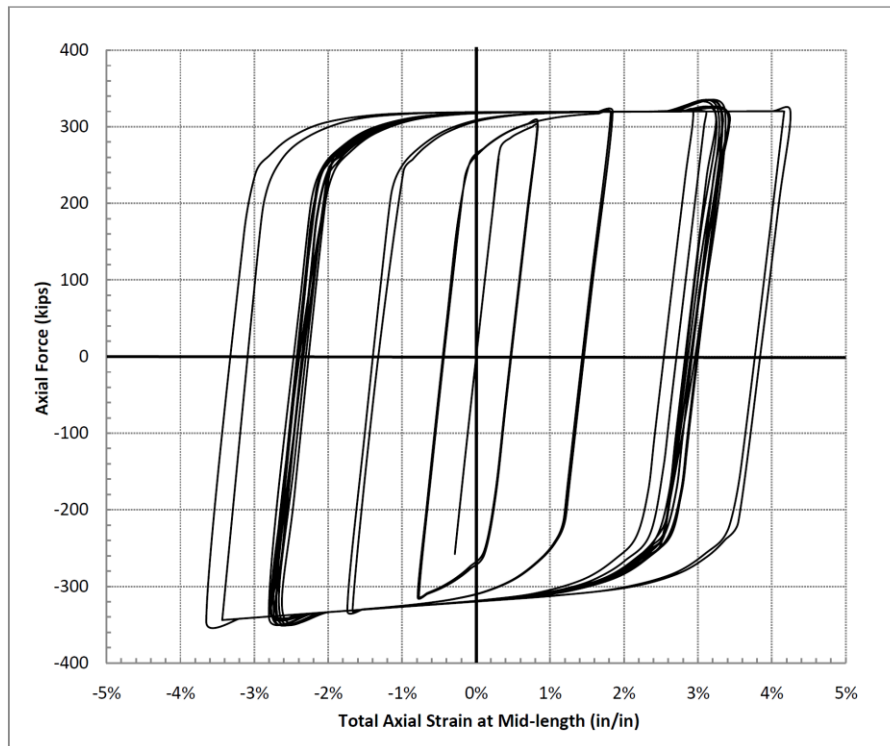


Figure 86 - Strain hysteresis for FS99, $\Psi = 0$

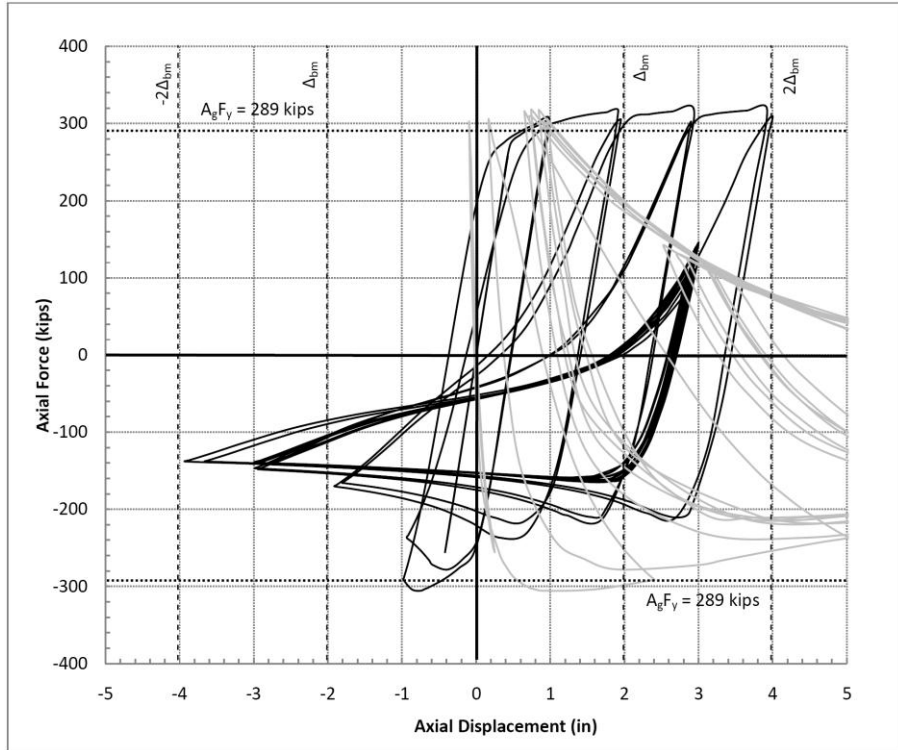


Figure 87 - Hysteresis for FS88, $\Psi = 0.15$ (light line is transverse disp.)

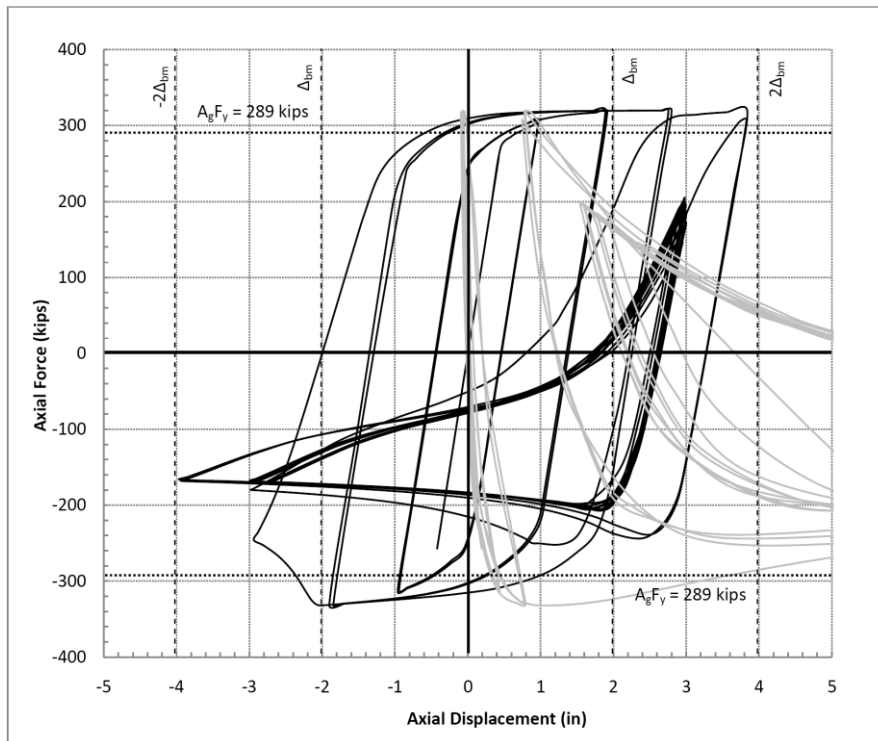


Figure 88 - Hysteresis for FS8.78.7, $\Psi = 0.15$ (light line is transverse disp.)

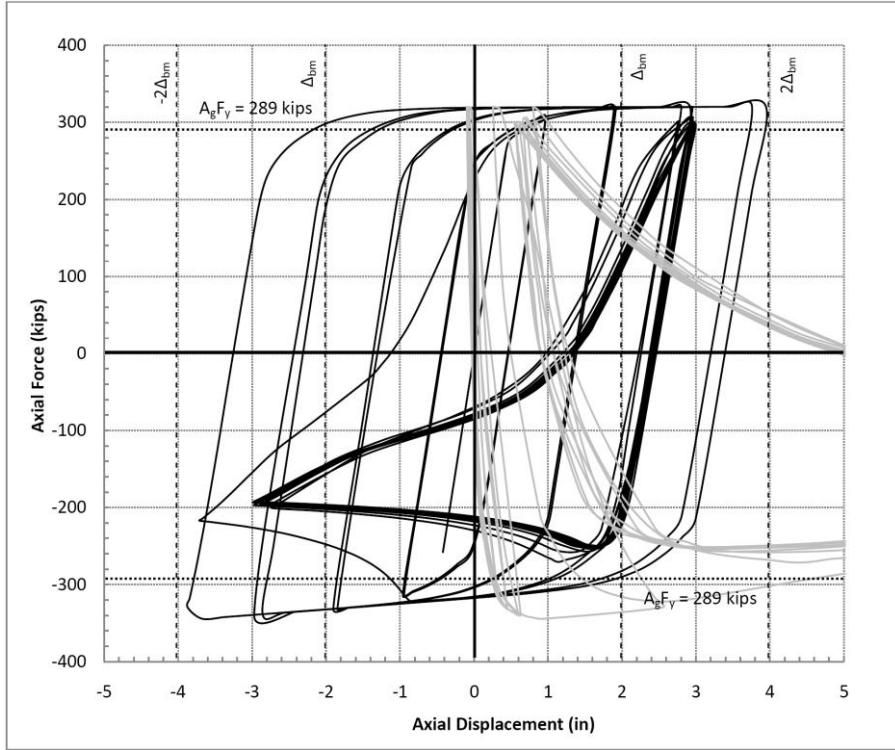


Figure 89 - Hysteresis for FS9.29.2, $\Psi = 0.15$ (light line is transverse disp.)

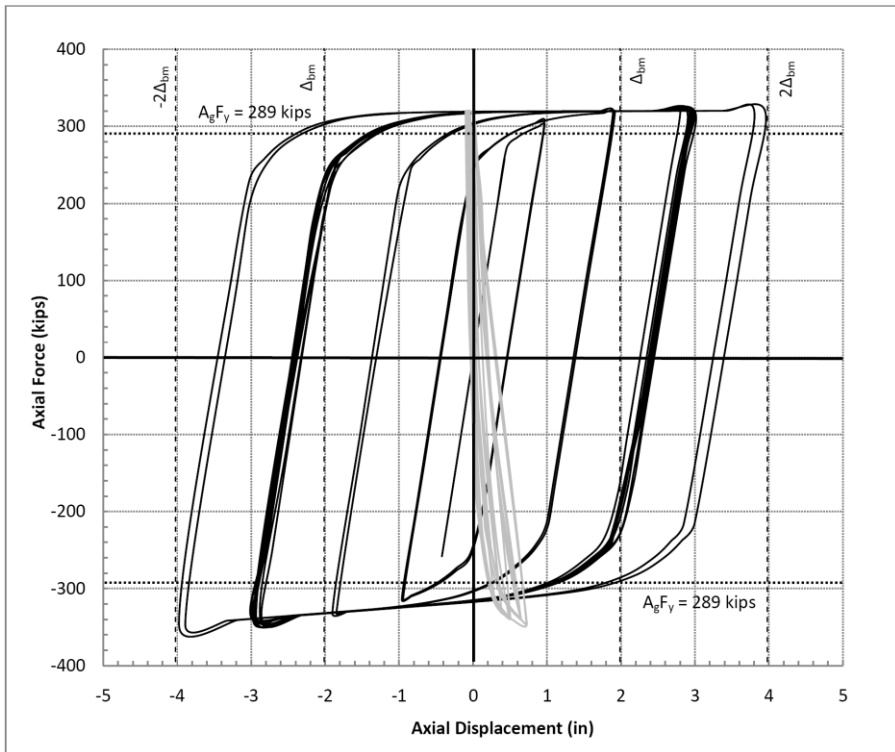


Figure 90 - Hysteresis for FS9.59.5, $\Psi = 0.15$ (light line is transverse disp.)

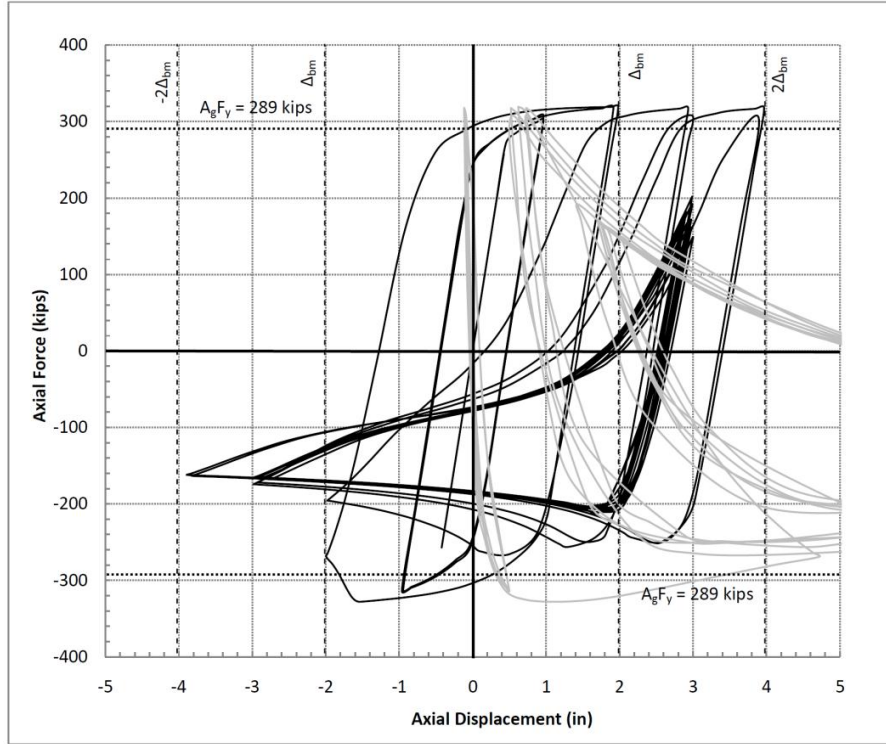


Figure 91 - Hysteresis for FS8.78.7, $\Psi = 0.30$ (light line is transverse disp.)

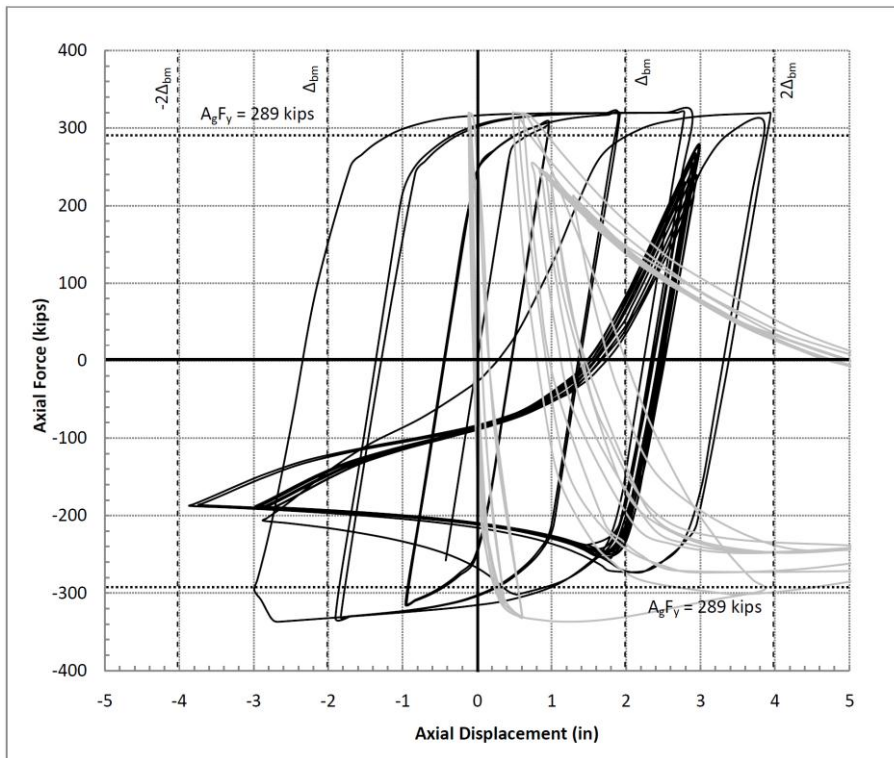


Figure 92 - Hysteresis for FS9.29.2, $\Psi = 0.30$ (light line is transverse disp.)

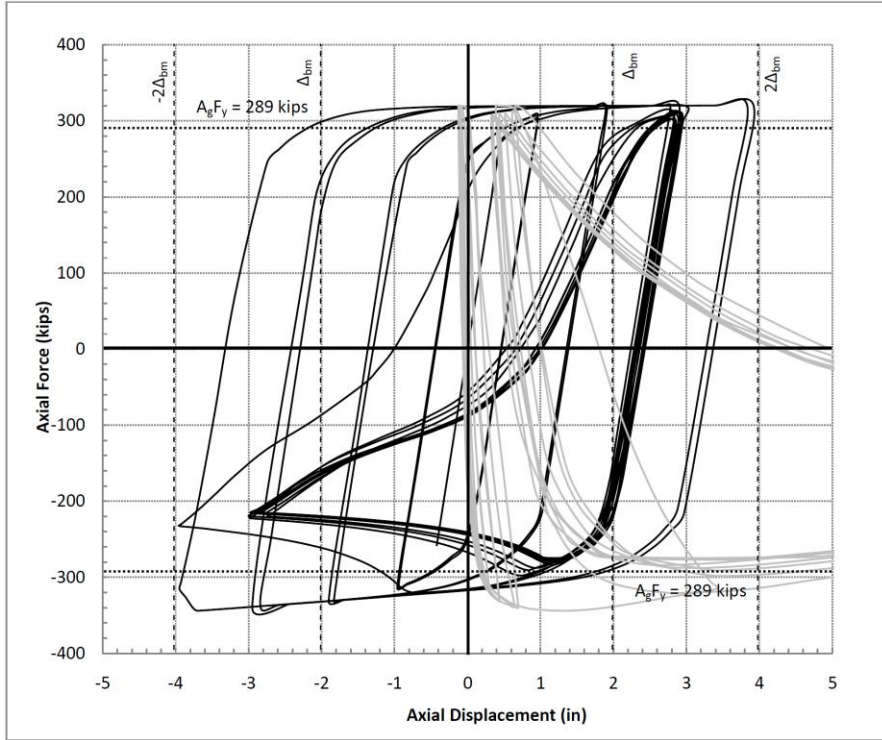


Figure 93 - Hysteresis for FS9.79.7, $\Psi = 0.30$ (light line is transverse disp.)

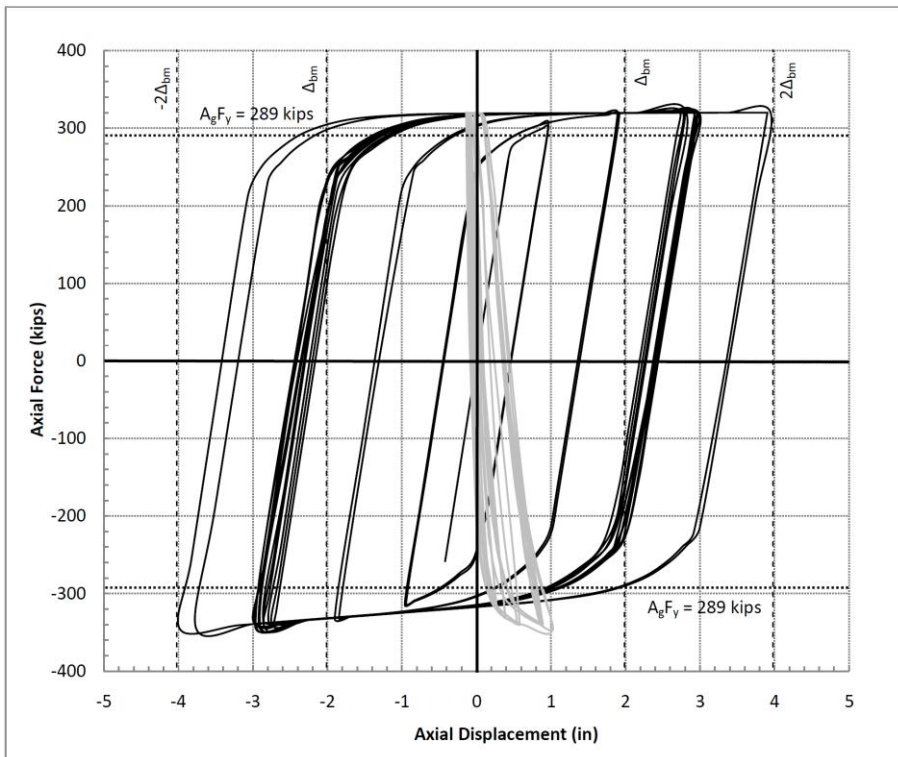


Figure 94 - Hysteresis for FS1010, $\Psi = 0.30$ (light line is transverse disp.)

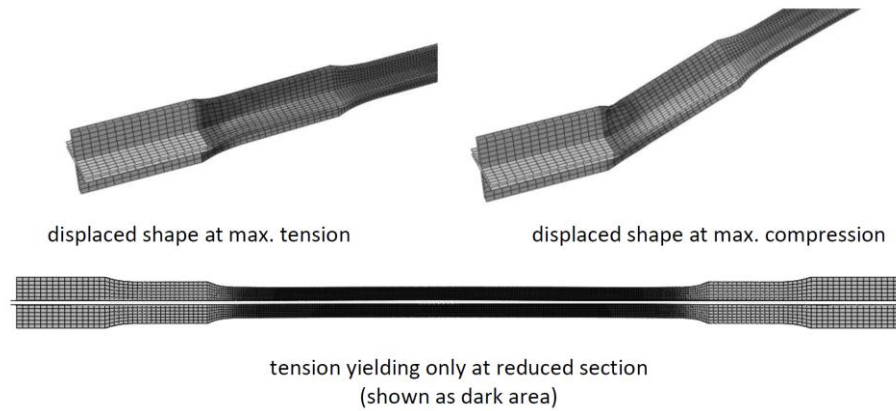


Figure 95 - Compression & tension deflected shapes of inadequately restrained brace

Lastly, cumulative energy dissipation ($\Sigma P\Delta$) is calculated for all test braces using a linear interpolation method as shown in Equation 94 and Figure 91 for a sample portion of the hysteresis plot. This parameter differs somewhat from cumulative plastic ductility (CPD) but gives an indication of the amount of energy dissipation each test brace has achieved and allows the comparison between the test braces in Table 30 and Figure 97.

$$\sum P\Delta = \sum \left(\frac{P_{i+1} - P_i}{2} \right) (\Delta_{i+1} - \Delta_i) \quad (94)$$

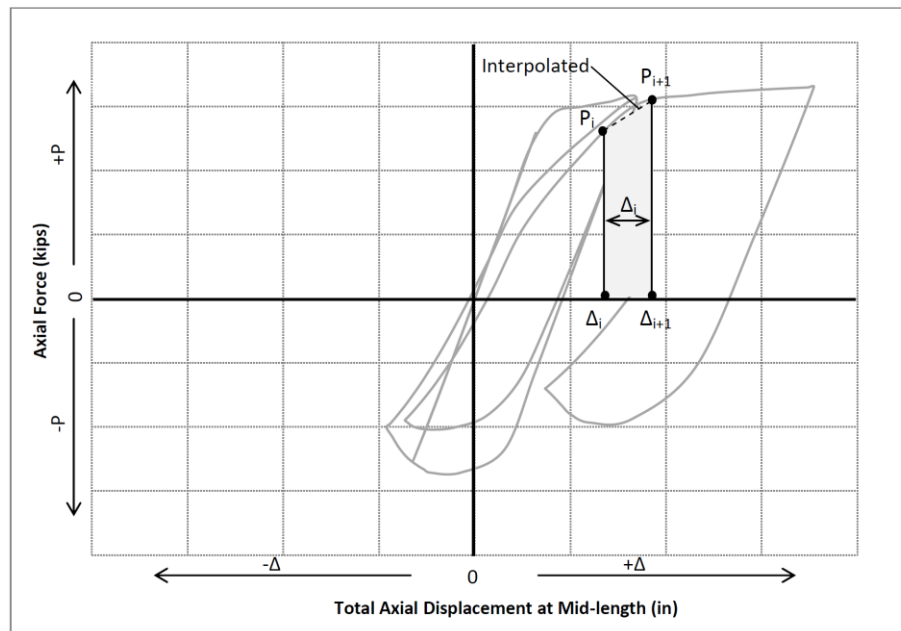


Figure 96 - Linear interpolation method for cumulative P-Δ

Table 30 – Cumulative P-ε					
Designation	ΣP-Δ (k-in)	Designation	ΣP-Δ (k-in)	Designation	ΣP-Δ (k-in)
FS77	20,153				
FS88	24,813	FS88-M1	24,718	FS8.78.7-M2	30,361
FS8.58.5	29,203	FS8.78.7-M1	32,539	FS9.29.2-M2	36,207
FS8.78.7	37,580	FS9.29.2-M1	41,491	FS9.79.7-M2	44,182
FS99	56,905	FS9.59.5-M1	57,988	FS1010-M2	56,995

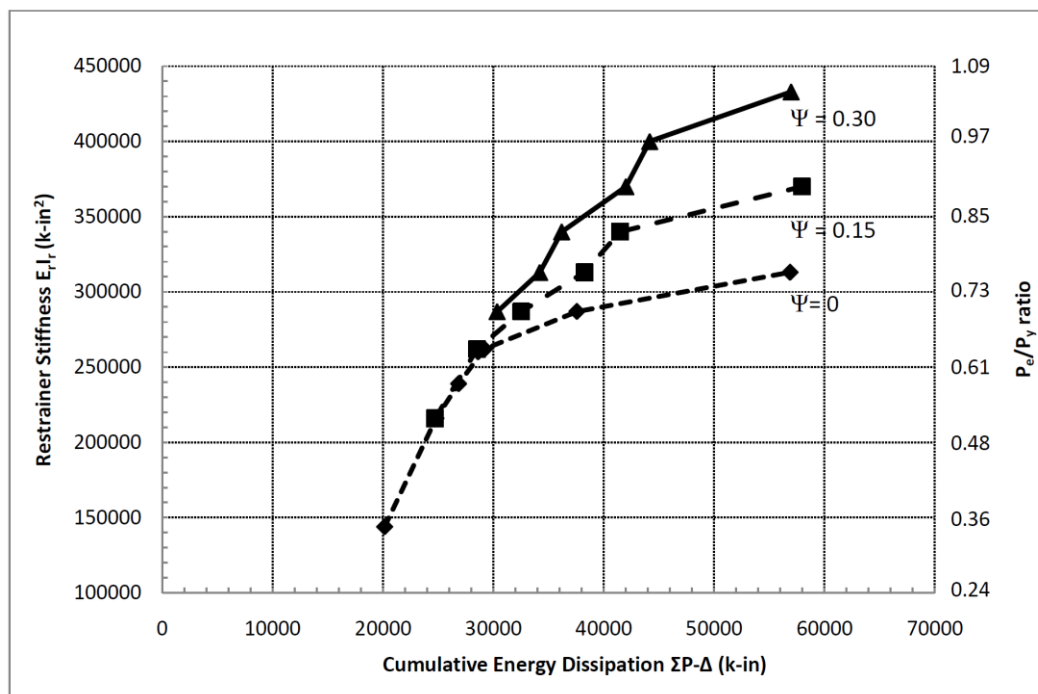


Figure 97 - Comparison of cumulative P-Δ vs. restrainer stiffness

Numerical modeling has explored the required restrainer stiffness for test braces loaded cyclically. The following list of conclusions can be drawn from the results:

1. Monotonic simulations effectively estimate the restrainer stiffness required to preclude global buckling and allow the cyclic numerical model to perform stably and symmetrically. Cyclic testing required a slightly lower restrainer stiffness which can be attributed to a less stiff kinematic

hardening model in lieu of the elasto-plastic model with 5% post yield hardening used in monotonic tests.

2. Strain symmetry is only possible if global buckling can be precluded by an adequately stiff restrainer.
3. Plastic hinging of the angle legs at the intermediate section can be prevented if brace axial alignment is maintained during cycling. This can be accomplished by providing sufficient global stiffness.
4. Local buckling potential of unsupported regions of the core angle legs appears to be high if continuous support is not provided over the length of the intermediate and reduced section. Adequate support also promotes uniform strain demand necessary for limiting effects of premature fatigue.
5. Examination of the required compressive modulus of plastic spacer plates and FRP tube walls is recommended as a future topic of study. Uniform rippling may exacerbate to cumulative and concentrated high-amplitude rippling if the wave is not straightened on each tension cycle. It is thought that adequate local buckling restraint may be able to prevent cumulative high-amplitude rippling if high modulus spacers and FRP tubes can effectively restrain the wave tangent points.
6. Local buckling of the core within the restrainer is anticipated as a highly likely failure mode that requires further research. Adequacy of shell element models should be considered when the buckling wavelength is small enough to impart high transverse shear strains. Continuum elements should be compared with shell results in these studies.

7. Cumulative P- Δ is shown to be asymptotic to provided $E_r I_r$ reaching a maximum value of approximately 57,000 k-in.
8. End moments have a significant effect on cumulative P- Δ . End moment ratios of $\Psi = 0.15$ and 0.30 reduce $\Sigma P-\Delta$ by 27% and 36%, respectively for the same brace with a restrainer stiffness of 340,000 k-in². For a restrainer stiffness of 216,000 k-in² the cumulative P- Δ is not affected by applying end moment because buckling influence is much greater.

8.0 CONCLUSION

8.1 Overall Assessment

A concept for an ultra-lightweight buckling-restrained brace was proposed based on a realistic model building with a defined load and deformation. The brace configuration was developed using knowledge from previously reported experiments to maximize ductility and weight savings potential by using readily available aluminum and FRP materials. To accomplish design of the proposed brace, an approximate analytical method was developed that used single degree of freedom (SDOF) buckling models based on convergence of transverse displacement. An easy to use design plot was constructed from the results of many convergence studies using the SDOF model. This model was compared with an already established Euler buckling model with a distributed force interaction and found to be conservative over the Euler model by a factor of two for most brace lengths. A modified method for determining additional effect of end moments increased the required restrainer stiffness by 200-300% using the available plastic moment in the intermediate core section as the upper bound. This high value indicated that this upper bound may be excessive.

Other analyses using the SDOF models found that the ends of the reduced section could be treated as pinned and the restrainer wrap served more as a means of transferring shear flow between the FRP restrainer tubes than a means of preventing the blow-out failure mode. This shear flow was made possible by orienting a minimum of one layer of wrap in both the $\pm 45^\circ$ directions to allow truss-like behavior between the restrainer

tubes. Composite behavior increased the transverse bending stiffness immensely. Finally, an easy to use analytical method for wrap design was presented that utilizes maximum shear flow stress at the restrainer's maximum transverse displacement.

Full-scale ULWBRB configurations were established using the developed analytical methods and found to have 24% and 41% the weight of mortar-filled tube and all-steel traditional BRBs, respectively. The final configuration was fully customizable using standard aluminum angle sizes and square FRP tubes of any size required by the specific design application. Design guidelines for the practical length of the reduced section of the core were also presented resulting in a realistic range of $0.2 < L_c/L_b < 0.5$ considering minimum length for plastic straining and length requirements for the full and intermediate sections. The exact selection of length shall be made by considering brace axial stiffness and target design story drift. An approximate analytical method for determining the brace displacement for a given story drift was verified using the numerical model. This approximate method gave values that were approximately 50% stiffer than the actual brace.

A partial-scale ULWBRB was also developed for numerical testing that used a target scaling ratio of 50%. Tensile yielding and compression buckling available strengths were used as scaling parameters. The same analytical design methods were used to design the restrainer tubes and wrap with a similar four angle core and square tube restrainer configuration. This partial scale brace was envisioned as an experimental test subject for recommended future laboratory testing where total length and yield strength needed to be limited for available equipment.

In order to verify the suitability of using the common structural aluminum alloy

6061-T6 for the core, coupons made from a 7/8 inch extruded rod were tested.

Monotonic results showed that excellent ductility up to 22% elongation was possible with little strain hardening. Low-cycle fatigue testing at +/- 2, 3, and 4% total strain showed material stability up to 24, 18, and 11 cycles for the three amplitudes, respectively.

Maximum cyclic stress for the three tests remained virtually constant up until failure with only a small amount of softening after two cycles of initial hardening. This small degree of softening increased proportionally with strain amplitude. A reliable plastic plateau at each reversal showed that the aluminum alloy was quite capable of dissipating seismic energy through plastic straining, but the number of reversals achieved before tensile fracture was deemed insufficient as compared to the LCF life of low yield point steels commonly used in traditional BRBs. Since the number of reversals expected in a seismic event can easily exceed 20 to 30, further coupon testing of other aluminum alloys was recommended.

A nonlinear combined kinematic-isotropic hardening model was used in numerical simulations. A coupon FEA using solid elements showed good calibration of experimental and numerical data for the 2 and 3% coupons and marginal correlation for the 4% sample due to slight buckling of the sample. Numerical modeling of the actual ULWBRB proceeded with a parametric study on the effects of brace length, restrainer stiffness, and applied end moment. Load vs. deformation plots of braces loaded monotonically showed that failure could occur by either buckling or excessive transverse deformation of the restrainer leading to bending stresses exceeding allowable. The effect of applied end moment on the required restrainer stiffness was determined to be one of superposition with approximately 932 - 977 k-in² of additional restrainer stiffness

required per unit of applied end moment. This relationship can be used in design to account for BRBF drift as determined from a nonlinear pushover analysis. The proposed Ψ ratio is not able to be used as a general design guideline for determining additional restrainer stiffness due to end moment since it varies depending on specific geometry of the intermediate section.

There was little correlation found between the proposed analytical and numerical methods with no clear indication of which methods were more conservative than others. A comparison of proposed analytical and numerical models highlighted the following for the partial-scale brace:

1. The numerical model and Euler model with $\Psi = 0$ correlated well with only 17% more restrainer stiffness required by using the Euler model.
2. Good correlation was also found between the modified Euler model and the numerical method for $\Psi = 0.82$. However, the same comparison at a $\Psi = 0.41$ indicates that the modified Euler model may be 43% over-conservative as compared to the numerical model.
3. Results indicate that the SDOF model may inherently accommodate for a significant amount of end moment through its conservatism.
4. The P_c/P_y empirical method appears sufficiently conservative to capture the effect of all realistic end moments, i.e. $\Psi < 1.0$.

The following comparison is for the full-scale brace:

1. Larger required restrainer stiffness was indicated by the numerical method over the modified Euler model. The SDOF method appears to be quite conservative for larger brace lengths and would accommodate and end

moment of $\Psi = 0.20$ when compared with the numerical results.

2. Since almost all numerical results gave higher required restrainer stiffness than the Euler based analytical methods for the longer brace, it is realized that they may be unconservative.
3. The Euler model is under conservative by 22% for braces with no applied end moment when compared with numerical results. The modified Euler model is under conservative by approximately 20% for $\Psi = 0.15$ and 0.30 .

Lastly, numerical cyclic tests were performed on the full-scale brace with different restrainer stiffness and applied end moment ratios.

1. Results showed that monotonic simulations effectively estimate the required restrainer stiffness for braces to be able to withstand the cyclic loading protocol without buckling.
2. End moments applied to these braces effect required restrainer stiffness with the same linear superposition principal found monotonic simulations.
3. Reliable hysteretic performance is possible if sufficient global stiffness is provided to prevent plastic hinging at the unrestrained portion of the core.
4. Local buckling through examination of elastic support provided by the FRP within the restrainer as well as torsional buckling of the unrestrained sections of the core requires further research.

8.2 Recommendations for Further Research

Throughout this body of work potential areas for further research have been mentioned in order to progress the development of the ULWBRB. The following list of topics would greatly benefit from further study:

1. Analytical local buckling analysis of core angle legs restrained by an elastic medium to determine the required stiffness and strength of local supports. This elastic medium is provided by either compressive deformation of the FRP spacer plates or local bending of the FRP tube walls. As presented in the literature review, methods for local buckling analysis have been proposed. The numerical model, or a similar model using solid elements for the core angles, can also be modified to examine local buckling effects. The slotted and slide plane connectors used are able to be assigned an elastic stiffness in the axial direction. This stiffness can be verified by small scale experimental load tests on representative FRP plates and tubes. The numerical model is also capable of modeling connector interaction with damage or non-linear material behavior.
2. Low cycle fatigue tests on aluminum alloys 2024-O, 2024-T3, 5086-O, 5086-T111, and 6061-O to determine ductility and LCF suitability for use in the ULWBRB. These alloys are readily available in round rods for test coupons, but may have limited stock availability in structural extrusions, except for 5086-T111 which is readily available.
3. Experimental testing of partial-scale prototypes to validate the analytical and numerical models proposed. Testing shall consist of both unrestrained and restrained aluminum cores as detailed in order to quantify gains in achievable compression displacement in the restrained version. Different restrainer stiffnesses should be tested to examine the incremental progression of restraint as well as different core reduced section lengths to examine the effect of different strain demands on the aluminum's low cycle fatigue performance.

4. Non-linear pushover analyses of representative BRBFs to determine the actual amount of brace end moment (or rotation angle) at design story drifts. This parametric investigation shall consider different frame geometries, frame member stiffnesses, end connections, and actual ULWBRB geometry and stiffness. A range of end moments (or rotations) able to be used in practical design situations should be established for typical BRBF/ULWBRB parameters. This will serve to calibrate values of Ψ used in this research. In addition, a general method for normalizing applied end moment by frame drift or brace length is desired that is independent of the variations possible in the design of the intermediate section of the core.

9.0 REFERENCES

- Abraham, E. J. (2006). Conceptual investigation of partially buckling restrained braces. *M.S. Thesis*. Pittsburg, PA: University of Pittsburgh.
- Accord, N. B., & Earls, C. J. (2006). Use of fiber-reinforced polymer composite elements to enhance structural steel member ductility. *Journal of Composites for Construction*, 10 (4), 337-344.
- Aluminum Association. (2000). *Aluminum Design Guide*. New York: Aluminum Association.
- American Concrete Institute. (2008). *Guide for the Design and Construction of Externally Bonded FRP Systems for Strengthening Concrete Structures*. Farmington Hills, MI: ACI.
- American Institute of Steel Construction. (2005a). *Code of Standard Practice for Steel Buildings and Bridges*. Chicago: American Institute of Steel Construction.
- American Institute of Steel Construction. (2005b). *Seismic Provisions for Structural Steel Buildings*. Chicago: American Institute of Steel Construction.
- American Society of Civil Engineers. (2005). *Minimum Design Loads for Buildings and Other Structures*. Reston, VA: American Society of Civil Engineers.
- ASTM, American Society for Testing & Materials. (2004). E 606 Standard practice for strain-controlled fatigue testing. In *Annual Book of ASTM Standards* (Vol. 3.01).

ASTM, American Society for Testing & Materials. (2008). E 8 Standard test methods for tension testing of metallic materials. In *Annual Book of ASTM Standards* (Vol. 3.01).

Black, C. J., Makris, N., & Aiken, I. D. (2004). Component testing, seismic evaluation and characterization of buckling-restrained braces. *Journal of Structural Engineering* , 130 (6), 880-894.

Black, C., & Aiken, I. (2002). *Component testing, stability analysis and characterization of buckling-restrained unbonded braces*. Berkeley, CA: Pacific Earthquake Engineering Research Center.

Borrego, L. P. (2004). Analysis of low cycle fatigue in AlMgSi aluminium alloys. *Engineering Failure Analysis* , 11 (5), 715-725.

Brando, G., De Matteis, G., & Mazzolani, F. M. (2009). Simplified analytical modeling of compact pure aluminum shear panels. *Stessa* (pp. 829-834). London: Taylor & Francis Group.

Brodrick, R. F., & Spiering, G. A. (1972). Low cycle fatigue of aluminum alloys. *Journal of Materials* , 7 (4), 515-526.

Brown, P., Aiken, I. D., & Jafarzahdeh, F. J. (2001, August). Seismic retrofit of the Wallace F. Bennett Federal Building. *Modern Steel Construction, American Institute of Steel Construction* , p. 29.

Brush, D. O., & Almroth, B. O. (1975). *Buckling of Bars, Plates and Shells*. New York: McGraw-Hill.

Castellano, M. G., Balducci, F., & Antonucci, R. (2008). Shaking table tests on R.C. frame with dissipative bracings. *Proc. of the 2008 Seismic Engineering Conference*

Commemorating the 1908 Messina and Reggio Calabria Earthquake (pp. 1358-1365).
Reggio Calabria, Italy: American Institute of Physics.

Chou, C. C., & Chen, S. Y. (2009). Subassemblage tests and finite element analyses of sandwiched buckling-restrained braces with a replaceable core. *Stessa* (pp. 945-951). London: Taylor & Francis Group.

D'Aniello, M., Della Corte, G., & Mazzolani, F. M. (2009). "All-steel" buckling-restrained braces for seismic upgrading of existing reinforced concrete buildings. *Stessa* (pp. 561-566). London: Taylor & Francis Group.

D'Aniello, M., Della Corte, G., & Mazzolani, F. M. (2008). Experimental tests of a real building seismically retrofitted by special buckling-restrained braces. *Proc. of the 2008 Seismic Engineering Conference Commemorating the 1908 Messina and Reggio Calabria Earthquake* (pp. 1513-1520). Reggio Calabria, Italy: American Institute of Physics.

Diceli, M., & Calik, E. E. (2008). Physical theory hysteric model for steel braces. *Journal of Structural Engineering* , 134 (7), 1215-1228.

Dusicka, P., & Wiley, B. (2008). Concept of buckling restraint of steel braces with fiber reinforced polymers. *Proc. of the 2008 Structures Conference*. Vancouver, Canada: American Society of Civil Engineers.

Dusicka, P., Itani, A. M., & Buckle, I. G. (2007). Cyclic response of plate steels under large inelastic strains. *Journal of Constructional Steel Research* , 63 (2), 156-164.

Ekiz, E., & El-Tawil, S. (2008). Restraining steel brace buckling using a carbon fiber-reinforced polymer composite system: experiments and computational simulation. *Journal of Composites for Construction* , 12 (5), 562-569.

Ekiz, E., El-Tawil, S., Parra-Montesinos, G., & Goel, S. (2004). Enhancing plastic hinge behavior in steel flexural members using CFRP wraps. *Proc. of the 13th World Conference on Earthquake Engineering*. Vancouver, Canada: IAEE.

El-Tawil, S., & Ekiz, E. (2009). Inhibiting steel brace buckling using carbon fiber-reinforced polymers. *Journal of Structural Engineering* , 135 (5), 530-538.

Fahnestock, L. A., Ricles, J. M., & Sause, R. (2007). Experimental evaluation of a large-scale buckling-restrained braced frame. *Journal of Structural Engineering* , 133 (9), 1205-1214.

Fahnestock, L. A., Sause, R., Ricles, J. M., & Le-Wu, L. (2003). Ductility demands on buckling-restrained braced frames under earthquake loading. *Earthquake Engineering and Engineering Vibration* , 2 (2), 255-268.

Federal Emergency Management Agency. (2000). *FEMA-355C*. Berkeley, CA: FEMA.

Harries, K. A., Peck, A. J., & Abraham, E. J. (2009). Enhancing stability of structural steel sections using FRP. *Thin-walled Structures* , 47 (10), 1092.

Hopperstad, O. S., Langseth, M., & Remseth, S. (1995). Cyclic stress-strain behavior of alloy AA6060 T4, Part I: Uniaxial experiments and modeling. *International Journal of Plasticity* , 11 (6), 725-739.

Hornqvist, M., & Karlsson, B. (2008). Influence of heat treatment on the cyclic deformation properties of aluminum alloy AA7030. *Materials Science and Engineering* , 479 (1-2), 345-355.

International Code Council. (2009). *International Building Code*. Country Club Hills, IL: International Code Council.

Kim, J., & Choi, H. (2005). Response modification factors of chevron braced frames. *Engineering Structures* (27), 285-300.

Kimura, K., Takeda, Y., Yoshioka, K., Furuya, N., & Takemoto, Y. (1976). An experimental study on braces encased in steel tube and mortar. *Proc., Annual Meeting of the Architectural Institute of Japan*. Architectural Institute of Japan.

Kushibe, A., Makii, K., Chiang, L. F., Tanaka, T., Kohzu, M., & Higashi, K. (2005). Application to seismic dampers in high-strain-rate superplastic Zn-Al alloy. *Materials Science Forum* , 475-479 (iv), 3055-3060.

Li, P., & Marchand, N. J. (1989). Crack initiation mechanisms in low cycle fatigue of aluminum alloy 7075-T6. *Materials Science and Engineering* , A119, 41-50.

Ma, C., Chen, L., Tian, Y., Che, X., & Liaw, P. K. (2009). Influence of heat treatment on low-cycle fatigue behavior of an extruded 6063 aluminum alloy. *Aluminum Alloys: Fabrication, Characterization and Applications II* , 123-128.

Mazzolani, F. M. (1985). *Aluminum Alloy Structures*. Boston: Prentice Hall Books.

Mazzolani, F. M., Della Corte, G., & D'Aniello, M. (2009). Experimental analysis of steel dissipative bracing systems for seismic upgrading. *Journal of Civil Engineering Management* , 15 (1), 7-19.

Mazzolani, F. M., Della Corte, G., & Faggiano, B. (2004). Seismic upgrading of RC buildings by means of advanced techniques: The ILVA-IDEM project. *13th World Conference on Earthquake Engineering*. Vancouver, Canada: IAEE.

Mazzolani, F. M., Piluso, V., & Rizzano, G. (2011). Local buckling of aluminum alloy angles under uniform compression. *Journal of Structural Engineering* , 137 (2), 173-184.

Mochizuki, N., Murata, Y., Andou, N., & Takahashi, S. (1980). An experimental study on buckling of unbonded braces under centrally applied loads. *Proc., Annual Meeting of the Architectural Institute of Japan*. Architectural Institute of Japan.

Murtha-Smith, E., & Adibjahromi, H. R. (1988). Restrained warping in cruciform compression members. *Journal of Structural Engineering* , 114 (1), 198-210.

Palazzo, G., Lopez-Almansa, F., Cahis, X., & Crisafulli, F. (2009). A low-tech dissipative buckling restrained brace. Design, analysis, production and testing. *Engineering Structures* , 31, 2152-2161.

Park, Y., Iwai, S., Kameda, H., & Nonaka, T. (1996). Very low cycle failure process of steel angle members. *Journal of Structural Engineering* , 122 (2), 133-141.

Rai, D. C. (2002). Inelastic cyclic buckling of aluminum shear panels. *Journal of Engineering Mechanics* , 128 (11), 1233-1237.

Rai, D. C., & Wallace, B. J. (2000). Aluminum shear-link for seismic energy dissipation. *Proc. of the 12th World Conference on Earthquake Engineering*. Auckland, New Zealand: IAEE.

Sabelli, R., Mahin, S., & Chang, C. (2003). Seismic demands on steel braced frame buildings with buckling-restrained braces. *Engineering Structures* , 25 (5), 655-666.

Sayed-Ahmed, E. Y. (2006). Numerical investigation into strengthening steel I-section beams using CFRP strips. *Proc. of the Structures Conference and Exposition*. St. Louis: American Society of Civil Engineers.

Schnerch, D., Dawood, M., Rizkalla, S., Sumner, E., & Stanford, K. (2006). Bond behavior of CFRP strengthened steel structures. *Advances in Structural Engineering* , 9 (6), 805-817.

Shaat, A., & Fam, A. (2006). Axial loading test on short and long hollow structural steel columns retrofitted using carbon fibre reinforced polymers. *Canadian Journal of Civil Engineering* , 33 (4), 458-470.

Shaat, A., & Fam, A. (2007). Fiber-element model for slender HSS columns retrofitted with bonded high-modulus composites. *Journal of Structural Engineering* , 133 (1), 85-95.

Shaat, A., & Fam, A. Z. (2009). Slender steel columns strengthened using high-modulus CFRP plates for buckling control. *Journal of Composites for Construction* , 13 (1), 2-12.

Simitses, G. J. (1986). *An introduction to the elastic stability of structures*. Malabar, Florida: Robert E. Krieger Publishing Company.

Skinner, R. I., Kelly, M. J., & Heine, A. J. (1975). Hysteretic dampers for earthquake resistant structures. *Earthquake Eng. Struct. Dyn.* (3), 287-296.

Sloan, F. E., & Talbot, J. B. (1992). Corrosion of graphite-fiber-reinforced composites I - galvanic coupling damage. *Corrosion* , 48 (10), 830-838.

Spyrakos, C. C., & Ermopoulos, J. (2005). Development of aluminum load-carrying space frame for building structures. *Engineering Structures* (27), 1942-1950.

- Takeuchi, T., Hajjar, J. F., Matsui, R., Nishimoto, K., & Aiken, I. D. (2010). Local buckling restraint condition for core plates in buckling restrained braces. *Journal of Constructional Steel Research* , 66, 139-149.
- Takeuchi, T., Ida, M., Yamada, S., & Suzuki, K. (2008). Estimation of cumulative deformation capacity of buckling restrained braces. *Journal of Structural Engineering* , 134 (5), 822-831.
- Tao, Z., Han, L. H., & Zhuang, J. P. (2007). Experimental behavior of CFRP strengthened concrete-filled steel tubular stub columns. *Advances in Structural Engineering* , 10 (1), 37-46.
- Timoshenko, S., & Gere, J. M. (1961). *Theory of Elastic Stability*. New York: McGraw-Hill.
- Tremblay, R., Bolduc, P., Neville, R., & DeVall, R. (2006). Seismic testing and performance of buckling-restrained bracing systems. *Canadian Journal of Civil Engineering* , 33, 183-198.
- Usami, T., Ge, H. B., & Kasai, A. (2008). Overall buckling prevention condition of buckling restrained braces as a structural control damper. *Proc. 14th World Conference on Earthquake Engineering*. Beijing, China: IAEE.
- Wada, A., Saeki, E., Takeuchi, T., & Watanabe, A. (1989). *Development of unbonded brace*. Japan: Nippon Steel Corporation.
- Wakabayashi, M., Nakamura, T., Katagihara, A., Yogoyama, H., & Morisono, T. (1973). Experimental study on the elastoplastic behavior of braces enclosed by precast concrete panels under horizontal cyclic loading - Parts I & II. *Technical Papers of Annual Meeting Architectural Institute of Japan* , 1041-1044.

Watanabe, A., & Nakamura, H. (1992). Study on behavior of buildings using steel with low yield point. *Proc., 10th World Conf. on Earthquake Engineering*, (pp. 4465-4468). Balkema Rotterdam, The Netherlands.

Watanabe, A., Hitomoi, Y., Saeki, E., Wada, A., & Fujimoto, M. (1988). Properties of braces encased in buckling-restraining concrete and steel tube. *Proc., 9th World Conf. on Earthquake Engineering, vol. IV*, (pp. 719-724). Tokyo-Kyoto, Japan.

Xie, Q. (2005). State of the art buckling-restrained braces in Asia. *Journal of Constructional Steel Research*, 61, 727-748.

Yang, T. Y., Moehle, J. P., & Stojadinovic, B. (2009). *Performance Evaluation of Innovative Steel Braced Frames*. Berkeley, CA: Pacific Earthquake Engineering Research Center (PEER).

Yoshino, T., & Karino, Y. (1971). Experimental study on shear wall with braces: Part 2. *Summaries of Technical Papers of Annual Meeting, vol. 11* (pp. 403-404). Architectural Institute of Japan.

Zhao, X., & Zhang, L. (2007). State-of-the-art review on FRP strengthened steel structures. *Engineering Structures*, 29, 1808-1823.

Zhu, J.-H., & Young, B. (2006). Tests and design of aluminum alloy compression members. *Journal of Structural Engineering*, 132 (7), 1096-1107.

APPENDICES

Appendix A: Calculation of Bolted End Connection (Full-scale brace)

Brace connection design requirements are borrowed from the *Seismic Provisions* (American Institute of Steel Construction, 2005b) as a reasonable starting point for determining the connections required for testing. Comparable AISC values for steel are used since no similar provisions exist for aluminum alloy structures. The strain hardening adjustment factor (ω) is taken as 1.0 since 6061 aluminum test coupons exhibited cyclic softening and a low amount of strain hardening. The compression strength adjustment factor (β) is taken as 1.1 per *Seismic Provisions* Chapter T10 acceptance criteria. The expected material strength exceeding nominal is accounted for by using the R_y factor. A value of 1.3 is used on par with ASTM A36 steel. This appears to be a reasonable value for the 6061-T6 material as well. Note that the base material is L6 x 6 x 3/8 and L5 x 5 x 1/4 angles for the full-scale and partial-scale braces, respectively.

Adjusted Brace Strength (AISC Provisions 16.2d)

$$F_{ysc} = 35 \text{ ksi}$$

$$\beta = 1.1$$

$$A_{sc} = 7.92 \text{ in}^2$$

$$\omega = 1.0$$

$$R_y = 1.3$$

$$P_{ysc} = F_{ysc}A_{sc} = 277 \text{ kips}$$

$$P_{adj} = \beta\omega R_y P_{ysc} = 396 \text{ kips}$$

Required Connection Strength (AISC Provisions 16.3a)

$$P_u = 1.1P_{adj} = 436 \text{ kips}$$

Bolt Shear Strength: (AA 5.1.17.4) (AISC 360-05 J3.6)

5/8" diameter ASTM A325X bolts (galvanized)

$$F_{nv} = 60 \text{ ksi}$$

$$\phi = 0.75$$

$$A_b = 0.307 \text{ in}^2$$

$$n = 16 \text{ bolts in double shear}$$

$$\phi r_n = \phi F_n A_b = 13.8 \text{ kips/bolt}$$

$$\phi R_n = \phi r_n n = 442 \text{ kips} > 436 \text{ kips} \therefore o.k.$$

Bearing Strength: (AA 3.4.5)

6061-T6 aluminum 11/16" diameter standard holes (pretensioned)

$$F_{tu} = 38 \text{ ksi}$$

$$\text{Edge distance} = 3 \text{ inches}$$

$$\phi_u = 0.85$$

$$n = 16 \text{ bolts in double shear}$$

$$t = 0.375 \text{ inches}$$

$$d = 0.625 \text{ inches}$$

$$\phi F_L = 2\phi_u F_{tu} = 64.6 \text{ ksi}$$

$$\phi R_n = \phi F_L n t d = 484 \text{ kips} > 436 \text{ kips} \therefore o.k.$$

Tension Strength of Net Section: (AA 3.4.1) (AISC Manual D3.3)

$$k_t = 1.0$$

$$n = 4 \text{ angles}$$

$$A_g = 4.35 \text{ in}^2$$

$$A_e = U A_n = 1.0(4.35 - 2*(11/16)*0.375) = 3.83 \text{ in}^2$$

$$\phi F_L = \frac{\phi_u F_{tu}}{k_t} = 28.5 \text{ ksi}$$

$$\phi R_n = n \phi F_L A_e = 436 \text{ kips} = 436 \text{ kips} \therefore o.k.$$

Block Shear Rupture Strength: (AA 5.4)

$$F_{su} = 24 \text{ ksi}$$

$$A_{nv} = (0.375)*(12 - 11/16*(4)) = 3.47 \text{ in}^2$$

$$F_{ty} = 35 \text{ ksi}$$

$$A_{gt} = (0.375)*(3 - 0.344) = 0.996 \text{ in}^2$$

$$\phi = 0.85$$

$$n = 8 \text{ blocks}$$

pitch = 3" on center

$$\phi R_n = n \phi (F_{su} A_{nv} + F_{ty} A_{gt}) = 803 \text{ kips} > 436 \text{ kips} \therefore o.k.$$

Appendix B: Calculation of Bolted End Connection (Partial-scale brace)

Adjusted Brace Strength (AISC Provisions 16.2d)

$$F_{ysc} = 35 \text{ ksi}$$

$$\beta = 1.1$$

$$A_{sc} = 3.88 \text{ in}^2$$

$$\omega = 1.0$$

$$R_y = 1.3$$

$$P_{ysc} = F_{ysc}A_{sc} = 136 \text{ kips}$$

$$P_{adj} = \beta\omega R_y P_{ysc} = 195 \text{ kips}$$

Required Connection Strength (AISC Provisions 16.3a)

$$P_u = 1.1P_{adj} = 214 \text{ kips}$$

Bolt Shear Strength: (AA 5.1.17.4) (AISC 360-05 J3.6)

1/2" diameter ASTM A325X bolts (galvanized)

$$F_{nv} = 60 \text{ ksi}$$

$$\phi = 0.75$$

$$A_b = 0.196 \text{ in}^2$$

$$n = 16 \text{ bolts in double shear}$$

$$\phi r_n = \phi F_n A_b = 8.82 \text{ kips/bolt}$$

$$\phi R_n = \phi r_n n = 282 \text{ kips} > 214 \text{ kips o.k.}$$

Bearing Strength: (AA 3.4.5)

6061-T6 Aluminum 9/16" diameter standard holes (pretensioned)

$$F_{tu} = 38 \text{ ksi}$$

$$\text{Edge distance} = 2 \text{ inches}$$

$$\phi_u = 0.85$$

$$n = 16 \text{ bolts in double shear}$$

$$t = 0.25 \text{ inches}$$

$$d = 0.625 \text{ inches}$$

$$\phi F_L = 2\phi_u F_{tu} = 64.6 \text{ ksi}$$

$$\phi R_n = \phi F_L n t d = 323 \text{ kips} > 214 \text{ kips o.k.}$$

Tension Strength of Net Section: (AA 3.4.1) (AISC Manual D3.3)

$$k_t = 1.0$$

$$n = 4 \text{ angles}$$

$$A_g = 2.35 \text{ in}^2$$

$$A_e = UA_n = 1.0*(2.35 - 2*(9/16)*0.25) = 2.07 \text{ in}^2$$

$$\phi F_L = \frac{\phi_u F_{tu}}{k_t} = 28.5 \text{ ksi}$$

$$\phi R_n = n\phi F_L A_e = 236 \text{ kips} > 214 \text{ kips} \therefore \text{o.k.}$$

Block Shear Rupture Strength: (AA 5.4)

$$F_{su} = 24 \text{ ksi}$$

$$A_{nv} = (1/4)*(10 - (9/16)*(4)) = 1.94 \text{ in}^2$$

$$F_{ty} = 35 \text{ ksi}$$

$$A_{gt} = (1/4)*(2.5 - 0.281) = 0.554 \text{ in}^2$$

$$\phi = 0.85$$

$$n = 8 \text{ blocks}$$

pitch = 2 1/2" on center

$$\phi R_n = n\phi(F_{su}A_{nv} + F_{ty}A_{gt}) = 449 \text{ kips} > 214 \text{ kips} \therefore \text{o.k.}$$

Appendix C: Calculation of Core Available Strengths (Full-scale brace)

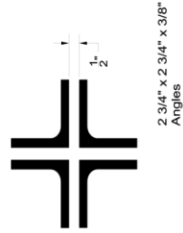
6061-T6 Aluminum Properties

F_{tu}	38 ksi
F_{ty}	35 ksi
F_{cy}	35 ksi
E	10100 ksi
G	3787.5 ksi

Seismically Compact $b/t < 6.45$

Section Properties

A	1.98 in ²
b_o	1.88 in
t_o	0.375 in
I_z	0.725 in ⁴
r_z	0.61 in
J	0.09 in ⁴
C_w	0.0492 in ⁶
L	96 in
k	1



Axial Tension (3.4.1)

Resistance Factor	ϕ_u	Resistance (3.4.1-4)	Available Stress (ksi)	Available Stress ϕF_L (ksi)	Available Strength ϕT_L (kips)	Available Strength ϕT_L (kips)
1.0	0.9	33.3	32.3	263.3	255.8	

Axial Compression Gross Section (3.4.7)

Resistance Factor	ϕ_{cc}	Buckling Constant (ksi)	Buckling Constant D_c (ksi)	Buckling Constant C_c	Buckling Constant D_c^*	Slenderness Limit S_1^*	Slenderness Limit S_2^*	Slenderness Parameter kl/r_z	Slenderness Parameter λ	Available Stress ϕF_L (ksi)	Available Strength ϕP_L (kips)
0.95	39.4	0.2	33.3	65.7	13.1	0.3	1.2	158.7	3.0	3.8	29.8

Axial Compression Gross Section Torsional Buckling (3.4.7.2)

Resistance Factor	Effective Length	K_c	x-coord. shear cent. (in)	x_o (in)	Polar moment of inertia, r_o (in)	Polar coefficient β	Twisting Length L_t (in)	Torsional Buckling Stress F_{et} (ksi)	Elastic Critical Stress F_e (ksi)	Slenderness Parameter $(kl/r_{xy})_e$	Slenderness Parameter λ for $\lambda < S_2^*$	Available Stress ϕF_L (kips)
ϕ_{cc}												
(3.4.1-4)			(3.4.7.2-7)	(3.4.7.2-8)	(3.4.7.2-6)	(3.4.7.2-2)	(3.4.7.2-1)	(3.4.7-6)	(3.4.7-4)			
0.91	1.0	0.80	1.00	0.4	96.0	171.4	24.1	0.5	30.3			239.7

Axial Compression Gross Section Flexural-Torsional Buckling (3.4.7.2)

Resistance Factor	Effective Length	K_x	x-coord. shear cent. (in)	x_o (in)	Polar moment of inertia, r_o (in)	Polar coefficient β	Twisting Length L_t (in)	Bending Length x-axis L_b (in)	Torsional Buckling Stress F_{et} (ksi)	Torsional Buckling Stress F_{ex} (ksi)	Elastic Critical Stress F_e (ksi)	Slenderness Parameter $(kl/r_{xy})_e$	Slenderness Parameter λ for $\lambda > S_2^*$	Available Stress ϕF_L (kips)
ϕ_{cc}														
(3.4.1-4)			(3.4.7.2-7)	(3.4.7.2-8)	(3.4.7.2-6)	(3.4.7.2-2)	(3.4.7.2-1)	(3.4.7-5)	(3.4.7.2-2)	(3.4.7-6)	(3.4.7-4)	(3.4.7.2-1)	(3.4.7-6)	(3.4.7-4)
0.95	1.0	1.0	0.76	0.97	0.4	96.0	96.0	183.3	4.0	3.9	160.4	3.0	3.7	29.2

Uniform Compression of Components Supported Along One Edge (3.4.8)

Resistance Factor	Width-Thickness Ratio b/t	Buckling Constant D_p (ksi)	Buckling Constant B_p (ksi)	Coefficient of Bending k_1	Coefficient of Bending k_2	Slenderness Limit S_1	Slenderness Limit S_2	Available Stress ϕF_L (kips)
ϕ_y								
(3.4.8-6)	(3.4.8-7)	(3.3-4)	(3.3-4)	(3.3-4)	(3.3-4)	(3.4.8-4)	(3.4.8-5)	(3.4.8-3)
0.95	0.85	45.0	0.3	0.35	2.27	3.9	10.3	31.7
								251.5

Appendix D: Calculation of Core Available Strengths (Partial-scale brace)

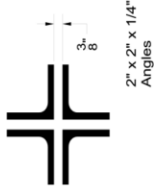
6061-T6 Aluminum Properties

F_{tu}	38 ksi
F_{ty}	35 ksi
F_{cy}	35 ksi
E	10100 ksi
G	3787.5 ksi

Seismically Compact $b/t < 6.45$

Section Properties

A	0.97 in ²
b_o	1.375 in
t_o	0.25 in
I_z	0.14 in ⁴
r_z	0.39 in
J	0.0195 in ⁴
C_w	0.00572 in ⁶
L	60 in
k	1



Axial Tension (3.4.1)

Resistance Factor ϕ_y	Resistance Factor ϕ_u	Available Stress ϕF_L (ksi)	Available Stress ϕF_L (ksi)	Available Strength ϕT_L (kips)	Available Strength ϕT_L (kips)
1.0	0.9	33.3	32.3	129.0	125.3

Axial Compression Gross Section (3.4.7)

Resistance Factor ϕ_{cc}	Buckling Constant B_c	Buckling Constant D_c (ksi)	Buckling Constant C_c	Slenderness Limit S_2^*	Slenderness Parameter kl/r_{xy}	Slenderness Parameter λ	Available Stress ϕF_L (ksi)	Available Strength ϕP_L (kips)
0.95	39.4	0.2	65.7	1.2	153.8	2.9	4.0	15.5

